



RÜDIGER HAAKE

Measurement of charged jets
in p–Pb collisions at $\sqrt{s_{\text{NN}}} = 5.02$ TeV
with the ALICE detector

2015

Experimentelle Physik

Measurement of charged jets
in p–Pb collisions at $\sqrt{s_{\text{NN}}} = 5.02 \text{ TeV}$
with the ALICE detector

Inauguraldissertation
zur Erlangung des Doktorgrades
der Naturwissenschaften im Fachbereich Physik
der Mathematisch-Naturwissenschaftlichen Fakultät
der Westfälischen Wilhelms-Universität Münster

vorgelegt von
Rüdiger Haake
aus Oberhausen

– März 2015 –

Dekan:	Prof. Dr. Christian Weinheimer
Erster Gutachter:	Prof. Dr. Johannes P. Wessels
Zweiter Gutachter:	Prof. Dr. Michael Klasen

Tag der Disputation:
Tag der Promotion:

FÜR ELISABETH

Contents

1. Introduction	1
2. Theoretical basics	5
2.1. A glimpse of the Standard Model	5
2.2. Quantumchromodynamics	8
2.2.1. QCD factorization	10
2.2.2. The QCD phase diagram	11
2.3. Basic properties of high energy collisions	12
2.3.1. Nucleon–nucleon collisions	12
2.3.2. Nucleus–nucleus collisions	13
2.3.3. Nucleon–nucleus collisions	14
2.3.4. A typical high energy collision	15
2.4. Jet production	16
3. Nuclear effects	17
3.1. Nuclear parton distribution functions	17
3.2. Details on initial state effects	19
3.3. Gluon saturation and the Color Glass Condensate	21
3.4. Final state effects	23
3.4.1. Jet quenching and parton energy loss	23
3.4.2. Collective flow	25
4. The ALICE detector	29
4.1. ALICE as the dedicated heavy-ion experiment at the LHC	30
4.2. Main tracking detectors	31
4.2.1. Inner Tracking System	32
4.2.2. Time Projection Chamber	33
4.3. Detectors used for event characterization and centrality estimation	34
4.3.1. V0	34
4.3.2. ZDC	34
5. Basic analysis techniques	37
5.1. Track reconstruction with ALICE	37

5.2.	Jet reconstruction	39
5.2.1.	The anti- k_T and k_T algorithms	40
5.2.2.	Jet area calculation	42
5.2.3.	Jet recombination scheme	42
5.3.	Centrality estimation	44
5.3.1.	The Glauber model	45
5.3.2.	NBD-Glauber fit approach	46
5.3.3.	Hybrid approach	49
5.4.	Event generation and detector simulation	51
5.4.1.	PYTHIA and POWHEG	51
5.4.2.	Detector simulation with GEANT	52
5.5.	Evaluation of uncertainties	53
5.5.1.	Statistical uncertainties	53
5.5.2.	Systematic uncertainties for the jet spectra	54
6.	Correction techniques	57
6.1.	Underlying event correction	58
6.1.1.	Methods using k_T jets	59
6.1.1.1.	Original approach in Pb–Pb	59
6.1.1.2.	Default approach in p–Pb	60
6.1.1.3.	Mean-based approach	61
6.1.2.	Method using tracks	62
6.1.3.	Background fluctuations	63
6.1.4.	Centrality and jet p_T dependence	65
6.1.5.	Pseudorapidity dependence	67
6.1.6.	Conclusions	69
6.2.	Unfolding jet spectra	72
6.2.1.	Unfolding algorithms	73
6.2.1.1.	SVD unfolding	73
6.2.1.2.	χ^2 -unfolding	74
6.2.1.3.	Bayesian unfolding	75
6.2.1.4.	Manual procedure	76
6.2.2.	Creating the response matrix	76
6.2.3.	Regularization parameter analysis	83
6.2.4.	Comparison and conclusion	86
7.	Data sample	91
7.1.	Utilized datasets	91
7.2.	Event selection	93
7.2.1.	Trigger	93
7.2.2.	Pile-up correction	94
7.2.3.	Vertex definition	94

7.3. Track selection	96
7.3.1. Track cuts	97
7.4. Jet selection	101
8. Jets in minimum bias p–Pb collisions	105
8.1. Charged jet production cross sections	105
8.2. Construction of the pp reference	109
8.3. Nuclear modification factor	111
8.4. Radial jet structure analysis	114
8.4.1. Jet production cross section ratio	114
8.4.2. Jet constituent profiles	119
8.4.2.1. Jet collimation in p_T	119
8.4.2.2. Comparison of jet profiles in p–Pb and pp	122
8.5. Low transverse momentum jets	124
8.6. Comparing results using good and all runs	128
8.7. Comparison to charged particles	130
8.8. Comparison to fully reconstructed jets in p–Pb	132
9. Systematic uncertainties	135
9.1. Unfolding	136
9.1.1. Unfolding method	136
9.1.2. Regularization strength	138
9.1.3. Prior	139
9.1.4. Minimum p_T threshold	141
9.2. Background	142
9.2.1. Signal exclusion in δp_T	142
9.2.2. Background estimate	142
9.3. Tracking efficiency	144
9.3.1. Evaluation of tracking efficiency uncertainty	144
9.3.2. Effect on jet observables	151
9.4. Normalization	153
9.5. Summary of uncertainties in minimum bias events	156
10. Jets in pp collisions	161
10.1. Charged jet production cross sections	161
10.2. Jet production cross section ratio	164
10.3. Summary of systematic uncertainties	165
11. Centrality dependence of jets in p–Pb collisions	169
11.1. Charged jet production cross sections	169
11.2. Nuclear modification factor Q_{pPb}	171
11.3. Central over minimum bias ratios R_{CM}	175

11.4. Jet production cross section ratios	177
11.5. Nuclear modification using NBD-Glauber fit centrality	179
11.6. Summary of systematic uncertainties in bins of centrality	181
Summary	185
Zusammenfassung	188
A. Appendix	191
A.1. Basic kinematics	191
A.1.1. Center-of-mass energy	191
A.1.2. Rapidity and pseudorapidity	192
A.2. Systematic uncertainties	194
A.2.1. Uncertainties for minimum bias $R = 0.2$ jets	194
A.2.2. Uncertainty summary for centrality-dependent $R = 0.2$ jets	198
List of tables	201
List of figures	201
Bibliography	205
Acknowledgements	213

1. Introduction

The wish to understand the universe and its smallest building blocks has raised human interest ever since. First concepts were already developed in antiquity, and an experimental verification of atomistic ideas was achieved in the last few hundred years. The observation and exploration of atomic nuclei took place essentially in the 20th century though. Virtually the whole conception of the history of the universe is driven by insights obtained over the last 150 years.

One major reason that the history of nuclear physics is relatively young is doubtless the need for more and more powerful measurement techniques. The smaller the objects of interest are the higher must be the resolution of the instruments to resolve them. To investigate objects on the atomic or even nuclear scale, the measurement devices, i.e. particle accelerators, have to reach extremely high energies. The energy scale of processes which take place between atoms and nuclei or even more fundamental particles like nucleons grows quickly: While processes on the atomic scale involve energies of the order of a few eV, excitations of nuclei happen on the MeV scale and of nucleons it is $0.1 - 1$ GeV [Loh05].

High energy physics is the research field that addresses the smallest constituents and their fundamental interactions at high energies. The most impressive tools of this research field are surely the huge colliders demanding hundreds of megawatts of peak electric power. The Large Hadron Collider (LHC) is probably the best known device of high energy physics, not least because of the recent discovery of the Higgs boson in 2012 by the ATLAS and CMS collaborations, which was made possible with beams of the LHC at energies of 3.5 and 4 TeV [Aad12, Cha12b].

There are also several other not less impressive experiments in high energy physics like IceCube, which is specialized in measuring neutrinos in one cubic kilometer of ice in Antarctica, or the (planned) International Linear Collider (ILC) that will probably be built in Japan and whose aim is to investigate the properties of the Higgs boson in detail.

The present work is based on data taken with the ALICE detector [Aam08], which is situated at the LHC. ALICE is the dedicated heavy-ion experiment at the LHC. Ultra-relativistic heavy-ion physics is a specialized subfield of nuclear physics at the interface to high energy physics. The ALICE detector is especially capable of measuring and identifying particles at relatively low momenta.

Ultra-relativistic heavy-ion collisions are studied to shed light on strongly interacting matter in extreme conditions. For instance, in collisions of lead-ions a strongly interact-

ing extended medium, the quark-gluon plasma, can be formed. This medium probably existed a few microseconds after the Big Bang. The investigation of this phase is therefore not only interesting for a better understanding of the strong interaction but also to address cosmological questions of the early universe.

A key measurement of heavy-ion physics is the observation of jet quenching. Jet quenching describes a suppression in particle and jet production in collisions of lead-ions compared to proton-proton (pp) collisions. Of course, the probability of more than one nucleon-nucleon interaction in a collision of two lead-nuclei is much higher than in a collision of two protons. This trivial effect can easily be corrected.

A priori, it is not known which portion of the suppression is caused by the nuclear environment in which the interactions take place and which portion by the medium which is formed after the collision.

Initially, it was believed that a strongly interacting medium is generally not created in proton-lead (p-Pb) collisions. Assuming this, the measurements in p-Pb can serve as baseline measurements, in which only the nuclear environment prior to the collision and potential nuclear final state effects influence the measurement. Correspondingly, the measurement can be used to disentangle *cold* nuclear matter effects from *hot* nuclear matter effects.

However, recent measurements have shown that this assumption is only partially correct. Collective effects, originally believed to occur only in connection with a formed medium, have also been observed in p-Pb collisions.

Apart from serving as a baseline measurement, the present work also gives an idea of the actual impact of the nuclear environment on jet production. In addition, more differential analyses on the jet radial structure are presented.

The chosen physics observable are high energy charged jets. These are collimated sprays of particles that originate from a hard parton interaction in high energy collisions. *Charged* jets specify the charged part of a full jet containing charged and neutral particles. The reason for measuring charged jets instead of full jets is that ALICE is especially capable of detecting (charged particle) tracks. An electromagnetic calorimeter is available, but it has only a limited acceptance.

Charged jets and full jets are expected to behave in a similar way but, of course, on a different energy scale, because full jets additionally contain neutral particles.

The thesis is structured as follows. Chapters 2 and 3 give a brief introduction to the theoretical basis of high energy collisions and nuclear effects that can possibly influence the jet production in p–Pb collisions. Chapter 4 provides information on those parts of the ALICE detector, which have been used for the subsequent analyses.

After an introduction to general techniques of jet analysis in Chapter 5, more specialized correction techniques are discussed in detail in Chapter 6.

The selected data sample and selection criteria for particle tracks and jets are shown in Chapter 7.

The main minimum bias analysis results, which have already been published in [Abe15], are presented in Chapter 8. Systematic uncertainties were calculated in great detail and are shown in Chapter 9.

Next to the analysis of p–Pb data, also pp collisions at $\sqrt{s} = 7$ TeV were analyzed in full detail. The main motivation for this analysis is that a pp baseline is necessary to estimate the nuclear modification. This analysis can be found in Chapter 10.

Centrality-dependent results are shown in Chapter 11. Those have also been published as preliminary results in a conference proceeding [Haa15].

2. Theoretical basics

In the following, a short overview of the fundamental theoretical basics of this thesis is presented. This includes properties of the Standard Model in particle physics and especially Quantumchromodynamics, the theory of strong interactions. Also, general considerations on high energy collisions are presented.

More specific theoretical foundations of the measurement presented in this thesis, i.e. nuclear effects, are given in Chapter 3.

For the sake of completeness, Appendix A.1 contains an introduction to the basic kinematic observables deployed throughout this thesis.

2.1. A glimpse of the Standard Model

The measurement of high energy collisions is a powerful tool to probe the most fundamental interactions in the universe that take place at highest energies. Currently, the understanding of the building blocks of the universe is governed by the Standard Model (SM). Although it is by construction not complete – e.g. gravity is missing, see below – its predictions are in extraordinarily good agreement with measurements.

Within the framework of the SM, the universe is described by three fundamental interactions: strong, weak, and electromagnetic reactions. The theory of the strong interaction is called Quantumchromodynamics (QCD). Quantumelectrodynamics (QED) as the theory of electromagnetic interactions and the theory of weak interactions can also be characterized by a combined electroweak theory. These fundamental forces act on a collection of fundamental particles: quarks, leptons, and gauge bosons.

Quarks are strongly interacting fundamental particles which form hadrons. They can be arranged in three families,

$$\begin{pmatrix} u \\ d \end{pmatrix} \begin{pmatrix} c \\ s \end{pmatrix} \begin{pmatrix} t \\ b \end{pmatrix}. \quad (2.1)$$

Quark	Mass	Lepton	Mass
u	$1.8 - 3.0 \text{ MeV}/c^2$	ν_e	$< 0.66 \text{ eV}/c^2$
d	$4.5 - 5.3 \text{ MeV}/c^2$	e	$0.511 \text{ MeV}/c^2$
c	$1.275 \pm 0.025 \text{ GeV}/c^2$	ν_μ	$< 0.66 \text{ eV}/c^2$
s	$95 \pm 5 \text{ MeV}/c^2$	μ	$106 \text{ MeV}/c^2$
t	$173 \pm 0.51 \pm 0.71 \text{ GeV}/c^2$	ν_τ	$< 0.66 \text{ eV}/c^2$
b	$4.18 \pm 0.03 \text{ GeV}/c^2$	τ	$1777 \text{ MeV}/c^2$

Boson	Mass
γ	massless
W^\pm	$80.4 \text{ GeV}/c^2$
Z^0	$91.2 \text{ GeV}/c^2$
g	massless
H^0	$125.7 \pm 0.4 \text{ GeV}/c^2$

Table 2.1: Elementary particles and their measured masses. Except for the neutrinos, the masses are taken from [Oli14]. For the quarks, the uncertainties are given like in this paper. For the leptons and gauge bosons, the uncertainties are not shown because of their smallness. Note that the given neutrino mass bound is model-dependent [Ade14].

Each quark carries a color charge: red, green, or blue. This is not related to the sensual perception of color. The color convention is chosen for the reason that red, green, and blue form white in additive color mixing – corresponding to no color. In the simple valence quark picture, baryons as bound states of three quarks can therefore be constructed with no net color charge. Also, mesons carrying color and “anti”-color in quarks and anti-quarks are effectively color-neutral particles.

The bare masses of the quarks and those of the other SM particles are summarized in Tab. 2.1.

Apart from their masses, both quarks in each doublet in Eq. 2.1 differ also in their electric charge. It is

$$Q_{\text{elec.}}(u, c, t) = +2/3e, \quad (2.2)$$

$$Q_{\text{elec.}}(d, s, b) = -1/3e. \quad (2.3)$$

Note that the quarks carry fractions of the fundamental electric charge e .

Like the quarks, also the leptons can be categorized into three families,

$$\begin{pmatrix} \nu_e \\ e^- \end{pmatrix} \begin{pmatrix} \nu_\mu \\ \mu^- \end{pmatrix} \begin{pmatrix} \nu_\tau \\ \tau^- \end{pmatrix}, \quad (2.4)$$

where the *up-type* particles in the doublets are neutrinos and the *down-type* particles are charged leptons, following the convention according to which the down-type particles of a doublet are those with lower charge.

Neutrinos are neutral, very light and only weakly interacting particles. The charged leptons have $Q_{\text{elec.}}(e^-, \mu^-, \tau^-) = -1e$ and can interact electromagnetically and weakly.

In addition to quarks and leptons, there also exist gauge bosons, the carrier particles of the fundamental forces: photons, W/Z -bosons, and gluons. Photons are the mediators of the electromagnetic interaction. They are massless spin-1 particles and do not carry an electromagnetic charge. The weak bosons W^\pm and Z^0 are the carrier particles of the weak interaction. W^+ and W^- are electrically charged with the elementary charge e , positive or negative, respectively, Z^0 is neutral. All three bosons are massive and carry spin 1. Due to their relatively high mass of $80 \text{ GeV}/c^2$ for the W 's and $91 \text{ GeV}/c^2$ for the Z , they are very short-lived particles with a half-life of roughly $2.6 \cdot 10^{-25} \text{ s}$ (Z^0) and $3.1 \cdot 10^{-25} \text{ s}$ (W^\pm) [Ber06].

For the strong interaction, the exchange particles are gluons. These massless and electrically neutral particles can exist in eight independent color states. This is a huge difference to the electrically neutral photons: Gluons, which mediate the strong interaction, do carry a strong charge. That is why color charges are bound within hadrons and cannot be observed freely. The phenomenon is called confinement.

Additionally, an important ingredient of the Standard Model, which particularly explains the massiveness of the weak bosons, is the Higgs Boson. It is neither electrically nor color charged and it is the only known fundamental scalar (spin-0) particle. It was recently discovered by the ATLAS and CMS collaborations. According to the Particle Data Group, the mass is $125.7 \pm 0.4 \text{ GeV}/c^2$ [Oli14].

All fundamental particles have their corresponding antiparticles or they are their own ones. As already stated above, up to now, all experimental observations agree amazingly well with Standard Model predictions. Many observations have been predicted in the context of the SM, e.g. the existence of the top-quark or the anomalous Landé factor of the electron. Although it describes all today known particles, it is not complete by concept. Apart from gravity and therewith general relativity, which are simply not included in the SM framework, several phenomena cannot be explained by the theory. Very prominent examples are dark matter and dark energy. But also the neutrino oscillation implying a non-zero neutrino mass has not yet been described within the scope of the Standard Model.

2.2. Quantumchromodynamics

In the middle of the 20th century, the analysis of cosmic rays and especially the data from particle accelerators at growing energies, revealed the existence of more and more supposedly fundamental particles. The increasing number of these particles is often called the *particle zoo*. Even before a model for a potential substructure had been developed, there were hints on a substructure in protons and neutrons (cf. e.g. [Das95]). In 1964, Gell-Mann and Zweig independently developed models to describe the hadronic spectra by introducing the *quarks* as the constituents of the hadrons [GM64, Zwe64]. In the beginning, the quark model was more or less a construct to simplify calculations, but during the late 1960s, deep inelastic scatterings at SLAC [Blo69, Bre69] suggested indeed the existence of fractionally charged hadron constituents that can be identified with the quarks.

The quark model postulates baryons and mesons that are made of u , d , c , s , and b flavored quarks. While the quark model describes also t flavored quarks, no hadronic states with a t -quark exist due to its short-livedness.

It became clear relatively quickly that the quarks need a new degree of freedom: color. One reason for this was the discovery of the Δ^{++} baryon. This baryon consists of three u -quarks,

$$\Delta^{++} = |u \uparrow u \uparrow u \uparrow\rangle, \quad (2.5)$$

and seemingly violates Pauli's principle. The introduction of the color charge for the quarks solves this problem.

As the name suggests (*chroma* (greek) = color), the theory of Quantumchromodynamics is the theory of the interaction of color charges. While QCD is formulated as a gauge theory in the same way as the extremely successful theory of Quantumelectrodynamics, it shows some crucial differences. QED is based on the abelian U(1) gauge symmetry and it predicts one uncharged gauge boson. In contrast, QCD obeys the non-abelian SU(3) symmetry connected to the three color charges. It therefore includes $N_C^2 - 1 = 8$ charged gauge bosons – the gluons –, which can interact with other gluons. Both quarks and gluons are called *partons*.

The theoretical basis of QCD is described by the QCD Lagrangian, given by

$$\mathcal{L}_{\text{QCD}} = -\frac{1}{4}F_{\mu\nu}^c F_c^{\mu\nu} + \sum_f \bar{\psi}_f (i\gamma^\mu D_\mu - m_f)\psi_f. \quad (2.6)$$

In this equation, the first term represents the self-interaction and propagation of the gluon fields and the second term describes the strong interaction of quark and gluon fields. Here, the index c runs over all considered colors, f over all considered flavors.

It is an experimental fact that there is up to now no evidence for free color charges and that all hadrons are color-neutral particles. This phenomenon is called *confinement* and is currently not fully understood in the framework of QCD. Phenomenologically, confinement can be described by a potential which linearly rises for color charge separation r [Gat10],

$$V(r) = A + B/r + \sigma r. \quad (2.7)$$

The origin of the part of the potential rising in r is found in the self-interaction of the gluons. Roughly speaking, the separation of two color sources creates a flux tube, in which the force carriers again participate in the field creation.

At a certain separation, the potential energy in the flux tube is high enough to spontaneously create quark-antiquark pairs that neutralize the color charges. This is sometimes called *string breaking*.

While the partons are confined for low energies, they behave as quasi-free particles at high energies. This phenomenon is called *asymptotic freedom*. In a phenomenological sense, the behavior can be understood by looking at the running coupling constant at leading order [Loh05],

$$\alpha_s = \frac{12\pi}{(33 - 2 \cdot N_f) \ln \left| \frac{Q^2}{\Lambda^2} \right|}, \quad (2.8)$$

where N_f is the number of effectively participating flavors and Λ the QCD scale parameter. Looking at this formula, it is clear that the coupling strength depends on Q^2 , the momentum transfer. The larger Q^2 is, the weaker is the coupling.

This QCD property allows the partons to deconfine whenever they form a dilute gas of weakly coupled particles at temperatures of the order of GeV or higher [Sar10].

Established tools for performing calculations in Quantumchromodynamics are perturbative QCD (pQCD) and lattice QCD (LQCD). Perturbative QCD cannot describe why partons are confined in hadrons because the basic assumption of perturbation theory – a small coupling constant – is not fulfilled. At high energies, partons show asymptotic freedom. Here, pQCD calculations become useful tools. Lattice QCD [Wil74] is principally able to perform calculations in the non-perturbative regime at low energies and, thus, it is a tool for calculating e.g. hadron masses. But those calculations demand enormous amounts of computing power and, therefore, the prediction power is limited. An additional approach to non-perturbative QCD properties are effective theories. These are phenomenological models used to describe low energy processes. For example, the hadronization during jet formation when the partons freeze out to color neutral hadrons can be described e.g. by the Lund string model [And83].

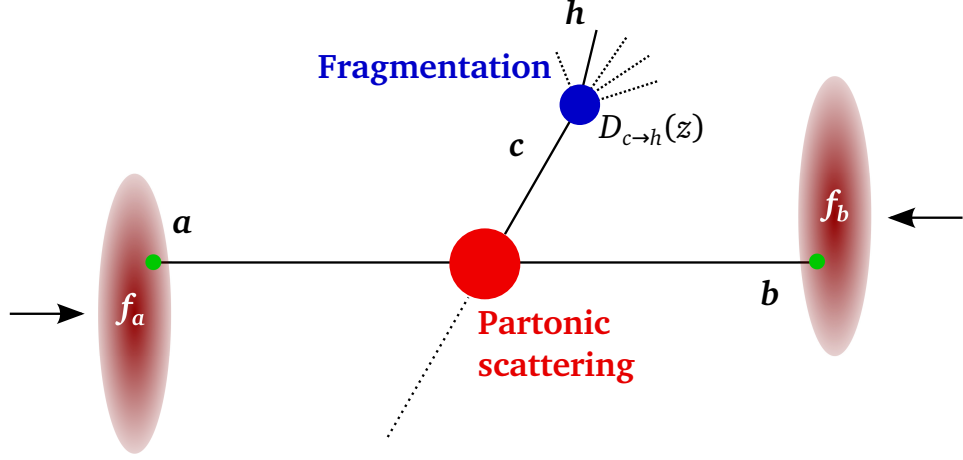


Figure 2.1: Illustration of the different elements in the factorized hard scattering process.

2.2.1. QCD factorization

Hard (high Q^2) and soft (low Q^2) processes in high energy collisions occur on different length and time scales. While the hard processes can be treated in perturbative QCD, soft processes cannot. The concept of factorization is the separation of those hard processes like the hard parton scattering and soft processes, essentially the interactions of bound partons in the initial state in nucleons or nuclei and fragmentation. These types of processes are considered as independent. At leading order, the production cross section of a hadron h in a nucleon–nucleon collision can be factorized by [Col85, Col88]

$$E \frac{d^3 \sigma_{NN \rightarrow h}^{\text{hard}}}{d^3 p} = \sum_{a,b,c} \int dx_a \int dx_b \int dz f_a(x_a, Q^2) \otimes f_b(x_b, Q^2) \otimes \frac{d^3 \sigma_{a+b \rightarrow c}^{\text{hard}}}{d^3 p}(Q^2) \otimes D_{c \rightarrow h}(z). \quad (2.9)$$

In this equation, the individual components are given by the parton distribution functions $f_i(x, Q^2)$, the partonic pQCD cross section for the hard scattering process $a+b \rightarrow c$, and the fragmentation function $D_{c \rightarrow h}(z)$.

The parton distribution function (PDF) $f_i(x, Q^2)$ specifies the distribution of parton type i and, thus, the initial state of the parton in a nucleon or nucleus. It is a non-perturbative quantity and cannot be calculated. PDFs have been measured for a variety of values for x and Q^2 in deep inelastic scattering experiments.

The cross section of the hard parton scattering process is directly calculable in pQCD. It describes the interaction of the point-like quarks and gluons inside the nucleons in a hard scattering with high momentum transfer Q^2 .

The last element in Eq. 2.9 is the fragmentation function $D_{c \rightarrow h}(z)$. This term represents the transformation of the parton c into an observable hadron h , carrying the fraction z of the parton c . Like the parton distribution function, the fragmentation function is a

non-perturbative quantity and can only be determined experimentally. An illustration of the scattering process in this factorization picture is found in Fig. 2.1.

2.2.2. The QCD phase diagram

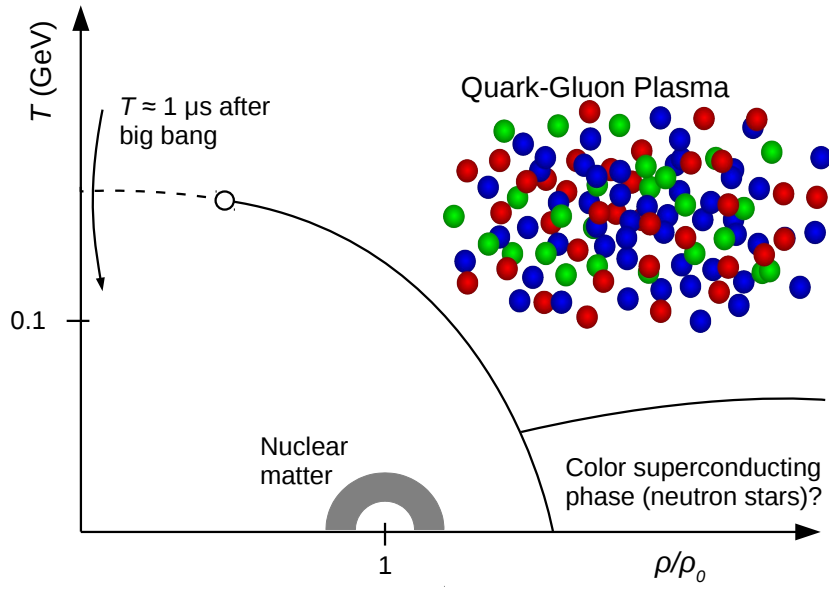


Figure 2.2: Sketch of the possible phases of nuclear media [KB04, Ste06].

Hadronic matter can be described as a bound state of quarks and gluons. In the simple valence or constituent quark model, baryons consist of three quarks while mesons are made of one quark and one antiquark bound by gluons. In a more differential model, also virtual quarks and gluons exist in the hadrons and contribute to their properties. For reactions at higher energies, they become more and more important.

Nuclear matter, for example given by a heavy nucleus, is a bound state of protons and neutrons and can to some extent be seen as a bound many-body system of quarks and gluons. This system can be described in terms of nuclear thermodynamics using concepts like temperature and pressure.

The ordinary nuclear matter, which mainly constitutes the universe, exists at low temperature and pressure. The partons are confined within the hadrons. At higher temperature, there is a phase transition to a deconfined plasma of quarks and gluons, in which they behave as quasi-free particles. This phase is believed to have only existed in a few microseconds after the Big Bang.

Conditions of very high temperature and pressure are fulfilled in heavy-ion collisions, in which a many-body system of highly-energetic partons is created. Predictions from lattice QCD suggest the critical temperature for the phase transition to be at roughly $T_C = 155$ MeV, corresponding to an energy density of 1 GeV/fm^3 [Bor13].

At very high pressure but lower temperature, an additional phase transition is expected that is probably only accessible through astrophysical observations in neutron stars [Alf01]. The phase diagram is depicted in Fig. 2.2.

2.3. Basic properties of high energy collisions

High energy collisions using accelerators like the LHC are powerful experimental environments to analyze QCD properties and to probe the hot and dense quark-gluon plasma. The properties of data obtained from colliding protons with protons or ions with ions differ markedly in terms of the general event structure and of the underlying physics. Proton-lead collisions combine details of both collisions types. In the following, the basic properties of

- nucleon–nucleon collisions,
- nucleon–nucleus collisions,
- and nucleus–nucleus collisions

are described.

2.3.1. Nucleon–nucleon collisions

Nucleon–nucleon or more precisely proton–proton collisions are conceptually the easiest reaction type. Through QCD interaction, partons inside the protons interact in an quasi-elastic scattering and produce a great number of new particles, mostly pions at low transverse momentum.

Most of the produced particles have a low transverse momentum and the spectrum is almost exponential. These particles originate mostly from soft processes, in which the squared momentum transfer Q^2 is of the order of the QCD scale parameter. Therefore, the analysis cannot be done in perturbation theory.

Rarer particles at the larger transverse momentum end of the spectrum are distributed according to a power law. They were produced in so-called hard processes. Hard processes are parton scatterings with high momentum transfer and can therefore be treated by perturbative QCD. The scattered parton can be considered as asymptotically free and produces typical signs of particle jets.

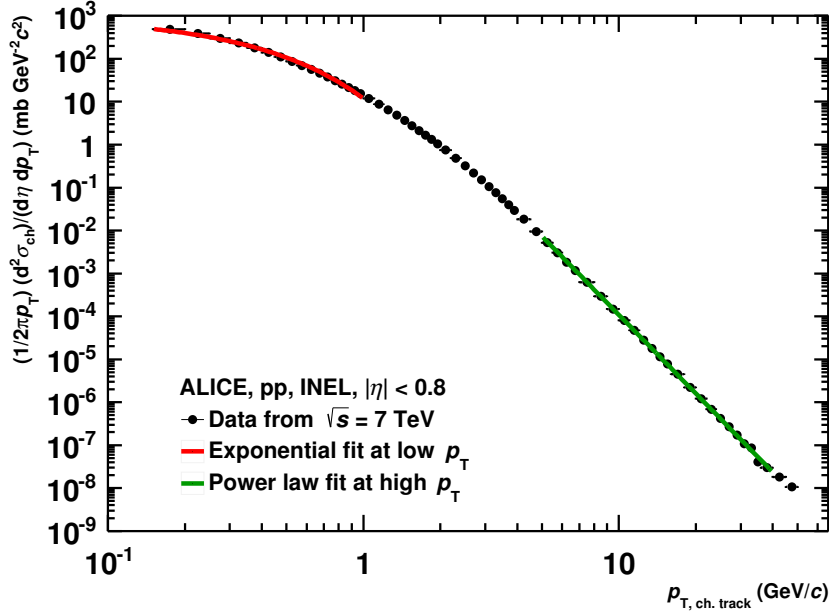


Figure 2.3: Charged track invariant yield for inelastic proton–proton collisions measured at 7 TeV with the ALICE detector [Abe13d]. Exponential and power-law fits show a good agreement in their p_T ranges.

Low- p_T exponential and high- p_T power-law behavior is nicely seen in Fig. 2.3.

Independent of the underlying production process of the particles – be it hard or soft processes – the particles in the final state are eventually *hadronized* into color-neutral particles. This process cannot be calculated by pQCD and can e.g. be understood phenomenologically in the framework of string models. Here, the field energy between two color sources is described as a string that allows the spontaneous creation of $q\bar{q}$ -pairs if the string breaks.

2.3.2. Nucleus–nucleus collisions

In addition to the processes that occur in nucleon–nucleon collisions, effects resulting from the collision geometry and of course resulting from the medium have to be taken into account. It turns out that nucleus–nucleus collisions cannot simply be described as incoherent superpositions of nucleon–nucleon collisions.

The general structure of the event strongly depends on the so-called impact parameter b , the distance between both colliding nuclei. If the impact parameter gets smaller, the overlapping regions in which reactions take place get larger. In fully head-on collisions, the multiplicity is the highest. This event property, which is also used as an event clas-

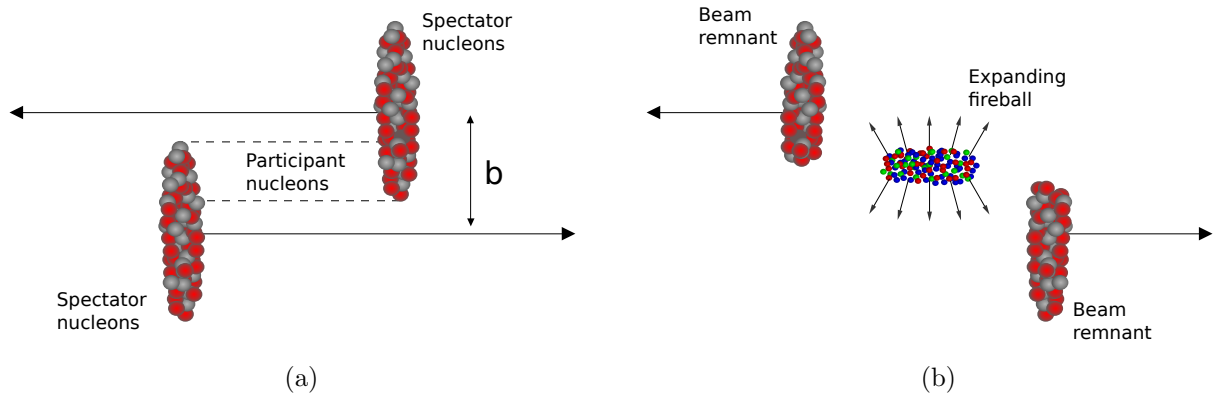


Figure 2.4: Illustration of a semi-central nucleus–nucleus collision before the interaction(a) and after the interaction(b).

sification criterion, is called *centrality*. A more detailed description is given in Sec. 5.3.

In heavy-ion collisions, one distinguishes between so-called *spectator* and *participant* nucleons. Due to the small de-Broglie wavelength of the nucleons at high energies, they are considered to be independent inside the nucleus. Thus, only nucleons within the overlapping interaction region are participants of the collision. The spectator nucleons remain more or less unaffected by the collision.

In contrast to nucleon–nucleon collisions, the elastic parton–parton reactions in heavy-ion collisions take place in a nuclear environment. On the one hand, the different initial state can potentially influence the scattering process, e.g. due to different parton distributions. On the other hand, the collision participants are affected by the final state since they have to traverse the medium that has been formed in the collision. It is a priori not clear how strong both effects are. For a correct interpretation of effects seen in nucleus–nucleus collisions, it is necessary to disentangle cold nuclear matter effects from the hot nuclear matter effects, which originate from the strongly interacting medium in the final state.

2.3.3. Nucleon–nucleus collisions

In nucleon–nucleus collisions, final state effects resulting from the formation of a strongly interacting medium like the QGP are expected to be small. However, those collisions take place in a nuclear environment. They are therefore an ideal candidate to separate hot and cold nuclear matter effects.

The general event structure of nucleon–nucleus collisions resembles that of nucleon–nucleon collision events: For the considered p–Pb collisions, the average multiplicity

and underlying event activity of soft processes is of the same order as in pp collisions. However, typical properties of heavy-ion collisions like event centrality can also be defined and small collective effects can also be observed in p–Pb collisions [Abe13b].

2.3.4. A typical high energy collision

To give an example of how a typical high energy collision can occur, a schematic timeline for an event including a hard process is given. A typical time scale is of the order of a few fm/ c .

- **Parton scattering:** In a high energy collision, e.g. a pp collision, two partons scatter. This process is likely to occur more than once in an event if heavy-ions are collided. The probability of such a scattering can be affected by a nuclear environment (initial state effects).
- **Parton showering:** High energy allows the formation of new partons between scattered partons. One parton *fragments* into many partons. This process is called fragmentation or QCD branching and can be described in the context of the DGLAP equations.
In heavy-ion collisions, a quark-gluon plasma can be created at sufficiently high energies. In this case, additional effects from the medium can occur, e.g. jet quenching resulting from QGP-induced gluonic bremsstrahlung.
- **Collective effects:** In a local thermal equilibrium, a collective motion can appear due to a partonic pressure gradient. In heavy-ion collisions, this gradient is mainly determined by the initial collision geometry.
- **Hadronization:** Since confinement forbids free color charges, the separated partons have to *hadronize* into color-neutral particles. This process is described by phenomenological models, e.g. by the Lund string model [And83], in which the color flux tube is considered as a string that can spontaneously form $q\bar{q}$ -pairs to neutralize the color charge.

The phase transition of a hot medium to hadronic matter takes place first. This is followed by the chemical freeze-out. Different hadron species decouple from the interaction and their relative yields remain unchanged. Finally, the kinematic freeze-out indicates the end of all strong interactions. The energy and momentum distributions are fixed.

While the medium formation occurs after around 1 fm/ c , the hadronization happens at roughly 10 fm/ c .

2.4. Jet production

If the momentum transfer in the parton scattering is large enough, jets can be formed in the collision.

From the perspective of the observer, jets are sprays of particles in the detector that flew roughly into the same direction. Analyzing collisions in lepton colliders at very high momentum transfers of the order of GeV/c , jets can be perceived by studying the tracks in the detector. For hadron colliders and especially for heavy-ion collisions, this turns out to be more and more difficult because the background and its fluctuations are enormous.

Jets as bunches of collimated particles are produced in an elastic scattering of partons in a high energy collision. The initial scattering can principally take place between all constituents of the collided hadrons. At lower virtualities Q^2 , i.e. low transferred (squared) four-momentum, collisions of valence quarks contribute to this initial scattering dominantly. At higher virtualities, interactions of sea quarks and gluons becomes more and more probable.

While all individual particles of the jets are created in a non-perturbative process (i.e. by hadronization), the four-momentum of the reconstructed jets is close to that of the incident partons. This means the jets are mainly determined by perturbative processes with high momentum transfer and, thus, the cross sections can be directly compared to pQCD calculations.

Since jets are produced at a very early point in the collision, they are also powerful probes of a medium that has potentially been formed later in a heavy-ion collision.

The jet definition given here as collimated bunches of particles is descriptive and conceptually very plain. However, the precise technical definition and analysis of jets is quite complicated though and will be described in detail later in Sec. 5.2.

3. Nuclear effects

Colliding heavy nuclei instead of nucleons in the collisions can influence the general event structure in several ways.

In general, it is convenient to distinguish hot nuclear and cold nuclear and also initial state and final state effects.

The difference between hot and cold nuclear matter effects is whether or not the effect is created by the formation of a medium. Initial and final state effects are characterized by the time when the effect takes place, meaning prior to or after the collision. Initial state effects are typically parametrized by nuclear parton distribution functions (nPDFs), which specify the partonic structure of a nucleus. A framework to describe the nuclei in heavy-ion collisions is the Color Glass Condensate (CGC) [Ia08]. Final state effects take place after the collision and describe the influence of the post-collision environment – e.g. a QGP or a remnant of a nucleus – on the objects created in the reaction.

While Pb–Pb collisions show both hot and cold nuclear matter effects due to the formation of a quark-gluon plasma and due to the presence of a nuclear environment, hot nuclear matter effects from the creation of an extended QGP medium are not expected in p–Pb collisions.

Compared to hot nuclear matter effects from the QGP in Pb–Pb collisions, cold nuclear matter effects are expected to be small. Nevertheless, detailed knowledge of all possibly expected effects is necessary to correctly interpret what is measured in p–Pb collisions.

3.1. Nuclear parton distribution functions

As the name suggests, a nuclear parton distribution function is a nuclear modified version of a parton distribution function (PDF) of a free nucleon. PDFs provide probability densities to find a certain parton for a given virtuality, i.e. momentum transfer Q^2 , and Bjorken- x in a nucleon. The Bjorken- x represents the momentum fraction carried by the parton. Roughly speaking, PDFs describe the inner structure of the nucleon. A recent distribution calculated by the CTEQ collaboration/Jefferson Lab is shown in Fig. 3.1.

Nuclear parton distribution functions extend the PDF concept to nuclei. They can be defined on the basis of PDFs, e.g. for a nucleus A ,

$$f_i^A(x, Q^2) \equiv R_i^A(x, Q^2) \cdot f_i^N(x, Q^2). \quad (3.1)$$

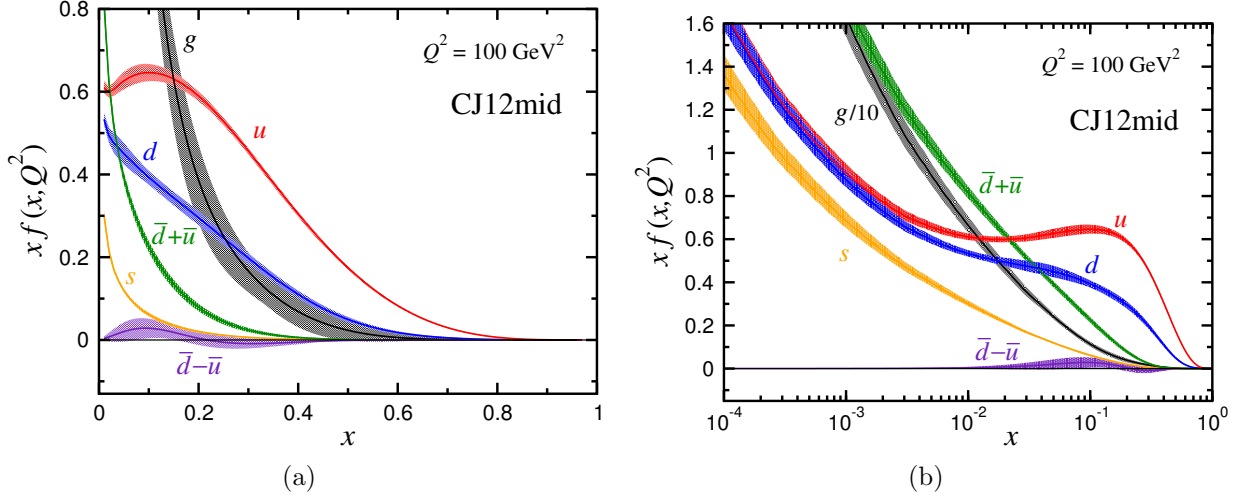


Figure 3.1: Example of parton distribution functions (CJ12mid) on linear (left) and logarithmic (right) x -scale. Taken from [Owe13].

Here, f_i^N represents the free nucleon PDF and $R_i^A(x, Q^2)$ is the nuclear modification. Typically, various measurements are used to constrain the nPDFs. For example, the EPS09 nPDF package [Esk09], which was used for several analyses in this thesis, is constrained by measurements of deep inelastic lepton–nucleus scattering, dilepton production in the Drell-Yan process, and inclusive pion production measured at RHIC.

Nuclear PDFs are often presented by their nuclear modification R_i^A to emphasize the effect from the nuclei (cf. Fig. 3.2).

Apart from the EPS09 set, there exist nPDF sets by other collaborations, e.g. the HKN set [Hir04] or the DSSZ set [DF12]. Especially for the distribution of the gluon at high virtualities, some tension does exist [Sal12].

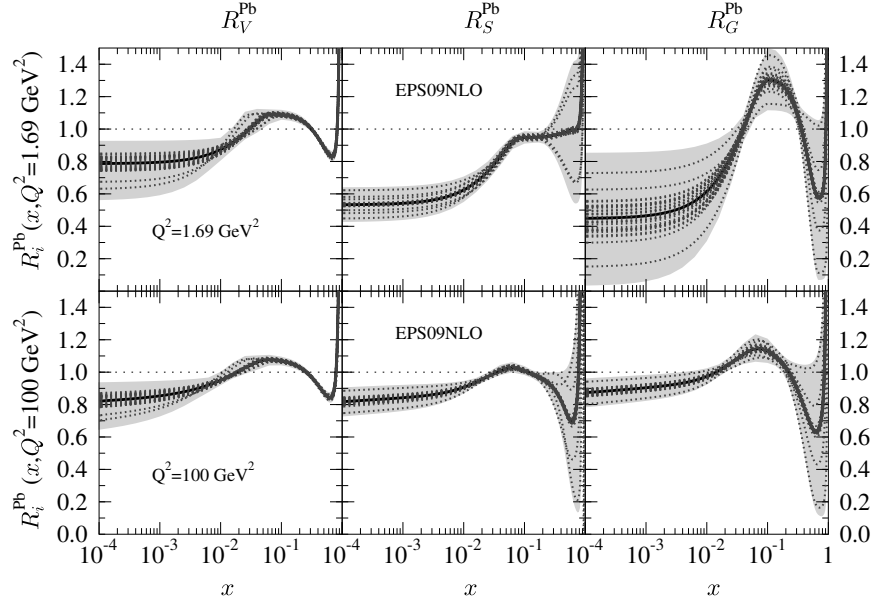


Figure 3.2: Nuclear modification for lead nuclei for two different Q^2 values for valence quarks (left plot), sea quarks (middle plot), and gluons (right plot) [Esk09].

3.2. Details on initial state effects

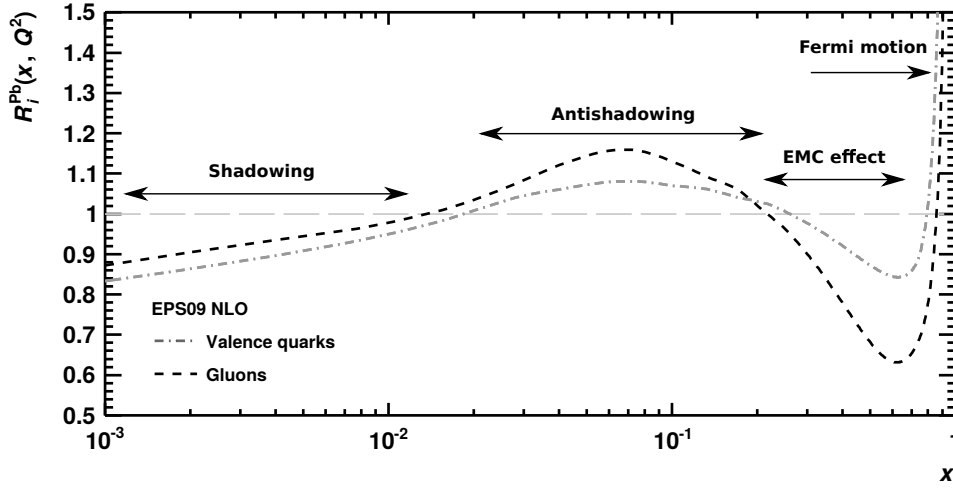


Figure 3.3: Nuclear modification for lead nuclei for $Q^2 = 100 \text{ GeV}^2$ for valence quarks and gluons.

Initial state effects describe effects that potentially influence the measurement by changes in the collision environment prior to the collision, i.e. by changes in the “initial state”.

They can be parametrized by nuclear PDFs. In general, four effects on the nuclear modification $R_i^A(x, Q^2)$ are typically considered. The effects and their corresponding regions are depicted in Fig. 3.3.

- **Fermi motion**

This is probably the most trivial nuclear effect: the motion of the nucleons in the nucleus. Even if the nucleus were to be considered as a simple accumulation of independent nucleons, Fermi motion would lead to a broadening in the parton momentum distributions compared to free nucleons. Calculations (cf. [Sai85]) show that this broadening leads to an enhancement in the bound-over-free PDF ratio at high- x . Because the parton distribution functions fall down to zero very quickly when approaching $x = 1$, descriptively the effect of a “smearing” of this distribution is most predominant near $x = 1$.

- **EMC effect**

The EMC effect is named after the European Muon Collaboration (EMC) which first observed [Aub83] a modification comparing deep inelastic scattering of muons on iron and deuterium for the region $0.2 \leq x \leq 0.8$. Until today, the effect is not fully understood. Recent measurements suggest short-range nucleon–nucleon correlations to be a possible source (cf. [Rit14]).

- **Antishadowing**

In the region $0.01 \leq x \leq 0.2$, a slight enhancement of the nuclear modification was measured. Also for this effect, there is currently no consensus on the reason. A possible explanation is momentum conservation (cf. [Arn94]), which demands more particles at higher x if there are less particles at lower x . The condition is fulfilled by the suppression in the shadowing region.

- **Shadowing**

For small $x < 0.01$, a suppression in the nuclear modification is visible. This effect has been known since the 1970s [Arn94]. Up to now, it is not fully understood, but maybe it is connected to saturation effects in the nucleus. A descriptive approach to understand this effect is already suggested in the name: In a nucleus, the inner nucleons are shaded by surface nucleons and the effective number of participating nucleons is lower than just their count in the nucleus.

Note that the given x values are just approximate numbers to specify the order of magnitude. They vary depending on different nPDFs and values of Q^2 .

Another effect that is defined by a modified particle production in nuclei is the Cronin effect. The effect is named after an experiment, which results were published by Cronin *et al.* in 1975 [Cro75]. In this fixed-target experiment, a proton beam with an energy of 200-400 GeV per proton was collided with W, Be, and Ti targets. The primary

observation was that the invariant cross section does not scale linearly with the number of target nucleons A ,

$$E \frac{d\sigma}{d^3p}(A, p_T) = E \frac{d\sigma}{d^3p}(1, p_T) \cdot A^{\alpha(p_T)}. \quad (3.2)$$

Below a certain p_T threshold, it is $\alpha < 1$ and, thus, a low- p_T suppression is observed. Depending on the produced hadron species, above roughly 2-4 GeV/ c in transverse momentum, an enhancement of the particle production is observed and it is $\alpha > 1$. Like for the initial state effects described above in this section, several possible explanations of the Cronin effect exist. One popular ansatz is that the effect is caused by multiple soft scatterings of the proton leading to a broader transverse momentum distribution of the incident proton [Acc02].

3.3. Gluon saturation and the Color Glass Condensate

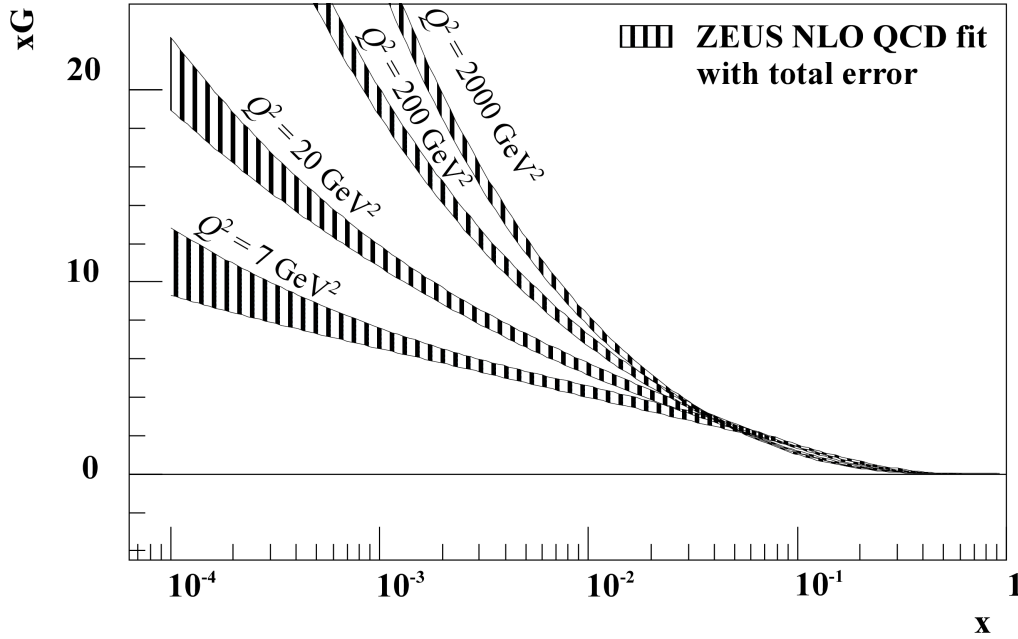


Figure 3.4: Gluon density in protons as a function of x . Calculated as NLO QCD of deep inelastic scattering data by ZEUS [Che03].

All parton distribution functions in Fig. 3.1 show the same behavior at low x : they rise. Especially the gluon distribution grows with decreasing Bjorken- x . This is not a nuclear effect but it was also measured in deep inelastic scattering experiments. For instance, this is suggested by HERA data [Adl01, Che03].

Apart from the increase of the gluon density with decreasing x , higher virtualities as well lead to larger gluon densities, as seen in Fig. 3.4.

To understand this phenomenon, the partonic structure of nucleons or nuclei has to be considered. At first order, the nucleon consists of three valence quarks bound by gluons. But more precisely, QCD allows these partons to temporarily fluctuate into states including quark-antiquark pairs or additional gluons. These fluctuations are very short-lived and at lower Q^2 it is unlikely that they influence a reaction.

Considering processes with increasing virtuality, the system is Lorentz-contracted and time-dilated. All physics processes, including the lifetimes of the fluctuations, take more time in the laboratory system. As an example, in a typical high energy collision at the LHC, the time is dilated by a factor of 7,000.¹

In such a collision, the probability that the fluctuations take part in the reaction becomes higher than for the participation of the valence quarks itself. The higher the collision energies are the more fluctuations become visible. As a side note, the rise in the gluon density can be explained by the non-abelian nature of QCD. Since gluons carry color charges, they can again split into gluons.

To some extent, one can interpret this behavior as a self-similarity of the inner structure of quarks and gluons, because they are again made of quarks and gluons.

Gluons that endlessly split into more gluons for higher virtualities are conceptually problematic. The measurement by the H1 collaboration in [Adl01] suggests that the proton structure function F_2 at $x < 0.01$ and with Q^2 between 1.5 and 150 GeV² shows a power law given by

$$F_2(x, Q^2) = c(Q^2)x^{-\lambda(Q)}, \quad (3.3)$$

while λ rises linearly with $\ln Q^2$. In this x -regime, the structure function is dominated by the gluon distribution and, thus, it is

$$xg(x) = x^{-\lambda(Q)}. \quad (3.4)$$

Given this gluon distribution, the total cross section also shows a power law [Per13]:

$$\sigma \propto s^{-\lambda(Q)}. \quad (3.5)$$

If this behavior continues for higher virtualities, it violates the Froissart bound for the total cross section in QCD. Making use of very basic considerations, the Froissart bound [Fro61] predicts the total cross section to increase with $\ln^2 s$ at most. This discrepancy is sometimes called “small- x problem” and it demands a mechanism that limits the increase in the gluon density for high virtualities.

¹The Lorentz factor is given by $\gamma = \frac{E_{\text{tot}}}{E_0} = \frac{E_{\text{kin}}}{m_0 c^2} + 1 \approx 7000$ in a 7 TeV proton–proton collision.

The concept of *gluon saturation* can serve as a solution. The general ansatz is that at a certain gluon density, the gluons overlap and it becomes likely that they recombine e.g. in $gg \rightarrow g$ processes. For a given x , the momentum scale at which saturation takes place is called *saturation scale*,

$$Q_s^2(x) \propto \alpha_s(Q_s^2) \frac{xg(x, Q_s^2)}{\pi R^2}, \quad (3.6)$$

where R is the radius of the colliding particle or hadron. This equation directly predicts a lower saturation scale in nuclei because of the radius dependence and, therefore, an easier accessibility of saturation in heavy-ion collisions.

In the saturation region, the Color Glass Condensate formalism (CGC) describes the dynamics in a heavy-ion collision as an effective classical field theory [Ian08]. In principle, the large- x partons are considered as static color sources interacting with classical fields given by small- x partons. Due to time dilation, large- x partons are essentially *frozen* on the time scale of the small- x partons.

3.4. Final state effects

The state of the system after the collision is called final state. Compared to the pp QCD vacuum, several additional effects can take place in heavy-ion collisions. The most prominent effect is *jet quenching*, which is created by parton interactions in the medium that has been formed in the final state.

While a strong jet quenching is only expected in the presence of a hot and dense quark-gluon plasma, other effects possibly also occur in collisions with lower energy densities like in p-Pb collisions, e.g. hydrodynamic-like effects such as *flow*.

3.4.1. Jet quenching and parton energy loss

Jet quenching was predicted as a “smoking gun” measurement [Bjo82], i.e. a strong evidence, for the formation of a quark-gluon plasma. It describes the suppression of jets (observed by the jet nuclear modification factor), which is generated by the presence of a medium in the final state.

Jet quenching in heavy-ion collisions was first measured at RHIC [Adc01].

The jet quenching is typically observed as

- suppression of the high- p_T hadron and jet spectrum (cf. Fig. 3.5),
- changes in azimuthal correlation of high- p_T hadrons,
- or changes in the jet constituent distributions, e.g. softer p_T distribution in jets.

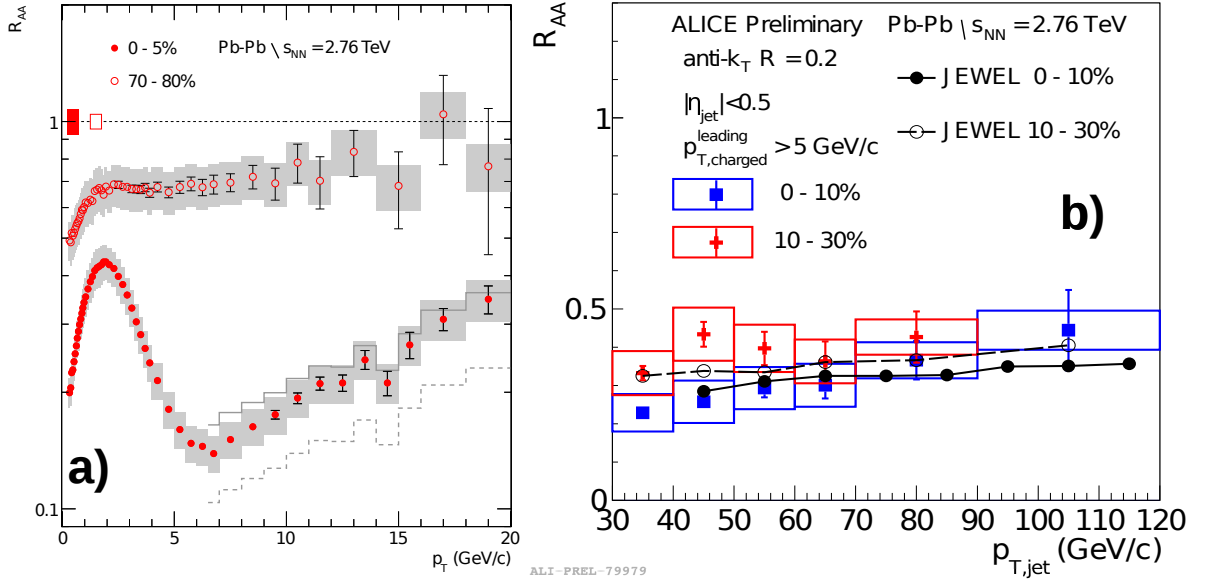


Figure 3.5: Indications for jet quenching from inclusive charged particle R_{AA} (a) and full jet R_{AA} (b) [Aam11, Aio14].

Jets in pp collisions are produced in a hard parton scattering. In heavy-ion collisions, jets traverse the medium that has been formed in the final state. The above mentioned modifications are created by subsequent energy losses of the scattered partons due to strong interactions with the medium.

Like in QED, two general types of medium interaction can be distinguished: On the one hand, partons can elastically scatter off other partons. This is called *collisional energy loss*. The elastic scatterings in a collision are independent and, therefore, the process is incoherent.

The other interaction type is called *radiative energy loss*. It describes the inelastic interaction of a parton with the medium, e.g. by radiating off a gluon. In analogy to the similar process in QED, this process is called *gluon bremsstrahlung*.

Several theoretical calculations exist (cf. [Ver13]). They are additionally complicated by possible interference phenomena in gluon emission.

Depending on the medium properties and the type of the probe which is used to test those properties, the impact of radiative and collisional energy loss varies. At larger transverse momenta p_T – which is the region of interest for jet physics –, the process of radiative energy loss dominates. For lower p_T , collisional energy loss becomes more and more important.

Especially the radiative energy loss strongly depends on the parton type. While the energy loss is strongest for gluons since they carry charge, light quarks also lose much

more energy than heavy quarks. The behavior of heavy quarks is influenced by the *dead cone* effect [Dok01], which describes the suppression of gluon radiation at smaller angles, which leads to a generally lower influence of the medium on heavy quarks.

3.4.2. Collective flow

Collective flow leads to correlated movements of particles created in the collision. Most predominant for current heavy-ion collisions are radial, directed, elliptical, and triangular flow. Radial flow (v_r) corresponds to a pressure gradient, which is spherically symmetric and influences the medium constituents to show larger momenta. Directed flow (v_1) vanishes at mid-rapidity in symmetric collisions and can only be observed near the beam rapidity and lower center-of-mass energies.

Elliptical flow is generated if the overlap region in a collision is not spherically symmetric. Typically, the collision volume is almond-shaped in symmetric heavy-ion collisions with non-vanishing impact parameter b . Roughly speaking, it is because of the form of the reaction volume that a pressure gradient pushes the particles predominantly in the direction of the reaction plane. The reaction plane is determined by the connection vector between the two colliding nuclei and the beam direction. An illustration of the reaction plane and elliptic flow can be found in Fig. 3.6. Furthermore, it can be shown that the quarks themselves show elliptic flow behavior [Ada07].

The much weaker triangular flow is presumably created as a result of fluctuations in the collision geometry.

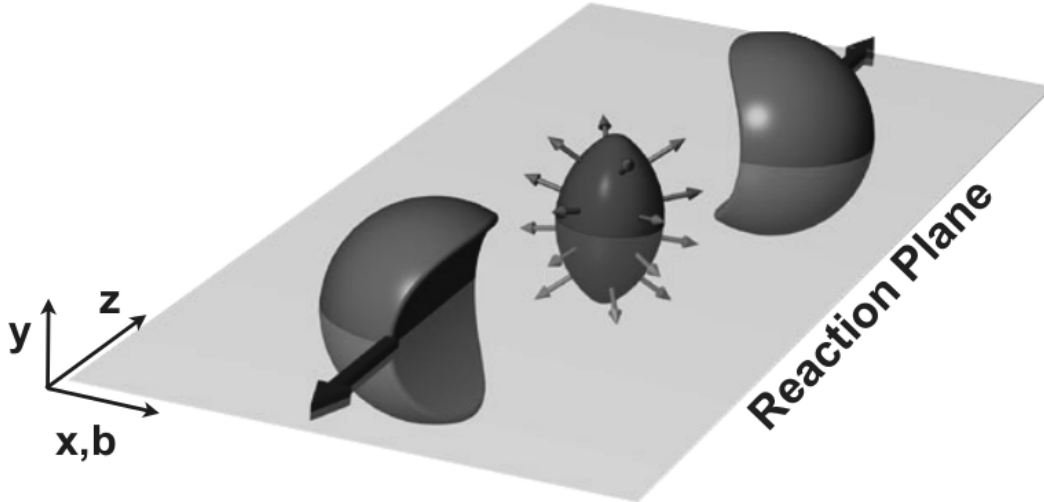


Figure 3.6: Illustration of elliptic flow in heavy-ion collisions, from [Sne11].

Directed, elliptical, and triangular flow are usually characterized by components v_i of a Fourier expansion of the particle distribution in the symmetry plane. Accordingly, also

higher flow orders like quadrangular, pentagonal flow, etc. can be defined. In general, the azimuthal distribution of particles is connected to the coefficients v_n in the following way [Abe14d]:

$$\frac{dN}{d\phi} \propto 1 + 2 \sum_n v_n \cos(n(\phi - \Psi_n)). \quad (3.7)$$

Here n is the flow order, ϕ the azimuthal angle of the particles, and Ψ_n the corresponding symmetry plane. The flow coefficients v_n represent anisotropies in the particle distribution. These anisotropies are believed to be related to anisotropies in the initial particle distribution when the medium is formed.

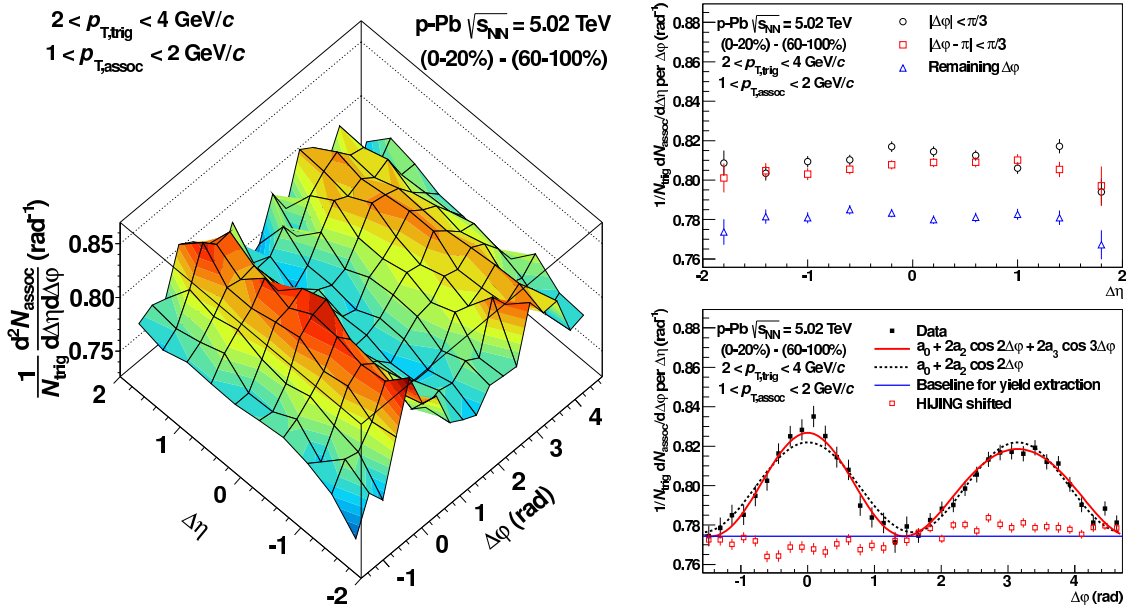


Figure 3.7: Observation of a “double-ridge” in p–Pb collisions with the ALICE detector (cf. [Abe13b]). Left: Associated yield per trigger particle, low multiplicity events were subtracted from high multiplicity events. Right: Projection on pseudorapidity axis (upper plot) and projection on azimuthal axis (lower plot).

In p–Pb and, to a smaller amount, in high-multiplicity pp collisions as well, long range two-particle angular correlations were observed [Abe13b, Kha10]. These correlations were originally believed to be a typical sign for hydrodynamic flow and are not reproduced by common heavy-ion event generators (e.g. HIJING, cf. Fig. 3.7 lower right plot). Apart from any hypothesis on the origin of the correlations, the Fourier components v_2 and v_3 are significantly different from zero (see Fig. 3.9). These coefficients are associated with elliptic and triangular flow and, indeed, the comparison of the data to recent hydrodynamic models shows a good agreement [Boz14], see Fig. 3.8.

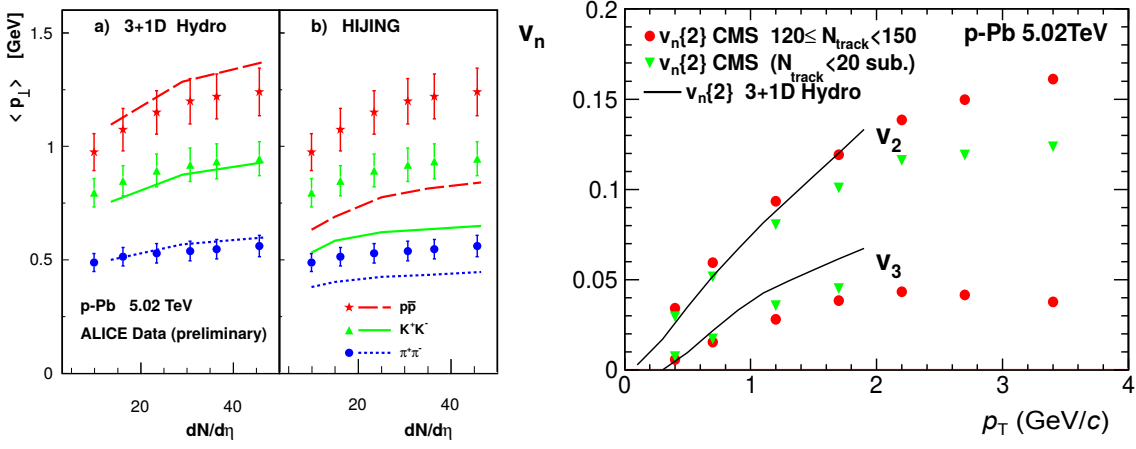


Figure 3.8: Comparison of p-Pb data to hydrodynamic models. Left: Average transverse momentum measurement for identified particles with ALICE. Right: Fourier coefficients measured with the CMS detector. Plots from [Boz14].

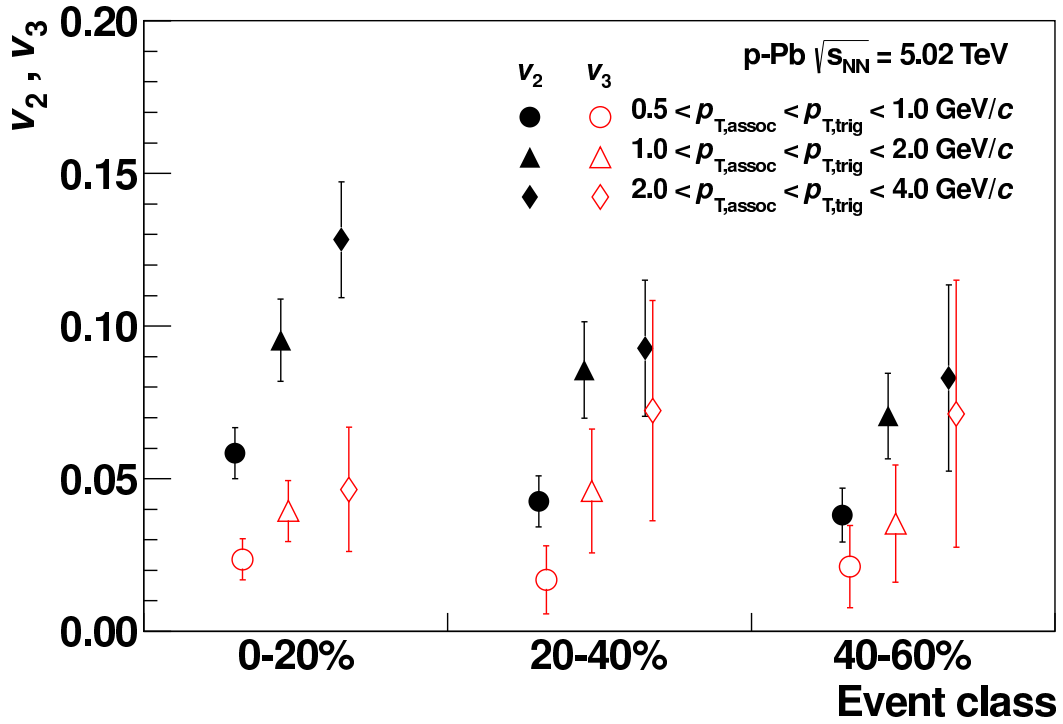


Figure 3.9: Fourier coefficients associated with elliptical and triangular flow (cf. [Abe13b]) measured in p-Pb by ALICE.

The measurement of long range angular correlations is performed by measuring the correlation in pseudorapidity and azimuth for a trigger particle and an associated particle in certain transverse momentum ranges. Eventually, the associated particle yield per trigger is filled into the histogram. A long range correlation is indicated by a ridge-like pattern in this histogram.

To conclude, there seem to be collective effects in p-Pb collisions that have not been expected before. The magnitude of these effects is relatively small compared to Pb-Pb collisions. Although the data agrees well with hydrodynamic models, it is not fully clear how to interpret the observation.

In this thesis, the focus is on jet spectra and effects caused by particle flow are expected to be negligible and not considered. However, the observed collective particle behavior is a potential sign for medium creation. The hypothesis of the existence of an extended, strongly interacting medium can be tested with jets through the observation of jet quenching.

4. The ALICE detector

This section gives an overview of the experimental setup used for data taking for the analyses presented in this thesis. After a short introduction to the capabilities of ALICE, the focus is mainly on the devices used for tracking and event selection.

As one of the big experiments at CERN, the ALICE detector is situated at an interaction point of the Large Hadron Collider (LHC). The LHC is a circular hadron collider in the former Large Electron Positron collider tunnel with a circumference of roughly 27 km at the Swiss-French border near Geneva. It is colliding protons and nuclei with unprecedented center-of-mass energies including 7 TeV for pp, 5.02 TeV for p-Pb, and 2.76 TeV for Pb-Pb collisions.

To achieve those energies, a complex chain of preaccelerators is used to prepare protons and lead ions for the main acceleration in the LHC. The chains differ depending on whether protons or lead ions are injected into the LHC.

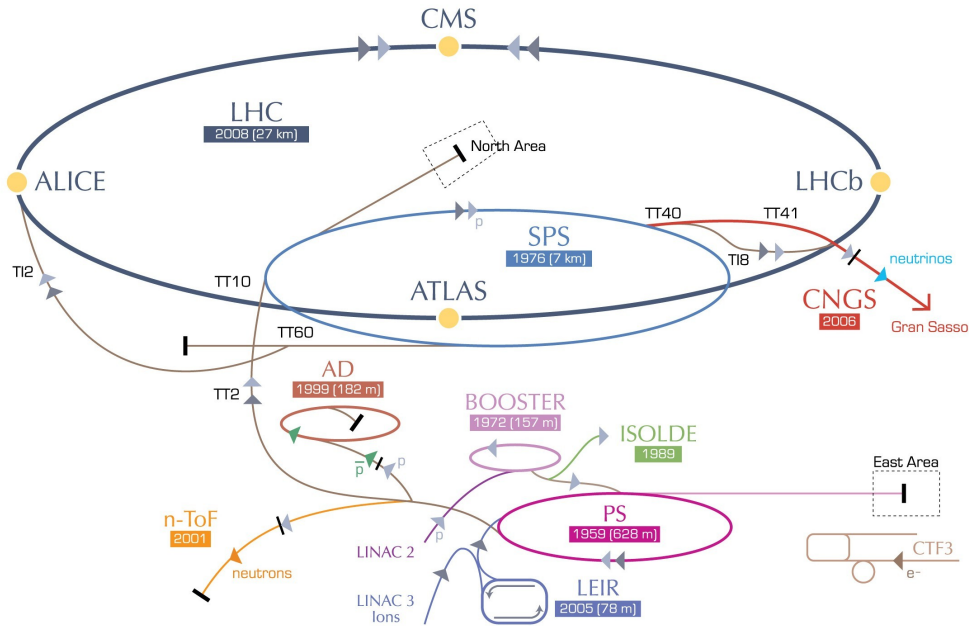


Figure 4.1: Sketch of the LHC accelerator chain. Taken from [Lef08].

Protons are produced by ionizing hydrogen and accelerating them to 50 MeV in LINAC 2, a linear accelerator. Then the protons subsequently pass the Proton Synchrotron

Booster (PSB), the Proton Synchrotron (PS), and the Super Proton Synchrotron (SPS) while they are accelerated to the LHC injection energy of 450 GeV. After injection into the LHC, the energy is ramped up to the desired energy. The highest proton–proton collision energies were currently given by $\sqrt{s} = 8$ TeV.

The lead ions are created by vaporizing highly purified lead. Like the protons, the ions are first accelerated by a linear accelerator, LINAC 3 in this particular case. After preacceleration in the Low Energy Ion Ring (LEIR), the PS, and the SPS, the lead ions are filled into the LHC for final acceleration. The accelerator chain is depicted in Fig. 4.1.

The reason to collide two beams instead of performing a fixed-target measurement is that the beam energies translate much more efficiently into the center-of-mass energy for colliders than for fixed-target configurations. While the cms energy grows linearly with the beam energy in colliders, it grows with the square-root of the beam energy in fixed-target experiments, see also Appendix A.1.

There are currently four big experiments using the LHC and several smaller ones. The bigger experiments are ATLAS, CMS, ALICE, and LHCb. While the ATLAS and CMS collaborations are more specialized on pp collisions, e.g. the discovery and precision measurement of new particles like the Higgs boson, the ALICE experiment is the dedicated heavy-ion experiment at the LHC, analyzing primarily properties of the quark-gluon plasma and the QCD phase diagram in general. LHCb is a more specialized detector focused on CP violation.

Regardless of their initial design purposes, it quickly turned out that the experiments can also contribute valuably to physical issues not directly linked to their primary field. Thus, the ATLAS and CMS collaborations also participate in the heavy-ion runs while ALICE can contribute also to high energy particle physics, especially in the low transverse momentum regime.

4.1. ALICE as the dedicated heavy-ion experiment at the LHC

The ALICE detector is designed as a general-purpose heavy-ion detector [Aam08] to measure and identify hadrons, leptons, and also photons down to very low transverse momenta of $p_T \approx 100$ MeV/ c and up to high transverse momenta of $p_T \approx 100$ GeV/ c in full azimuth. For muons, there is a specialized spectrometer, built asymmetrically on the C side of the detector. The ALICE detector and a depiction of A and C side are shown in Fig. 4.2.

The most constricting design requirement was the need to cope with very high particle multiplicities. In Pb–Pb collisions, the charged particle multiplicity per rapidity unit was estimated to be up to 6,000 [Car04] at midrapidity. The tracking system of the

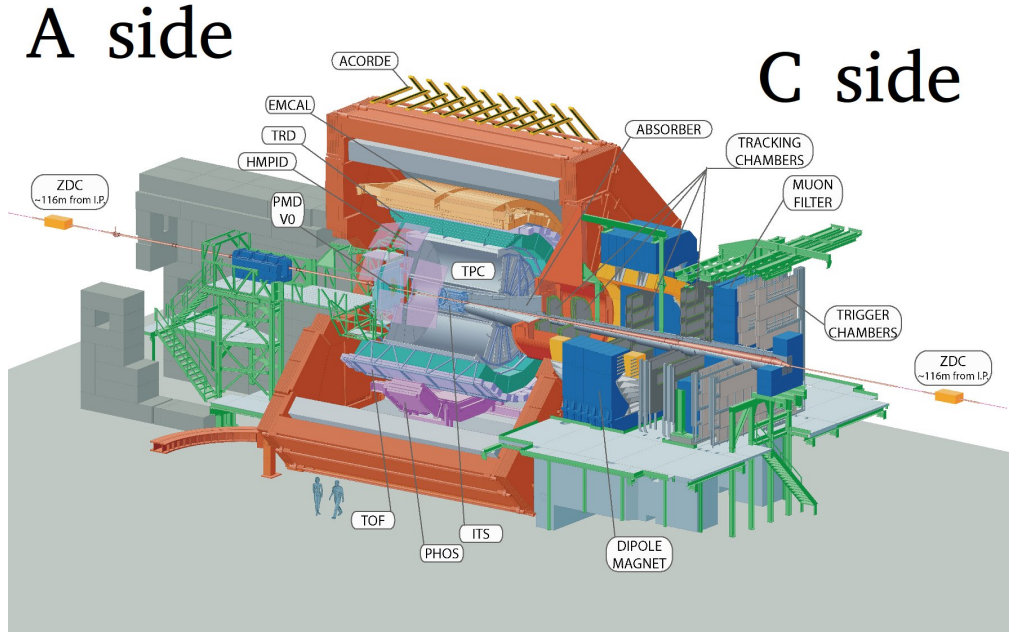


Figure 4.2: The general layout of the ALICE detector [Aam08].

ALICE detector was designed with a safety margin to produce reliable results up to a multiplicity of 8,000 charged particles per rapidity unit.

Aside from tracking abilities, special attention was paid to the particle identification system (PID). ALICE uses several complementary techniques to gather as much PID information as possible: energy loss information (ITS and TPC), transition radiation (TRD), time-of-flight information (TOF), and Cherenkov radiation (HMPID).

Since PID information have not been used in any of the analyses of this thesis, for further details see e.g. [Car04].

4.2. Main tracking detectors

Compared to the other LHC experiments, the ALICE detector is foremost characterized by excellent charged particle tracking abilities down to very low transverse momenta. The tracking is performed mainly using information from the Inner Tracking System (ITS) and the Time Projection Chamber (TPC). These two devices are the main tracking detectors in ALICE and they are located in the central barrel. Additionally, information from the Transition Radiation Detector (TRD) can be used to improve the p_T resolution of the tracks at high transverse momentum.

The ALICE central barrel is enclosed by a solenoid magnet that was originally built for

the L3 experiment. It has a nominal magnetic field of 0.5 T. The magnetic field is an important component of the tracking procedure. Through the Lorentz force it bends the charged particle tracks in the magnetic field, allowing a tracking algorithm to determine the momenta of the particles.

As a heavy-ion experiment, ALICE was designed to cope with very high multiplicities. Before first collisions at the LHC took place, the multiplicity in heavy-ion collisions at energies on the TeV scale was unknown. Therefore, a very robust and reliable technology was chosen for the tracking: a time projection chamber. Only this detector is capable to ensure solid tracking with of the order of 10,000 charged particles in the acceptance. Using complementary information from the ITS, the tracking system can reconstruct tracks with transverse momenta in the range of $0.1 - 100 \text{ GeV}/c$ and within $|\eta| < 0.9$ in pseudorapidity.

4.2.1. Inner Tracking System

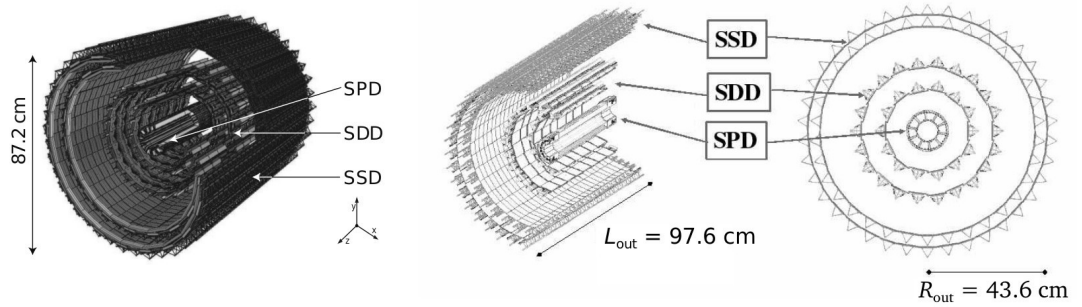


Figure 4.3: The general layout of the Inner Tracking System [Aam08, Aam10a].

The ITS [Aam08, Aam10a] is a cylindrical device consisting of six layers of three different silicon detectors directly surrounding the beryllium beampipe. The Silicon Pixel Detector (SPD) is closest to the beampipe, followed by the Silicon Strip Detector (SSD) and the Silicon Drift Detector (SDD) ranging up to a radius of 43 cm. In Fig. 4.3, the detector is depicted.

As a complementary tracking device for the TPC, the length of the ITS is optimized so that a straight track with $|\eta| = 0.9$ is traversing all layers of the ITS and is fully contained within the TPC. The outer layers have a length of roughly one meter.

Its main purpose is the reconstruction of primary and secondary vertices. The primary vertex can be reconstructed with a resolution better than $100 \mu\text{m}$. Besides, it also significantly contributes to the tracking of low- p_T particles below $200 \text{ MeV}/c$ and improves the momentum resolution of tracks found by the TPC. For example, the relative momentum resolution of pions in the range of $0.1 - 3.0 \text{ GeV}/c$ is better than 2%. The

sensor granularities are optimized for a charged particle multiplicity of 8,000 tracks per unit rapidity at midrapidity. At the time of design, this was the upper estimate for the multiplicity in Pb–Pb events at the LHC.

In addition, the two outer silicon detectors are involved in the particle identification via dE/dx energy loss measurements and the SPD can be used for event triggering. Participating in all these fields, the ITS is at least indirectly involved in nearly all analyses.

4.2.2. Time Projection Chamber

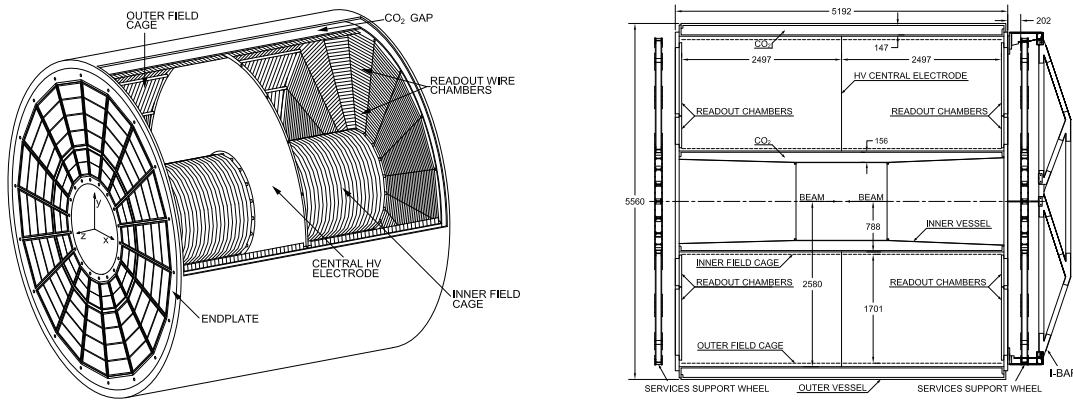


Figure 4.4: Layout of the ALICE Time Projection Chamber [Alm10].

The Time Projection Chamber [Alm10] is the main tracking device of the ALICE detector. It has excellent tracking capabilities up to transverse momenta of 100 GeV/ c and is – like the ITS – designed to reconstruct particles in a pseudorapidity interval of $|\eta| < 0.9$ in full azimuth. In principle, also particles above this interval can be reconstructed. But those tracks have not traversed the full TPC and are thus reconstructed with a lower momentum resolution.

In Fig. 4.4, a schematic sketch of the chamber can be found.

The general working principle of the TPC can be described as follows. Traversing charged particles ionize the gas mixture, leaving a track of ionized gas molecules on their way through the gas volume. The gas volume is in a strong electric drift field, generated by the end caps and an electrode at the center of the chamber. Due to this field, the charged particles of the ionization tracks are accelerated to the end plates. There, multi-wire proportional chambers are used to measure the electron current. Additionally, information about the third dimension orthogonal to the endcaps is encoded in the arrival time of the ion trace. This two-dimensional time-dependent projection of the track on the end caps is used to reconstruct a three-dimensional track.

With a radius of 250 cm and a length of 500 cm, the ALICE TPC is the largest time projection chamber in use. Its gas volume consists of roughly 90 m³ of neon, CO₂, and nitrogen (85%, 10%, 5%) at atmospheric pressure. The field cage is of cylindrical shape and the end plates are subdivided into 18 trapezoidal sectors.

The electric voltage between central electrode and end plates is 100 kV, leading to an electric field strength of $E = 400$ V/cm.

Compared to the other tracking devices, the TPC is relatively slow due to a large drift time of roughly 90 μ s. For pp collisions, the design readout rate is 1.4 kHz and for Pb–Pb collisions, the readout rate is 300 Hz.

4.3. Detectors used for event characterization and centrality estimation

For the selection of minimum bias events and also for the estimation of the event centrality, two additional subdetectors were used: The V0 detectors and the Zero Degree Calorimeter.

4.3.1. V0

The V0 detector system consists of two detectors, V0A and V0C, located asymmetrically on both sides of the interaction point [Aam10b]. A or C specifies on which side the detector is situated: A is opposite to the muon spectrometer and the C side refers to the side of this spectrometer.

V0A is located at $2.8 < \eta < 5.1$, V0C at $-3.7 < \eta < -1.7$ in pseudorapidity. This corresponds to a distance to the interaction vertex of 340 cm and 90 cm, respectively. Both detectors are ring-shaped scintillator counters, covering the full azimuth, 32 counters in four rings for each detector.

Their main purpose is the selection of minimum bias events. In Pb–Pb collisions and partly also in p–Pb collisions, the V0 information can be used for defining centrality.

4.3.2. ZDC

The Zero Degree Calorimeter (ZDC) system [Arn07] consists of two sets of calorimeters, both 116 m away from the interaction point. On each side, two hadronic calorimeters measure proton (called ZPA, ZPC) and neutron (called ZNA, ZNC) spectators that do not participate in the collision.

Due to the magnetic fields of the LHC beam line, the spectator protons are deflected and, thus, spatially separated from the spectator neutrons. This is the reason why neutron and proton calorimeters are separated: the ZN calorimeter is between the two beampipes, the ZP calorimeter is where the positively charged protons are deflected to.

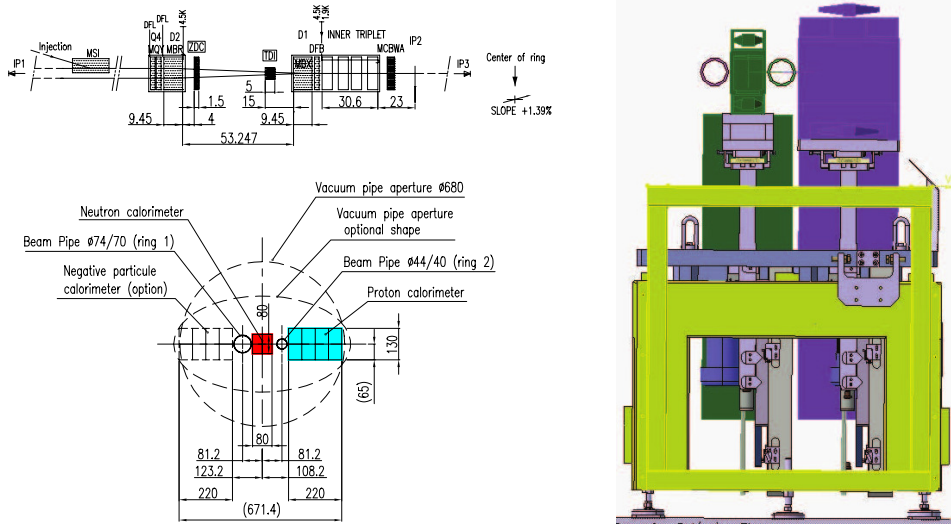


Figure 4.5: Layout of the Zero Degree Calorimeter [Car04]. On the right side, the support structure is depicted in front view. Depicted in dark green is the neutron calorimeter, in magenta the proton calorimeter. The light green structure represents the lift that can be used to take the calorimeters out for radiation protection purposes.

The hadronic calorimeters used for the ZDCs are quartz fibers sampling calorimeters [Gan95]. Those devices have a good radiation resistance, which is necessary because of their position close to the beampipe.

The calorimeters consist of an absorber material interfused with quartz fibers. If a shower is created in the absorber, Cherenkov radiation is created in the fibers and detected by photomultipliers. The neutron calorimeters have harder constraints to their size due to their positions between the two beampipes. Therefore, a very dense tungsten alloy was used as absorber material. For the proton calorimeter absorber, brass was used.

At least in principle, the number of participants can be estimated through the measurement of spectator nucleons. This number is an important observable for the centrality estimation.

For the centrality estimation in p-Pb, the information from the ZNA calorimeter is used to characterize the centrality of an event. Note that the ZNA neutron calorimeter is located where the Pb-nucleus remnants fly to.

5. Basic analysis techniques

Jet analysis is a relatively complex approach. Definition, cuts, and correction techniques – several factors make a jet an ambiguous object. In the end, one has to be content with the fact that oneself somehow *defines* what a jet is. The main constraint is that such a defined jet shares as many properties as possible with the conceptual physical objects evolving from hard parton scatterings and, of course, the comparability to other measurements.

This part contains a detailed description of basic techniques and algorithms used for the analysis of the data. After the description of the basics of track and jet reconstruction, the centrality estimation is described in detail. Because PYTHIA, POWHEG, and GEANT are important for several of the presented analyses, a brief introduction to the basic principles of those frameworks are given. Finally, this chapter closes with an explanation, how statistical and systematic uncertainties are handled in this thesis. Correction techniques applied to the jet measurement are presented in the next chapter.

5.1. Track reconstruction with ALICE

The ALICE detector with its huge TPC provides excellent charged particle tracking capabilities, especially for low transverse momenta. Tracks are the main basic objects of interest for this thesis since they are used to reconstruct the jets.

Track reconstruction or tracking in general refers to the momentum measurement of charged particles traversing a detector. In contrast to the energy measurement in a calorimeter, the measurement is non-destructive, though the particles of course lose energy in the detector.

A complex multi-step procedure is applied to reconstruct the tracks. Here, only the basic procedure is described. A detailed technical overview can be found in Volume II of the ALICE Physics Performance Report [Ale06].

It can be distinguished between three basic parts of the track reconstruction.

- Space point reconstruction: Raw detector output is used to reconstruct space points that are presumably created by traversing particles.
- Primary vertex reconstruction: The primary vertex, where the collisions took place, can be used as an additional constraint for the tracking procedure.

- Track finding: The space points and the vertex are used to reconstruct the actual tracks in the detector.

Note that the *space points* are also often referred to as *clusters*. The reconstruction of the space points is a subdetector-specific procedure. They are formed by the raw detector output. Within the space point reconstruction procedure, the corresponding spatial position and uncertainty are calculated and finally used for the track fitting procedure.

To find the primary vertex of a collision, the two innermost layers of the ITS, corresponding to the layers of the Silicon Pixel Detector, are used. As the beams are collimated at the interaction point, the vertex diamond, where the collisions are expected, is Gaussian-shaped in the z -direction (beam direction) and in the xy -plane. While the beams are strongly collimated in the xy -plane ($\sigma_{xy} \approx 10 \mu\text{m}$), it is much broader in z ($\sigma_z \approx 5 \text{ cm}$). The resolution of the vertex position strongly depends on the particle multiplicity and, thus, on the collision system. For Pb–Pb collisions, it is of the order of $10 \mu\text{m}$. For pp collisions, in which the average multiplicity is much lower, it is of the order of $100 \mu\text{m}$ [Aam08].

The algorithm to determine the vertex position is performed separately for the z -direction and the xy -plane. For the z -coordinate of the vertex, the procedure works as follows.

A first estimate of the vertex position is given by calculating the centroid of the reconstructed spatial z -coordinates in the SPD. This centroid is monotonously correlated to the true vertex position if this position is within $z_{\text{true}} < 12 \text{ cm}$. The correlation is known and, therefore, the vertex position is calculable.

Using this first vertex estimate, the final vertex position is given by correlations of hits in the first and second layer of the SPD. Eventually, the correlations form a Gaussian distribution of the position estimate. The centroid of a Gaussian fit is taken as primary vertex position.

ALICE' track finding procedure is based on a Kalman filter [Fru87]. It allows a computationally relatively fast simultaneous track fitting.

The first step consists in finding seed space points at outer radii of the TPC, in which the occupancy is lower than in the middle of the detector. Proceeding to smaller TPC radii, space points are associated to the track candidates. At the inner radius of the TPC, the ITS tracking system prolongs the TPC tracks through the ITS using the vertex position. Reconstructed ITS clusters lying on that track are assigned to it. Additionally, the ITS tracker searches for ITS-standalone tracks that do not correspond to a TPC-found track, e.g. due to inefficiencies in the TPC or because of too low transverse momentum.

The tracking is run a second time, now from the vertex to the outer radius of the TPC. In this step, the tracks are also extrapolated to other central barrel detectors like the TRD, TOF, etc.

Ultimately, another refit procedure is performed from the outer side of the detector to the vertex.

This procedure is utilized for the reconstruction of all tracks examined in this thesis. Internally, the tracks are represented as a set of five parameters for the curvatures and angles of the track. Additional constraints on the track quality are applied by imposing track cuts (see Sec. 7.3).

5.2. Jet reconstruction

Having a close look at high- p_T events, jet structures are often visible “to the eye” as several higher- p_T particles, roughly distributed in the same detector region. As already described in Sec. 2.4, those structures are typically created in a hard scattering of incident partons that subsequently branch and hadronize into observable particles. Thus, reconstructing jets reveals properties of the original parton and allows access to the physics of the hard scattering and, therefore, also the possibility to test pQCD.

While jet production is already interesting in its own right, in heavy-ion collisions the jets are also sensitive probes of the partonic medium formed in high energy collisions.

A jet algorithm is in principle a set of definitions of how to group particles in the detector and how to assign their momenta to the jets’ momenta. The rules how to cluster particles together are given by a distance measure, the jet momentum definition by the so-called recombination scheme.

Good jet algorithms must be somehow universal [Sal10]: They should be experiment- and detector-independent and should be applicable to all experimental or theoretical levels.

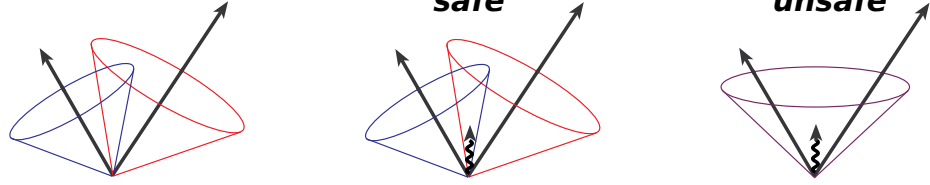
Infrared and Collinear (IRC) safety (see Fig. 5.1) is an important property of many jet algorithms. While an infrared-safe algorithm should not yield different results if a very soft particle is added to the event, collinear safety of an algorithm means the insensitivity to the splitting of one jet into two collinear ones.

The main reason why an IRC-safe algorithm is favored is simple: Due to their partly non-perturbative nature, the effect of those collinear splittings and soft particle emissions is not calculable and not predictable for a given event. IRC-safe algorithms are not affected by those differences.

Many jet algorithms exist and they are typically divided into two classes: Cone algorithms and sequential recombination algorithms. While cone algorithms rely on the assumption that the QCD branching and the hadronization do not change the parton properties in the considered cones, sequential algorithms subsequently cluster all particles into jets according to a given distance measure.

In this thesis, only sequential recombination algorithms are used: the k_T and anti- k_T algorithms. The implementation in the FastJet package [Cac12] is used. Those algorithms are briefly described in the following.

Infrared safety



Collinear safety

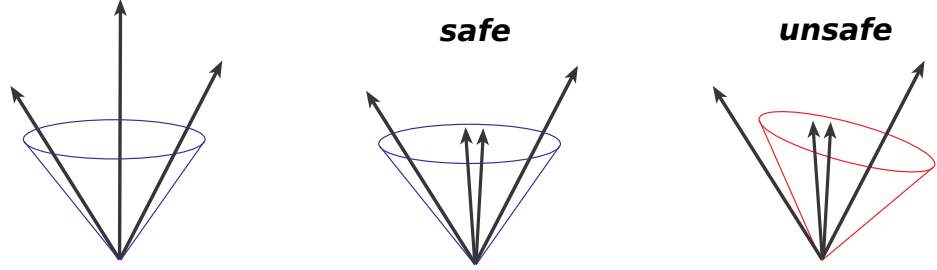


Figure 5.1: Illustration of infrared and collinear safety. The lines are particles in a spatial representation and the cones indicate how the jet algorithm clusters the jet. Figure adapted from [Bla00].

5.2.1. The anti- k_T and k_T algorithms

Together with the Cambridge/Aachen jet finding algorithm [Dok97], the anti- k_T and k_T algorithms belong to a general class of sequential recombination algorithms [Cac08b]. Those algorithms are based on the following iterative procedure:

1. Calculate distances according to a given measure between the objects (particles, in later iterations pseudojets) and between objects and beam by

$$d_{ij} = \min(p_{T,i}^{2\alpha}, p_{T,j}^{2\alpha}) \frac{\Delta R_{ij}^2}{R^2} \quad (5.1)$$

and

$$d_{iB} = p_{T,i}^{2\alpha}, \quad (5.2)$$

where α is an algorithm-specific parameter, $\Delta R_{ij} \equiv \sqrt{(\eta_i - \eta_j)^2 + (\varphi_i - \varphi_j)^2}$ a measure for the geometric distance of the objects, and d_{iB} is the “distance to the

beam”. In the paper in which this algorithm was introduced, the transverse momenta $p_{T,i}$ are labeled by k_T , which explains the names of the algorithms. R is referred to as resolution parameter and often called *radius* of the jets.

2. Find the smallest distance d_{ij} or d_{iB}
 - If d_{ij} is the smallest value, both objects i and j are combined to a new object (pseudojets)
 - If d_{iB} is the smallest value, object i is considered as a jet and removed from the iteration process
3. Repeat procedure until no more particles or pseudojets remain.

The difference between the anti- k_T and k_T algorithms is given by different choices of α : The k_T algorithm uses $\alpha = 1$, the anti- k_T algorithm is defined by $\alpha = -1$. This apparently “inverts” the behavior of the distance measure. While the function $\min(p_{T,i}^{2\alpha}, p_{T,j}^{2\alpha})$ in Eq. 5.1 favors particles with low p_T for $\alpha = 1$, high- p_T particles are preferred for the anti- k_T algorithm with $\alpha = -1$.

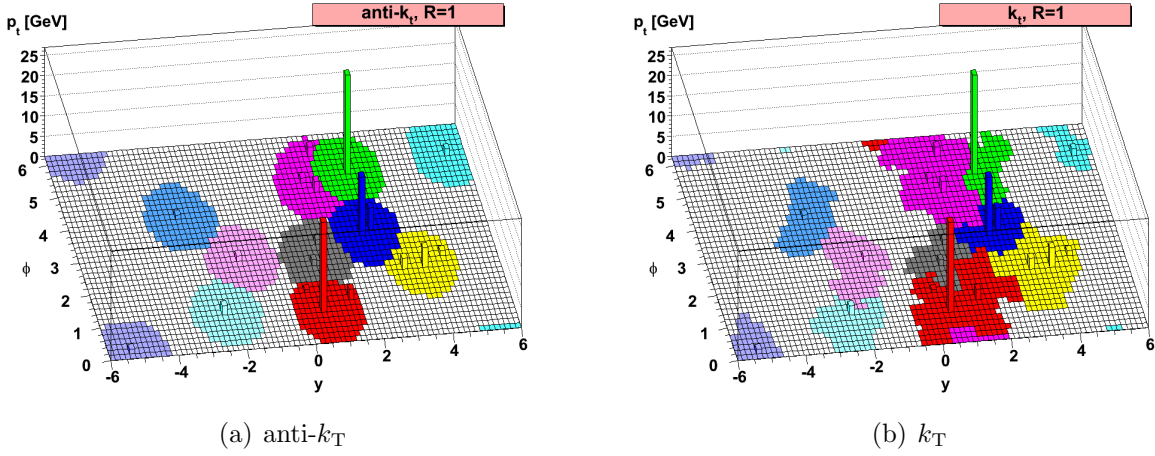


Figure 5.2: Illustration of an event clustered with the anti- k_T and k_T algorithms. The colored areas represent the areas that are associated to the jets. Plots taken from [Cac08b].

This results in different orderings of how particles are clustered and in different shapes for k_T and anti- k_T jets.

The anti- k_T jets are very regular, cone-shaped jets. In recent analyses at the LHC, they are often utilized as signal jets for the jet spectra. But also k_T jets with their relatively irregular shape are of great value: They are often used for background subtraction

(later described in Sec. 6.1). An event display illustrating the jet shapes can be found in Fig. 5.2.

The computational costs of earlier implementations of these algorithms for N particles scales with $\mathcal{O}(N^3)$, which limits their application to low multiplicity systems. However, further developments [Cac06] allow a much faster implementation in recent versions of FastJet with $\mathcal{O}(N \ln N)$ for multiplicities $N \leq 20,000$ (cf. also [Cac12]).

According to the “Snowmass accord” published in 1990 [Hut90] – one of the key documents on the future of jet measurements in hadron colliders – the optimal jet resolution parameter or radius R in the $(\eta - \varphi)$ -plane should be $R = 0.7$. However, all presented analyses in this thesis utilize smaller resolution parameters/radii.

The main reason for this can be found in the limited acceptance $|\eta| < 0.9$ of the tracking detectors of ALICE in pseudorapidity. Using $R = 0.7$ would massively limit the statistics. On the other hand, jets are strongly collimated objects and, therefore, the major part of jets is already contained in smaller radii. This justifies the measurement with relatively small resolution parameters.

Additionally, in heavy-ion Pb–Pb collisions and to a smaller extent also in p–Pb collisions, using smaller resolution parameters is important to limit the impact of the underlying event. Independent from the jet, the underlying event density grows with R^2 while the jet signal falls approximately exponentially for larger R .

5.2.2. Jet area calculation

To subtract the correct amount of background energy on a jet-by-jet basis, knowledge of the jet area is necessary. The calculation is performed with the *active area approach*, implemented in FastJet (cf. [Cac08c]). It works as follows.

For each jet, the area A is determined by distributing so-called ghost particles to the detector acceptance. Ghost particles have vanishing momenta and, therefore, do not influence jets that include these particles in the jet finding procedure.

On the other hand, the amount of ghost particles in a jet is a direct measure for the jet area. The area resolution is driven by the size that is assigned to the ghost particles and thereby by their density. A smaller size corresponds to more ghost particles but also requires more computational power. For the presented analyses, the area of one ghost particle corresponds to an area of 0.005 in the (η, φ) -plane.

5.2.3. Jet recombination scheme

The jet recombination scheme defines how the jet momentum is calculated with respect to its constituents. Several schemes are commonly used: the E -scheme, p_T -scheme, and boost-invariant p_T -scheme.

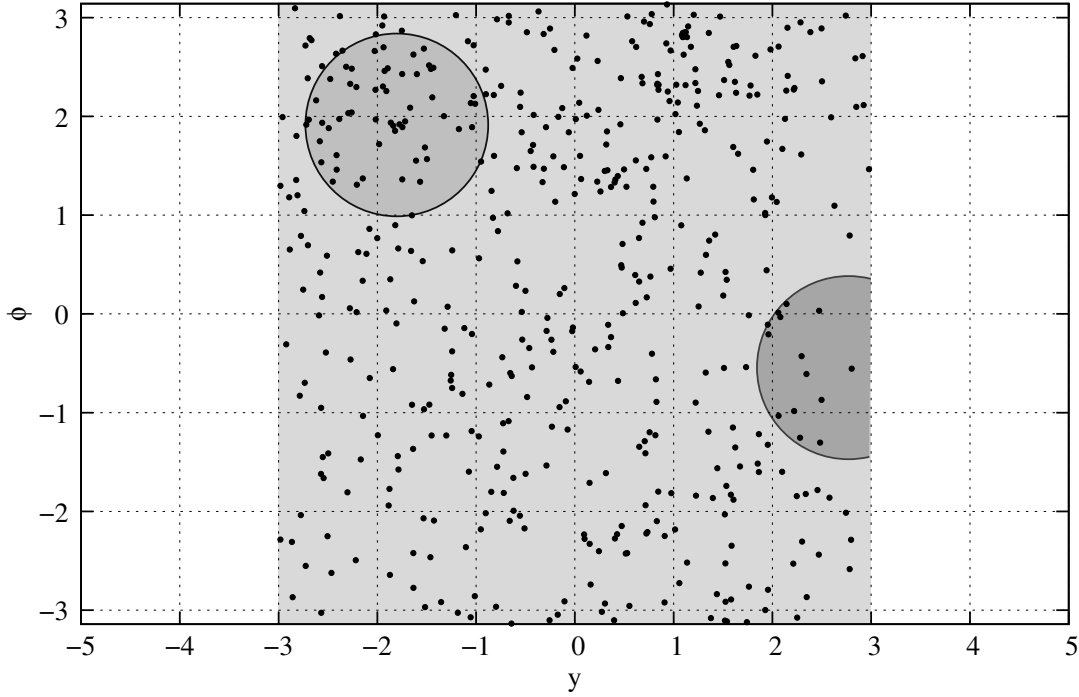


Figure 5.3: Distribution of ghosts in the whole acceptance of the detector. Plot from [Cac12].

The E -scheme is conceptually the simplest approach: It adds up the four-momenta of the particles.

When combining two particles or pseudojets in the p_T or boost-invariant p_T -scheme, the direction of the jet axis is formed using the p_T -weighted directions of the single objects. The transverse momentum is simply added up:

$$p_T = p_{T,1} + p_{T,2} \quad (5.3)$$

$$\eta = \frac{p_{T,1}\eta_1 + p_{T,2}\eta_2}{p_{T,1} + p_{T,2}} \quad (5.4)$$

$$\varphi = \frac{p_{T,1}\varphi_1 + p_{T,2}\varphi_2}{p_{T,1} + p_{T,2}}. \quad (5.5)$$

In contrast to the boost-invariant p_T -scheme, the p_T -scheme includes a preprocessing stage, in which the energy is rescaled assuming massless particles. This does not change the particles momenta but the jets (pseudo)rapidity is affected by the rescaling.

On the other hand, an exemplary calculation shows that the effect of the energy rescaling is negligible for jets in measured data even if low- p_T jets are considered. The jet energy

difference for p_T - and boost-invariant p_T -scheme is given by:

$$\Delta E = E_{\text{BIpt}} - E_{\text{pt}} \quad (5.6)$$

$$= \sqrt{p^2 + m^2} - |p|. \quad (5.7)$$

Note that technically, the track mass m is fixed to the pion mass 0.1396 GeV/ c , because the mass is only known with a certain probability. As an example, the ΔE for different recombination schemes using jets with a momentum of 10 GeV/ c consisting of 5 particles is given by

$$\Delta E = 0.024 \text{ GeV}, \quad (5.8)$$

corresponding to 0.24 % energy difference. Note that this example already shows the largest possible effect for measured jets. For jets with larger momenta, the effect is even smaller.

In this thesis, the p_T -scheme is used.

5.3. Centrality estimation

Atomic nuclei are extended objects with sizes of the order of a few femtometer. Depending on how they collide, the overlap region in which the nucleons interact and, therefore, also the number of interacting nucleons vary widely.

The concept of centrality is a measure to quantify how central or how peripheral collisions are. It is directly connected to the overlap of the colliding nuclei and also to the impact parameter. The impact parameter is the distance between the centers of the nuclei in the plane transverse to the beam direction.

Especially for nucleus–nucleus collisions, the concept of centrality in a collision is extremely useful. Basic event characteristics vary strongly with centrality. For example, the multiplicity in a central Pb–Pb event at the LHC is orders of magnitude larger than in a peripheral event.

This satisfies the expectation, because a more central event has a larger overlap region and more interacting nucleons per definition. Therefore, all effects are stronger. In addition, also qualitatively new effects, independent from the trivial multiplicity dependence, are visible for more central collisions. For example, while the charged particle nuclear modification factor R_{AA} shows a strong suppression and a visible transverse momentum dependence for the most central events, both effects are much more subtle for peripheral events [Aam11].

The concept of centrality can also be applied to nucleon–nucleus or, more specifically, proton–lead collisions. In this case, the differences between the centrality classes are less strong compared to Pb–Pb collisions.

Because of the very different collision systems, it is a priori not clear if the method for

centrality determination that has originally been developed for Pb–Pb collisions [Abe13a] can simply be applied to p–Pb collisions as well.

And indeed, in [Ada14] the method formerly used in Pb–Pb – the NBD-Glauber fit approach – is shown to be biased especially for hard processes. In the same paper, a new method is presented that includes the Zero Degree Calorimeter of the ALICE detector to extract an unbiased centrality estimate – the hybrid approach.

In the following, after introducing the Glauber model, both approaches to estimate the event centrality are briefly presented.

5.3.1. The Glauber model

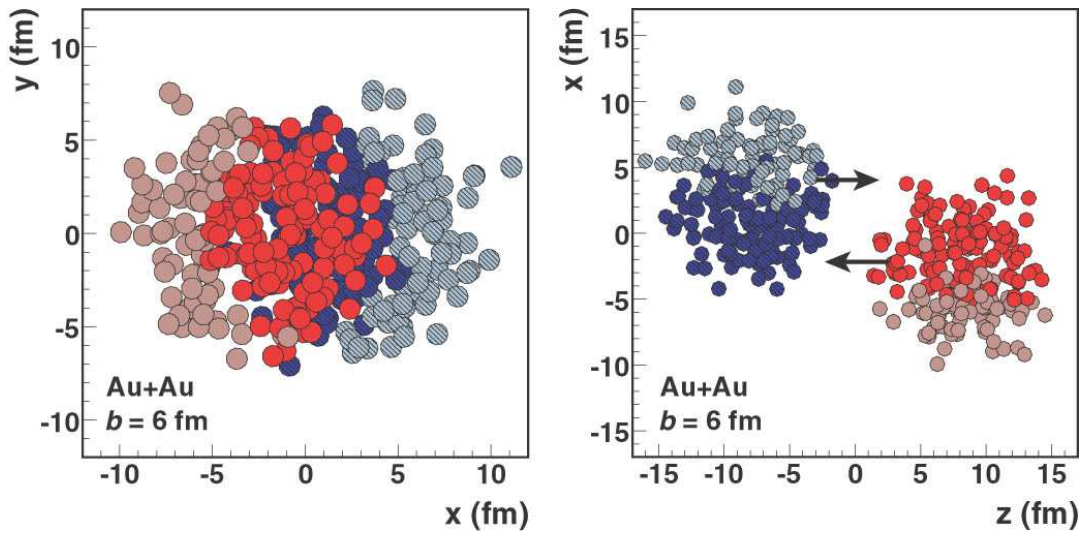


Figure 5.4: Illustration of an event of a Glauber Monte Carlo simulation for Au–Au collisions. The radius of the graphical representation of the nucleons is related to the inelastic nucleon–nucleon cross section (see Eq. 5.10). Darker circles depict nucleons participating in the collision. Figure from [Mil07].

Typical quantities to describe the centrality of an event are the number of participants N_{part} and the number of binary nucleon–nucleon collisions N_{coll} . Those numbers are strongly correlated with the size of the overlap region. In collider beam experiments, they cannot be measured directly but have to be estimated by simulations.

For the calculation of the number of participants N_{part} depending on the impact parameter b , the Glauber model can be used. In this model, a heavy-ion collision is a superposition of multiple nucleon–nucleon collisions. The movement of the nucleons is approximated by straight lines along the beam axis [Mil07].

In a Monte Carlo simulation, the probability distribution for N_{part} can be calculated.

For every event, the nucleons are distributed according to a Wood-Saxon potential,

$$\rho(r) = \frac{\rho_0}{1 + \exp((r - R)/a)}. \quad (5.9)$$

In this equation, $R = 6.62 \pm 0.06$ fm is the radius of the Pb-nucleus and $a = 0.546 \pm 0.010$ fm is the skin depth. ρ_0 is the nucleon density. The numbers are taken from low-energy eA scattering experiments. During the distribution procedure of the particles, a so-called hard sphere exclusion is applied, meaning that a minimum distance between the nucleons, here 0.4 fm, is demanded.

When the collision is simulated, a nucleon is considered a participant, if its distance to another nucleon is below a certain threshold in the modeled collision. In a simple Glauber Monte Carlo simulation, this distance is chosen to depend on the (inelastic) nucleon–nucleon cross section of the collision system in the following way:

$$d = \sqrt{\sigma_{\text{NN}}^{\text{inel}}/\pi}. \quad (5.10)$$

In principle, the probability distributions for N_{part} and N_{coll} can solely be extracted from the Monte Carlo simulation. But the centrality classes that yield those values are defined for sharply defined impact parameter ranges.

Since the impact parameter is not measurable, the centrality classes eventually used for the measured data have to be defined by using a measured distribution. Therefore, more suitable N_{part} values have to be calculated using those centrality classes.

5.3.2. NBD-Glauber fit approach

To define the centrality classes independent of the (non-measurable) impact parameter, the Glauber model has to be connected to measured data. This can be done by fitting a multiplicity distribution measured in data to a generated distribution produced by the Glauber model connected to the number of participants N_{part} .

To generate this multiplicity distribution using a Glauber calculation, a model for particle production is needed. It is necessary to know how the collision geometry – characterized by a specific number of participants N_{part} – is connected to the measured multiplicities in the detector.

It can be shown that a well-suited model for particle production is based on a Negative Binomial Distribution (NBD) [Abe13a]. For this model, the probability distribution for the number of particles n hitting the multiplicity detector per interaction is given by

$$P(n) = \frac{\Gamma(n+k)}{\Gamma(n+1)\Gamma(k)} \cdot \frac{(\mu/k)^n}{(\mu/k+1)^{n+k}}. \quad (5.11)$$

Here, μ is the mean multiplicity per participant and k is connected to the width of the distribution. Applying the NBD for N_{part} interactions and fitting the generated

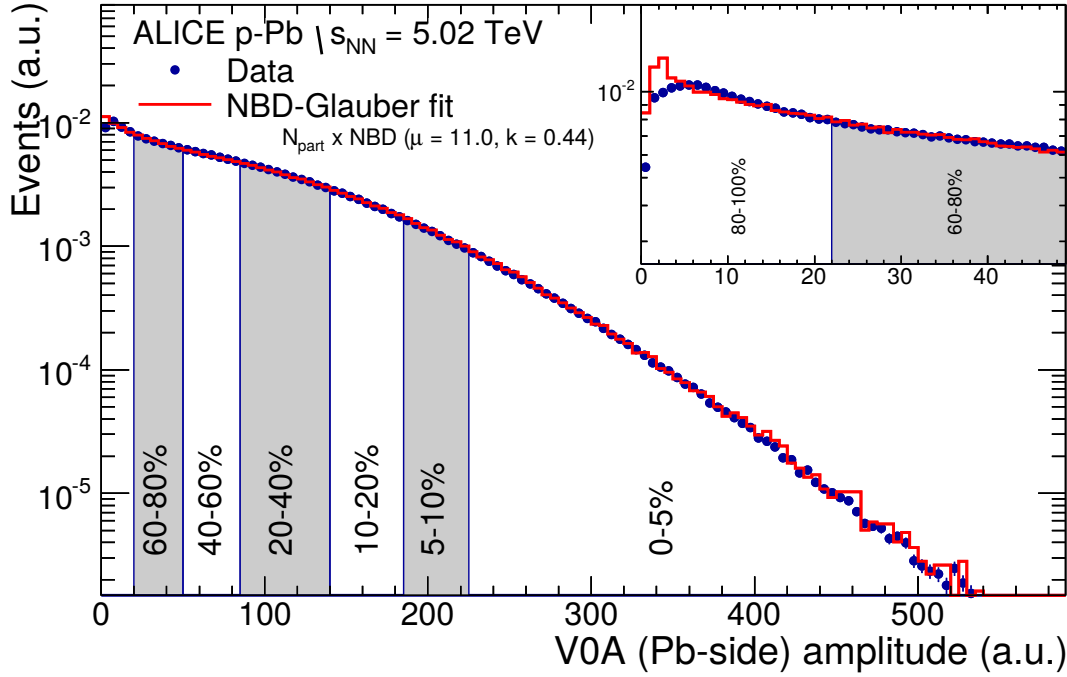


Figure 5.5: Measured V0A multiplicity distribution fitted by an NBD-Glauber simulation in p-Pb. Figure from [Ada14].

distribution to a measured multiplicity, the multiplicity can be simulated. μ and k are the free parameters of the model, N_{part} is calculated in Glauber model calculations. Using the fitted multiplicity distribution, it is possible to select centrality classes in the Glauber model as it can be done in the measured data. For those centrality classes, the mean numbers of binary collisions N_{coll} and participants N_{part} can be calculated.

For the centrality estimation with the NBD-Glauber fit approach in p-Pb, the measured multiplicity distributions are given by either V0A, V0M, or CL1 distributions. The V0A distributions are given by the amplitudes measured by the V0A detector. While the V0A detector is located on the Pb-going side of the interaction point, the V0C detector is found on the p-going side. The V0M distribution is created as the sum of the amplitudes of both V0 detectors. The CL1 estimator is given by the number of clusters in the second layer of the Silicon Pixel Detector of the ITS. An illustration of the NBD-Glauber fit is provided in Fig. 5.5.

The usage of the NBD-Glauber approach for p-Pb collisions suffers from several biases. Conceptually, the NBD “simulates” fluctuations of the multiplicity depending on the number of participants in a collision that has been calculated by a Glauber model. The relative fluctuations of N_{part} are much higher in p-Pb compared to Pb-Pb (see Fig. 5.6). Hence, the probability to measure e.g. a high-multiplicity fluctuation of a peripheral

event with the same multiplicity like a more central event is higher in p-Pb than in Pb-Pb. Using the NBD-Glauber approach in p-Pb to fit a multiplicity distribution, e.g. given by V0A amplitudes, the average multiplicity per N_{part} is much larger for central events (roughly 30% enhancement for 0-20% most central events) than the NBD-fitted value μ described in Eq. 5.11. On the other hand, for the most peripheral events, the average multiplicity per N_{part} is much lower than the parameter μ (roughly 70% suppression for 80-100% most peripheral events). The numbers are for V0A multiplicities, for further details, see [Ada14].

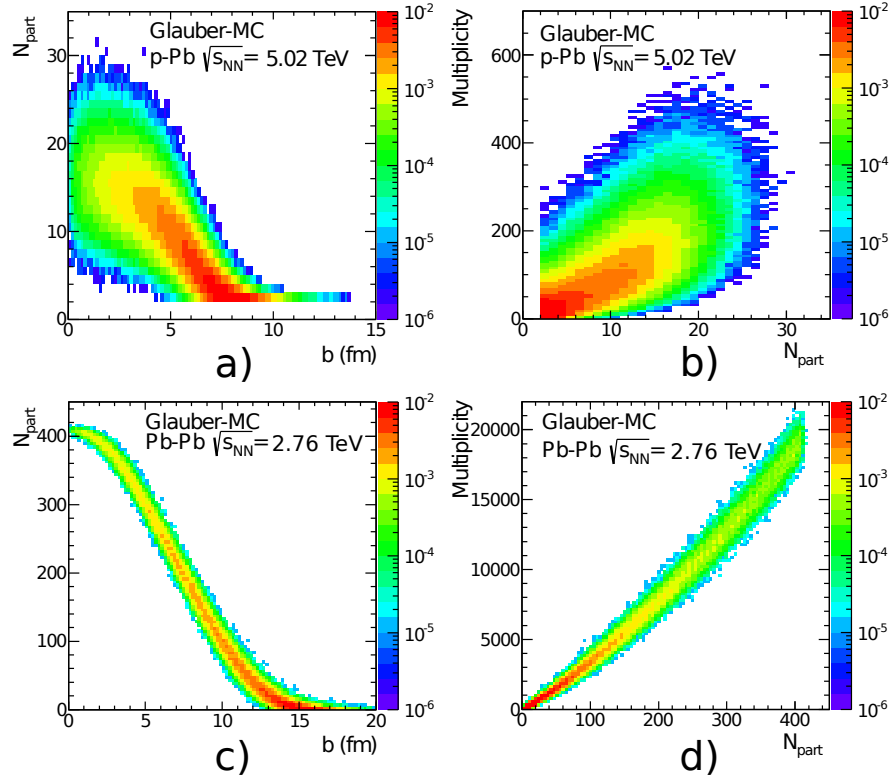


Figure 5.6: Correlations of multiplicity, number of participants N_{part} , and impact parameter b in p-Pb (a, b) and Pb-Pb (c, d). Figure from [Ada14].

This means, selecting the events based on the characterization of the NBD-Glauber fit biases the central events towards more high-multiplicity events while the peripheral events contain more low-multiplicity events. Not only do those high-multiplicity events differ by a different average N_{part} from the low-multiplicity events, they are also harder events with larger mean particle transverse momentum.

Apart from this multiplicity bias, there also exist the jet-veto and the geometry bias. The jet-veto bias describes that the selected multiplicity range represents a veto on hard processes producing jets: Since the centrality is here directly connected to the

multiplicity, peripheral events have lower multiplicity and will therefore contain less jets. The geometry bias enhances results in central and suppresses results in peripheral collisions due to a lower mean nucleon–nucleon impact parameter b_{NN} for peripheral events. b_{NN} changes for the reason of the geometry of the nucleus and depends on the modeled spatial parton density in the Glauber model.

5.3.3. Hybrid approach

To overcome the difficulties of the NBD-Glauber fit approach, the p–Pb centrality task force in ALICE developed a method that is not affected by the biases described above. First, the general ansatz of this method is that the event selection is not biased by multiplicities at midrapidity if it is based on the deposited energy in the Zero Degree Calorimeters. Second, the number of participants N_{part} and binary collisions N_{coll} is assumed to scale with multiplicity in a particular way. In p–Pb collisions, both numbers are directly connected by $N_{\text{part}} = N_{\text{coll}} + 1$.

At least in principle, the N_{coll} values in p–Pb could also be calculated using a fit of the Glauber distribution to the energy E_{ZDC} measured by the ZDC. The ZDC measures so-called slow nucleons created in nuclear de-excitation processes or knocked out by participant nucleons. Therefore, the particle production cannot be described by an NBD but with a heuristic slow nucleon model that relates E_{ZDC} to N_{coll} .

This method is discussed in detail in the p–Pb centrality paper [Ada14]. As the result depends on the slow nucleon model, a different method was chosen for the hybrid approach to avoid the introduction of larger systematic uncertainties.

By using E_{ZDC} measured by the neutron calorimeter ZNA on the Pb-going side, the event centrality is estimated. This can be done for roughly 96% of the accepted events. For the remaining 4%, no information from the ZDC is available. Since those events show the same CL1, V0A, and V0M distributions like events from the 80–100% centrality bin, they are classified as belonging to the most peripheral bin. E_{ZDC} , as a measure for the slow nucleon multiplicity, is expected to be monotonically related to the number of binary collisions.

For the number of binary collisions, three estimators are developed in the centrality paper.

- $N_{\text{coll}}^{\text{mult}}$: This estimator assumes that the charged particle multiplicity at midrapidity is proportional to N_{part} .
- $N_{\text{coll}}^{\text{Pb-side}}$: The charged particle multiplicity on the Pb-going side is assumed to be proportional to the number of participating target nucleons $N_{\text{part}} - 1 = N_{\text{coll}}$.

- $N_{\text{coll}}^{\text{high pT}}$: The main assumption for this estimator is that the yield of high transverse momentum particles is proportional to N_{coll} . For jet measurements of the nuclear modification, this assumption is not sensible as it assumes a flat nuclear modification factor. The estimator is therefore not used in this thesis.

The estimators are defined by

$$\begin{aligned} N_{\text{coll}}^{\text{mult}}(c) &= N_{\text{part}}^{\text{mult}}(c) - 1 \\ &= N_{\text{part}}(\text{MB}) \cdot \left(\frac{\langle dN/d\eta \rangle(c)}{\langle dN/d\eta \rangle(\text{MB})} \right)_{-1 < \eta < 0} - 1, \end{aligned} \quad (5.12)$$

$$N_{\text{coll}}^{\text{Pb-side}}(c) = N_{\text{coll}}(\text{MB}) \cdot \frac{\langle S \rangle(c)}{\langle S \rangle(\text{MB})}. \quad (5.13)$$

In these equations, c represents the centrality bin and MB stands for minimum bias. For the evaluation of $N_{\text{coll}}^{\text{mult}}$, the mean charged particle multiplicity density $\langle dN/d\eta \rangle$ is used. S in the formula for $N_{\text{coll}}^{\text{Pb-side}}$ is the mean (multiplicity) signal in the innermost ring of the V0A detector.

The values for the number of binary collisions that have also been used in the presented analysis are given in Tab. 5.1.

Table 5.1: Number of binary collisions for different centrality classes calculated with varying assumptions. The minimum bias value is computed in Glauber calculations only.

Centrality class	$N_{\text{coll}}^{\text{mult}}$	$N_{\text{coll}}^{\text{Pb-side}}$
0-20	11.5	12.1
20-40	9.56	9.60
40-60	7.08	6.74
60-80	4.30	4.00
80-100	2.11	2.06
Minimum bias	6.88	

5.4. Event generation and detector simulation

Monte Carlo (MC) based simulation techniques are essential tools for today's high energy physics. The main applications include the generation of collision events according to a theoretical model and a full simulation of the detectors used for data taking.

In this thesis, PYTHIA and POWHEG are applied for event generation and GEANT is used for the full detector simulation.

5.4.1. PYTHIA and POWHEG

Monte Carlo based generation of collisional events can be realized with relatively simple approaches like the Glauber model, in which the collision is more or less considered geometrically and in which the output is, essentially, the number of interactions.

But there also exist very sophisticated event generators like PYTHIA, which use complex multi-step procedures generating leading-order QCD-based events with a good accuracy. Which generator is best depends strongly on the problem.

Monte Carlo generated events serve as a basis for the creation of a response matrix (see Sec. 6.2.2) or for comparisons to the data. Comparing to data, the underlying physics assumed for the event generation can be tested. For instance, by comparing p-Pb collisions to PYTHIA events, it can be checked whether those collisions can be described as an incoherent superposition of multiple nucleon-nucleon interactions or not – at least in principle.

PYTHIA [Sjo06] is an event generator for leading-order processes but it is designed to reproduce event properties as accurate as possible for many soft and hard processes in high energy collisions. For example, it includes modeling of the parton showers, multiple-parton interactions, fragmentation and particle decays. The underlying physics are implemented as a combination of conclusions from analytical calculations and QCD-based models. It combines perturbative and non-perturbative approaches to describe as many aspects of the collision as possible.

Especially because of the modeling of initial and final state showers and the inclusion of many soft processes, the described physics go beyond “leading-order” physics.

The program has many free parameters. For this reason, much effort was spent on choosing certain parameter configurations that produce events in good agreement especially with LHC data. The “Perugia”-tunes [Ska10] are used throughout this thesis unless noted otherwise.

Another important feature is that PYTHIA can be configured to create events which contain a hard interaction in a certain $p_{T, \text{hard}}$ range. Here, $p_{T, \text{hard}}$ specifies the momentum transfer of the initial hard scattering. This is very useful since it allows the efficient creation of extremely rare events. Of course, those spectra are strongly biased. But

since the average cross section for a given range is known from PYTHIA, the resulting spectra can be scaled correctly and a spectrum can be combined by merging simulations of the full $p_{T, \text{hard}}$ range. The advantage is that one needs much less statistics to produce jet spectra in the whole transverse momentum range of interest.

In this thesis, also next-to-leading-order (NLO) calculations are used for data comparison. The NLO spectra have been simulated by Michal Vajzer and Philipp Kähler primarily to serve as a theory-comparison for the charged jet spectra in [Abe15]. They are created using the POWHEG box framework [Nas04] and PYTHIA8. PYTHIA is still used for the parton showering/QCD branching and the (non-perturbative) hadronization while the POWHEG framework replaces the first initial scattering. This scattering is modeled by PYTHIA as a leading-order $2 \rightarrow 2$ process. In contrast, POWHEG simulates this process according to NLO matrix elements.

The non-perturbative hadronization process in PYTHIA is based on an effective model. In principle, it already contains corrections also present in NLO calculations, e.g. gluon radiation in the final state. This is taken into account in the implementation of the POWHEG framework.

5.4.2. Detector simulation with GEANT

Typically, events generated by programs like PYTHIA cannot directly be compared to measured events. The reason is that the detectors are not fully efficient for any type of particle and that the momentum resolution is of course finite. Additionally, there can be dead or less efficient regions in some parts of the detector. To overcome this problem and to get directly data-comparable generated events, in ALICE a full detector simulation is used within the GEANT3 framework [Bru94] to propagate the generated particles through the detector. This is especially important for the creation of a detector response matrix that is essential for precise jet analysis.

Using a precise description of all parts of the ALICE detector, GEANT3 simulates the interactions of the incoming generated particles in the whole detector including support materials. Also potential decays of those particles in the material are taken into account. The energy loss of the incident particles is calculated depending on particle and detector material. Additionally, the response of the detectors according to the energy deposit of the particles – the electronic signal – is also simulated.

Finally, the data generated by GEANT3 is expected to be similar to what the detector would produce for the same incoming particles.

5.5. Evaluation of uncertainties

For the sake of completeness, this section contains a description how the systematic and statistical uncertainties were calculated. Both types of uncertainties are typically shown separately.

5.5.1. Statistical uncertainties

The general measurement process is to some extent a simple counting experiment. An observable is defined and measured on an event-by-event basis. While the measurement of the observable itself can be arbitrarily complex, the per-event values of the observable fill a histogram. The bins of those histograms then contain the number of events in which the observable has a specific value. Here, the size of the bins defines the resolution of the observable used for further analysis.

A simple example is the number of charged particles per event. To extract this number, a complex tracking procedure is performed on data from a complex detector. But eventually, it is only one number for each event that is filled into a histogram. In this case, the bins of this histogram represent the “counts” (number of events) for a certain number of charged particles.

Statistical uncertainties are in general calculated using the default method of the ROOT [Bru97] framework. ROOT automatically saves the sum of squared values that were added to the histograms given by

$$\Delta_{\text{stat}}(x) = \sqrt{\sum_N f_i(x)^2}, \quad (5.14)$$

where x specifies the bin of the histogram and N is the number of events. $f_i(x)$ represent the values filled into the histogram. For the considered counting case, these values are always one and the statistical uncertainty simplifies to

$$\Delta_{\text{stat}}(x) = \sqrt{N}, \quad (5.15)$$

the uncertainty known from counting experiments following a Poisson distribution.

In case of composed quantities, e.g. ratios, the uncertainty is recalculated on the basis of Gaussian error propagation. Two (total) uncertainties σ_x and σ_y can be combined to [Tay97]

$$\sigma_u^2 = \left(\frac{\partial u}{\partial x}\right)^2 \sigma_x^2 + \left(\frac{\partial u}{\partial y}\right)^2 \sigma_y^2 + \left(\frac{\partial u}{\partial x} \frac{\partial u}{\partial y}\right) \text{Cov}(x, y). \quad (5.16)$$

Here, the last term containing the covariance vanishes for uncorrelated quantities. This error propagation is implemented in ROOT but by default uncorrelated uncertainties

are assumed. For some of the observables in this thesis, the full uncertainty including the correlation term is calculated.

5.5.2. Systematic uncertainties for the jet spectra

In contrast to the calculation of statistical uncertainties, there exists no common general procedure for the evaluation of systematic uncertainties. Therefore, it is important to precisely define how to calculate the uncertainties.

This section is meant to give an overview of the general problem of calculating systematic uncertainties and of how the procedure principally works. Detailed analyses of the systematic uncertainties of the measured jet observables are presented in Chapter 9.

The measurement of jet spectra depends on various parameters. Some of the parameters are chosen for good reasons or they define the considered observables, e.g. the jet resolution parameter or the jet algorithm. Others are more or less arbitrary or at least less verified to be the best and unique choice like the background correction method. Systematic uncertainties are calculated to account for different possible configurations and parameter settings.

In this thesis, a simple approach is used to calculate these uncertainties on a bin-by-bin basis. The procedure works as follows:

1. The tunable parameters are chosen. For example, the jet resolution parameter is not considered a free parameter since it is an integral part of the applied jet definition. However, which parameters are chosen as tunable depends on what is supposed to be measured.
2. A certain parameter configuration is defined to give the *baseline* result. This particular choice is the one considered to be the optimal and least biased choice.
3. For every tunable parameter, a reasonable variation is defined. What a reasonable variation is, depends strongly on the parameter and is sometimes a bit arbitrary. The parameter can be a number, e.g. the tracking efficiency, or a method like the unfolding algorithm. For some parameters, more than one variation is taken into account.
4. The measured distribution is recalculated for every varied tunable parameter, one at a time.
5. Those measurements are compared to the baseline result and the deviations are taken as the uncertainty $\Delta_{\text{sys}}^i(x)$, where i specifies the changed parameter and x the bin. In case that more than one parameter was tested, the higher uncertainty or a mean value is selected, depending on the analysis parameter.

A drawback of this bin-by-bin calculation is that potentially also statistical fluctuations contribute to the systematic uncertainties. To get a smooth estimate, for some parameters the uncertainty is only allowed to rise with transverse momentum: If the originally estimated uncertainty is smaller for a higher p_T bin, the uncertainty estimate is set to the value of the preceding bin.

Also, for some parameters, one mean value is taken as uncertainty. Details can be found in Chapter 9.

It has to be emphasized that the choice of the baseline configuration (step 2), the values for the reasonable variations (step 3), and even the calculation of the particular uncertainties (step 4) contain a certain arbitrariness: For the baseline, it is not always obvious which configuration to choose. The same also holds for the reasonable variations of step 3. For the uncertainties in step 4, it is not clear whether the obtained deviation is to be taken as the maximum error or “Gaussian” error. For this thesis, we assume the uncertainties are of the latter type so that the total systematic uncertainty can be calculated by

$$\Delta_{\text{sys}}^{\text{tot}}(x) = \sqrt{\sum_i \Delta_{\text{sys}}^i(x)^2}. \quad (5.17)$$

Note that this equation implicitly assumes uncorrelated uncertainties. This assumption is based on the fact that the degree of correlation of the single uncertainties is unknown.

6. Correction techniques

In the previous chapter, the most important principles and techniques of the presented jet analyses have been shown. This chapter mainly focuses on correction techniques. Correcting raw spectra is necessary to compare to theory predictions and other measurements. For instance, when comparing jet spectra in pp and p-Pb collisions, one is interested in the differences in jet production and not in the differences of the background.

The first part of this chapter provides a detailed description of the applied underlying event correction techniques and how to evaluate in-event fluctuations of the background. Then, the approach to model the detector response is described. Since background fluctuations and detector effects are corrected for in unfolding algorithms, an introduction to the techniques used in the analyses of this thesis is presented.

The second part of this chapter contains a description and a comprehensive analysis of the unfolding techniques. This also includes an analysis to evaluate the optimum parameters and a direct comparison of the unfolding methods.

6.1. Underlying event correction

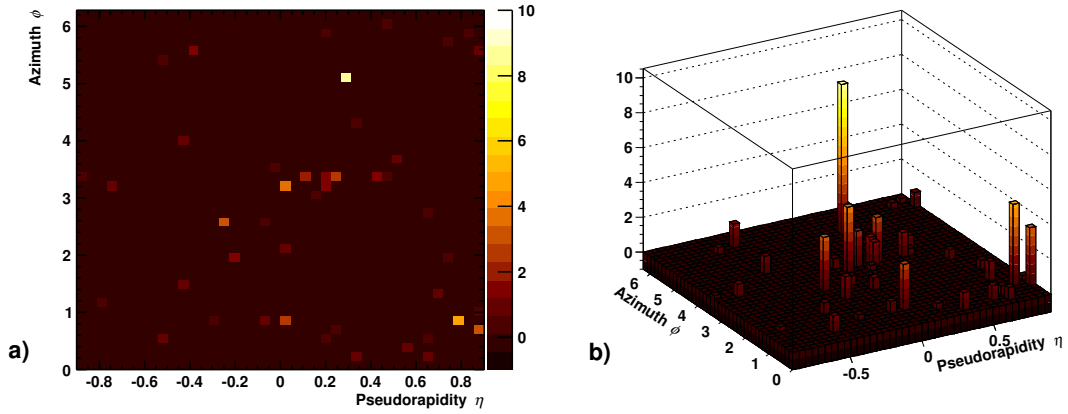


Figure 6.1: Event display of a typical p-Pb collision containing a 10 GeV/c jet.

In p-Pb collisions, reconstructed high- p_T jets are most likely produced in hard parton-parton interactions. Next to these hard interactions with high momentum transfer Q^2 , there are also softer contributions summarizing everything that does not originate from a hard collision. The contributions are mainly from semihard parton interactions at transverse momenta of the order of a few GeV/c that cannot be resolved as jets. These objects are sometimes called minijets. A typical event with a low- p_T jet is depicted in Fig. 6.1. Given a measured event, it is not clear which particle tracks or energies originate from a hard collision and which do not. Even for simulated Monte Carlo events, for which the initial hard scattering is known, it is not clearly recognizable what to define background and what signal. Like for jets, what to call background is also defined by the algorithm. However, in contrast to the jet definition, particles are not divided in background and non-background particles. Background is defined as a property of the whole event.

In Pb-Pb collisions, the background has a huge impact on the reconstructed jet momentum. In ALICE, it is estimated using a statistically robust median of all jet transverse momenta per area within one event for clusters/jets reconstructed with the k_T algorithm. For the 10% most central Pb-Pb events at $\sqrt{s_{NN}} = 2.76$ TeV, the mean background transverse momentum density ρ_{ch} is estimated to be roughly 140 GeV/c per unit area [Abe12a].

For the sparser environment of p-Pb collisions, several approaches for a reliable background estimate have been developed or applied and have been used for systematic uncertainty studies. In the measurements reported, the approach described in Sec. 6.1.1.2 is used as default method.

The general approach of all methods is to estimate the background density on an event-by-event basis and to correct the jets, depending on their area, on a jet-by-jet basis.

$$p_{T,\text{jet}} = p_{T,\text{jet}}^{\text{rec}} - A_{\text{jet}}^{\text{rec}} \cdot \rho. \quad (6.1)$$

Several of the background approaches, which are described in the following, reduce the influence of the hard scattering signal by excluding *signal jets*. Those jets are fully contained within the detector acceptance and have at least $p_{T,\text{jet}} \geq 5 \text{ GeV}/c$.

6.1.1. Methods using k_T jets

The k_T jet finding algorithm [Cac08a] is used in several jet analyses for constructing a background estimation technique.

6.1.1.1. Original approach in Pb–Pb

As mentioned above, background subtraction is a large correction in Pb–Pb collisions. The approach is well proven to work in Pb–Pb (cf. [Cac08a], [Ver13]), but it is not necessarily working for the much diluter p–Pb collision system. And indeed, the method cannot simply be used for p–Pb but has to be adapted as described below.

In the original ansatz, the background density is calculated by

$$\rho_{\text{PbPb}} = \text{median} \left\{ \frac{p_{T,i}}{A_i} \right\}, \quad (6.2)$$

where i is to be understood as the index of k_T jets with $p_T > 0.150 \text{ GeV}/c$.

The full k_T jet sample also contains signal from hard interactions. The usage of the median already provides stability with regard to outliers in a distribution, in this case outliers from the hard signal. Another method to reduce the influence of the signal is k_T jet exclusion. Here, the n leading jets are excluded from the jet sample. Leading jets are those with the highest transverse momentum p_T . n is typically chosen to be $n = 2$.

In [Cac08a], the authors suggest to include ghost jets in the jet sample when calculating this background in a sparser environment to account for empty areas. As described in Sec. 5.2.2, the acceptance is filled uniformly with ghost particles that have vanishing momentum to calculate the area. In relatively sparse environments, the jet algorithm can combine these to ghost jets that do not contain real particles. In Pb–Pb, these ghost jets do not really play a role, because of the high mean background density. In p–Pb, the situation is different: For most of the events, a sizable part of the acceptance does not contain particles.

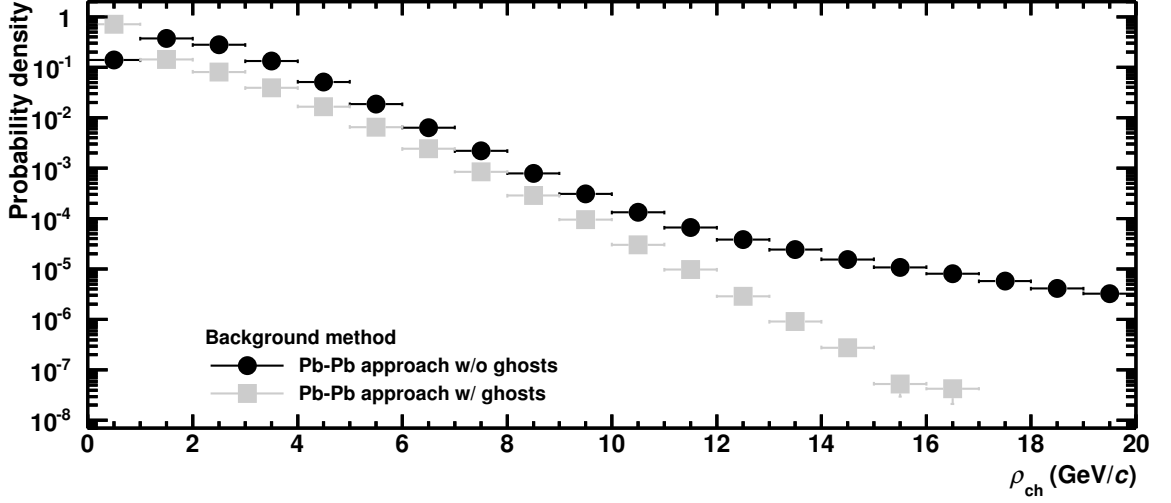


Figure 6.2: Background density in p–Pb collisions for the original Pb–Pb approach with and without using ghost jets.

Of course, just neglecting the ghost jets biases the background density to larger values, because it does not take into account empty areas. On the other hand, including ghost jets entails a limitation on the minimum particle occupancy of the acceptance: If more than 50% of jet sample consist of ghost jets, the median in Eq. 6.2 is zero and the background density is not a continuous variable. This is indeed often the case with p–Pb events.

In Fig. 6.2, the background distribution is shown for including and not including the ghost jets. It is plainly visible that the inclusion of ghosts reduces the overestimation of the background. However, the strong enhancement of the first bin in this distribution hints at the fact that the minimum particle occupancy is often not given. This leads to vanishing background densities in those events.

This method is not considered in the systematic uncertainty calculation because of its strong conceptual drawbacks in the p–Pb collision system.

6.1.1.2. Default approach in p–Pb

In [Cha12a], a method was introduced that is especially suitable for sparse systems and that circumvents the problems arising from the inclusion of ghost jets. The basic idea is to account for empty areas not by including ghost jets but by introducing a factor correcting for the emptiness of the event.

The background density is defined similar to the density in Pb–Pb,

$$\rho_{\text{CMS}} = \text{median} \left\{ \frac{p_{T,i}}{A_i} \right\} \cdot C, \text{ with } C = \frac{\text{Covered area}}{\text{Total area}}. \quad (6.3)$$

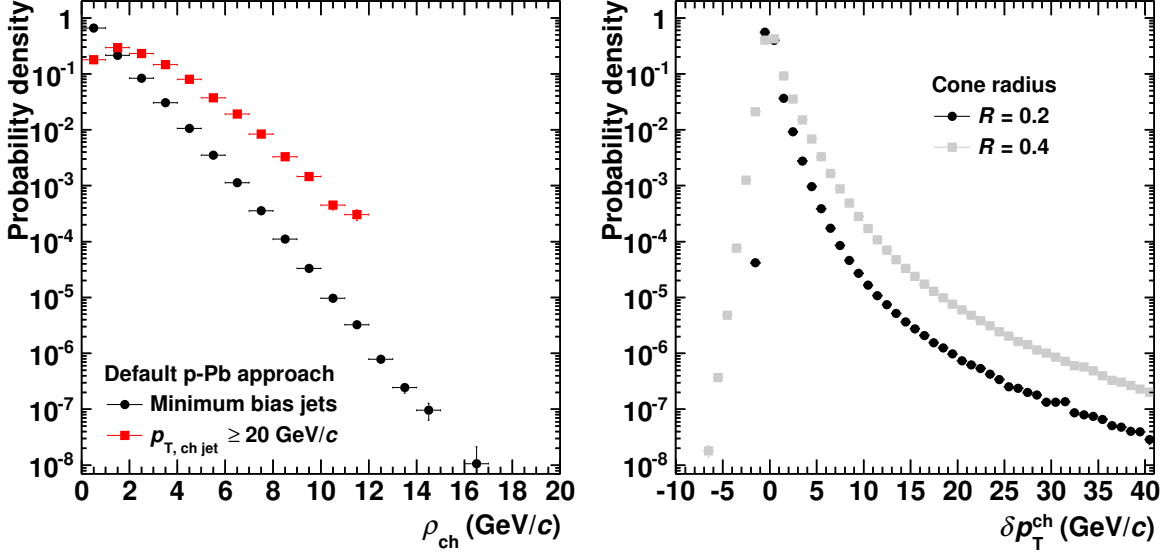


Figure 6.3: Background density (left) and fluctuations (right) in p–Pb collisions using the default approach. Information on the calculation of δp_T is given in Sec. 6.1.3.

In this equation, C is the charged particle occupancy factor. It represents the fraction of the area populated by charged particles. Which area is populated by the particles is decided by the k_T jet finding algorithm. Roughly speaking, the factor specifies how full or empty the event is.

This method can further be refined for the specific use case of p–Pb collisions. Conceptually, the exclusion of the first two k_T jets from the set in Eq. 6.3 – like it was done in the Pb–Pb approach – should enhance the background quality due to signal suppression. This assumption is supported by investigations of the background fluctuation distribution in strongly biased PYTHIA events (a similar analysis is presented in Fig. 6.11 and the accompanying text). In this distribution, a larger or smaller contamination of the background with signal from hard interactions can be recognized. It turns out that the exclusion of the first two hardest k_T jets reduces the contamination.

A distribution of the background can be found in Fig. 6.3.

6.1.1.3. Mean-based approach

For the Pb–Pb approach including ghost particles, the background density is zero if more than 50% of the jets are ghost jets because the approach uses the median. The mean-based background density calculation method arose from a first naive idea to solve this problem. The ansatz is to calculate the background density by

$$\rho_{\text{Mean}} = \text{mean} \left\{ \frac{p_{T,i}}{A_i} \right\}. \quad (6.4)$$

In contrast to the median, the mean of a distribution is continuous but also much more affected by outliers. Therefore, it is important for this method to exclude the hard interaction signal jets (fully contained within the detector acceptance, $p_{\text{T, jet}} \geq 5 \text{ GeV}/c$) from the jet sample used in Eq. 6.4. They are excluded by neglecting k_{T} jets that share tracks with those signal jets.

A variation of the mean-based approach follows from Eq. 6.4 if the k_{T} jets all have roughly the same area or transverse momentum. In this case, it is approximately

$$\rho_{\text{Mean}} = \text{mean} \left\{ \frac{p_{\text{T}, i}}{A_i} \right\} \approx \frac{\text{mean} \{p_{\text{T}, i}\}}{\text{mean} \{A_i\}} = \frac{\sum_i p_{\text{T}, i}}{\sum_i A_i} = \rho_{\text{Mean II}}. \quad (6.5)$$

In Eqs. 6.4 and 6.5, the index i specifies the k_{T} jet. An illustration of the background density distributions produced by both mean-based methods can be found in the background comparison plot in Fig. 6.10.

Both methods suffer from two conceptual problems. First, the mean is sensitive to outliers in the distribution. Even if the exclusion of the signal by excluding signal jets worked perfectly, ρ would be biased to larger values due to fluctuations. This already hints at the second problem: The exclusion affects signal jets above a certain p_{T} threshold, which is $5.0 \text{ GeV}/c$ in this case. A $p_{\text{T}} = 4.9 \text{ GeV}/c$ jet will be considered as background but contains signal with a high probability. This is a conceptual problem of the need to explicitly distinguish signal and background jets. So again, the background will be biased to larger values. The median-based methods do not have this problem as they are relatively insensitive to signal contamination in sparse events.

6.1.2. Method using tracks

The background estimate utilizing tracks is conceptually the simplest. The summed transverse momentum of all non-signal tracks is divided by the associated area, leading to the background density

$$\rho_{\text{Track}} = \frac{\sum_i p_{\text{T}, i}}{A}. \quad (6.6)$$

Like for the mean-based approach, the background definition strongly depends on the signal definition. In this case, tracks are defined to belong to the background if they lie outside a rigid cone with $R = 0.6$ around the signal jet's axes. The area A is calculated by a Monte Carlo approach and represents the acceptance excluding the area of the $R = 0.6$ -cones around the jets.

This background estimate suffers from the same conceptual problems as the mean-based approach and is even more affected by a signal contamination. A depiction and comparison can be found in Fig. 6.10.

6.1.3. Background fluctuations

On an event-by-event basis, the background density is calculated by using particles in the full acceptance. Every jet is corrected according to its area, assuming a uniform background distribution. This assumption is necessary, because it is impossible to calculate the *real* background of a jet. However, the background is in fact not uniformly distributed but fluctuates within the acceptance. This is mainly caused by the statistical nature of the fluctuations. Uncorrelated random fluctuations in the particle production lead to a Poissonian distribution of the particle count. Another source of background originates from the jets themselves. Due to multiple nucleon–nucleon interactions in an event, it is possible that two jets overlap in the acceptance.

In Fig. 6.3, a plot of the background fluctuation distribution δp_T is depicted. The statistical fluctuations can cause both negative and positive values of δp_T . Fluctuations caused by overlapping jets or, in general, hard scattering processes, only affect the positive part of the distribution.

The mean intra-event fluctuations can be taken into account on a statistical basis in an unfolding procedure. In order to calculate the fluctuations, the Random Cone (RC) approach is used for the analyses in this thesis [Abe12a]:

For every event, one or multiple rigid cones are placed somewhere in the acceptance. The angular positions are randomized; so the cones are called *random cones*. For all tracks in the cones, the transverse momentum is summed up and compared to the global background density of the current event. The fluctuation is called δp_T and is defined by

$$\delta p_T = \sum_i p_{T,i} - \rho A_{\text{cone}}. \quad (6.7)$$

Random cones are supposed to probe the background under a jet for different positions in the detector acceptance. The δp_T distribution gives therefore an estimate of how the background fluctuates under a jet within the event. For this purpose, δp_T is calculated with a cone radius corresponding to the jet resolution parameter. However, the probability for the cone to overlap a jet is larger than for the jets themselves to overlap. This is because the random cone is placed into a full event with, say, N jets. But every single jet in such an event is accompanied by only $N-1$ jets. Thus, random cones are on average accompanied by one jet in addition compared to the jets themselves. Note that this consideration is only an approximation. While the random cones are distributed completely randomly and can overlap by construction, jets are potentially produced in the same hard scattering and cannot overlap.

For the default δp_T calculation, this effect is ignored because there is no distinct correction technique. However, a modified δp_T calculation was developed for this thesis and the results are considered for the systematic uncertainties. The modification introduces a probability to discard a random cone that overlaps a signal jet. On a statistical basis, just enough overlapping cones are accepted to let the overall probability be given by the

mean $(N_{\text{sig}} - 1)/N_{\text{sig}}$ value. N_{sig} represents the mean number of signal jets in the event. Since this modified δp_T calculation strongly depends on the signal definition and also on how an overlap is defined, it is not used by default. The final effect on the jet spectra is small and is considered for systematic uncertainties. A direct comparison of the raw distributions is depicted in Fig. 6.4.

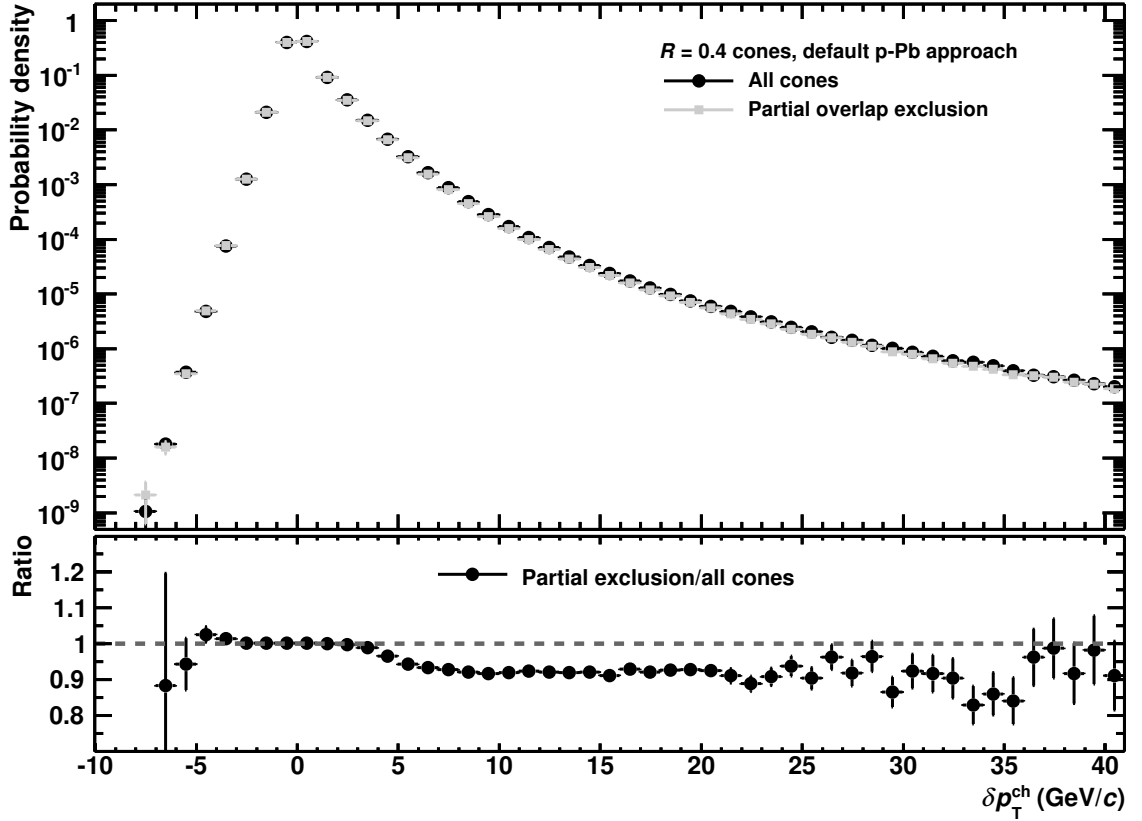


Figure 6.4: Background fluctuations for the default method (all cones) and the alternative method taking the signal jet overlap probability into account.

It may seem easy to calculate background fluctuations in bins of jet p_T . But if the δp_T distribution is considered for example for events containing jets from $20 \text{ GeV}/c < p_{T, \text{ch jet}} < 30 \text{ GeV}/c$, the distribution does not correspond to the fluctuations under such a jet, but it strongly biased. In Fig. 6.5, this effect is depicted.

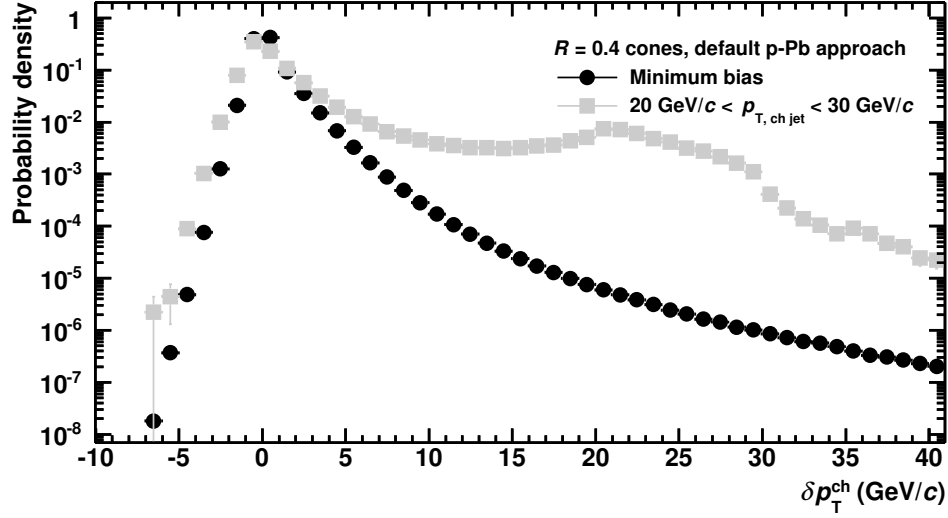


Figure 6.5: Background fluctuations δp_T for minimum bias and jet p_T biased events.

6.1.4. Centrality and jet p_T dependence

The technique to evaluate background density and fluctuations is the same regardless of centrality. All methods are applied equally to every selected event as described above.

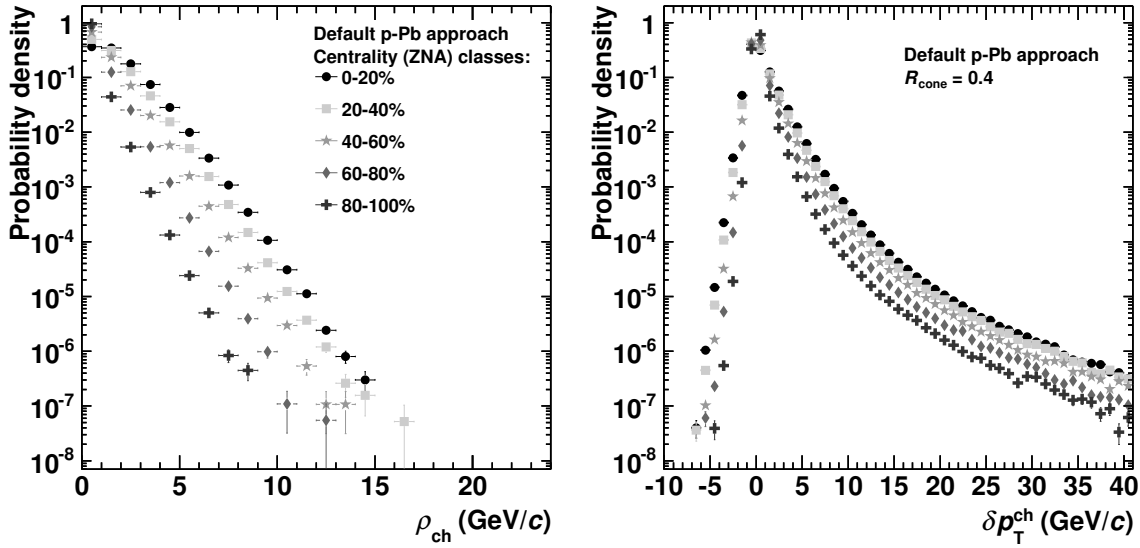


Figure 6.6: Background density (left) and fluctuations (right) using the default approach for different centrality intervals.

However, the distributions of background density and its fluctuation depend on the event centrality.

First, this is true for different bins of centrality. Central collisions have larger background densities with larger fluctuations than peripheral collisions (cf. Fig. 6.6).

Second, the background distributions also differ for various centrality estimators. As described in Sec. 5.3, the NBD-Glauber fit approach centrality estimators exhibit a multiplicity bias. This is also reflected in the background distributions (cf. V0A, V0M, and CL1 estimators in Fig. 6.7).

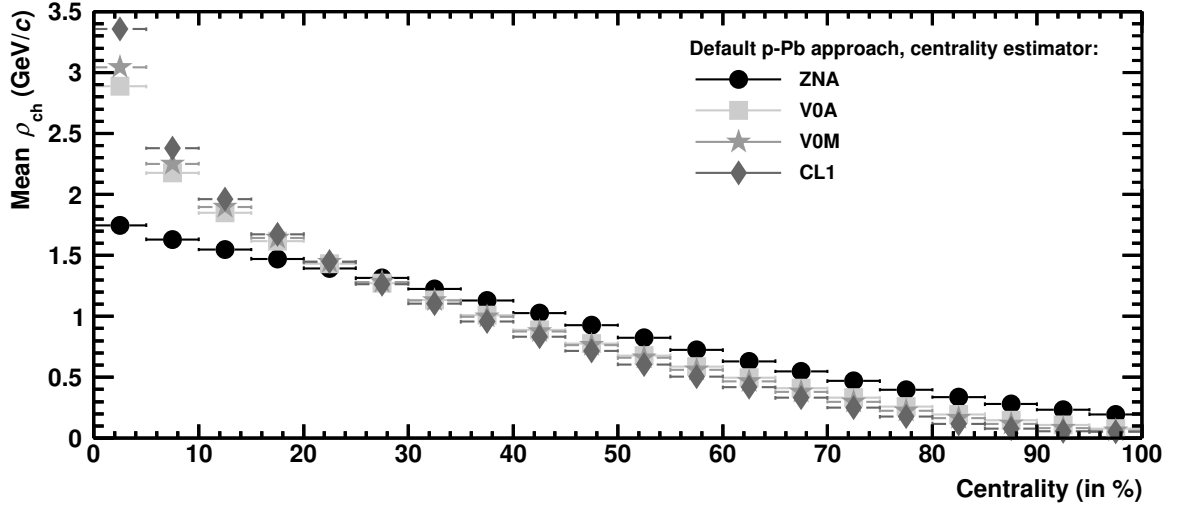


Figure 6.7: Mean background density in bins of different centrality estimators.

What is also interesting is the actual dependence of the background density on the jet transverse momentum to estimate which background is effectively subtracted with regard to the jet. In Fig. 6.3, the background distribution is also shown for events containing a jet with raw $p_T \geq 20$ GeV/c. A more differential analysis for the calculation of the mean background densities reveals the jet p_T dependence of the background, see Fig. 6.8.

For low jet transverse momenta, also a lower background is subtracted. This behavior is expected and was already measured in pp collisions. It has been investigated with more differential measures, e.g. in [Abe12b]. Events containing low- p_T jets dominate the full data sample and have therefore a huge impact on the shape of the background distribution. At a raw jet momentum of roughly 10 GeV/c, the background density saturates and is more or less constant up the highest measured jet transverse momenta.

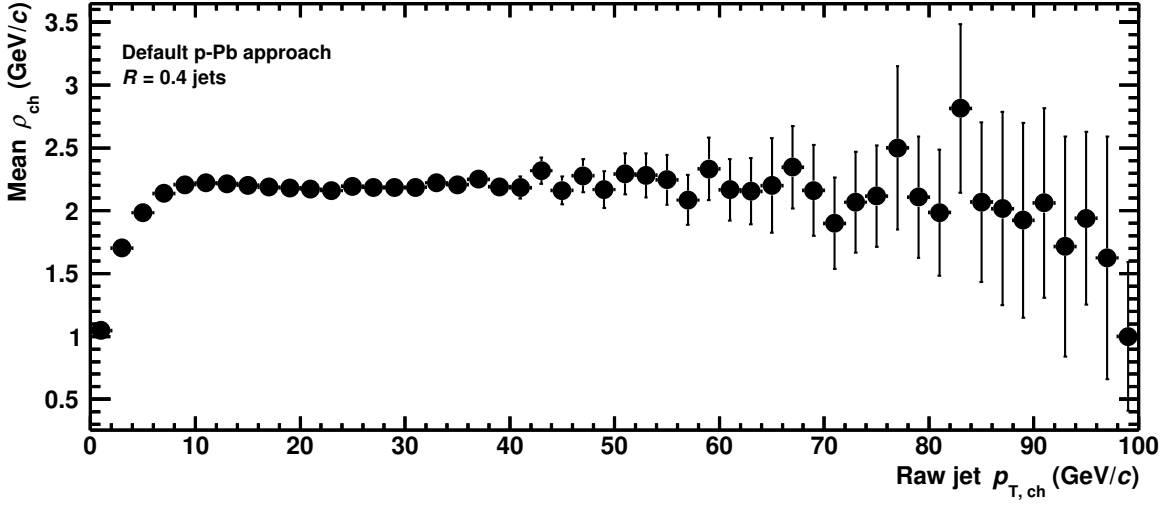


Figure 6.8: Mean background density in bins of raw jet p_T .

6.1.5. Pseudorapidity dependence

The p-Pb collision system is asymmetric, the tracks are generally not distributed symmetrically in pseudorapidity η around the interaction point [Abe13e]. This is directly visible for the uncorrected track pseudorapidity distribution in Fig. 6.9(a). In this plot, the dip around $\eta = 0$ is mainly caused by the inefficiency of the TPC due to the central electrode. Electrons of the ionization tracks of charged particles crossing the TPC membrane are accelerated to the respective end caps – the track is “torn apart”.

All background subtraction methods work on data using the whole pseudorapidity acceptance within $|\eta| < 0.9$. One global event value is calculated and subtracted from all jets regardless of their η . This implicitly assumes a uniform background. This condition is – at least in principle – not fulfilled. However, the background density distributions in Fig. 6.9(b) for different pseudorapidity intervals indicate that the assumption is actually not that bad. The lower panel shows the ratio plot that compares to the midrapidity background in $|\eta| < 0.2$.

The ρ distributions are shown for the track-based approach, because this approach is expected to be most affected by a possible pseudorapidity dependence.

While the background density for the negative η range is 1.56 GeV/c per unit area and 1.52 GeV/c for the positive η range, it is 1.415 GeV/c for the full η range. Note that the background density of both considered η regions is slightly larger than the value of the full range. The main reason for this is that the signal exclusion is not working as efficient as for the full interval. For instance, a jet at midrapidity $\eta = 0.1$ is not excluded in the background calculation in the positive η region. Although the extracted differences are probably overestimated, they are still small compared to the differences among the other

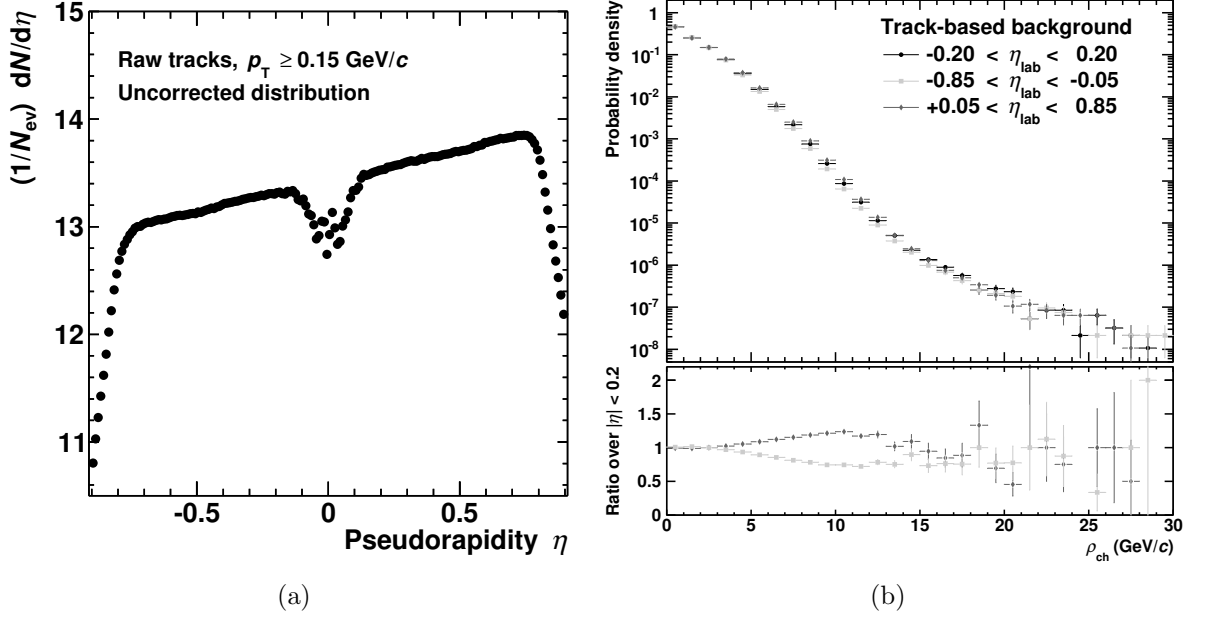


Figure 6.9: Asymmetric track pseudorapidity distribution in p-Pb (a) and track-based background distribution for different η intervals (b).

background methods. For the calculation of the systematic uncertainties, the possible deviation from the pseudorapidity dependence is therefore considered to be covered by the uncertainty which has been calculated by the comparison to the other background correction approaches.

One could argue that – even though the η dependence of the background is small – the background value could be calculated by default for the suitable pseudorapidity range. Several tests have been carried out, including those for the default p-Pb approach, and it turned out that the relatively small acceptance of the ALICE detector limits the applicability of η -differential background subtraction. Calculating the background density in bins of pseudorapidity possibly takes into account the small η dependence, but on the other hand also yields less precise background values due to the smaller data sample.

Additionally, for an η -differential background density it is more difficult to reduce the influence of the hard scattering signal, i.e. to exclude signal jets, because of the smaller acceptance.

6.1.6. Conclusions

Several background estimators have been implemented or developed, because it was a priori not clear, which method to use. There is no established default background method for p–Pb collisions in ALICE yet. However, despite all drawbacks of the particular methods, the differences in the background density distributions are relatively small for all considered methods, see Fig. 6.10.

Table 6.1: Values of background density and fluctuations per unit area and its variances for different methods (in GeV/ c). Due to the available statistics, the statistical uncertainties are much smaller than the last given digit and therefore not shown. All centrality classes use ZNA centrality.

Background estimate	Mean $\langle\rho_{\text{ch}}\rangle$	Variance $\sigma(\rho_{\text{ch}})$	Variance $\sigma(\delta p_{\text{T}})$	Gaussian width of δp_{T} (left tail)
Minimum bias				
Default p–Pb	1.044	0.924	1.093	0.552
Track-based	1.415	1.180	1.084	0.680
Mean-based	1.271	1.158	1.091	0.648
Mean-based II	1.412	1.141	1.083	0.683
Centrality-dependent default p–Pb				
$p_{\text{T, ch jet}} \geq 20$ GeV	2.419	1.600	-	-
0-20%	1.615	1.178	1.404	0.735
20-40%	1.266	1.036	1.266	0.682
40-60%	0.876	0.842	1.071	0.556
60-80%	0.512	0.603	0.846	0.450
80-100%	0.262	0.372	0.638	0.370

For the final jet spectra, the chosen background subtraction method has only a minor influence. The preferred approach is the technique defined in Sec. 6.1.1.2, called “default p–Pb approach”.

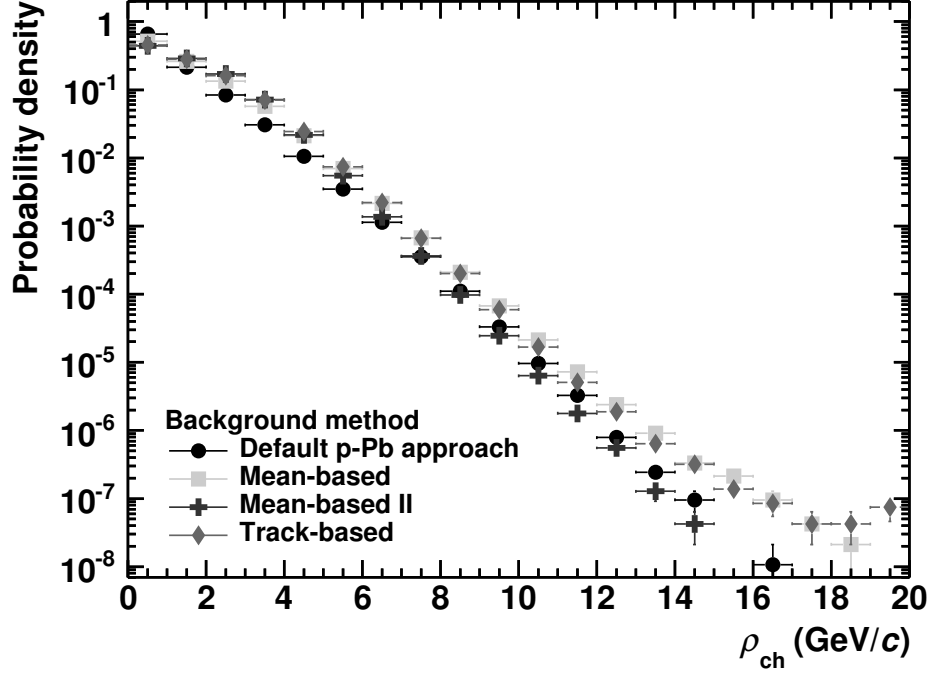


Figure 6.10: Background density in p–Pb collisions for different background estimates. Numerical values are given in Tab. 6.1.

In summary, it can be said that all other methods presented suffer from conceptual drawbacks:

- Pb–Pb approach: Without ghost jets, the background is highly overestimated since the empty areas are neglected. On the other hand, including ghost jets gives a vanishing background density for most of the events because of the discontinuous property of the median if more than 50% of the jets are ghosts. On account of these strong conceptual problems, this approach is not considered for the systematic uncertainty calculation.
- Mean-based approaches: Using the mean is conceptually more susceptible to the high- p_T outliers. Also, because of the signal exclusion, the background depends on the signal definition.
- Track-based approach: The method has similar drawbacks as the mean-based approaches. The problem resulting from high- p_T outliers is even worse, because tracks measure both hard and soft contributions similarly. In contrast, k_T jets are clusters/samples of particles.

There is also another possibility to get a grasp of the quality and reliability of each background method, namely by having a closer look at the background fluctuation distributions δp_T : The left-hand side of the peak in the δp_T distribution represents on the

one hand downward fluctuations of the background in the probing cone. On the other hand, those negative δp_T values can also be interpreted by an overestimated background. Roughly speaking, the background can be influenced by the signal.

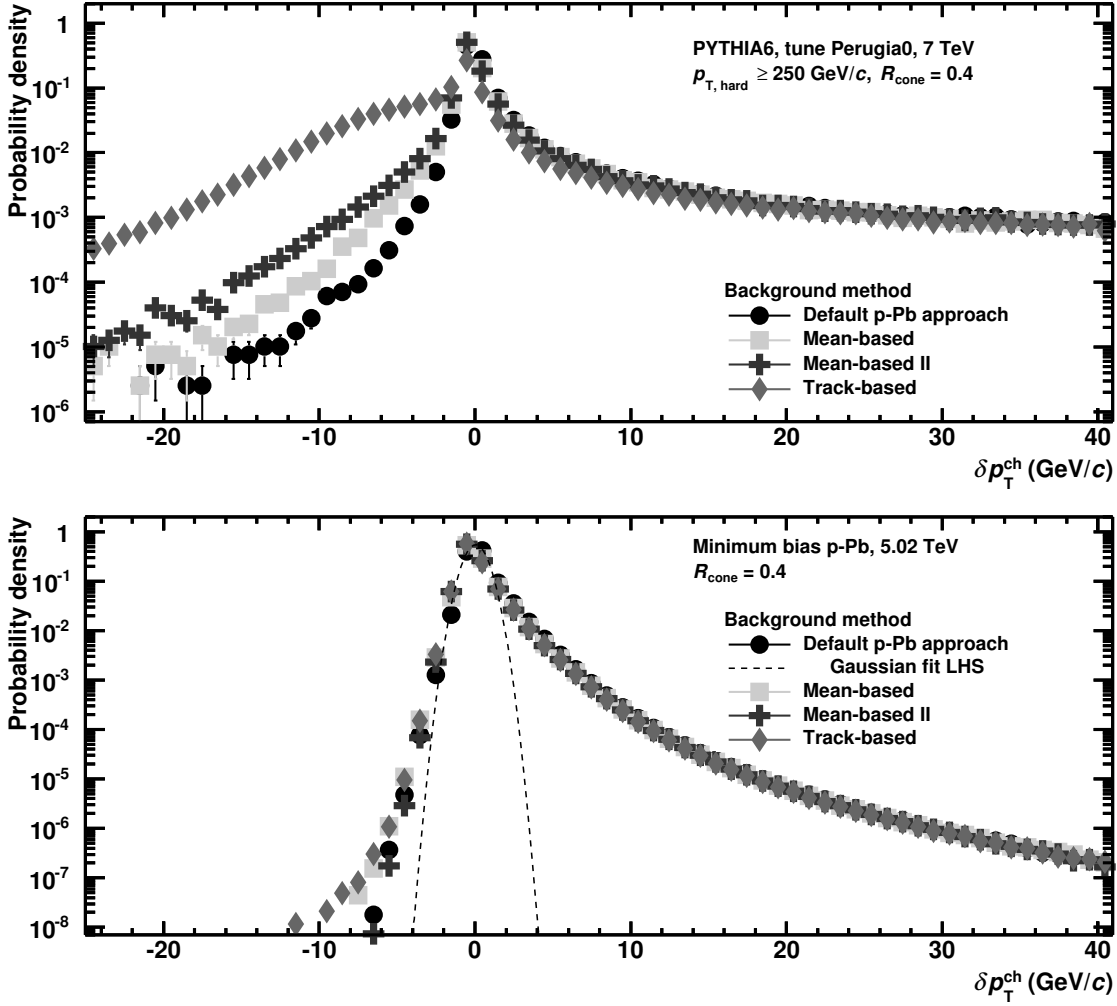


Figure 6.11: Background fluctuations δp_T for strongly biased PYTHIA jets (upper plot) and minimum bias p-Pb collisions (lower plot).

In the lower plot in Fig. 6.11, the difference between the background fluctuations using different estimates is observed to be small. Note that this plot also contains a Gaussian fit using the left-hand side (the negative part) of the δp_T distribution. It is obvious that the fit does not describe the data very precisely, neither the left-hand side nor the right-hand side of the distribution. The Gaussian fit has been performed, because it was done in the fluctuation distribution for Pb-Pb collisions. Here, the fit is more suitable [Abe12a]. However, the distribution of the background fluctuations is not expected to

follow a Gaussian shape for the negative values. The underlying particle counts show Poissonian fluctuations and the sampled momentum distribution is a steeply falling spectrum. The deviations of particle p_T are therefore not distributed according to a Gaussian distribution. In [Abe12a], the distribution in Pb–Pb is shown to be fit relatively well by a modified Γ -function.

In Pb–Pb, the particle count sampled with the random cones is much larger. This is the reason why the Gaussian fit works much better for Pb–Pb data. For completeness, the numerical values can be found in Tab. 6.1.

In contrast to the lower plot in Fig. 6.11, the upper plot shows the δp_T distribution for extreme conditions with a strong signal from a hard interaction. The strongly biased event sample was created by PYTHIA by demanding a hard parton–parton interaction of at least 250 GeV/ c .

Under those artificial conditions, δp_T shows differences from the expected form that can be interpreted as a signal contamination of the background. As expected, the track-based method is influenced the most. The default p–Pb approach shows no strong contamination. It has to be emphasized that these findings can only be seen as an indication of the reliability of the background method, but they support the choice of default method.

6.2. Unfolding jet spectra

In order to compare the obtained jet results to data from other experiments and theory predictions, they should be as similar as possible to the *true* spectrum that would be measured by a hypothetical perfect detector without any disturbing influences.

In this thesis, the measured background-corrected jet spectra differ from the *true* spectra mainly in two aspects. First, they are detector-specific. Due to the finite single-track momentum resolution and efficiency, jets are reconstructed with different transverse momenta than in a perfect detector. Second, although the mean background is subtracted, the jets can contain background fluctuations. Both effects cannot be corrected on an event-by-event basis but only statistically for the whole event sample.

The measured spectrum can be described as the true distribution convoluted with the measurement response. In the general case, the response can be considered as a two parameter function $f(y, x)$ representing the probability density that a measured observable value y in the distribution is caused by a true value x . Since the distribution is given as a binned histogram of the measured observable, the measurement response is given by a matrix.

How the measurement process affects the true distribution can mathematically be represented by

$$y_i = \sum_j R_{ij} x_j. \quad (6.8)$$

Here, i and j specify the bin numbers and R_{ij} the components of the response matrix. This explanation and its mathematical expression in Eq. 6.8 is valid for the full measurement response. The response matrix R_{ij} describes how the detector affects the jet measurement and also how background fluctuations smear the spectrum.

Knowing the measurement response matrix R_{ij} , unfolding methods can be used to reconstruct the true distribution x for a given measured distribution y . The procedure to create the response matrix is described in Sec. 6.2.2.

For the analyses of this thesis, several well-known unfolding algorithms were applied and considered for systematic uncertainty calculations. The default unfolding method was chosen to be Singular Value Decomposition (SVD) unfolding.

6.2.1. Unfolding algorithms

The naive approach to extracting the true from the measured distribution using Eq. 6.8 is the inversion of the response matrix R . However, because the detector resolution and single-particle tracking efficiency are limited and the number of simulated events is finite, the problem is mathematically ill-posed and results in a highly fluctuating solution. Therefore, unfolding algorithms have to include some sort of regularization.

Singular value decomposition (SVD), χ^2 -unfolding, and a manual unfolding procedure which makes direct use of the response matrix were applied in the present analyses and are described in detail in this section. In addition, the Bayesian unfolding technique was also tested and Bayesian-unfolded spectra will be often shown for comparison. However, the method does often not produce smooth results (also seen in Pb–Pb, see [Ver13]).

6.2.1.1. SVD unfolding

The description and detailed introduction of an unfolding algorithm based on *singular value decomposition* known from linear algebra was published in 1996 [Hö96]. The technique described there serves as the default unfolding algorithm in the current analyses. The implementation in the RooUnfold package is used [Ady11]. On the basis of the matrix representation of Eq. 6.8, the unfolding problem can be formulated as a weighted least square problem by

$$(Rx - y)^T C^{-1} (Rx - y) = \min, \quad (6.9)$$

where R is the unfolding matrix, x and y are the true and measured distributions in vector representation, and C is the covariance matrix of the measured spectrum.

“min” formulates the problem as a minimization problem. The usage of the covariance matrix introduces a weighting for the significance of the entries of the measurement vector with respect to the measurement uncertainties.

For the algorithm, matrix and vectors are rescaled and rotated. The unfolding matrix and the measured spectrum vector are rotated and rescaled so that the covariance matrix simplifies to the unit matrix and the true spectrum is represented as a ratio relative to the prior, $\tilde{x} = x/x^{\text{prior}}$.

The reformulation of the problem is not circumventing the general need for a regularization. Thus, an additional regularization term is introduced. Finally, the problem to solve is given by

$$(\tilde{R}\tilde{x} - \tilde{y})^T(\tilde{R}\tilde{x} - \tilde{y}) + \beta(D\tilde{x})^T D\tilde{x} = \min. \quad (6.10)$$

Here, β is the regularization strength and D is a matrix, which defines the regularization condition. In this thesis, this condition is defined to be the smoothness of the unfolded spectrum by requiring that the second derivatives of the unfolded spectrum are not too large. The evaluation of the optimum regularization parameter is described in detail in Sec. 6.2.3.

6.2.1.2. χ^2 -unfolding

The χ^2 -unfolding is based on the minimization of a χ^2 -function which can be defined by

$$\chi^2(x) = \sum_i \left(\frac{y_i - \sum_j R_{ij}x_j}{\delta y_i} \right)^2 + \beta P(x), \quad (6.11)$$

where y are the measured values, x the unfolded values, and R_{ij} are the entries of the unfolding matrix. The second term $\beta P(x)$ is the so-called penalty term and is described below. The χ^2 -unfolding procedure can in principle be understood as a χ^2 -fit where y_i denotes the free parameters. In the framework applied for the presented analyses, this is done using the AliUnfolding package, which is part of `aliroot` (cf. [GO09]). AliUnfolding itself uses MINUIT [Jam75] for the minimization.

The penalty term is used to artificially prefer or penalize a certain property of the unfolded spectrum. It serves as a regularization of the unfolding spectrum by imposing additional constraints to the spectrum. These constraints can be such basic properties as smoothness or positiveness of the unfolded distribution but also detailed restrictions as the preference of a certain distribution shape. The latter constraint is also utilized in the present analyses. The penalty term prefers a power-law shape for the unfolded distribution via the definition:

$$P(x) = \sum_i [\ln x_i (\ln p_T)]'', \quad (6.12)$$

where the variables are to be understood as in Eq. 6.11. The summand is to be read as the second (discrete) derivative of the double-logarithmic representation of the unfolded spectrum. The demand to minimize this quantity means that the penalty term prefers an unfolded spectrum that is linear in the double-logarithmic representation. And the spectrum that is linear in this scale is indeed the power-law spectrum.

The regularization strength β should not be chosen too large, otherwise the penalty term dominates the minimization procedure and the unfolded spectrum is too much influenced by the properties induced by the penalty term. On the other hand, it should not be too small in order to incorporate the desired properties and to suppress fluctuations. Like for the SVD unfolding, the approach to calculate the optimum regularization parameter is outlined in Sec. 6.2.3.

6.2.1.3. Bayesian unfolding

Bayesian unfolding [D'A03] is based on Bayes' theorem on conditional probabilities. The theorem connects several probabilities by

$$P(A|B) = \frac{P(B|A) \cdot P(A)}{P(B)}. \quad (6.13)$$

Here, $P(A)$ and $P(B)$ represent the probabilities for an event A or B . $P(B|A)$ and $P(A|B)$ are conditional probabilities that an event B occurs under the condition of event A , and vice versa.

Since jet spectra can be interpreted as probability distributions and a response matrix is a distribution of conditional probabilities, this theorem can be written as [GO09]

$$S_{ji} = \frac{R_{ij}T_j}{\sum_k R_{ik}T_k}, \quad (6.14)$$

where R is the response matrix, T the true spectrum. The denominator is equivalent to the measured spectrum. The matrix S is the smearing matrix that can be directly applied to extract the true spectrum for a given measured distribution by

$$T_j = \sum_i S_{ji}M_i, \quad (6.15)$$

in which M is the measured distribution.

However, to extract the true distribution T in Eq. 6.15, the smearing matrix S has to be known. According to Eq. 6.14, S can be calculated, if the true distribution is known. Apparently, a direct calculation is not possible.

This relations can be utilized in an iterative procedure though: First, the smearing matrix S is calculated for a chosen prior (introduced as T) using Eq. 6.14. This is

typically a flat distribution or also a distribution similar to the measured one. Second, the unfolded result is calculated using Eq. 6.15. For the next iteration, this unfolded distribution is used as the prior. This procedure is repeated several times. Eventually, the unfolded result is expected to be a good approximation of the true distribution.

6.2.1.4. Manual procedure

For comparison and validity checks of the other unfolding methods, a simple unfolding procedure solely based on the response matrix is used.

The response matrix can be understood as a mapping of true and measured jet p_T . Every true jet p_T is connected to a probability distribution of measured jet transverse momenta. On the other hand, a measured jet p_T is also connected to a distribution of true jet p_T specifying the probability that a measured jet is created by a certain true jet.

In a bin-by-bin procedure, the contents of the measured jet transverse momentum distribution are redistributed according to the true jet p_T probability distribution. No (explicit) regularization is applied.

6.2.2. Creating the response matrix

The response matrix directly connects two physical quantities: the measured and true jet transverse momenta. As already stated above, the response matrix utilized in the unfolding procedure includes detector effects and also the smearing caused by background fluctuations. In the matrix representation, a perfect detector and no background fluctuations would produce a 1-matrix with vanishing off-diagonal elements. While the unfolding of detector response and background fluctuation matrices can principally be carried out separately, it is more convenient to combine both matrices in one response matrix through matrix multiplication so that the unfolding is only performed once. The total response matrix is given by

$$R = F \times D, \quad (6.16)$$

where F represents the background fluctuations and D the detector response. Measured and true spectra are connected by

$$y_{\text{measured}}^* = (F \times D) y_{\text{true}}. \quad (6.17)$$

Here, y_i are the measured/true jet transverse momentum distributions. In this representation, y_{measured}^* is the measured distribution without background, i.e. background-corrected. However, the distribution contains the background fluctuations though. Note that the order of the matrices in the multiplication is not arbitrary. Roughly speaking,

the fluctuations matrix F has to be applied on jets which have already been smeared by the detector response matrix.

As a side note it should be mentioned that, principally, the full background correction can be done with the help of unfolding. In this case, the complete background distribution and not only its fluctuation is considered in the modified smearing matrix F^* . Eq. 6.17 which describes the connection of true and measured spectrum would then turn into

$$y_{\text{measured}} = (F^* \times D) y_{\text{true}}. \quad (6.18)$$

The measured distribution y_{measured} would contain background in this representation. However, this procedure is not taking into account event-by-event fluctuations of the background but treats it only statistically. Therefore, using event-by-event background density subtraction is preferred.

The predominant contribution to the response matrix is given by the detector response. It is evaluated for a PYTHIA-generated jet sample that has been propagated through a full detector simulation with GEANT. *Particle-level* information are available from PYTHIA, GEANT generates *detector-level* information using a detailed model of the ALICE detector. Particle-level jets are jets as they would be seen by a perfect detector, detector-level jets include all detector effects.

Both jet collections are matched by calculating the distance between the jets following a geometrical approach. This connects the true, particle-level jet and the reconstructed, detector-level jet. After applying the background correction, the transverse momenta of the matched jets are used to fill the response matrix. The background correction is done for consistency and, thus, the default p-Pb approach is applied.

For the present analyses, two types of response matrices were created: one for the unfolding of 7 TeV pp, one for 5 TeV p-Pb jets. The focus of this thesis is clearly on the p-Pb analysis and, therefore, all plots included for illustration purposes show the version for p-Pb collisions. Qualitatively, the matrices do not differ for pp and p-Pb collisions, because both are created by PYTHIA and are therefore pp simulations.

The utilized PYTHIA-generated jet sample was created for 10 $p_{\text{T, hard}}$ bins (cf. Sec. 5.4.1). For every $p_{\text{T, hard}}$ -bin, roughly one million events were generated, adding up to altogether ten million events. In pp, the tune Perugia-0 with $\sqrt{s} = 7$ TeV has been used. For p-Pb collisions, the generator utilized the Perugia 2011 tune with $\sqrt{s_{\text{NN}}} = 5.02$ TeV. A Lorentz boost which is connected to the asymmetry of the collision system is taken into account. That the detector response in p-Pb is also modeled with PYTHIA jets – i.e. corresponding to pp collisions – can be understood when considering Eq. 6.17: The detector response D must be defined for bare (background-corrected) jets. This condition is fulfilled for PYTHIA-generated jets.

Note that the different tunes have not been selected intentionally, but because of the

availability of the simulations: While the 5 TeV simulations have been created for jet analyses in p-Pb, the 7 TeV data already existed before. Full detector simulations require a huge amount of computing power and the differences on the response matrix introduced by using different tunes is expected to be very small. Therefore, a new simulation dataset was not produced.

Technically, the detector response matrix is created separately for every $p_{T, \text{hard}}$ -bin. To merge the matrices to one full detector response matrix, the single matrices have to be scaled according to the average jet production cross section of the $p_{T, \text{hard}}$ bins and the number of events, in which PYTHIA was executed, using the scaling factor

$$c = \frac{\sigma(p_{T, \text{hard}})}{N_{\text{events}}}. \quad (6.19)$$

The cross section for the specified $p_{T, \text{hard}}$ bin is directly obtained from PYTHIA.

The second contribution to the response matrix is the smearing matrix, which corresponds to the distribution of background fluctuations δp_T . This smearing matrix is created drawing on the δp_T distribution calculated for the whole event sample assuming that the background fluctuations are independent of jet transverse momentum.

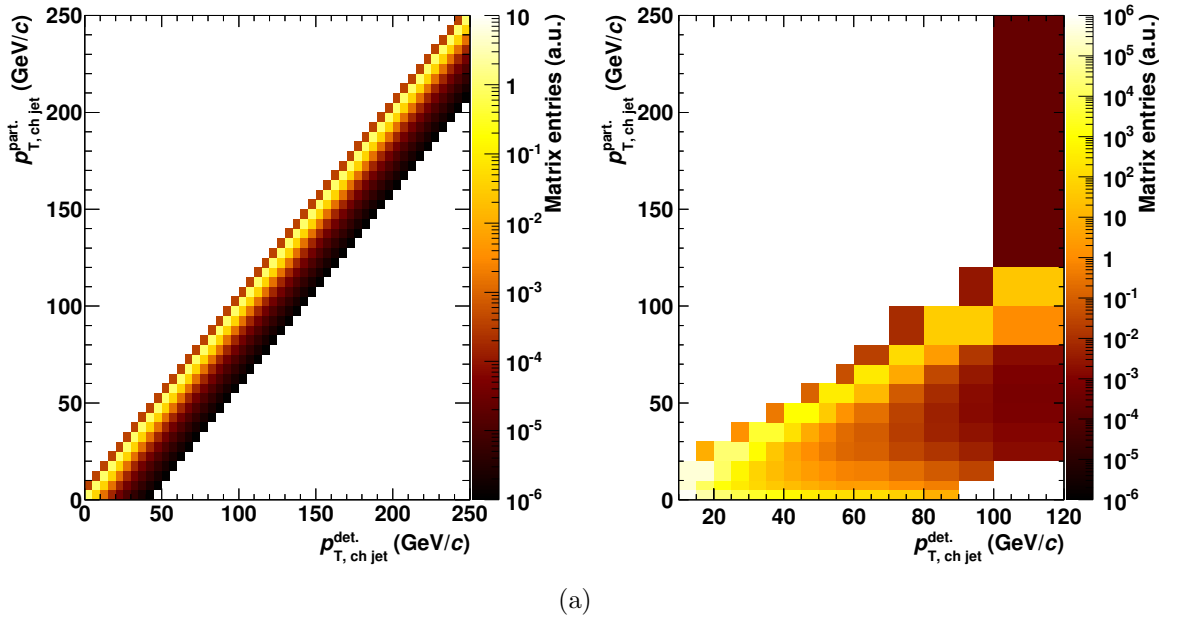


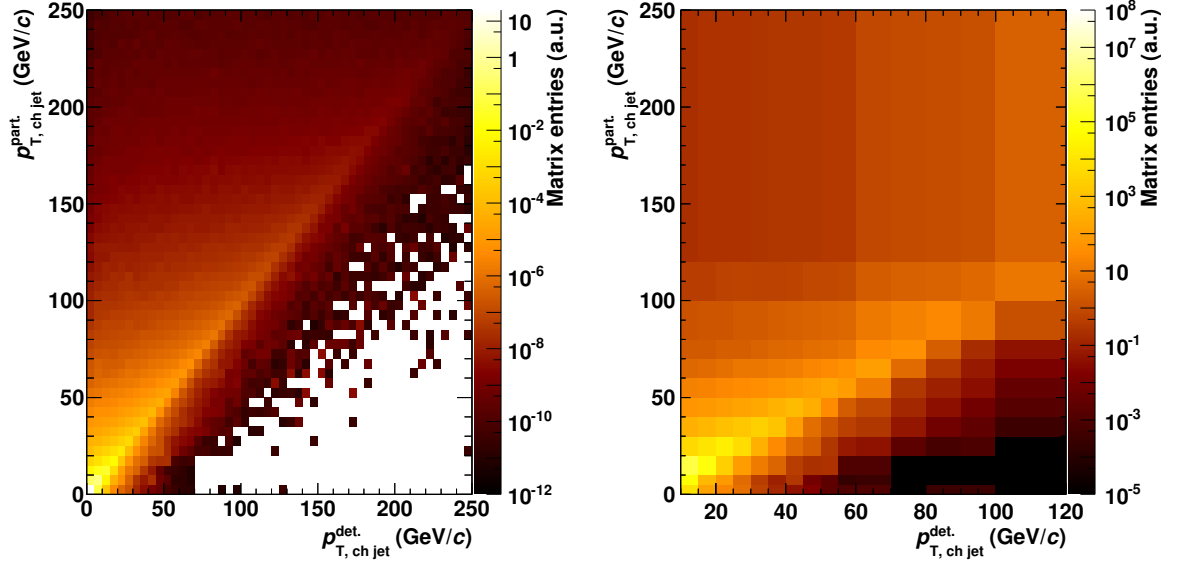
Figure 6.12: Response matrices corresponding to background fluctuations. The right plots are rebinned and reweighted versions of the left plots (see text).

Technically, the matrix is constructed by inserting the one-dimensional δp_T distribution to all slices in particle-level jet transverse momentum. The distribution is shifted by the $p_{T, \text{ch jet}}^{\text{part.}}$ according to the single slices. This guarantees the correct behavior of the smearing matrix: If the δp_T distribution were a δ function, the matrix would simplify to the unit matrix.

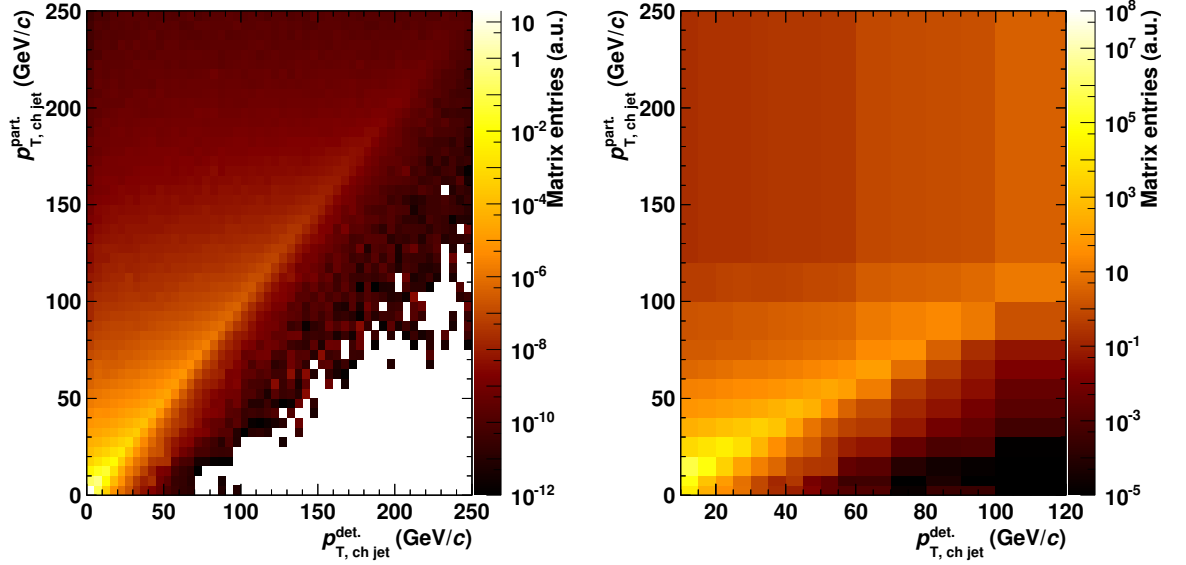
In Fig. 6.12 the background fluctuation matrix is shown. Figure 6.13 depicts detector response matrix and the combined matrix. The right-hand plots show the rebinned and reweighted versions of the left plots that has ultimately been used in the unfolding procedure.

The binning of the matrices have to be set according to the desired binning of the final unfolded spectrum and according to the binning of the measured spectrum, which is adapted to the spectrum fluctuations. Both binnings are given by the following sets:

- Unfolded: $\{0, 5, 10, 20, 30, 40, 50, 60, 70, 80, 100, 120, 250\}$
- Measured pp & p-Pb: $\{10, 15, 20, 25, 30, 35, 40, 45, 50, 55, 60, 70, 80, 90, 100, 120\}$



(a) Detector response matrix



(b) Combined response matrix

Figure 6.13: Response matrices. It is the combined matrix in (b) which is finally used. The right plots are rebinned and reweighted versions of the left plots (see text).

The reweighting procedure renormalizes the matrices so that the projection on the $p_{T, \text{ch jet}}^{\text{part.}}$ -axis is normalized to the *prior distribution*. This distribution should be as similar as possible to the true jet spectrum. It is also used in all unfolding algorithms. In this thesis, the prior distribution is chosen to be a power-law fit of the measured

data. Since it is a priori not clear which prior to use, different prior steepnesses were taking into account for systematic uncertainties. By comparing the left and right plot in Fig. 6.12, the reweighting of the $p_{T, \text{ch jet}}^{\text{part.}}$ -axis to a steeply falling spectrum can be observed. The detector response already has by construction a very similar normalization and, therefore, the reweighting procedure is hardly visibly in Figs. 6.13(a), (b).

Reweightings is done before rebinning and it is necessary to correctly take into account the different “weights” of individual bins that are combined to a larger bin. Consider for example a response matrix with two bins between 50 and 60 GeV/ c on both axes which are combined to one bin. The rebinning combines 2×2 bins in one large bin. This bin connects particle- and detector-level jets for 50-60 GeV/ c . Due to the steeply falling jet spectrum, the bin should predominantly describe the connection of the lower p_T jets in this bin.

However, in an unweighted response matrix, the influence of the 55-60 GeV/ c jets is in principle as strong as the influence of the 50-55 GeV/ c jets. The reweighting introduces the weighting of the jets according to the probability to find them with the given transverse momentum. This probability is determined by the prior distribution.

Eventually, the normalization is chosen so that the particular slices for a fixed $p_{T, \text{ch jet}}^{\text{det.}}$ exhibit a steeply falling spectrum. Alternatively, also the slices for a fixed $p_{T, \text{ch jet}}^{\text{part.}}$ can be normalized in this way instead.

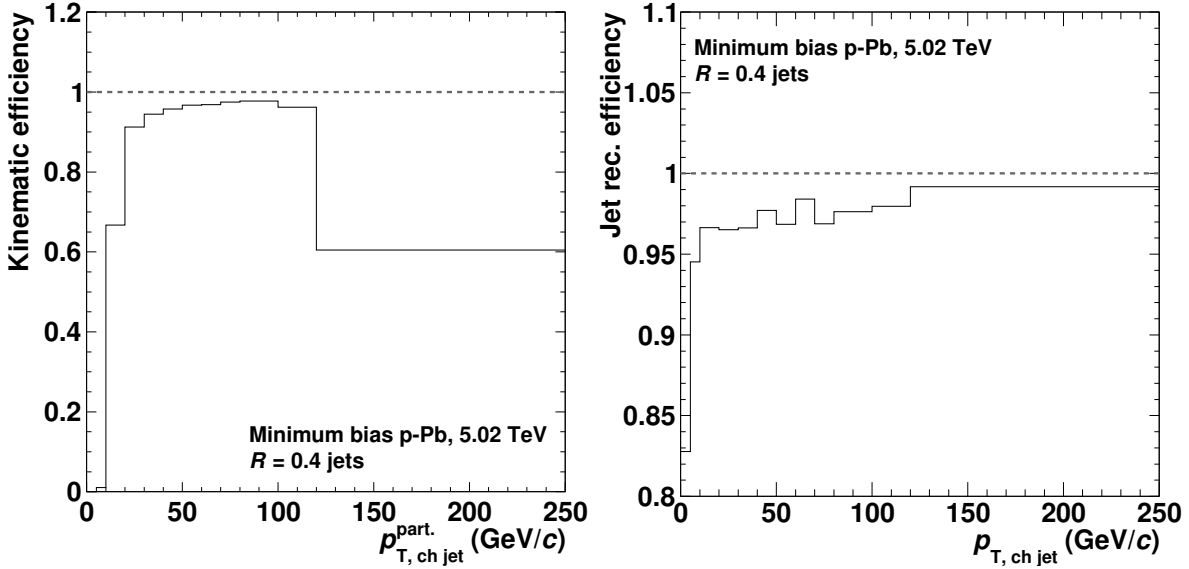


Figure 6.14: Kinematic efficiency (left) and jet reconstruction efficiency for p-Pb.

In the rebinning, the response matrices are also truncated according to the p_T range used for input. Therefore, a certain amount of jets is lost for a given particle-level jet p_T .

Roughly speaking, those jets would be reconstructed outside the transverse momentum acceptance of the analysis. An efficiency can be given by comparing to the particle-level/true jet p_T distribution. It is called kinematic efficiency and is corrected for in the unfolding process. In Fig. 6.14, the left-hand side plot shows the kinematic efficiency for the given binning and response matrix.

In this figure, also another efficiency is shown in the right plot: the jet reconstruction efficiency. It is obtained by comparing detector- and particle-level jet projections of the response matrix. It is corrected for after the full unfolding process has taken place.

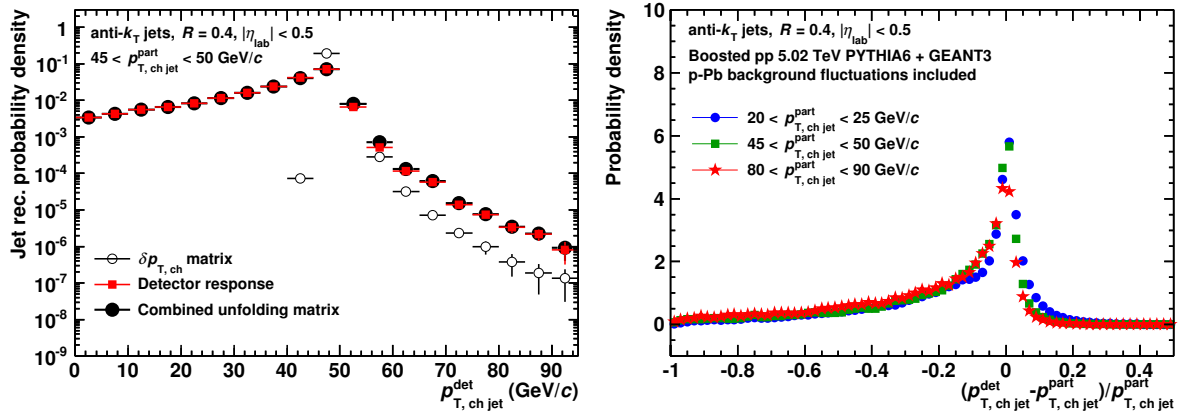


Figure 6.15: Left: Slice of response matrices for jets with particle-level momentum $45 < p_{T, \text{ch jet}}^{\text{part.}} < 50 \text{ GeV}/c$. Right: Probability distribution of the relative difference between particle-level and detector-level including background fluctuations for jets with different momenta. Characteristic values of the distributions are summarized in Tab. 6.2.

A more quantitative view on the response matrices showing the different contributions exemplary for jets between 45 and 50 GeV/c can be found in Fig. 6.15. The left-hand side of the plot shows the probability for the reconstruction of a jet in a given p_T range into a certain p_T bin. Additionally, the right-hand side represents the residuals $(p_{T, \text{ch jet}}^{\text{det.}} - p_{T, \text{ch jet}}^{\text{part.}})/p_{T, \text{ch jet}}^{\text{part.}}$ for several transverse momentum ranges. Here, $p_{T, \text{ch jet}}^{\text{det.}}$ also includes the background fluctuations.

The residual distribution is a descriptive measure of how and with which probabilities an incident particle-level jet is measured with a different transverse momentum. In Tab. 6.2 characteristic values for this distribution can be found.

From both plots in Fig. 6.15, it can be directly seen that the detector effects are causing more jets to be reconstructed with lower than with higher p_T . This is mainly for the reason of the finite single-particle tracking efficiency of the detector.

Table 6.2: Characteristic values for the distribution of residuals of the total charged jet response matrix shown in Fig. 6.15(b), including the effect of background fluctuations: most probable value determined in a Gaussian fit to the central peak region, first and second moment (mean and width σ), and quartiles. The precision of the quartiles is limited by the finite bin width of 0.01. In parentheses, the values are shown for the distribution without background fluctuations, i.e. the pure detector response.

$p_{T, \text{ch jet}}^{\text{part.}}$	20-25 GeV/ c	45-50 GeV/ c	80-90 GeV/ c
MPV (Gaussian Fit)	0.006 ± 0.002	-0.001 ± 0.002	-0.010 ± 0.004
	(0.007 ± 0.001)	(-0.003 ± 0.002)	(-0.013 ± 0.004)
Mean	0.149 ± 0.030	-0.181 ± 0.030	-0.222 ± 0.030
	(-0.163 ± 0.030)	(-0.188 ± 0.030)	(-0.226 ± 0.030)
Width σ	0.238 ± 0.030	-0.246 ± 0.030	-0.259 ± 0.030
	(0.233 ± 0.009)	(0.245 ± 0.005)	(0.258 ± 0.003)
Quartile, 25% above	0.01 ± 0.01	-0.01 ± 0.02	-0.01 ± 0.02
	(0.01 ± 0.01)	(-0.01 ± 0.02)	(-0.03 ± 0.02)
Quartile, 50% above	-0.05 ± 0.04	-0.09 ± 0.01	-0.13 ± 0.04
	(-0.07 ± 0.04)	(-0.09 ± 0.04)	(-0.13 ± 0.04)
Quartile, 75% above	-0.25 ± 0.06	-0.29 ± 0.05	-0.37 ± 0.04
	(-0.27 ± 0.04)	(-0.29 ± 0.06)	(-0.37 ± 0.04)

6.2.3. Regularization parameter analysis

Except for the manual correction method, all unfolding algorithms need a regularization parameter. This parameter specifies how strong the final result is regularized. The optimum parameters depend on the measured distribution and have to be evaluated individually for all algorithms.

For the SVD unfolding, the regularization parameter has to be an integer value. The optimum parameter is determined according to the procedure described in [Hö96]: An artificial truth distribution is created that is expected to be similar to the unfolded distribution. A power-law distribution was used. The true distribution is folded with the full response matrix and statistically varied according to the statistical uncertainties of the measured jet spectrum. The obtained distribution is expected to behave like the measured jet distribution. This procedure creates a variable toy distribution that has also been used for other purposes.

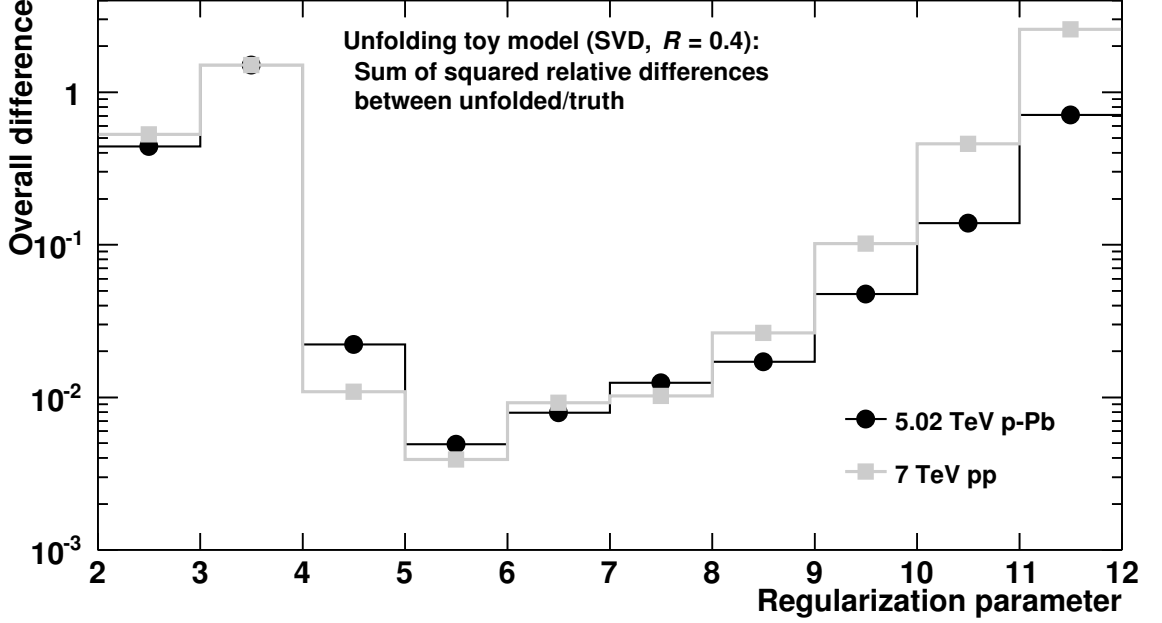


Figure 6.16: Quadratic differences of SVD-unfolded and true jet distribution for different regularization parameters.

By comparing the unfolded and initial true jets, the quality and validity of the unfolding settings can be estimated. A perfect unfolding technique should perfectly reconstruct the initial true jets. The optimum regularization parameter is expected to be the one yielding the smallest deviation between unfolded and true distribution. The corresponding analysis is done for p-Pb and 7 TeV pp jets. For both systems, the regularization parameter $\tau = 5$ is the optimum choice. For illustration purposes, the quadratic differences for varying regularization parameters are shown for p-Pb and pp in Fig. 6.16. Additionally, the ratio unfolded over truth is explicitly shown for three different regularization parameters in Fig. 6.17 together with the corresponding Pearson matrices. The result is consistent with the expectations from [Hö96]: A very small regularization parameter overregularizes the spectrum, a very large parameter shows strong fluctuations caused by a too weak regularization.

The Pearson matrices are shown for illustration purposes. They are a measure for the correlation of the unfolded spectrum. The Pearson coefficients – the entries of the matrix – are given by

$$P_{ij} = \frac{\text{Cov}(i, j)}{\sigma_i \sigma_j}. \quad (6.20)$$

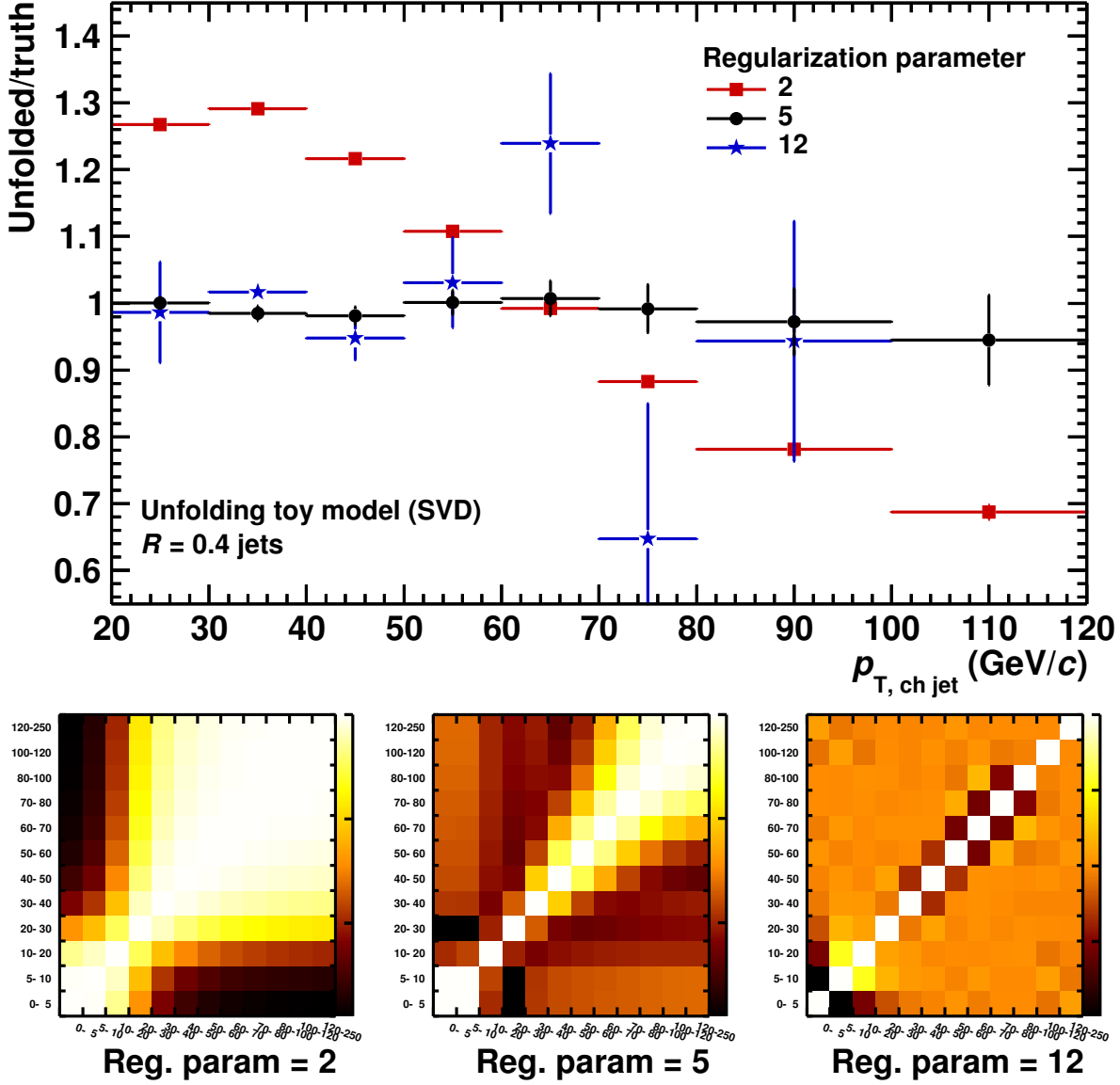


Figure 6.17: Upper panel: Ratios of SVD-unfolded and true jet distribution. The unfolded distribution is created by a toy model (see text). Lower panel: Pearson coefficients.

Note that this procedure gives only a rough estimate for the optimum regularization parameter. Therefore, the variation of the regularization parameter is considered for systematic uncertainties.

For χ^2 -unfolding and Bayesian unfolding, the optimum regularization parameters/number of iterations are evaluated by checking the Pearson coefficients like it was done in [Ver13].

Results from the unfolding toy model initially used for the SVD regularization parameter estimation have also been taken into account. The optimum regularization turns out to be the same in pp and p-Pb. The optimum count of iterations for the Bayesian method is $k = 3$ and the weight for the penalty term of the χ^2 -unfolding is chosen to be 0.1. In Fig. 6.18, the matrices with the Pearson coefficients for real p-Pb data are included by way of illustration. They look similar for the toy model and for pp data (not shown). Note that the correlations for the lowest bins are expected since no data is passed to the unfolding in that p_T region – of course, those bins are not used.

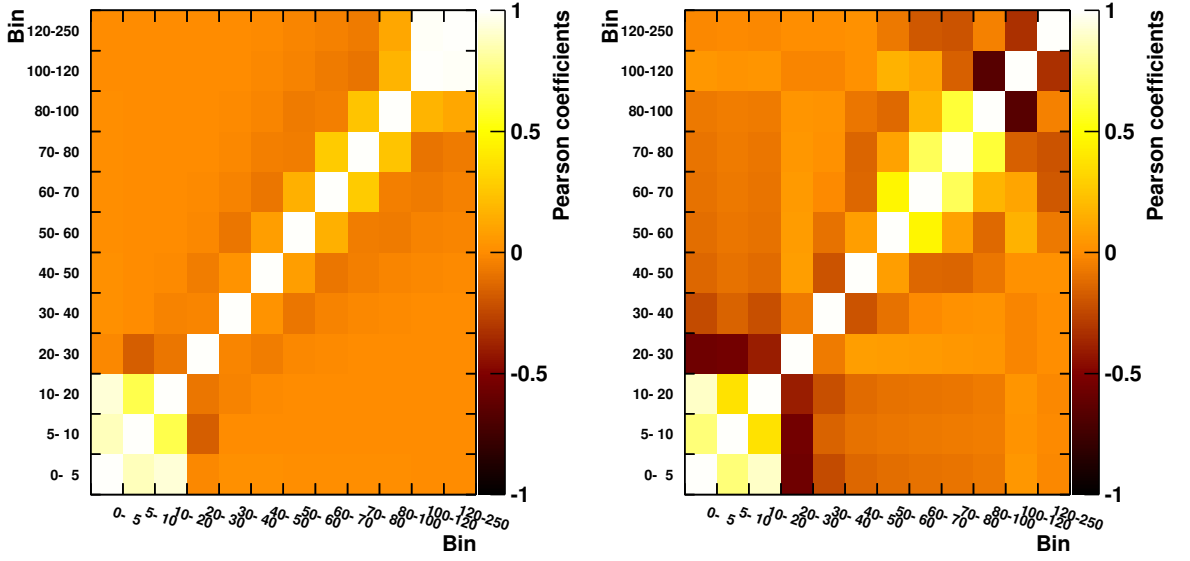


Figure 6.18: Pearson coefficients for Bayesian (left) and χ^2 -unfolding (right) for the optimum regularization parameter on real p-Pb data.

6.2.4. Comparison and conclusion

In the following section, the results of the different unfolding methods are compared. All parameters, like binning and regularization, are chosen in the way they have been described in the preceding sections.

The purpose of this section is rather to validate the unfolding settings and parameters than to evaluate the systematic uncertainties for the unfolding method. Systematic uncertainties are dealt with in Chapter 9.

In Fig. 6.19, results from the unfolding toy model are shown. In the previous section, the toy model was applied to evaluate the best regularization parameters. It can also be used to check the general validity of the unfolding implementations and their quality.

It can be seen that the SVD method yields the best results with minimal fluctuations compared to the truth, but all other unfolding methods as well produce reasonable results that differ by up to roughly 10% in the full transverse momentum range from 20 to 120 GeV/ c . A slightly stronger deviation is observed for the Bayesian-unfolded spectrum though.

Note that even the manual unfolding method without any explicit regularization produces similar results compared to the other unfolding methods.

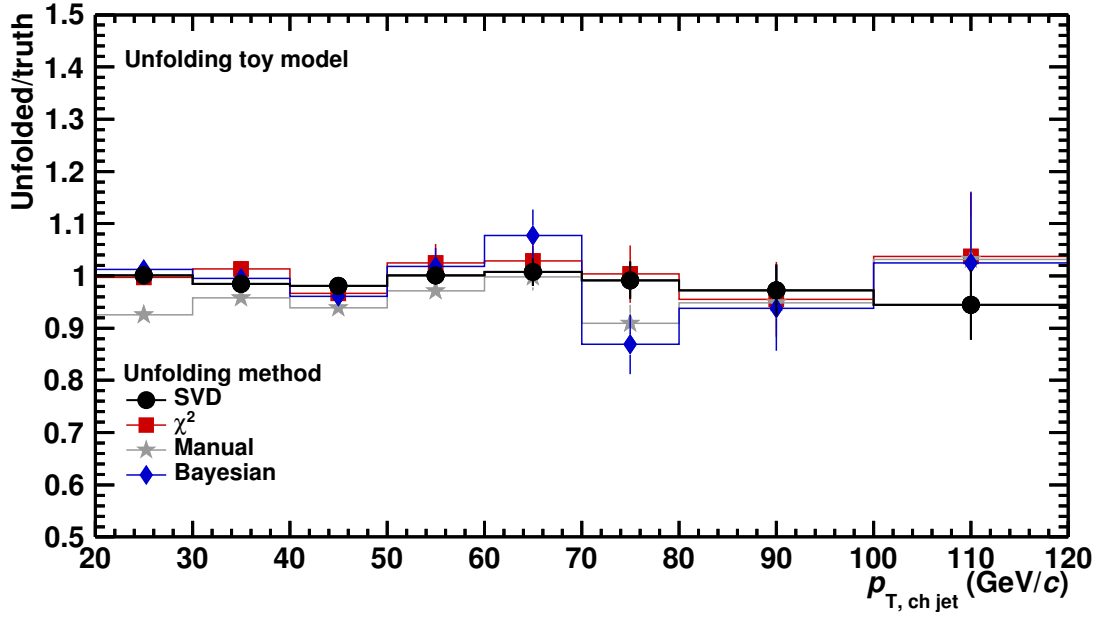


Figure 6.19: Unfolded over truth ratio for several unfolding methods using the toy model.

In Figs. 6.20 and 6.21, the results from the different unfolding methods are directly compared to the SVD solution for real data used in this thesis.

For both collision systems, pp and p-Pb, the agreement of all methods including the naive manual approach is very good. The overall differences are of the order of a few percent for the full p_T range between 20 and 120 GeV/ c . The strongest deviation is seen for the last p_T bin, which is most affected by fluctuations due to the small number of jets in this bin.

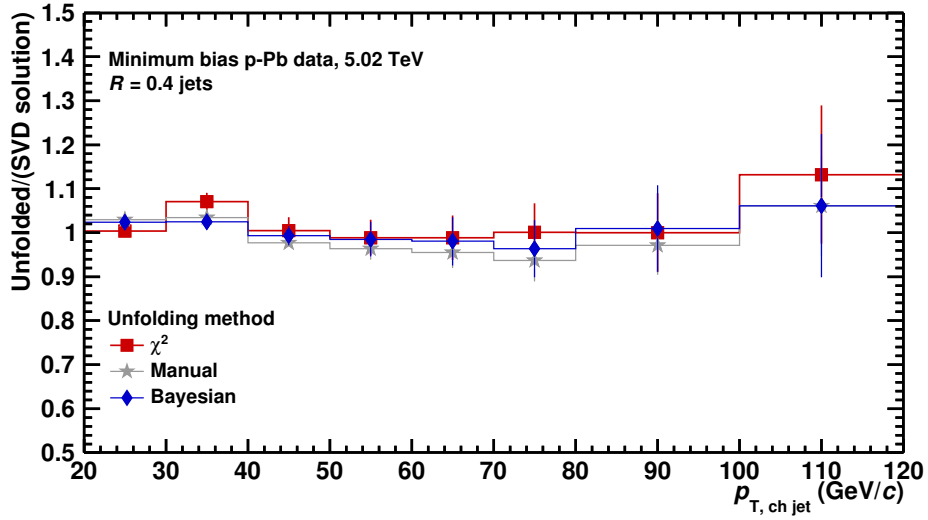


Figure 6.20: Ratio of several unfolded solutions and the baseline SVD solution. Real p-Pb data is used.

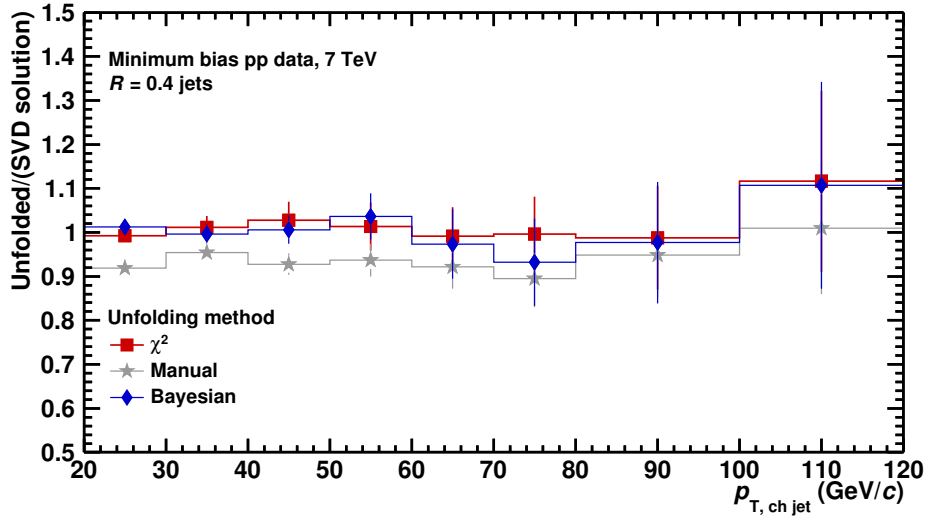


Figure 6.21: Ratio of several unfolded solutions and the baseline SVD solution. Real pp data is used.

As another sanity check for the baseline SVD method, the ratio of refolded and measured spectra can be considered. The refolded spectrum is the unfolded spectrum folded with the full response matrix used in the unfolding. Both spectra, refolded and measured, have to agree within uncertainties if the unfolding procedure is successful. Indeed, for p-Pb and pp the refolded/measured spectra ratio shows reasonable values, as can be seen in the bottom panels of Fig. 6.22. In the same figure, the measured, unfolded, and refolded spectra are shown for illustration. Note that the error bars only represent the statistical and not the systematic uncertainties.

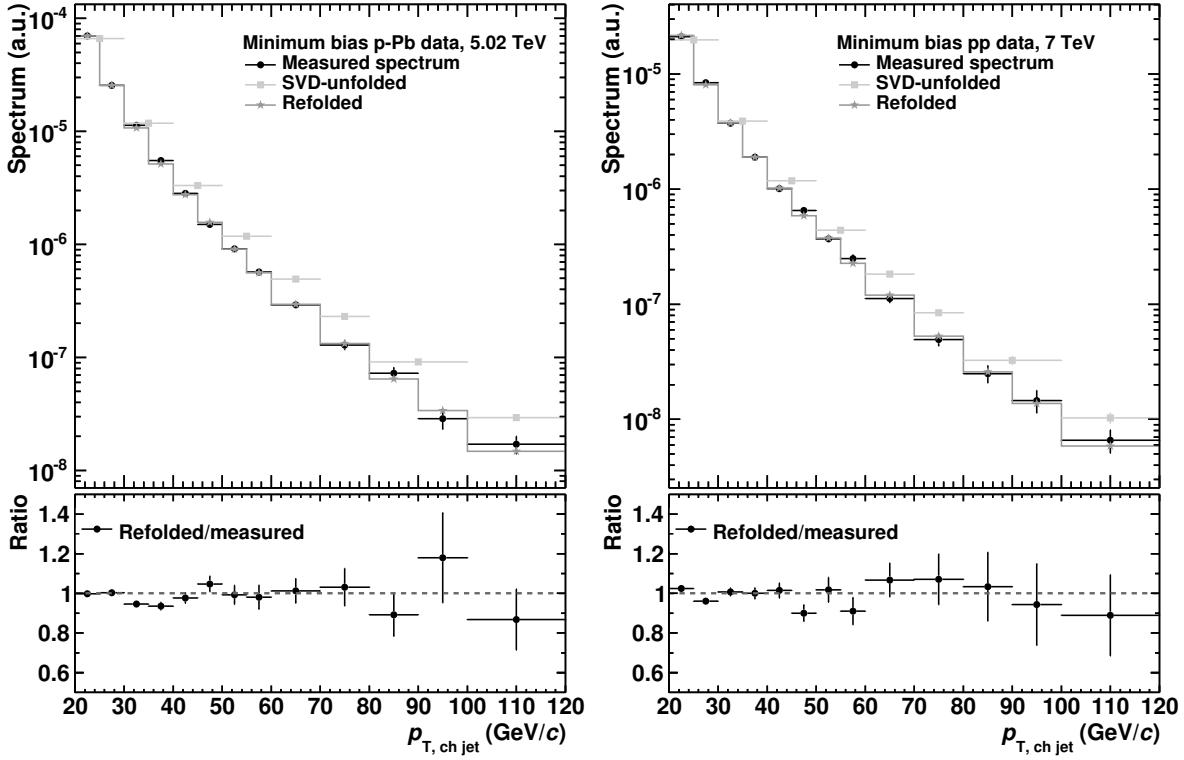


Figure 6.22: Measured, unfolded, and refolded spectrum for p-Pb (left) and pp (right) using the default SVD unfolding. The bottom panels show the refolded/measured ratios as an indicator that the unfolding actually worked.

To conclude, the analyses reveal that the unfolding procedure is reliable, regardless of whether SVD, χ^2 -unfolding, or Bayesian unfolding is used. Even the manual unfolding method yields only slightly deviating results. This observation holds for 5.02 TeV p-Pb and 7 TeV pp data. Additionally, a toy model was used to validate the methods. Bayesian-unfolded results seem to be most affected by fluctuations compared to the other methods; the results are compatible though.

7. Data sample

In this chapter, the data selection criteria are presented. After characterizing the datasets used in this thesis, the event selection is described for pp and p-Pb data. A detailed definition of the tracks as the basic jet constituents follows. At last, the applied cuts on the jets are discussed.

7.1. Utilized datasets

For this thesis, several datasets have been analyzed: Monte Carlo simulations for cross checks, predictions, and correction techniques, ALICE datasets for the main analyses of charged jets in p-Pb and – mainly for the calculation of the reference of the nuclear modification factor R_{pPb} – in pp.

Basic properties and settings of the Monte Carlo simulations used for this thesis can be found in Sec. 5.4. The most important simulated datasets are the full detector simulations using the PYTHIA6 event generator and GEANT3.

Two datasets with detector-level simulated jets are employed for this thesis: one dataset for 5.02 TeV, one for 7 TeV. Both are simulated at energies at which the p-Pb and pp data was taken. These datasets also contain full particle-level information and are used to create the response matrix (see Sec. 6.2.2).

For the creation of the p-Pb response, a production generated with tune Perugia 2011 and a center-of-mass (cms) energy of $\sqrt{s_{\text{NN}}} = 5.02$ TeV has been processed. In total, the production consists of ten million jet-jet events, divided into ten bins of $p_{\text{T, hard}}$. A Lorentz boost which takes into account the asymmetric per-nucleon energies in p-Pb collisions was applied. The dataset consists of two parts, of which one is anchored in a run of the data taking period LHC13b and one in a run of LHC13c to reflect a small difference in the detector configuration in both periods. LHC13b and LHC13c are the main data taking periods in p-Pb, see below. *Anchoring* describes that the detector and its configuration is modeled in the same way as in the specified run.

The ALICE-internal name of the dataset is LHC13b4_fix.

The pp response is created by processing a PYTHIA-generated full detector simulation at a nucleon-nucleon cms energy of 7 TeV using the Perugia-0 tune. This dataset is called LHC11a1 internally. Like in p-Pb, LHC11a1 was created in bins of $p_{\text{T, hard}}$ but with

five million jet–jet events in total. The dataset is anchored in a run from LHC10d.

The main data analysis is rest upon two datasets recorded with the ALICE detector. Both, p–Pb and pp collisions were analyzed in great detail. The main purpose of the proton–proton data is the calculation of the reference spectrum for the charged jet nuclear modification factor R_{pPb} .

First p–Pb collisions with $\sqrt{s_{\text{NN}}} = 5.02$ TeV took place in a pilot run at the end of 2012 to check if the accelerator and the whole data taking setup work as expected before the main p–Pb data taking period in the beginning of 2013. In this main data taking period, roughly 110 million minimum bias events were recorded. For the analyses in this thesis, some runs are excluded a priori for quality reasons. For instance, run 195390 was excluded because it was tagged as a bad run on the ALICE run condition table due to deactivated SSD, or run 195346 was excluded because of missing SDD information. Basic quality checks have been performed on the remaining runs, e.g. to validate that the spatial track distribution of the detector exhibits no dead regions in the detector or that the transverse momentum distribution looks similar for all runs. These checks also revealed the existence of two distinct runs types (see below).

Eventually, 107 million events have been processed for this analysis. Internally, the recorded p–Pb periods are called LHC13b and LHC13c. For the sake of completeness, the processed run numbers are listed here.

- LHC13b: 195344, 195351, 195389, 195391, 195478, 195479, 195481, 195482, 195483,
- LHC13c: 195529, 195531, 195566, 195567, 195568, 195592, 195593, 195633, 195635, 195644, 195673, 195675, 195677.

The utilized runs from the LHC13b period and those from LHC13c can be clearly distinguished by having a closer look on the track collections in both periods: the high-quality track distribution shows a much larger dip in azimuth for the data of period LHC13c than of period LHC13b (see the later Fig. 8.16). Since jets are composed of tracks including these high-quality and additional tracks, the resolution is in principle a bit worse in LHC13c. Track selection for jets is described in Sec. 7.3.

However, it turns out that the actual impact on the jet spectra is within statistical uncertainties (see Sec. 8.6) and, therefore, the full dataset is used throughout the whole analysis.

In concordance with earlier jet analyses, the runs are called good and semigood runs.

The pp dataset with collisions at $\sqrt{s} = 7$ TeV was recorded in the middle of 2010. Nearly 200 million selected events are processed for the present analyses. In contrast to p–Pb, no additional quality assurance (QA) was carried out for pp. As already stated above, the data have been analyzed by ALICE before and the run list is taken from the

corresponding analysis (cf. [Abe14a]). The run numbers for the pp periods LHC10d and LHC10e are given by

- LHC10d: 122374, 125023, 125085, 125097, 125100, 125101, 125134, 125139, 125140, 125156, 125186, 125296, 125630, 125632, 125633, 125842, 125843, 125844, 125847, 125848, 125849, 125850, 125851, 125855, 126004, 126007, 126008, 126073, 126078, 126081, 126082, 126088, 126090, 126097, 126158, 126284, 126285, 126351, 126352, 126359, 126403, 126404, 126405, 126406, 126407, 126408, 126409, 126422, 126424, 126425, 126432, 126437,
- LHC10e: 127712, 127714, 127718, 127719, 128495, 128498, 128503, 128504, 128505, 128507, 128605, 128615, 128621, 128677, 128678, 128777, 128778, 128820, 128823, 128824, 128833, 128835, 128836, 128843, 128850, 128853, 128855, 128913, 129512, 129513, 129514, 129599, 129639, 129641, 129652, 129653, 129654, 129659, 129667, 129960, 129961, 130157, 130158, 130179, 130519, 130601, 130608, 130696, 130704, 130793, 130798, 130799, 130834, 130840.

7.2. Event selection

Several criteria are applied to select events. First, the hardware trigger decides if a collision event is recorded or not. Second, pile-up events with multiple reconstructed collision vertices are discarded. Third, only events with collision vertices that fulfill certain restrictions are used.

7.2.1. Trigger

The minimum bias (hardware) trigger condition varies for p–Pb and pp datasets. An event is selected by the minimum bias trigger in p–Pb, if there is at least one hit in each of both V0 detectors. Internally, the trigger condition is called V0AND and it is represented by the numeric constant `AliVEvent::kINT7`. From a van-der-Meer scan, it is known that the cross section seen by this trigger is given by $\sigma_{V0} = 2.09 \pm 0.07$ b [Abe14c]. Furthermore, Monte Carlo studies indicate that the sample mainly consists of non-single diffractive (NSD) events and that the contribution of single diffractive and electromagnetic interactions is negligible. The employed trigger is not fully efficient for NSD events. This inefficiency only affects events without a reconstructed vertex, i.e. no particles produced at midrapidity. It is estimated to be 2.2% with large systematic uncertainties of 3.1% [Ada14].

For the considered 7 TeV pp data, an event is recorded and considered as a minimum bias event if there is at least one hit in one of the V0 detectors. Accordingly, the trigger is called V0OR. It is represented by the tag `AliVEvent::kMB`. The visible cross section

was measured and the trigger efficiency of the V0OR trigger was simulated by ALICE [Abe13c]. The total inelastic cross section is calculated using both quantities.

ALICE measured the visible cross section for the trigger utilized in pp to be 62.4 mb. The total inelastic cross section was calculated to be $73.2^{+2.0}_{-4.6} \pm 2.6(\text{lumi})$ mb with a trigger efficiency of $85.2^{+6.2}_{-3.0}\%$

For the centrality-dependent results in p–Pb, the same trigger condition is applied. Here, the minimum bias sample is subdivided with regard to centrality. Centrality selection is performed as described in Sec. 5.3.

7.2.2. Pile-up correction

For p–Pb collisions, events with multiple reconstructed vertices are excluded from the considered data sample. This is called pile-up correction and has only a very small impact: Only 0.146% of the trigger-selected events are characterized as pile-up events and discarded.

7.2.3. Vertex definition

For both datasets, all selected events must have a reconstructed collision vertex. The z -position along the beam axis is only allowed to be within $|z_{\text{vertex}}| < 10$ cm of the nominal interaction point. This is a quality cut to ensure that a major part of the event is contained in the acceptance. The underlying physics, i.e. the jet production, is not affected by z_{vertex} .

However, the demand for a vertex itself biases the data sample by discarding jet-less events without a vertex. Those events represent minimum bias physics and they have to be taken into account. Therefore, the number of events considered for the normalization of jet spectra are corrected for this number. Details can be found later in Sec. 8.1.

The applied vertex definition differs for analyses in p–Pb and pp. For p–Pb, a commonly defined vertex selection function (`AliAnalysisUtils::IsVertexSelected2013pA()`) is used. To pass the cut, the following conditions must be fulfilled:

- primary vertex has to be reconstructed with at least one contributor,
- primary vertex must be reconstructed using data from the SPD,
- if the vertex is reconstructed with the fallback vertex finder *VertexerZ*, the errors have to be small (see `AliAnalysisUtils::IsVertexSelected2013pA()`),
- deviation of the z -coordinate of the vertex has to be within 10 cm of the nominal interaction point.

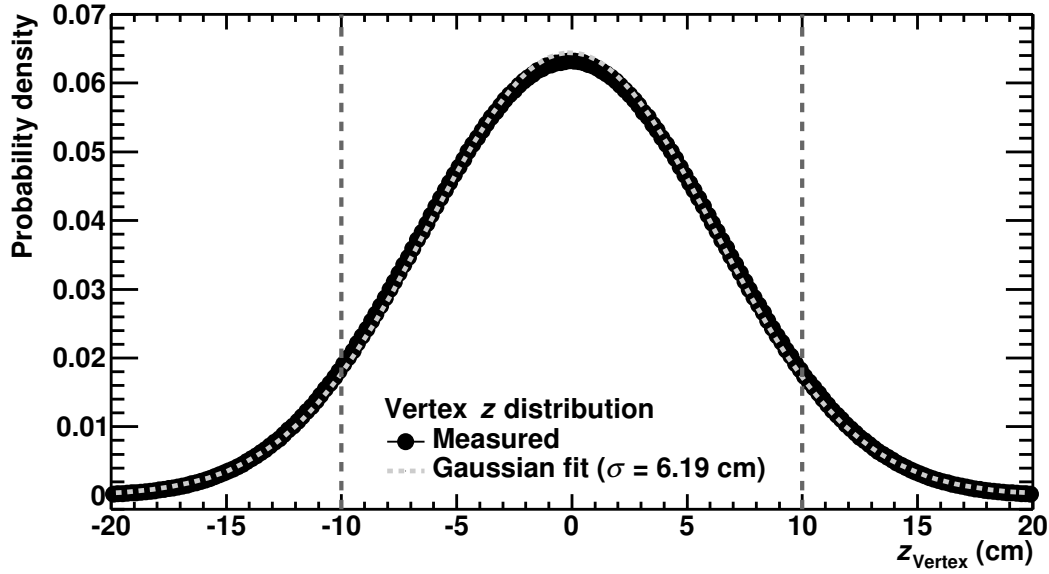


Figure 7.1: Distribution of the vertex displacement in z for p-Pb collisions.

Table 7.1: Number of events with and without vertex cut. The percentages are to illustrate the vertex acceptance rates.

Dataset	All events	pile-up corrected	with vertex	with vertex, $ z_v < 10$ cm
p-Pb	107.10M	106.94M (100%)	105.17M (98.3%)	93.96M (87.9%)
pp	197.44M	197.44M (100%)	161.70M (81.9%)	144.21M (73.0%)

In pp, the same definition as for the corresponding ALICE analysis [Abe14a] was applied, given by:

- primary vertex has to be reconstructed with at least two contributors,
- radial deviation of the primary vertex r is within 1 cm of the nominal interaction point,
- deviation of the z -coordinate of the vertex has to be within 10 cm of the nominal interaction point.

In Tab. 7.1, the number of events for different cut stages is given. Note that the fractions differ significantly in pp and p-Pb. For illustration purposes, the vertex distribution can be found for p-Pb collisions in Fig. 7.1.

7.3. Track selection

Tracks are the sole constituents of charged jets. Which tracks are considered for jet finding and how they are constructed decides on validity and quality of the jets. In Sec. 5.1, the track reconstruction with the ALICE detector is described in detail. However, in order to successfully use these tracks for jet finding, several further steps are necessary.

First, the tracks suffer from acceptance effects. Depending on the vertex position, tracks can be reconstructed for pseudorapidities up to $|\eta| < 1.4$. The efficiency falls steeply in the outer η regions though. Therefore, tracks are only accepted, if they are reconstructed within $|\eta| < 0.9$ where the efficiency is relatively uniform, see Fig. 7.2. In addition, due to the steeply falling tracking efficiency for very low track transverse momenta, the minimum track p_T must be $p_{T, \min} > 0.150$ GeV/c. These two cuts have been used in several ALICE jet analyses.

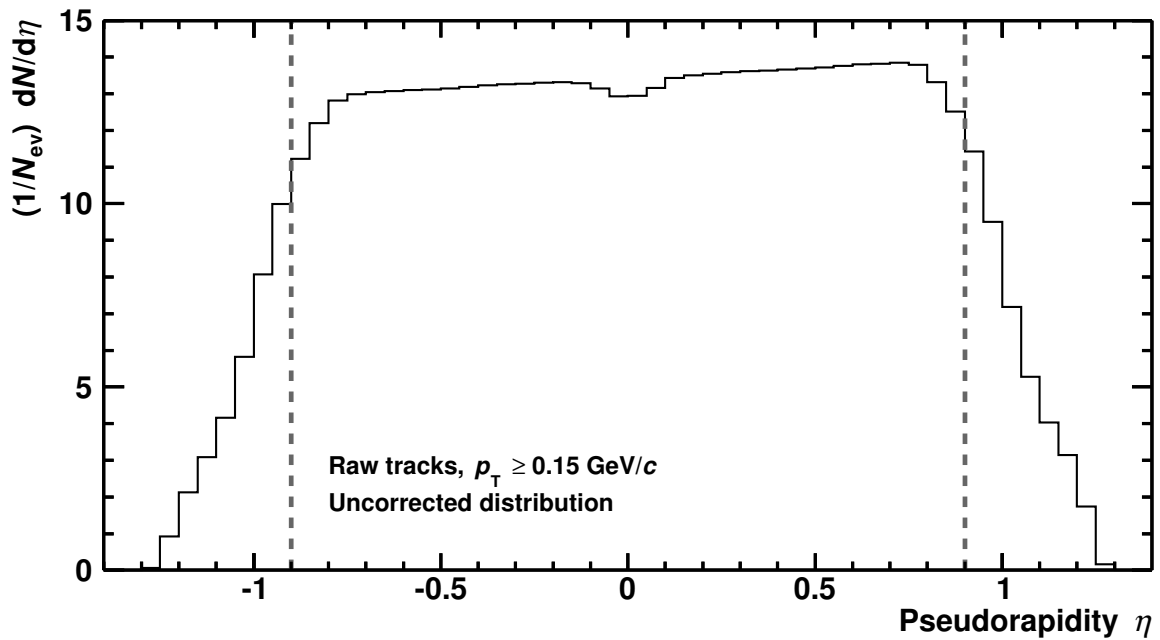


Figure 7.2: Pseudorapidity distribution of raw hybrid tracks in p-Pb collisions (see text). The dotted lines indicate the applied cuts. Errors bars are not shown.

Second, the tracking efficiency for high-quality tracks is not completely uniform in the $\eta - \varphi$ plane. This can be ascribed to detector inefficiencies that might vary between two runs. A non-uniform track distribution can lead to “edge effects” of the jet distribution in the corresponding regions: The pseudorapidity distribution of the jets and thereby the clustering of the jet finder is affected by these inefficient regions. To overcome this

problem, the hybrid track concept is introduced: The tracks passed to the jet finding algorithm are composed of two track types, high-quality tracks and additional tracks without ITS refit or hit in the SPD (cf. Sec. 7.3.1 for all cuts).

If a track does not fully meet the requirements of a high-quality track (also called global track), it is accepted as a complementary track without ITS refit or hit in the SPD, if possible. This procedure guarantees a quite uniform track distribution, see Fig. 7.3. The large “holes” in the global track distribution can be explained because parts of the SPD were turned off. Note that the usage of the hybrid tracks is a common feature of all ALICE jet analyses, cf. e.g. [Abe13d, Abe14b, Abe14a].

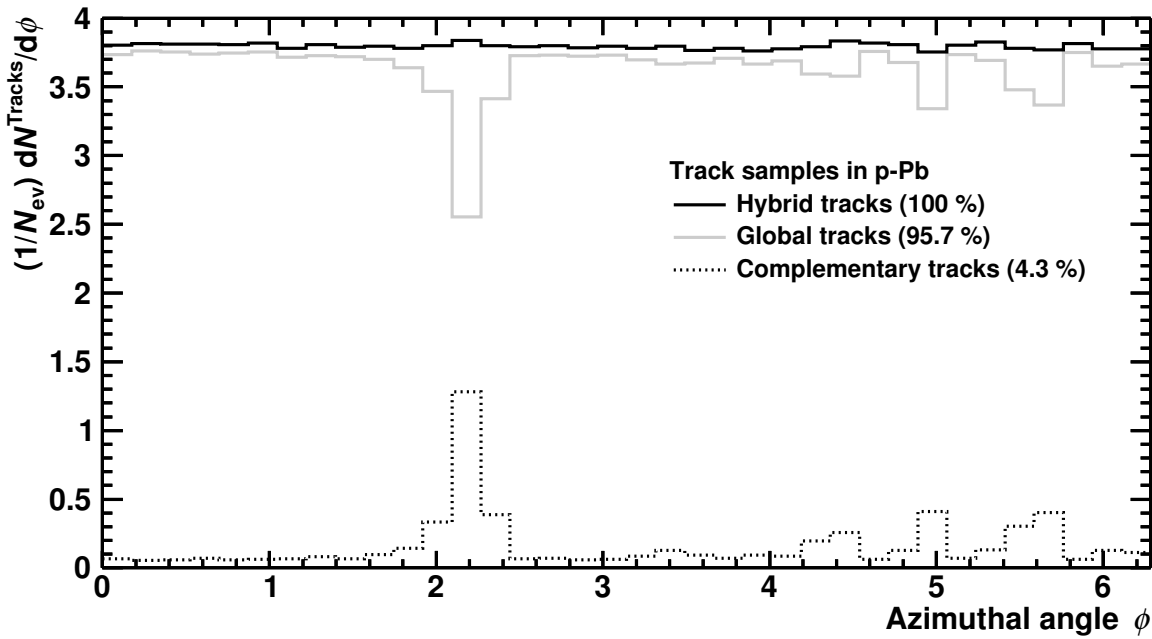


Figure 7.3: Azimuthal distribution of different track samples in p–Pb collisions.

7.3.1. Track cuts

The chosen track cuts are commonly used by the ALICE jet working group on the utilized datasets. As described in the last section, the tracks principally consist of two sets: global and complementary tracks. At the time when the pp data was taken and the corresponding jet analysis took place, the track cuts were slightly different from the cuts used in the recent p–Pb analysis. In Tab. 7.2, all cuts are listed and described in detail.

Table 7.2: Cuts applied in track cut definitions for global and complementary tracks in pp and p–Pb. The right column indicates for which tracks and collision systems the cuts apply.

Cut values and description	p–Pb	pp	global	compl.
Minimum number of TPC crossed rows: 70 Minimum ratio crossed rows/findables: 0.8 <p>The pads at the end caps of the TPC are arranged in rows relative to the beam axis. In total, 160 rows contain sensor pads. A “crossed row” means that clusters in two pads directly next to a row are reconstructed. The number of crossed rows thus corresponds to the amount of information the track encoded into the ion trace in the TPC on at least partly continuous lines. This cut guarantees that the tracks have a minimum quality. It rejects for example tracks with strongly overestimated p_T as a result of too few information available from the TPC.</p> <p>Connected to this cut is the requirement that at least 80% of the theoretically findable rows (known from trajectory) are found as crossed rows. This rejects tracks poorly reconstructed in the TPC.</p>	✓		✓	✓
Minimum number of TPC clusters: $70 + 1.5p_T, p_T < 20 \text{ GeV}/c$, $100, p_T \geq 20 \text{ GeV}/c$ <p>This cut is in principle another version of the preceding crossed-rows cut. It also rejects poorly reconstructed tracks in the TPC. For low transverse momentum tracks, the minimum number of clusters is p_T-dependent. Above $p_T > 20 \text{ GeV}/c$, generically at least 100 clusters are required for a track to pass this cut.</p>		✓	✓	✓

Cut values and description	p-Pb	pp	global	compl.
TPC refit: required During the third phase of the tracking procedure, the tracks are reconstructed inwards from the outer side of the central detector barrel to the primary vertex. This procedure is a refit, which uses the TPC and ITS clusters found in previous stages of the reconstruction. Tracks with succeeded TPC and ITS refit have significantly better momentum resolution. A TPC refit is required for all tracks.	✓	✓	✓	✓
Maximum fraction of shared TPC clusters: 40% Mainly to reject multiple reconstructed versions of one physical track, a track is only allowed to share a certain percentage of its TPC clusters with another track.	✓	✓	✓	✓
Allow kinks: no Tracks that show a kink in their trajectories, e.g. those that originate from a decay, are discarded.	✓	✓	✓	✓
Maximum χ^2 for TPC clusters: 4 Maximum χ^2 for ITS clusters: 36 To ensure that a track is reconstructed with a good accuracy, a strong agreement between the track curve and its associated detector clusters is demanded. As a measure for the agreement, χ^2 values between track curves and clusters can be calculated. Those values are normalized to the number of ITS or TPC clusters. This cut is imposed for ITS and TPC clusters.	✓	✓	✓	✓

Cut values and description	p-Pb	pp	global	compl.
Maximum χ^2 for vertex-constrained tracks: 36 The agreement of the normal track itself and a version using only TPC information and the assumption that the track originates from the primary vertex should be high for good quality tracks. The explicit definition can be found e.g. in [Ver13] and depends on the track parameters and covariance matrices.	✓	✓	✓	✓
Maximum DCA to vertex z: 3.2 cm Maximum DCA to vertex xy-plane: 2.4 cm One constraint for the tracks we are interested in is that the corresponding particle was created in the primary collision vertex. Therefore, the reconstructed track must start in or near the reconstructed primary vertex. This cut rejects many material-generated background particles and also secondaries of weak decays. Technically, the smallest distance between the track curve and the primary vertex is evaluated for the z -direction (along the beam) and in the xy -plane with a <i>distance of closest approach</i> (DCA) technique. Due to differing resolutions in z and xy , the procedure is split. The cut is on the distances of closest approach in both dimensions.	✓	✓	✓	✓
ITS refit: required The ITS refit cut is introduced for the same reasons as the TPC refit cut: in order to improve the momentum resolution of the tracks.	✓	✓	✓	
Minimum hits in SPD: 1 A hit in the SPD, which is very close to the interaction point, improves the momentum resolution of the reconstructed tracks.	✓	✓	✓	

7.4. Jet selection

Not all jets, which have been found by the jet finding algorithm, are considered for further physics analysis. In general, three cuts are applied on raw jets, directly after the jet finding.

First, only jets whose axes are within a certain pseudorapidity interval are accepted. Jet axes are defined using the p_T -weighted directions of the constituent particles. These cuts avoid edge effects (see Fig. 7.4(b)) from the jet finding algorithm introduced by the finite acceptance of the detector in pseudorapidity. Exploiting the very regular shape of anti- k_T jets, the cut values are chosen in such a way that all theoretically expected jet cones fit just into the acceptance.

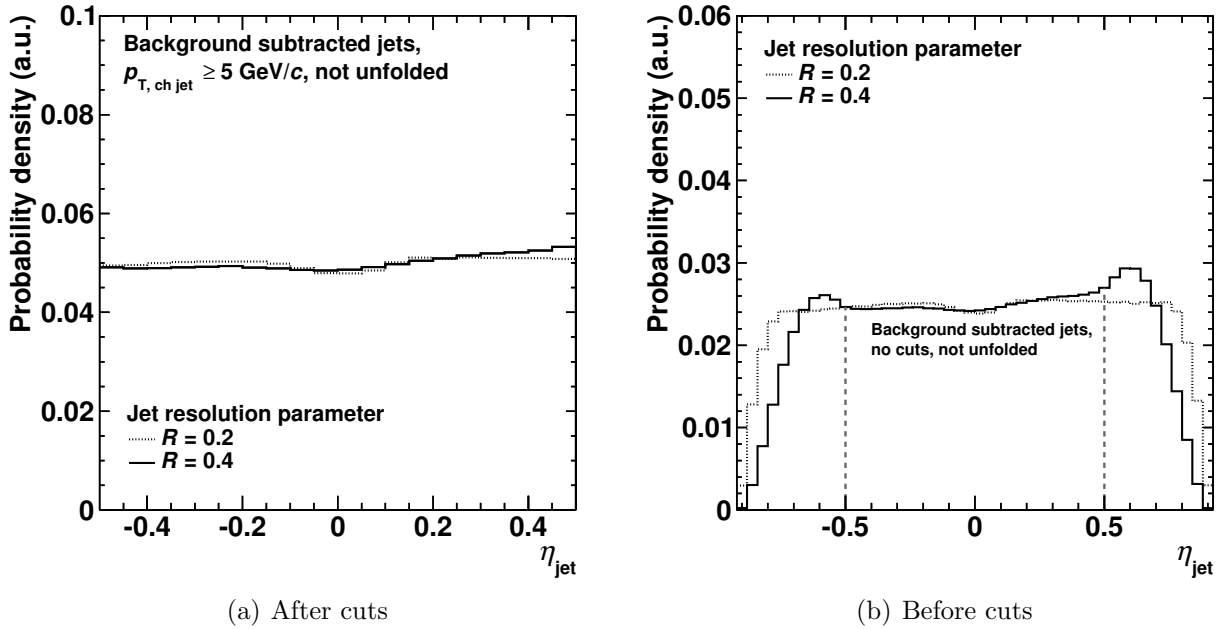


Figure 7.4: Jet pseudorapidity distribution after (a) and before (b) cuts. Note that the binning is different. The dotted lines in the right-hand plot represent the η cut.

In order to consistently select jets from the same η interval, the cut is the same regardless of the jet radius/resolution parameter: $|\eta_{\text{jet}}| < 0.5$. This allows jets with radii up to $R = 0.4$ to be fully contained within the acceptance. The drawback of a common η cut for several resolution parameters R is that a large number of fully-contained jets is not used for $R = 0.2$. Additionally, it has to be noted that although the jet pseudorapidity acceptance is the same for both resolution parameters $R = 0.2$ and $R = 0.4$, the particle acceptance is different: While jets with $R = 0.4$ contain particles from $\eta < 0.9$, jets with

$R = 0.2$ effectively contain particles only from $\eta < 0.7$. Since the jets are dominated by particles near their axes, it was decided to rather keep the acceptance of the jet axes consistent than the acceptance of the particles.

Though the dip around $\eta = 0$, which is already visible for the tracks, is slightly stronger for jets with $R = 0.2$, the pseudorapidity distributions look very similar for $R = 0.2$ and $R = 0.4$, see Fig. 7.4(a). Note that the distribution in Fig. 7.4(a) is normalized to one. The same normalization was applied to Fig. 7.4(b) for comparability. Beyond the chosen acceptance, the above mentioned edge effects are clearly visible.

The second cut is on the jet transverse momentum. This property is demanded implicitly in the unfolding procedure, in which only jets above a certain p_T threshold enter the procedure: Only jets above 10 GeV/c are accepted (cf. also Sec. 6.2.2). This cut is somehow arbitrary, but motivated by the fact that low- p_T jets below, say, 10 GeV/c were mostly not created in a pure hard parton-parton interaction and are not of interest for this thesis.

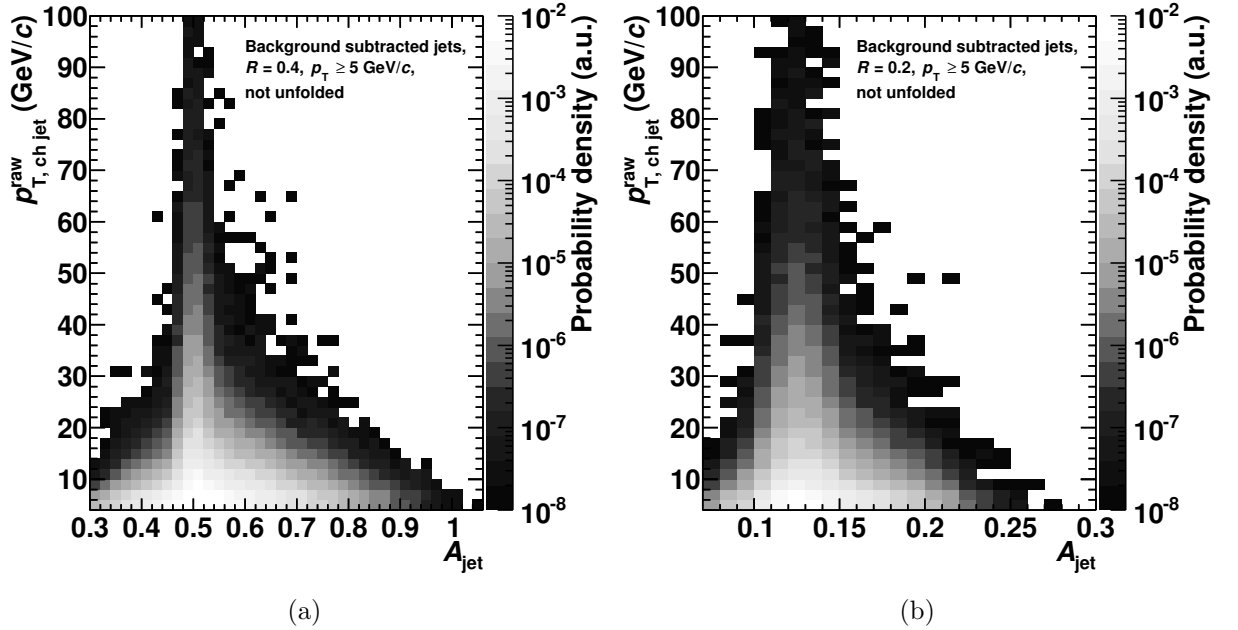


Figure 7.5: Probability density (in arbitrary normalization) for a certain jet area and transverse momentum for $R = 0.4$ (a) and $R = 0.2$ (b).

The third cut introduces a constraint on the area associated to a jet: The area has to be at least 60% of the area that is expected from the theoretical cone, i.e. πR^2 . It is applied for conceptual reasons, because in Pb-Pb jet analyses with the ALICE detector it was shown that the area cut effectively removes low- p_T jets and reduces the amount

of combinatorial jets caused by soft background [Ver13]. In the considered p–Pb and pp analyses, it has only a negligible effect on raw jets above $p_T > 5$ GeV/ c : Less than 0.02% of those jets in p–Pb and even less in pp do not pass this area cut.

In Figs. 7.5(a) and 7.5(b), the jet area distributions are shown in bins of jet p_T . The steeply falling slope of the p_T spectrum is not removed from the plots. Note that the color scale is logarithmic. This actually means that the spectrum falls steeply for those areas which differ from the expected πR^2 . It is also visible that the higher the jet p_T is the more regular is the jet area.

8. Jets in minimum bias p -Pb collisions

This chapter presents the main minimum bias results and the techniques for their careful analysis. Centrality-dependent results follow in Chapter 11. The systematic uncertainties and how they are determined is presented in Chapter 9.

In the following, charged jet spectra are shown in terms of fully corrected cross sections. Afterwards, the construction of the nuclear modification factor reference using measured data is presented in detail. This lays the ground for the introduction and presentation of the nuclear modification factor R_{pPb} . As a basic measure for the radial jet structure, the jet production cross section ratio $R = 0.2$ over $R = 0.4$ and several jet constituent analyses are shown.

To conclude, selected properties of jets at very low transverse momentum are presented.

Note that preliminary results of this analysis were first published by the author in [Haa13]. The final result is published in [Abe15].

8.1. Charged jet production cross sections

The background-corrected and SVD-unfolded charged jet production spectra are shown as cross sections for the resolution parameters $R = 0.2$ and $R = 0.4$ in Figs. 8.1 and 8.2. The spectra are defined by

$$\frac{d\sigma}{dp_T} = \frac{c_{\text{vtx}}}{N_{\text{ev}}} \frac{dN}{dp_T} \cdot \sigma_{V0}. \quad (8.1)$$

In this equation, the p_T -differential yield dN/dp_T is normalized by the total number of events seen by the trigger after applying all cuts, as described in Sec. 7.2. In order to transform the yield into a cross section, it is multiplied with the total cross section seen by the trigger, which is $\sigma_{V0} = 2.09$ mb as already presented in Sec. 7.2.

The event cut on the vertex z -coordinate is not expected to change the jet production cross section. Broadly speaking, the fraction of discarded events is equal to the fraction of discarded jets. This is different for the vertex demand itself. Triggered events without a reconstructed collision vertex contribute to the total cross section σ_{V0} but do not contain any jets. Thus, the total number of events needs to be corrected for the vertex finding

efficiency by introducing the factor

$$c_{\text{vtx}} = \frac{N_{\text{events}}^{\text{w/ vertex}}}{N_{\text{events}}^{\text{all}}} = 0.983. \quad (8.2)$$

The full systematic uncertainties are visualized as red bars in Figs. 8.1 and 8.2. The basic ansatz of the statistical and systematic uncertainty calculation has been described in Secs. 5.5.1 and 5.5.2. However, a detailed uncertainty analysis can be found in Chapter 9.

In addition to the bare spectra as such, comparisons to NLO pQCD calculations with POWHEG are shown as well in the bottom panels of Figs. 8.1 and 8.2. The POWHEG spectra are also corrected for a Lorentz boost expected from the asymmetric per-nucleon collision energy and include the EPS09 nPDFs [Esk09]. Systematic uncertainties of the NLOs (dashed lines) include the uncertainties of the CTEQ parton distribution functions, EPS09 nPDFs, and scale variations. In total, systematic uncertainties are estimated to be 17%.

To compare the p–Pb spectra to NLO calculations in the bottom panels of the spectrum figures, the normalization has to be adapted. The ratio can be described by

$$R_{\text{NLO}} = \frac{d\sigma_{\text{pPb}}/dp_{\text{T}}}{d\sigma_{\text{NLO}}/dp_{\text{T}} \cdot \frac{N_{\text{coll}}}{\sigma_{\text{NN}}^{\text{tot}}} \cdot \sigma_{\text{pPb}}^{\text{tot}}}. \quad (8.3)$$

Here, N_{coll} takes into account the trivial binary scaling and σ^{tot} corrects for the different total cross sections in pp and p–Pb. Roughly speaking, the total cross sections “convert” the jet production cross sections into per-event jet yields.

As a side note, the ratio in Eq. 8.3 is another representation of the nuclear modification factor R_{pPb} , which is introduced in Eq. 8.6. The only difference is the reference: While the later introduced reference is data-based, the reference in Eq. 8.3 is given by the NLOs.

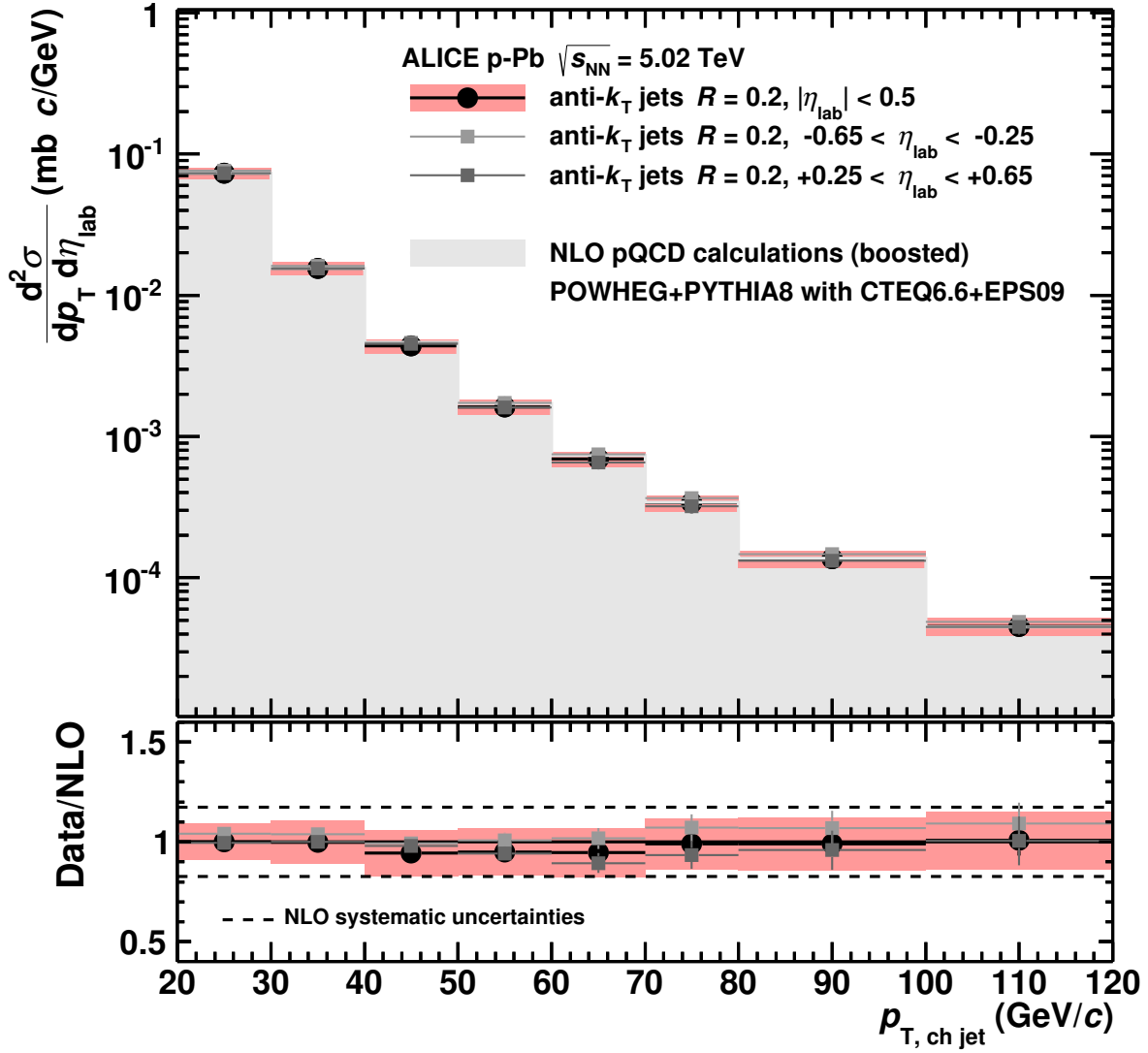


Figure 8.1: Top panel: Charged jet production cross section for $R = 0.2$. Bottom panel: Ratio of data and NLO pQCD calculations. The global uncertainty of the visible cross section is 3.5% and not shown. The uncertainties on the pQCD calculation are only shown in the ratio plot as dashed lines.

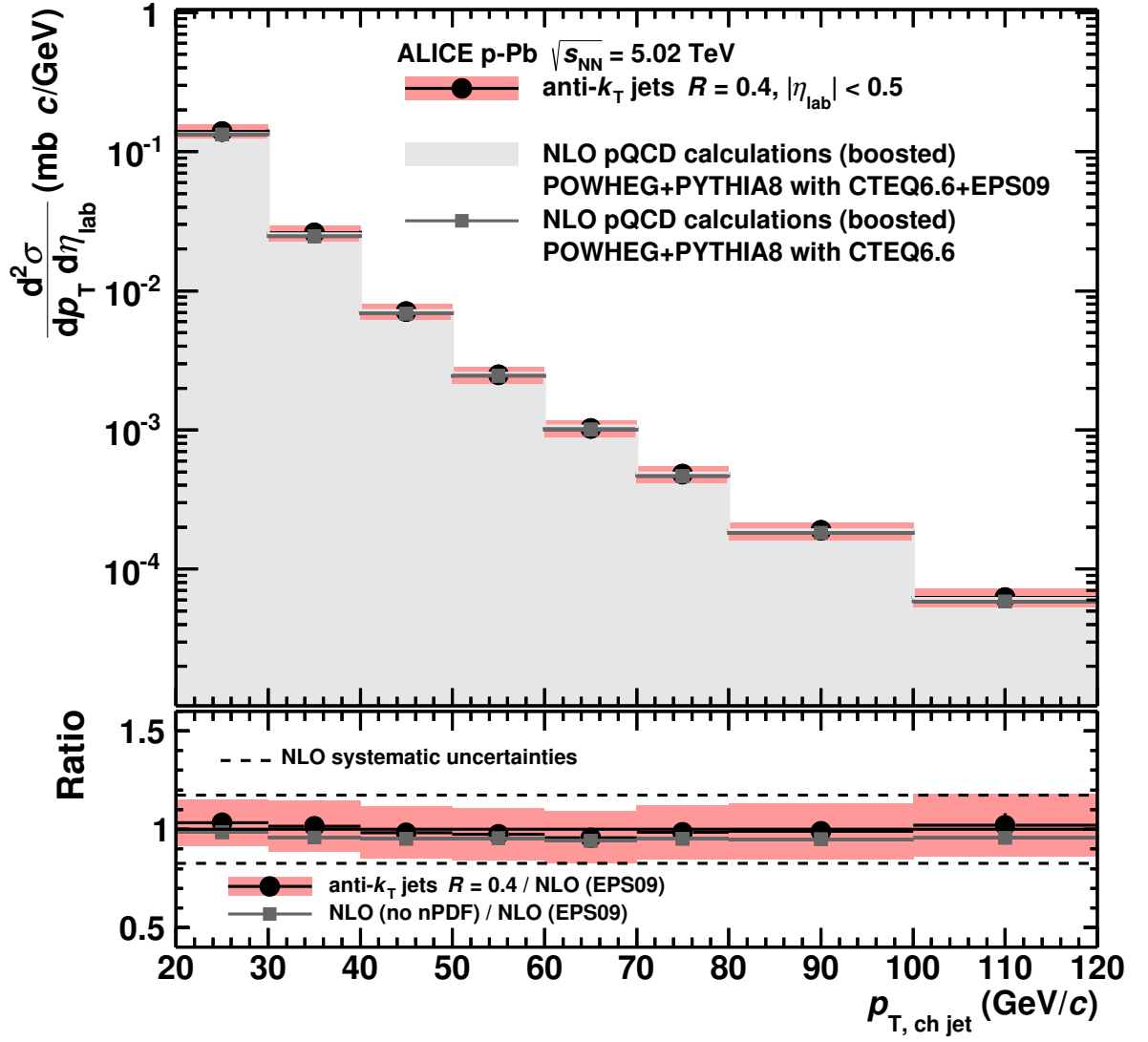


Figure 8.2: Top panel: Charged jet production cross section for $R = 0.4$. Bottom panel: Ratio of data and NLO pQCD calculations. The global uncertainty of the visible cross section is 3.5% and not shown. The uncertainties on the pQCD calculation are only shown in the ratio plot as dashed lines.

The presented charged jet spectra for both resolution parameters show an excellent agreement with the NLO calculation. Within the uncertainty, measurement and calculations agree.

Additionally, for the $R = 0.2$ jets in Fig. 8.1 also smaller pseudorapidity intervals are shown. This is to prove that the slight pseudorapidity dependence because of the asymmetric particle production has only a minor impact on the jet spectrum. No significant effects are visible for both chosen intervals. There is a small tendency that jet production is slightly enhanced for negative pseudorapidities, but it is not significant and within the systematic uncertainties. In Figs. 7.4(a) and 7.4(b), the pseudorapidity distribution of raw (not unfolded) jets is shown. For $R = 0.2$, an η dependence is hardly visible.

In Fig. 8.2, also NLO pQCD calculations without applied nPDFs are shown to illustrate the effect predicted by the nPDFs. The effect is of the order of 5% and therefore relatively small. Including nPDFs slightly increases the cross section.

As an additional cross check, the influence of tracks with $p_T > 100$ GeV/ c has been evaluated. The reason is that those very high transverse momentum tracks potentially suffer from a bad momentum resolution. But, it turned out that there are only two jets in p -Pb and one jet in pp that contain such a track. On the final spectrum, the influence of excluding those jets is 1-2% and, therefore, does not at all change the physical interpretation.

8.2. Construction of the pp reference

The nuclear modification factor R_{pPb} , which is introduced in Sec. 8.3, directly compares p -Pb to pp collisions. Therefore, pp spectra, which are comparable to the measured p -Pb spectra, are a stringent necessity.

Up to date, there have been no pp collisions at $\sqrt{s} = 5.02$ TeV in a collider. That is why a pp reference needs to be constructed. This can be principally done by using Monte Carlo simulations as the reference or by utilizing data from a different collision energy and scaling it to $\sqrt{s} = 5.02$ TeV.

In fact, a Monte Carlo based reference has already been constructed. The comparison of p -Pb jets to this reference is shown in the bottom panels of Figs. 8.1 and 8.2. However, such a nuclear modification factor strongly relies on our understanding of the applied Monte Carlo generators.

Therefore, a (mostly) data-based reference is preferred for the nuclear modification factor.

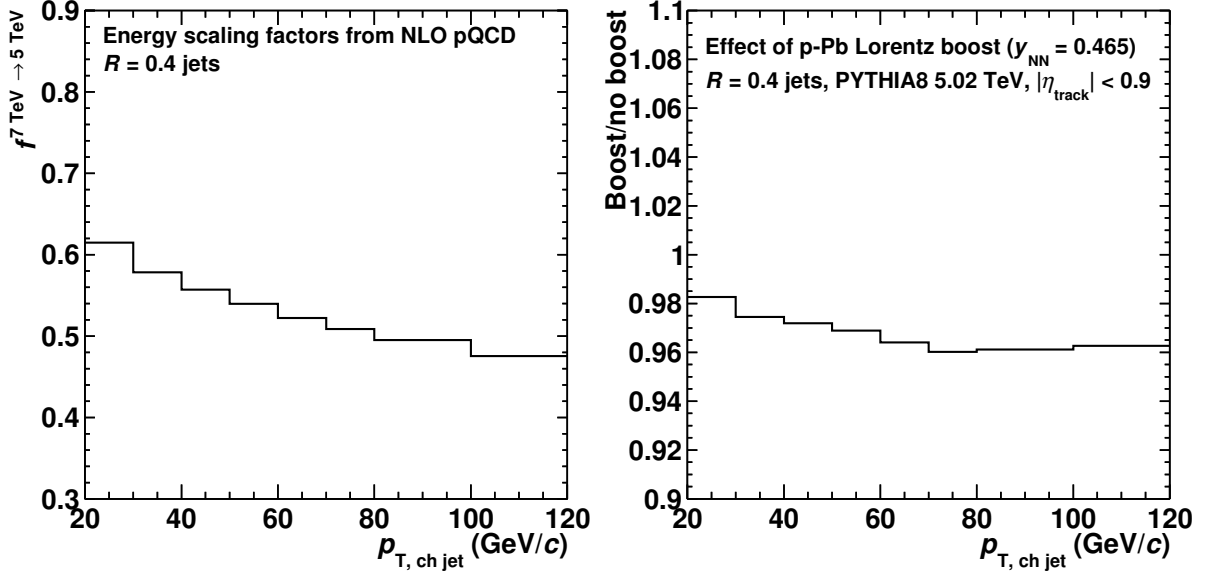


Figure 8.3: Left: Full scaling factors to scale 7 TeV pp charged jets to boosted 5 TeV pp charged jets. Right: Effect of boost alone. Both plots show results for $R = 0.4$ jets, the corresponding $R = 0.2$ results are nearly identical and are not shown for this reason.

In this thesis, 7 TeV pp data is analyzed to build the reference. Of course, jet production depends on the cms energy \sqrt{s} , but this dependence is grasped rather well. Also, the pp reference has to include the Lorentz boost.

The idea of using the final ALICE measurement of 7 TeV pp charged jets published in [Abe14a] is rejected for several reasons. The most important reason is that the pp reference should be calculated as similar as possible as the p-Pb spectra. Otherwise, the nuclear modification factor could be different from unity due to differences connected to the analysis and not due to potential nuclear effects. In addition, it is of utmost importance that the partial cancellation of the largest uncertainty, i.e. the tracking efficiency uncertainty, is only accurately possible if the same systematic variation is performed in pp and p-Pb (see Sec. 9.3.2).

For the purpose of the pp reference, the full pp analysis is performed. In Chapter 10, the fully corrected charged jet production cross sections, the jet shape, and also a summary of systematic uncertainties is presented.

The different jet production behavior, resulting from the differing center-of-mass energy of the considered pp dataset and from the boost, can be implemented by applying scaling factors bin-by-bin.

In principle, the energy scaling factors are given by the ratio of generated 5 TeV and 7 TeV jets,

$$f^{7 \text{ TeV} \rightarrow 5 \text{ TeV}}(p_T) = \frac{d\sigma_{\text{sim}}^{5 \text{ TeV}}/dp_T}{d\sigma_{\text{sim}}^{7 \text{ TeV}}/dp_T}. \quad (8.4)$$

The scaling factor of the Lorentz boost is directly applied to the generated 5 TeV spectrum using simulations from PYTHIA. The ALICE detector acceptance is taken into account. By default, NLO pQCD simulations are used for the energy scaling, but several other scaling methods, including a data-based power-law interpolation, are tested for the estimation of systematic uncertainties. The energy scaling of the pp reference can be described by

$$\frac{d\sigma^{5 \text{ TeV}}}{dp_T}(p_T) = f^{7 \text{ TeV} \rightarrow 5 \text{ TeV}}(p_T) \frac{d\sigma^{7 \text{ TeV}}}{dp_T}(p_T). \quad (8.5)$$

Note that the vertex finding efficiency in pp, $c_{\text{vtx}} = 0.82$, is taken into account for the measured spectrum as in Eq. 8.1.

In Fig. 8.3, the energy scaling factors and the effect of the Lorentz boost are depicted.

8.3. Nuclear modification factor

One of the most common observables for testing nuclear matter effects is the nuclear modification factor. For p -Pb collisions, it is called R_{pPb} and is defined as the ratio of p -Pb spectra and pp spectra, taking into account the higher mean number of binary collisions per event in p -Pb.

R_{pPb} can be interpreted in a very direct way: As its name indicates, a significant deviation of the factor from unity can be interpreted as a nuclear modification. A suppression corresponds to a suppressed, an enhancement to an enhanced jet production. For example, the strong suppression of R_{AA} for Pb-Pb collisions is typically interpreted as suppression of jet production due to QGP medium interaction.

The nuclear modification factor R_{pPb} is defined by

$$R_{\text{pPb}} = \frac{dN^{\text{pPb}}/dp_T \cdot c_{\text{vtx}} \cdot c_{\text{NSD}}}{d\sigma^{\text{pp}}/dp_T} \cdot \frac{1}{T_{\text{pPb}}} \frac{1}{N_{\text{ev}}^{\text{pPb}}}, \quad (8.6)$$

where c_{vtx} is the vertex finding efficiency given in Eq. 8.2 and dN^{pPb}/dp_T represents the background-corrected and SVD-unfolded charged jet yield in p -Pb collisions. $d\sigma^{\text{pp}}/dp_T$ is the cross section of the constructed reference, defined in Eq. 8.5. $N_{\text{ev}}^{\text{pPb}}$ is the number of p -Pb collisions, which pass all cuts described in Sec. 7.2.

T_{pPb} is called nuclear overlap function [Mil07] and takes into account the different collision systems. It is calculated by

$$T_{\text{pPb}} = \frac{N_{\text{coll}}}{\sigma_{\text{pp}}^{\text{inel}}}. \quad (8.7)$$

Here, N_{coll} is the number of binary collisions and $\sigma_{\text{pp}}^{\text{inel}}$ the inelastic nucleon–nucleon cross section for $\sqrt{s} = 5.02$ TeV pp collisions. It is $T_{\text{pPb}} = 0.0983 \text{mb}^{-1} \pm 3.4\%$ [Ada14].

Another correction factor in Eq. 8.6 is c_{NSD} , the correction for the NSD efficiency already introduced in Sec. 7.2.1.

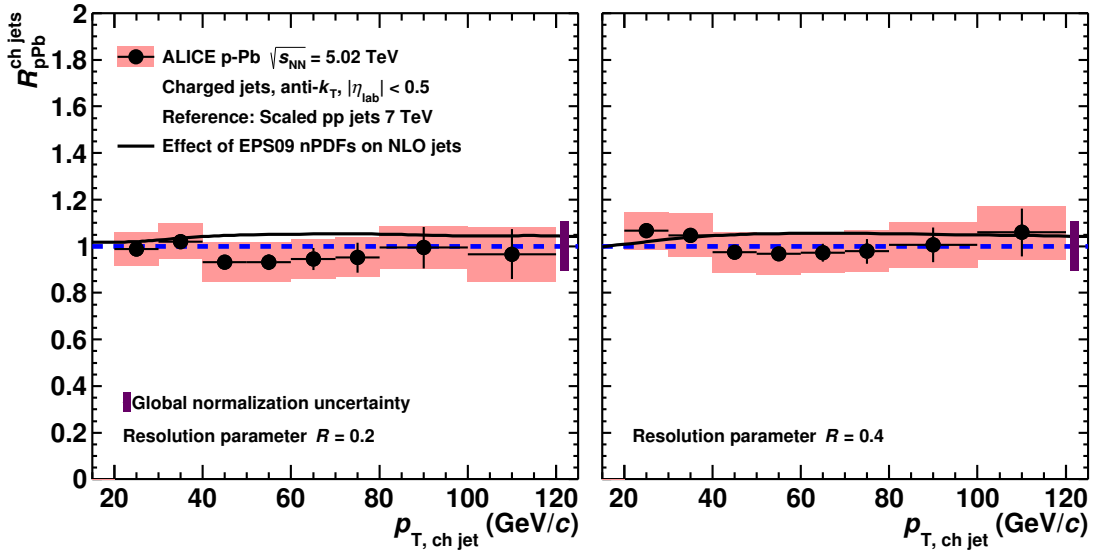


Figure 8.4: Nuclear modification factor R_{pPb} of charged jets for $R = 0.2$ (left) and $R = 0.4$ (right). The combined global normalization uncertainty in $\langle T_{\text{pPb}} \rangle$, the correction to NSD events, the pp cross section, and the reference scaling is depicted by the box around unity. Also, the effect of EPS09 nPDFs on POWHEG NLO pQCD jets is shown (see text).

In Fig. 8.4, the nuclear modification factor R_{pPb} is shown. Systematic uncertainties are given as red boxes, the magenta box around unity represents the global normalization uncertainty.

All details on systematic uncertainties can be found in Chapter 9. Within uncertainties, the result shows no strong nuclear effects and is even compatible with no nuclear modification in the analyzed transverse momentum range $20 \leq p_{\text{T, ch jet}} \leq 120$ GeV/c. Additionally, also the effect of using EPS09 nPDFs is shown. The histograms show the effects on generated NLO pQCD jets from POWHEG. Uncertainties of the NLO calculations are not shown for the simulated curve for better visibility. The effects

predicted by the EPS09 nPDFs are of the order of a few percent. Comparing the predictions to the uncertainties of the measured results, it can plainly be seen that already the normalization uncertainty of the nuclear modification factor is larger. Hence, although the order of magnitude of the measured nuclear modification agrees with the order predicted by the EPS09 nPDFs, the measurement is not sensitive enough to reach detailed conclusions on the validity of the nPDFs. For instance, the nuclear modification factor would also agree with the nPDFs if they showed a suppression of the same size instead of an enhancement.

The obtained result can also be compared to results that were measured by the ATLAS collaboration at the same $\sqrt{s_{\text{NN}}}$ [Aad14]. It must be emphasized that the presented and the ATLAS results can only be compared on an elementary level, since ATLAS measured fully reconstructed jets including neutral particles. Therefore, the jet energy scale is different and the relation is not fully known. In the present case, this is not an issue for the interpretation, because the nuclear modification factors should not differ too much in ATLAS and ALICE measurements as the factors are relatively flat and at unity.

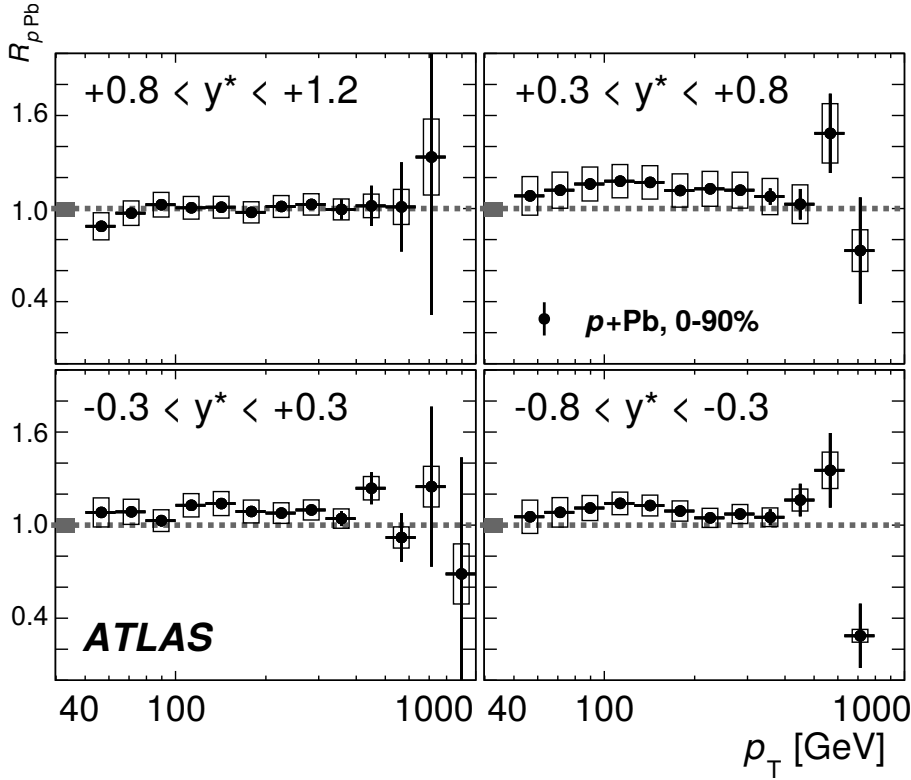


Figure 8.5: Nuclear modification factor $R_{p\text{Pb}}$ measured by the ATLAS collaboration for $R = 0.4$ jets for selected rapidity intervals. y^* represents the jet rapidity.

In Fig. 8.5, the ATLAS measurement is shown for selected rapidity intervals. The

presented ALICE results are measured within $|\eta_{\text{lab}}| < 0.5$ around $\eta_{\text{lab}} = 0$, which corresponds to $y = -0.465$ in the center-of-mass system of the nucleon–nucleon collision due to the rapidity shift of the p–Pb collision system. The results from this thesis can therefore be best compared to $0.3 < y^* < 0.8$.

The ATLAS results are in good agreement with the results in this thesis. Note that the ATLAS results continue to much larger transverse momenta because of their different detector.

8.4. Radial jet structure analysis

The radial jet structure provides information on the energy distribution of the jet relative to its axis. This was an especially interesting observable in Pb–Pb jet analyses, in which it was e.g. used to probe jet broadening.

In [Abe14b], the radial jet structure measured by the jet production cross section ratio was shown to be not significantly modified in Pb–Pb collisions using jets with $R = 0.2$ and $R = 0.3$ measured with the ALICE detector. Therefore, a modification is not expected in p–Pb collisions.

However, the observable is very easy to calculate if jets have already been measured with two resolution parameters. Additionally, the measurement had been done in several analysis before [Abe13d, Abe14b, Abe14a]. Hence, also in this work the radial jet structure was probed with the jet production cross section ratio.

To shed more light on the radial jet structure, more sensitive tests have been performed by analyzing jet constituent distributions relative to the jet axis.

8.4.1. Jet production cross section ratio

The jet production cross section ratio is the simplest observable to study possible jet structure modifications. In the present p–Pb analysis, jets have been measured with $R = 0.2$ and $R = 0.4$ and, therefore, the natural definition of the ratio is given by

$$\mathcal{R}(0.2, 0.4) = \frac{d\sigma_{\text{pPb}, R=0.2}/dp_{\text{T}}}{d\sigma_{\text{pPb}, R=0.4}/dp_{\text{T}}}. \quad (8.8)$$

In this ratio, most uncertainties cancel each other. This is reflected in relatively low systematic uncertainties.

In Fig. 8.6, the jet production cross section ratio for charged jets in p–Pb collisions is depicted. It is shown together with NLO pQCD calculations with POWHEG (already shown with the charged jet spectra), PYTHIA6 Perugia 2011 simulations, and with the jet production cross section ratio in pp collisions at 7 TeV. Note that the ratio obtained using 7 TeV pp collisions was not calculated in the present analysis but in the analysis for [Abe14a]. Later in Sec. 10.2, the jet production cross section ratio for 7 TeV pp collisions is shown using the analysis of this work.

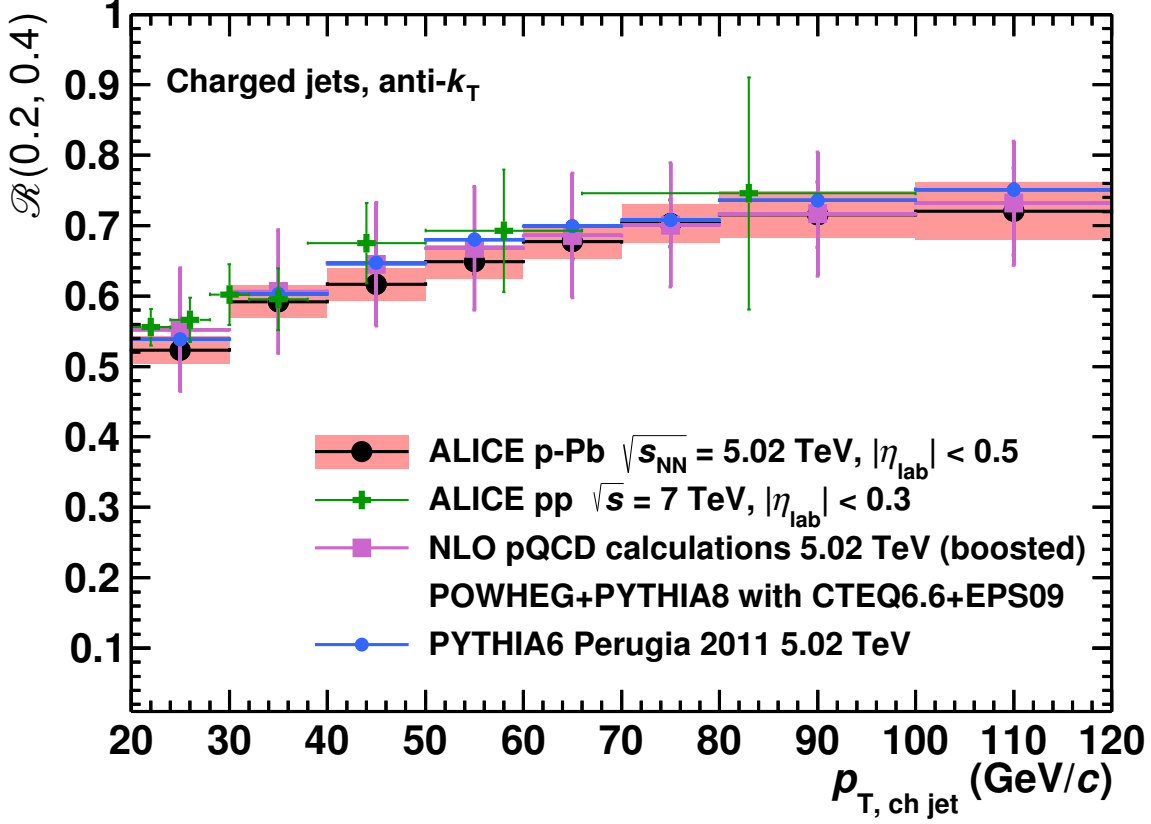


Figure 8.6: Charged jet production cross section ratio for different resolution parameters. The data in p–Pb collisions at $\sqrt{s_{\text{NN}}} = 5.02$ TeV is compared to PYTHIA6 (no uncertainties shown) and POWHEG+PYTHIA8 (stat. uncertainties shown as error bars) at the same energy and to pp collisions at 7 TeV [Abe14a].

Within uncertainties, the measured jet production cross section ratio in p–Pb is compatible with all shown ratios. No medium modification of the jet production cross section ratio is observed. It is also plainly visible that jet is more collimated for larger $p_{\text{T, ch jet}}$. A more differential analysis is given in Sec. 8.4.2.1.

Numerator and denominator of the jet production cross section ratio are correlated, since they are evaluated on the same database. With a certain probability, a jet with $R = 0.2$ falls into the same p_T bin as the corresponding jet with $R = 0.4$.

Using the default error propagation (assuming no correlation) would overestimate the uncertainty. One possibility to circumvent the problem is to split the dataset into two sets, e.g. odd and even events, and to use different datasets for numerator and denominator. This was actually done in [Abe13d], but has the drawback that half of the statistics is effectively lost.

For this thesis, another approach was chosen: The statistical uncertainty has been calculated taking into account a partial correlation of $R = 0.2$ and $R = 0.4$ jets. This allows the error calculation according to the general error propagation formula, see Eq. 5.16.

It is necessary for the calculation of the partially correlated error to have knowledge of the covariance. The covariance is defined by

$$\text{Cov}(N_{0.2}, N_{0.4}) = \frac{1}{N_m} \sum_i (N_{0.2}^i - N_{0.2})(N_{0.4}^i - N_{0.4}), \quad (8.9)$$

where the sum is for N_m measurements. The value for each is given by N^i . Of course, the yields have been just measured once (so $N_m = 1$). However, any number of values N^i can be generated by randomly varying the yield according to its statistical uncertainty and correlation. The following algorithm is used to create the covariance value for a given correlation for jets with $R = 0.2$ and $R = 0.4$:

1. Vary $N_{0.2}$ according to a Gaussian with a width given by the statistical uncertainties of $N_{0.2}$,
2. vary $N_{0.4}$ according to a Gaussian with a width given by the statistical uncertainties of $N_{0.4}$,
3. with a probability given by the correlation probability, the variation of $N_{0.4}$ is set to the same value as for $N_{0.2}$.
4. Alternatively, set the variation of $N_{0.2}$ to that of $N_{0.4}$ (explanation see below).

The correlation probability is evaluated with a correlation matrix created by geometrically matching measured $R = 0.2$ and $R = 0.4$ jets. Note that this is a data-based approach and no simulations are necessary to calculate the correlation. The matching criterion is that their distance is below 0.25. The uncorrected matrix is depicted in the left plots of Fig. 8.7.

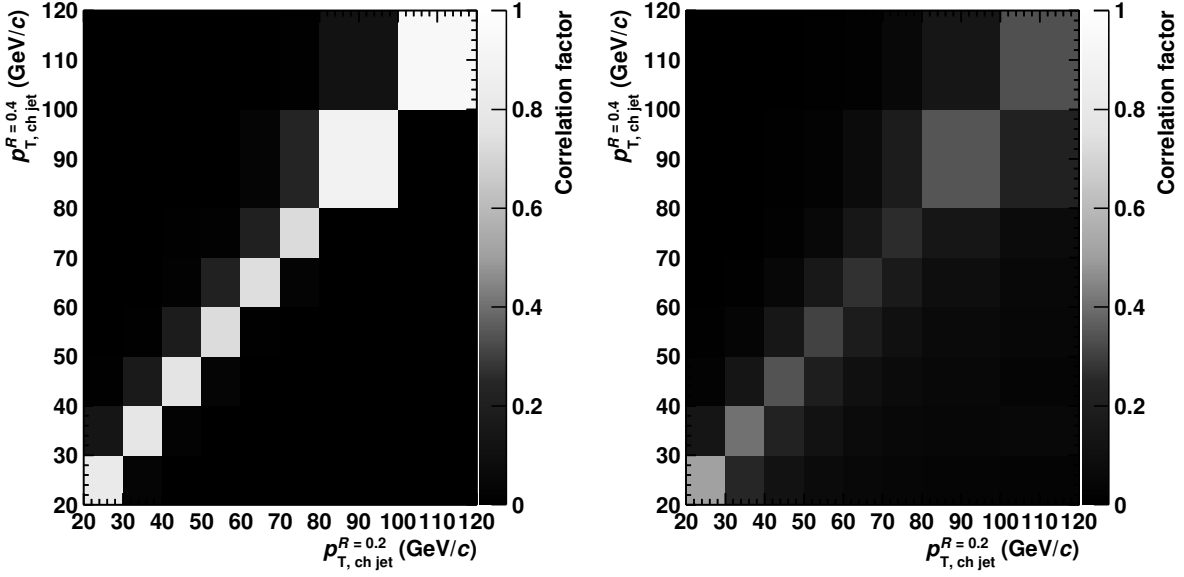


Figure 8.7: Left: Correlation matrix for $R = 0.2$ and $R = 0.4$ jets. Right: Correlation matrix corrected for detector effects.

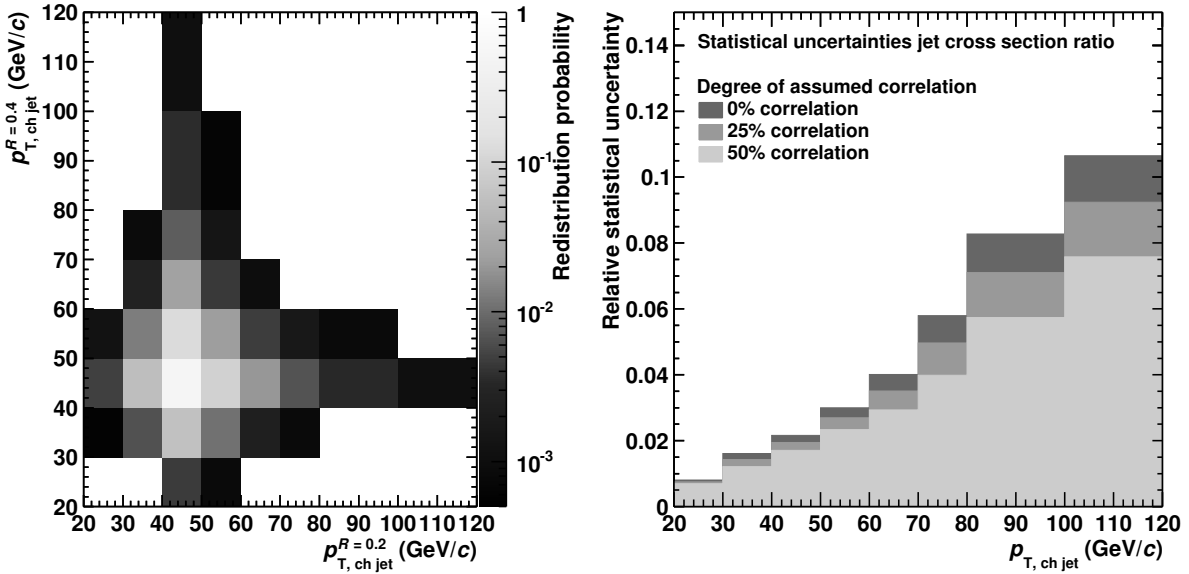


Figure 8.8: Left: Smearing matrix for inclusion of detector effects for one bin of the correlation matrix (40-50, 40-50). Right: Statistical uncertainties for different correlations (nominally assumed value: 25%).

Whether step 3 or step 4 of the algorithm is used depends on how the correlation probability is evaluated. Using step 3, the correlation probability must give the probability

for how many $R = 0.2$ jets are correlated to $R = 0.4$ jets. Using step 4, the correlation probability must give the probability for how many $R = 0.4$ jets are correlated to $R = 0.2$ jets. In principle, both steps should yield roughly the same result. Small differences can occur because technically it is not the same whether $R = 0.2$ jets are matched to $R = 0.4$ or $R = 0.4$ jets are matched to $R = 0.2$ jets. For example, a $R = 0.4$ jet that is reconstructed as two $R = 0.2$ jets, can only be matched to one $R = 0.2$ jet. The other jet is simply lost. When matching $R = 0.2$ jets, these jets are not lost and, therefore, this is the default matching method.

Detector effects are also taken into account using a technique that migrates bin contents according to the probability extracted from the response matrix. An example how a bin is smeared out can be seen in Fig. 8.8, left plot. The final fully corrected correlation matrix can be found on the right-hand plot of Fig. 8.7.

The correlation of jets with $R = 0.2$ to those with $R = 0.4$ is calculated to be between 25% and 50%. As a conservative choice (potentially larger statistical uncertainties), it is fixed to 25% correlation in the calculation. How different correlation values eventually affect the uncertainties is shown in the right-hand plot of Fig. 8.8.

8.4.2. Jet constituent profiles

The jet production cross section ratio has a fundamental flaw when describing the radial jet structure: It is calculated inclusively for all jets within a certain p_T range. This means that numerator and denominator do not even contain the exact same jet sample. The radial distribution is not measured individually for every jet. Therefore, the interpretation of the ratio should be carefully considered. It should be seen more as a rough estimate for strong radial changes.

A more differential measure for the radial structure is given by the jet constituent density, i.e. track density in bins of jet axis distances. Of course, this measure strongly depends on the chosen jet definition and, hereby, also on the jet finding algorithm. For this reason and also because the constituent distributions are uncorrected, a too detailed interpretation is avoided.

8.4.2.1. Jet collimation in p_T

After branching (multiple gluon emission) and hadronization of the initially scattered partons, the resulting jet cones measured in the detector have finite sizes. This experimental fact applies to jets in general and is not reserved to jets in heavy-ion collisions. For instance, the CDF collaboration measured jet shapes in $\bar{p}p$ collisions at $\sqrt{s} = 1.8$ TeV [Abe93]. The general result was that jets become narrower for increasing transverse energy/momentum. An example of a more recent measurement is given by an analysis by the ATLAS collaboration of pp data at 7 TeV [Aad11].

In this thesis, an analysis of jet constituents is presented to investigate the collimation of charged jets in p -Pb. In Fig. 8.9, constituent (count) density profiles are shown for p -Pb jets using the resolution parameter $R = 0.4$. Plots (a), (b), and (c) depict the distributions for tracks of selected p_T intervals. Jet $p_{T, \text{ch jet}}$ ranges are given for background-corrected, non-unfolded jet spectra. The same jets were used for the spectra in Sec. 8.1 after unfolding. A transverse momentum distribution of the constituents for various $p_{T, \text{ch jet}}$ ranges can be found in Fig. 8.9(d).

Note that the profiles represent constituent count densities for given distances around the axis. The jet axis is calculated using the p_T -weighted directions of the tracks. The overall normalization is adjusted to the integrated density being one.

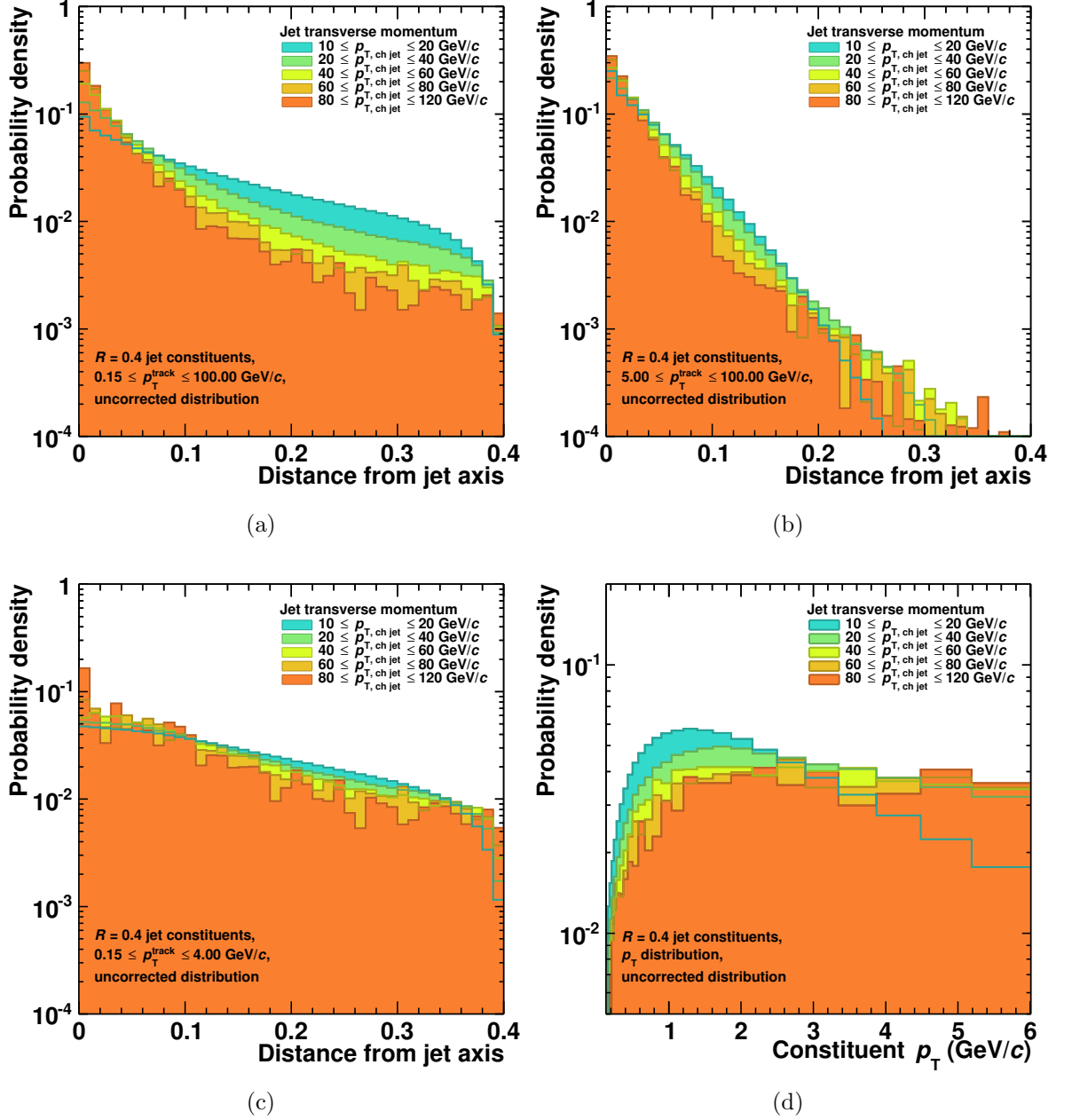


Figure 8.9: (a, b, c) Jet constituent densities for different $p_{T, \text{ch jet}}$ (p_T for background-corrected, non-unfolded jet spectra). Each plot shows different jet constituent transverse momentum intervals: All selected tracks (a), tracks above $p_T \geq 5$ GeV/c (b), and tracks within the p_T range 0.15 – 4.0 GeV/c (c). (d) Constituent p_T distributions for different $p_{T, \text{ch jet}}$. All plots show p-Pb data. The range 0.15 – 4.0 GeV/c was arbitrarily chosen as an example for low transverse momentum.

In Fig. 8.9(a), the basic observation of the jet production cross section ratio is confirmed: Jets with larger transverse momenta are narrower in radial direction, i.e. they are more collimated. The current analysis results allow a more detailed explanation of this collimation.

Interestingly, the main source of the $p_{T, \text{ch jet}}$ dependence of the jet collimation is not a $p_{T, \text{ch jet}}$ dependence of soft or hard constituents. In both cases, the distributions show only a relatively small jet p_T dependence, see Figs. 8.9(b) and 8.9(c).

A striking difference of both distributions is the slope that describes how fast the track density falls towards larger distances relative to the jet axis. While the harder jet components above 5 GeV/ c are falling rapidly, the soft contributions with $0.15 \leq p_T^{\text{track}} \leq 4.0$ GeV/ c are falling relatively slow. Broadly speaking, this means that the soft particles are distributed essentially over the whole jet (cf. also Fig. 8.10) and that the hard contributions are much more collimated.

Considering the transverse momentum distribution of the jet constituents for different jet p_T in Fig. 8.9(d), the jet collimation for larger jet p_T can be understood: Jets with lower transverse momenta contain – relatively – much more soft contributions than jets with higher p_T . A direct consequence is that the overall low- p_T jet profile is dominated rather by the soft constituent profile (Fig. 8.9(c)) than by the hard constituent profile (Fig. 8.9(b)).

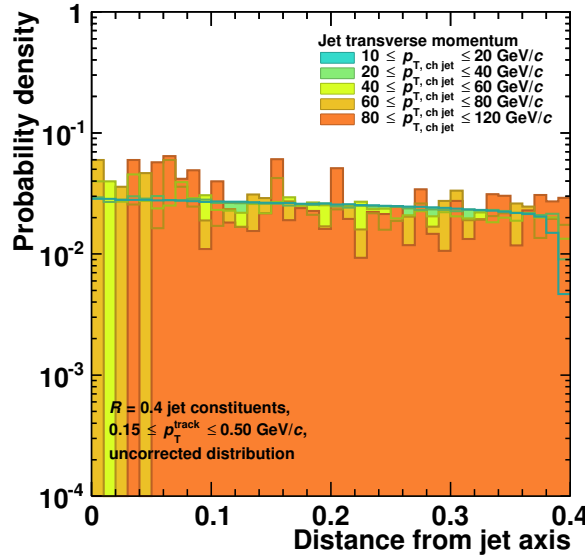


Figure 8.10: Charged jet constituent density ($0.15 - 0.50$ GeV/ c tracks) for different jet transverse momenta in p -Pb collisions.

Therefore, the profile must be broader for jets with lower transverse momenta. In Tab. 8.1, the mean values of the profile distributions are listed. Those numbers should be interpreted with care as corrections are missing. However, they clearly show the order

Table 8.1: Mean values of the constituent density distributions. Note that the numbers are only valid for raw jet and track transverse momenta. In addition, the tracks are uncorrected and the jets are not unfolded.

Track p_T (GeV/ c) Jet p_T (GeV/ c)	Mean of constituent density distribution					
	0.15-100		5.0-100		0.15-4.0	
	p-Pb	pp	p-Pb	pp	p-Pb	pp
10-20	0.116	0.090	0.040	0.035	0.139	0.124
20-40	0.089	0.077	0.040	0.038	0.132	0.120
40-60	0.067	0.061	0.034	0.033	0.124	0.110
60-80	0.056	0.056	0.030	0.033	0.120	0.110
80-120	0.047	0.049	0.027	0.028	0.105	0.126
10-120	0.114	0.088	0.040	0.035	0.139	0.123

of magnitude of the different jet dimensions. Note that also comparison values for 7 TeV pp data are shown in this table, which is described in Sec. 8.4.2.2.

A broader distance distribution is a hint that particles are not correlated to the jet, a hint that the jet constituents are background. These particles have not been produced in the hard scattering. In Fig. 8.10, the distribution is shown for very low momentum jet constituents: The particles are relatively loosely correlated to the jet axis. As shown in Figs. 8.9(b) and (c), the broadening is connected to the momentum of the particles. The larger the transverse momentum of the constituents is the higher is the probability that they are connected with the jet axis in a given event.

However, at least in principle, it is also possible that the different degree of collimation of soft and hard constituents relative to the jet axis is somehow connected to the jets. In addition, it is not clear how the jet finding algorithm influences the jet collimation. Further investigations would be necessary to give more detailed answers, in particular concerning whether or not the broadening of soft particles is solely generated by background. For instance, the analysis of constituent distance distributions in cones perpendicular to the jets could shed more light on the particle distribution outside of jets. To probe the influence of the jet finder, events with randomized tracks (in azimuth) could be analyzed.

8.4.2.2. Comparison of jet profiles in p-Pb and pp

A comparison of jet profiles in the analyzed p-Pb and pp data is only possible to some extent. Although the jet fragmentation functions should be universal for fixed jet momentum and flavor [Kni01], both datasets were recorded in 2010 and 2013, respectively, and with different energies. Thus, the collider and the ALICE detector were potentially in slightly different states.

According to the jet production cross section ratio, the expected result is that the

jet profiles should be quiet similar in pp and p-Pb collisions. However, although not significantly, the p-Pb jet cross section ratio is slightly smaller than the compared ratios.

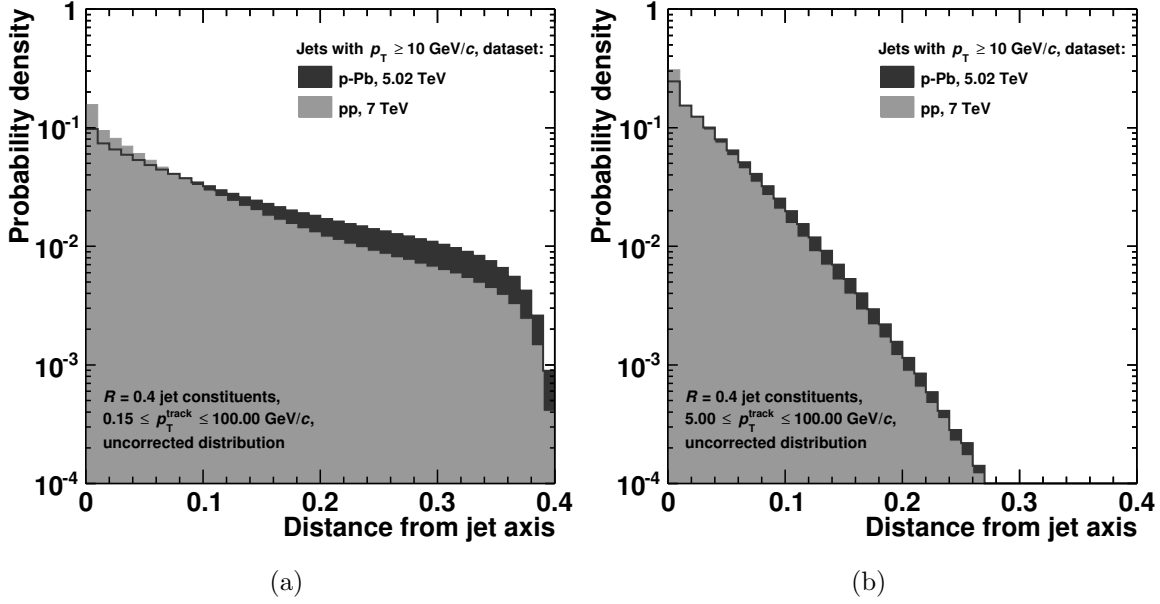


Figure 8.11: Jet constituent densities for different $p_{T, \text{ch jet}}$: Distribution for all (a) and $p_T \geq 5$ GeV/c tracks (b).

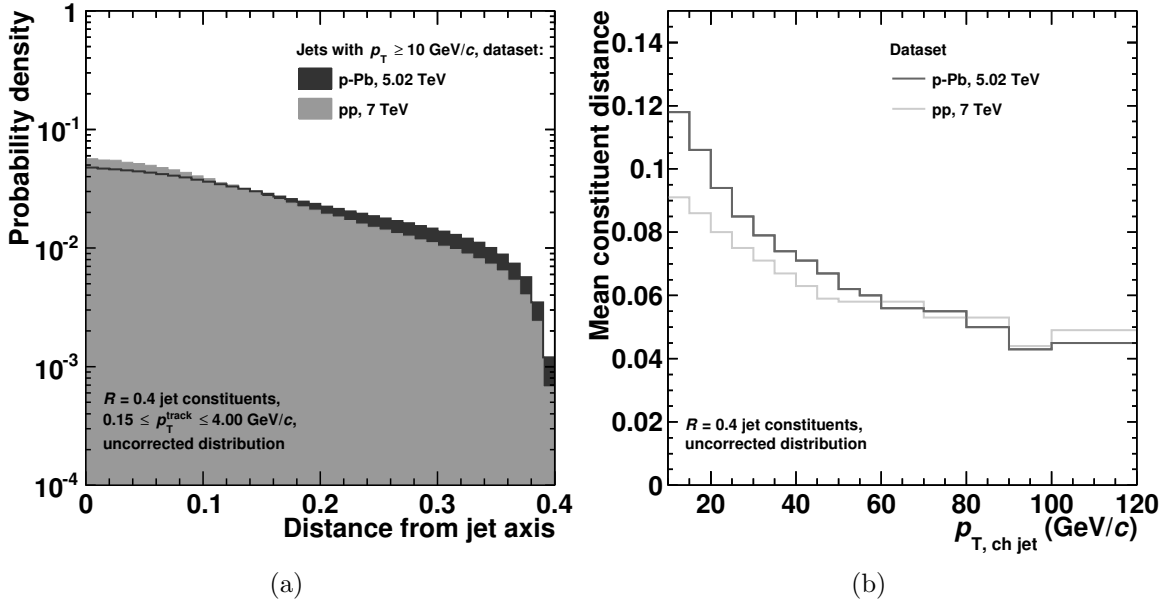


Figure 8.12: (a) Jet constituent densities for pp and p-Pb. (b) Distribution of the mean constituent distance distribution for pp and p-Pb.

In Figs. 8.11(a) and 8.11(b), the constituent density jet profiles are shown for all tracks above $p_T > 0.15$ GeV/ c and $p_T > 5$ GeV/ c , respectively. The plots show a general agreement of the jet profiles, though the p-Pb profile is less collimated, predominantly due to the lower- p_T jets. The soft particle distribution in pp and p-Pb jets is depicted in Fig. 8.12(a).

Table 8.1 summarizes the differences of the profile distributions in pp and p-Pb. In Fig. 8.12(b), the mean constituent distance distribution is plotted. Here, a finer raw jet p_T binning was used for illustration purposes. It is clearly recognizable that the mean distance is larger in p-Pb, especially for lower transverse momenta. This corresponds to broader jets. For higher p_T , the difference seems to level off, but the statistics are relatively poor in this region and, therefore, this observation should be treated with care. It should be noted that, in principle, a low- p_T jet broadening is expected, because a larger background density pushes the mean constituent distance to larger values.

In summary, it can be stated that quantitative answers are difficult to give on the basis of the presented analysis. Using the applied definition of a jet “width”, namely the mean constituent distance, charged jets in p-Pb are indeed measured to be broader than those in pp, especially for lower transverse momenta.

Note that here a jet means explicitly the object found by the algorithm. The observed behavior is at least partly expected due to the larger soft particle background in p-Pb collisions. On the other hand, a slight broadening is also seen for the tracks with $p_T > 5$ GeV/ c that do probably not belong to the soft background, see for example Fig. 8.11(b).

8.5. Low transverse momentum jets

One of the main strengths of the ALICE detector is clearly the capability of very low transverse momentum tracking. High quality tracks are reconstructed down to momenta as low as $p_T = 0.15$ GeV/ c . Despite this tracking capability, the considered minimum bias jets are published only above 20 GeV/ c .

The main reason for that is that the interpretation of jets with very low transverse momentum is difficult. For low momenta, it becomes increasingly blurred whether the jet really originates from a clean hard parton scattering or if it is an accumulation of upward fluctuations of background or a mixture of both. In Pb-Pb collisions, jets constituted by background upward fluctuations are not negligible. These so-called combinatorial jets are also possible to occur in p-Pb collisions.

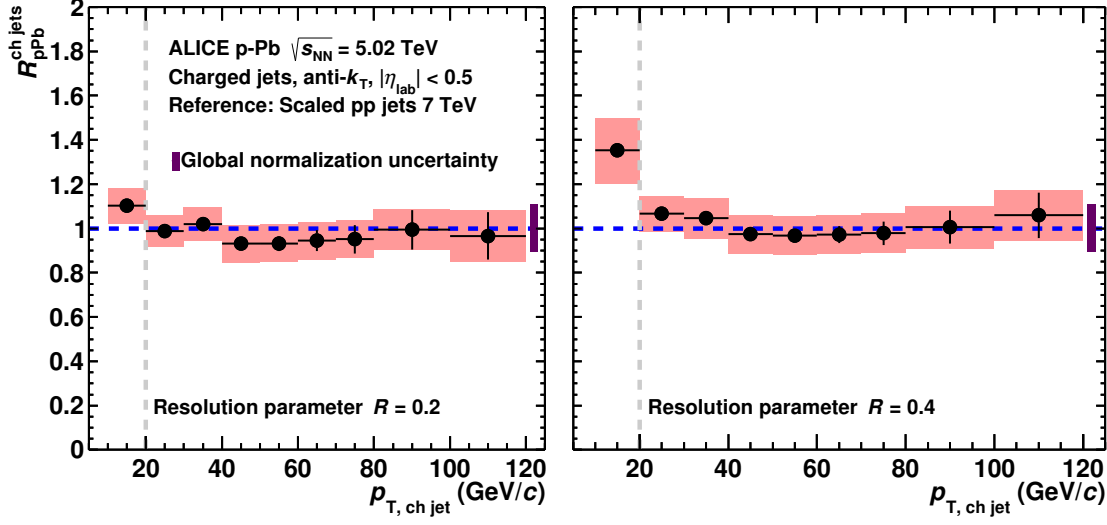


Figure 8.13: Nuclear modification factor including one bin below 20 GeV/ c .

However, the jet spectrum unfolding was performed down to 0 GeV/ c using data down to 10 GeV/ c . This means that the spectra can principally be interpreted down to 10 GeV/ c . In Fig. 8.13, the low- p_T bin is shown for the nuclear modification factor. While the results are unsuspicious for $R = 0.2$ jets, the additional bin for $R = 0.4$ shows a strong upward deviation.

In the following, the origin of this deviation for low transverse momentum jets is investigated in more detail. The absence of the deviation for the smaller resolution parameter jets with $R = 0.2$ already hints at a soft particle effect: While the (hard) signal is rapidly falling with respect to the jet axis distance, the soft particles are distributed much broader, as shown in Sec. 8.4.2.1. Therefore, soft contributions have a much stronger impact on the $R = 0.4$ jets, which are four times larger than the $R = 0.2$ jets.

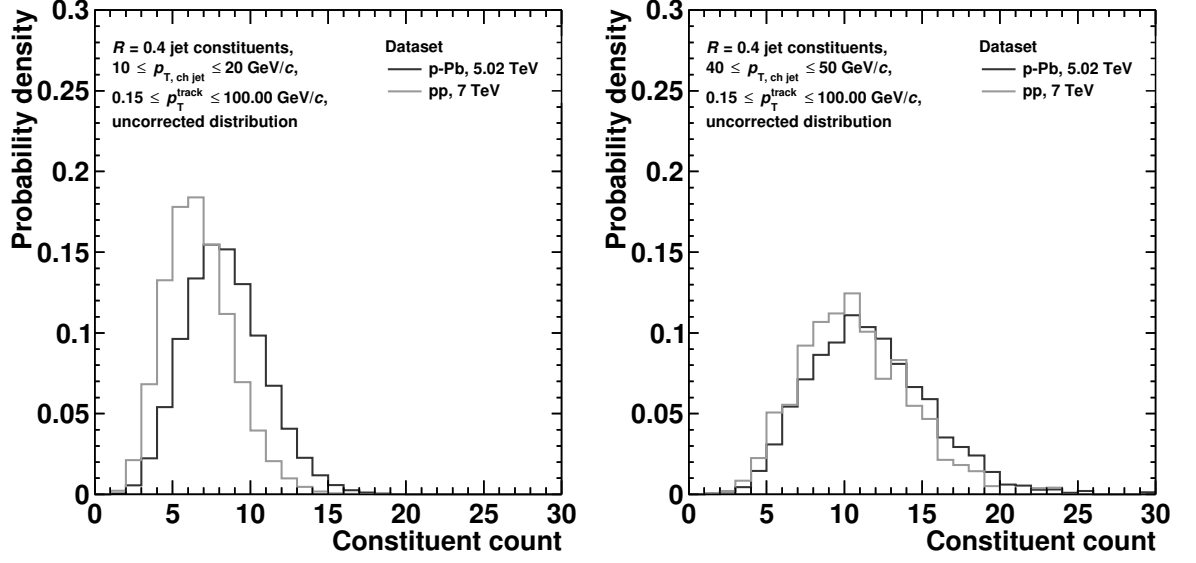


Figure 8.14: Jet constituent count distribution for 10-20 GeV/ c jets (left) and for 40-50 GeV/ c jets (right).

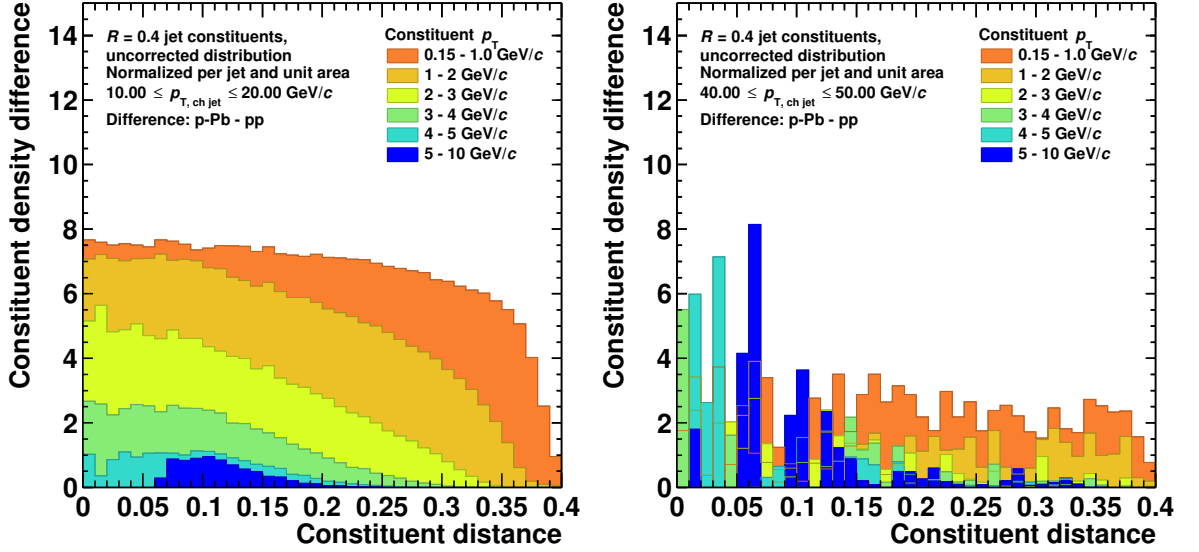


Figure 8.15: Difference of p-Pb and pp constituent densities normalized per jet and unit area. Distribution for 10-20 GeV/ c jets (left) and for 40-50 GeV/ c jets (right).

In Fig. 8.14, the jet constituent count distributions are shown. The left plot shows the count distribution for low- p_T jets with a raw p_T between 10 and 20 GeV/ c . In the right plot, the same distribution is depicted for jets with higher p_T . Note that the count

distributions are uncorrected and the jet p_T is not unfolded.

Both plots clearly differ in how much both distributions for pp and p-Pb coincide: Low transverse momentum jets have on average more constituents in p-Pb compared to larger momentum jets. Roughly speaking, p-Pb jets consist of more tracks at low p_T while they have approximately the same composition at higher p_T .

To probe the properties of the additional jet constituents in p-Pb for low- p_T jets, the difference of the constituent density distributions is evaluated and shown in Fig. 8.15 for low- and higher- p_T jets, respectively. The difference is normalized per jet and unit area. It is shown for several constituent momenta. While the constituent difference is quite huge for the lowest momentum tracks, the difference levels off for higher momentum tracks.

This can be interpreted in such a way that the enhancement of low transverse momentum jets, which is observed in the nuclear modification factor, is mainly caused by lowest track momenta, i.e. soft contributions. Additional analyses carried out for this thesis support this conclusion by showing that constituent count distributions become very similar if low transverse momentum tracks are neglected.

8.6. Comparing results using good and all runs

As already described in Chapter 7, the dataset contains good and semigood runs. By default, both runtypes were used for analysis after performing several cross checks. The most convincing sanity check is presented in the following: the direct impact on the data if only the good runs were used.

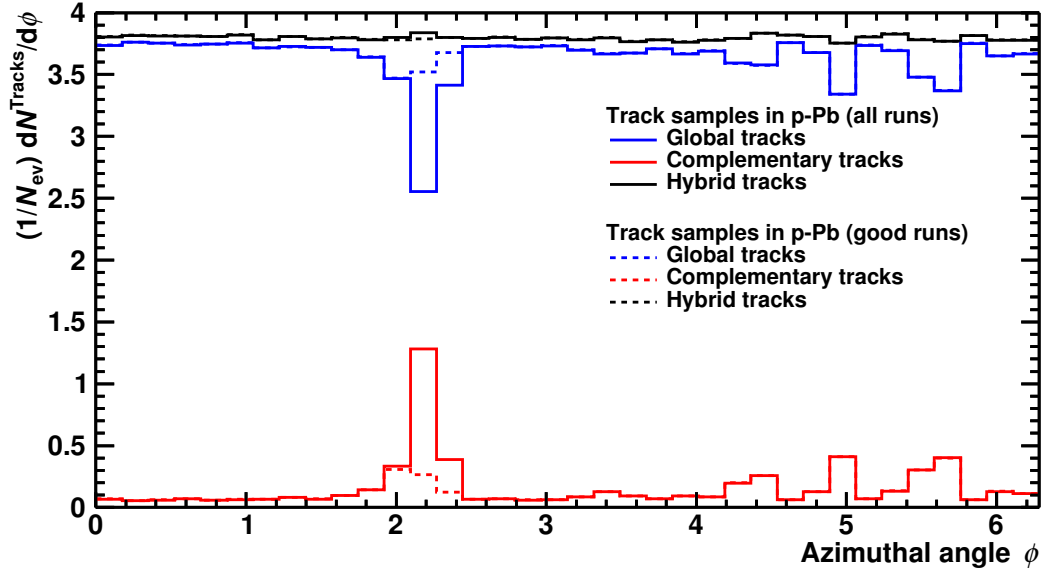


Figure 8.16: Azimuthal distributions of different track subsamples, shown for using all runs or just a run subset (“good” runs).

Figure 8.16 shows the difference of good runs and the full data sample. The dashed lines represent the distribution for good runs only. The dip in the distribution of the global tracks is much smaller than for all runs. Finally, the utilized track sample is flat in azimuth, because the hybrid tracks are constructed so that a complementary track is used in case a global track is not available. But since the complementary tracks suffer from a worse momentum resolution, the jets are also potentially affected. Both, global and complementary tracks have a relative p_T resolution of $\sigma(p_T)/p_T \approx 1\%$ at 1 GeV/ c . At 50 GeV/ c , the relative resolution is 10 and 20 % for global and complementary tracks, respectively [Abe14b]. It has to be noted, though, that the complementary tracks constitute only 4.3% of the track sample.

Comparing the raw jet transverse momentum spectra before unfolding, no significant deviation is observed. This is depicted in Fig. 8.17(a) for $R = 0.2$ and $R = 0.4$ jets. The lower limit of the p_T range is chosen to be 10 GeV/ c , which is the lower limit for measured jets entering the unfolding procedure. The upper limit is chosen to be 100 GeV/ c because of smaller statistics if only good runs are utilized.

In Fig. 8.17(b), the same ratio is shown for fully corrected jets. The detector matrix for the unfolding procedure is created drawing on a detector model appropriate for the good runs. Also for the fully corrected jet spectra, the effect is statistically not significant. The range on the ordinate is chosen differently in Figs. 8.17(a) and 8.17(b) due to a larger fluctuation of the raw data, which is more regularized in the unfolded results.

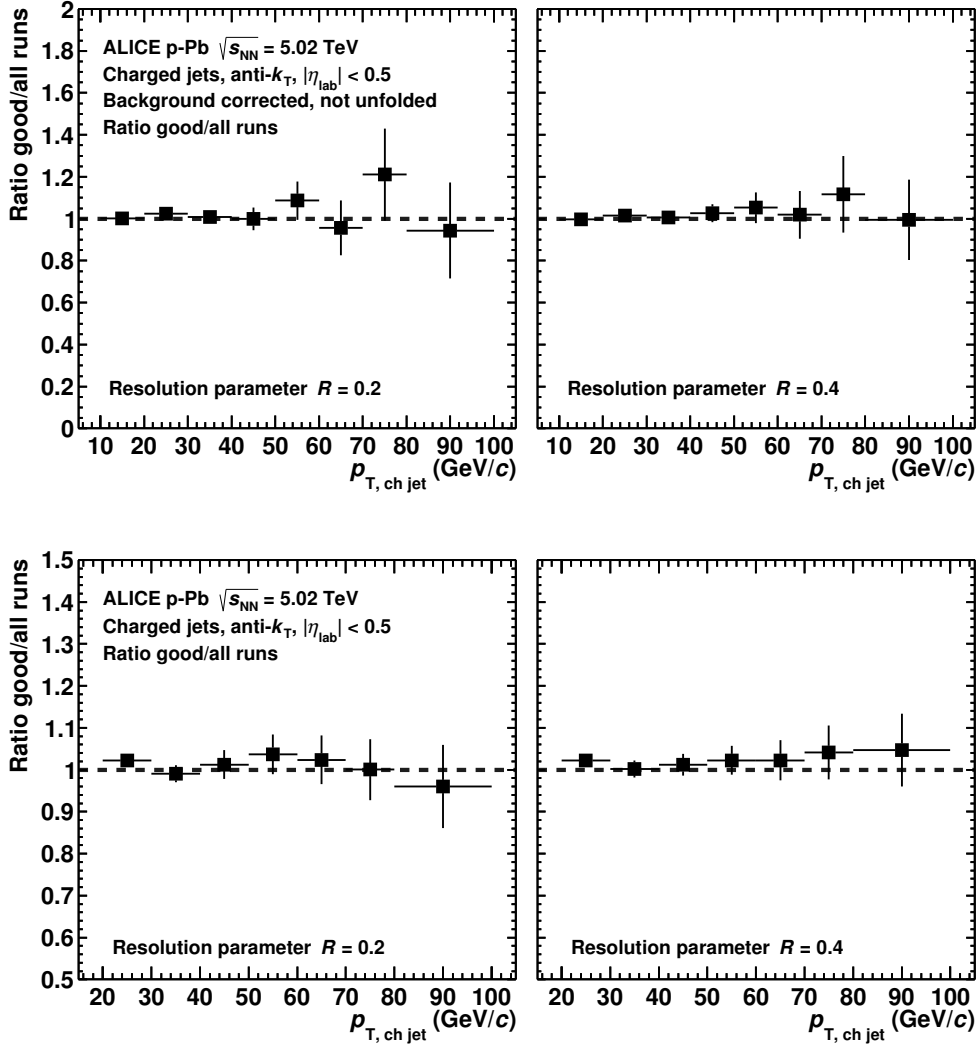


Figure 8.17: Ratio comparing background corrected raw jet spectra (upper plot) and fully corrected spectra (lower plot) for all and good runs only. The statistical uncertainties are calculated taking into account the correlation of both datasets.

Note that the good runs contain only about 20% of the total statistics. The comparison is thus expected to deviate within statistical uncertainties.

8.7. Comparison to charged particles

The main motivation for this comparison is found in the exciting measurement first presented by the CMS collaboration [Cha13]. At high transverse momentum, the charged particle nuclear modification factor shows a clear enhancement. The corresponding ALICE measurement shows no hint of this rise. Unfortunately, the ALICE transverse momentum range is too small to draw a final conclusion on the compatibility at high p_T . In Fig. 8.18(a), both measurements are presented.

Charged jets, which consist solely of charged particles, can principally be used to contribute to the discussion.

On the one hand, it must be emphasized that jet spectra are not equal to particle spectra. Jets and particles are very different objects on two different energy scales. On the other hand, both spectra are about the same if the different scales are adapted by “stretching” the particle transverse momenta scale to larger momenta. The reason for this is that the cross sections of the jet constituents and those of the initial partons have similar shapes. This connection is also known as Bjorken’s parent–child relationship [Bjo73] (cf. also [KB13]).

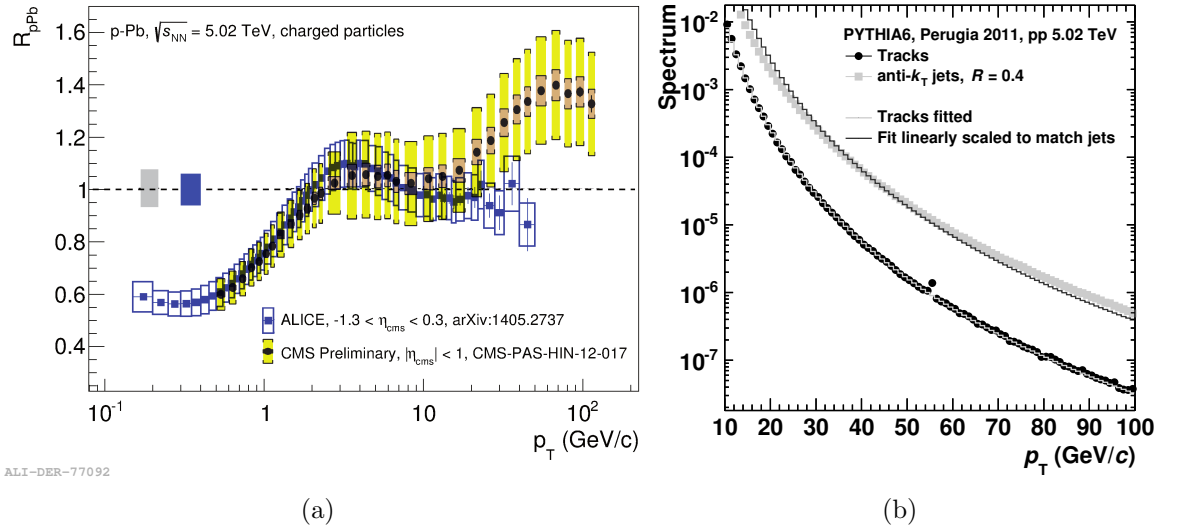


Figure 8.18: (a) Comparison of charged particle R_{pPb} measured by ALICE and CMS on logarithmic plot. (b) PYTHIA-generated jet and track distributions. The track distribution is fitted using a modified power-law function. The transverse momentum of the fit function is scaled according to Eq. 8.10 to match the jet distribution (also taking the Jacobian into account).

To obtain the relation of charged particle and jet spectra, a simple PYTHIA simulation has been performed. In Fig. 8.18(b), the generated track and jet distributions are de-

picted. Using a modified power-law function, the track distribution is fitted. Because of the parent–child relationship of partons and jet constituents, this fitted function has to be scaled linearly in transverse momentum. Technically, the optimum scaling factor is estimated again in a fit procedure, also taking into account the Jacobian as in [KB13]. It is used to scale the particle transverse momentum and is defined through

$$p_{T, \text{track}}^{\text{scaled}} = c \cdot p_{T, \text{track}}. \quad (8.10)$$

From the fit procedure, the dimensionless factor is evaluated to be 1.45. To put it simply, this means that a 10 GeV/ c track behaves like a 14.5 GeV/ c jet. The scaled track curve (black line) fits the jet spectra relatively well in first approximation.

However, a closer look reveals that the slope of the scaled curve is different than the jet distribution. In particular, the jet spectrum exhibits a harder distribution. Therefore, the evaluated scaling factor should only be understood as a reasonable guess and as a rough value of a first-order approximation. For the purpose of scaling relatively flat curves, i.e. the nuclear modification factors, the precision suffices though.

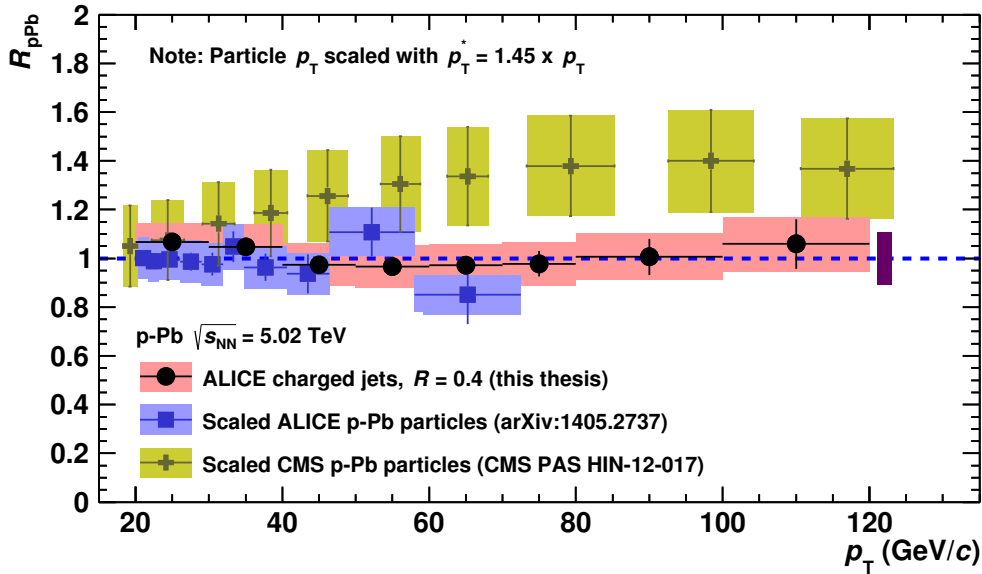


Figure 8.19: Comparison of different nuclear modification factors R_{pPb} for jets and particles. Note that the particle spectra are linearly scaled in p_T (see text).

In order to compare the nuclear modification factors for particles and jets, the particle spectra have been scaled. In Fig. 8.19, different nuclear modification factors are shown: for charged jets measured with ALICE (this thesis) and charged particles from ALICE [Abe14e] and CMS [Cha13].

While the difference of jet and particle spectra measured with ALICE is fully within uncertainties, the comparison to CMS charged particles introduces some tension though. Taking the systematic uncertainties fully into account, including the global normalization uncertainty of the charged jet R_{pPb} given by the magenta box, both results – ALICE charged jets and CMS charged particles – are still compatible within uncertainties.

It has to be emphasized again that jets are not particles. There is no reason to expect the jets to behave exactly like particles over the full transverse momentum range.

Consider as a simple example the abundance of gluon and quark jets, i.e. jets originating from scattered gluons or quarks. While gluon jets fragment softer and, therefore, contain more particles with less momentum, quark jets are harder. If there were more quark jets at high transverse momentum in p-Pb collisions compared to pp collisions, the particle R_{pPb} could possibly be enhanced, while the jet nuclear modification factor could remain unchanged. This could be checked by future analyses applying Monte Carlo simulations.

The CMS collaboration also measured jets in p-Pb. Here, a mild enhancement is observed, which is compatible within uncertainties with no enhancement and with the present work [Cha14].

And as shown in Fig. 8.5, also ATLAS measured jets, which are compatible with the results of this thesis. On the other hand, it is interesting that the ATLAS collaboration also measured an enhancement at highest p_T for charged particles [Bal14].

To conclude, there is no tension between the results of this thesis and the ATLAS or CMS results: The jet nuclear modification factors are fully compatible. However, it is currently not clear why the nuclear modification of the charged particles shows an enhancement at high p_T in the measurements of ATLAS and CMS.

In all collaborations, much work has already been done on finding the reason for this issue and to further investigate the findings. A massive improvement of the uncertainties for the particle nuclear modification factor is expected from a dedicated pp run at 5 TeV. Currently, the reference is interpolated and introduces a relatively large uncertainty. In principle, this also holds for jets. A smaller uncertainty in the pp reference would not change the physics conclusion though, because other uncertainties are also relatively large and, within uncertainties, the nuclear modification factor agrees with unity.

8.8. Comparison to fully reconstructed jets in p-Pb

In parallel with the charged jet analysis presented here, also fully reconstructed jets have been analyzed in ALICE (cf. e.g. [Con14]). In ALICE, full jets are reconstructed including also neutral particles (mainly photons), which can be measured with the EM-Cal [Cor08], an electromagnetic calorimeter. The calorimeter covers the pseudorapidity

interval $|\eta| < 0.7$ and roughly 107° in azimuth. While the EMCal is very sensitive to photons, e.g. from neutral pion decays, the neutron reconstruction capability is less precise.

Full and charged jets of course differ by construction. Because full jets additionally contain neutral particles, different jets are considered at the same measured jet transverse momentum. However, the nuclear modification factor R_{pPb} has been measured to be flat and compatible with one. Assuming a simple full jet/charged jet scaling relation, the same should pretty much hold also for full jets.

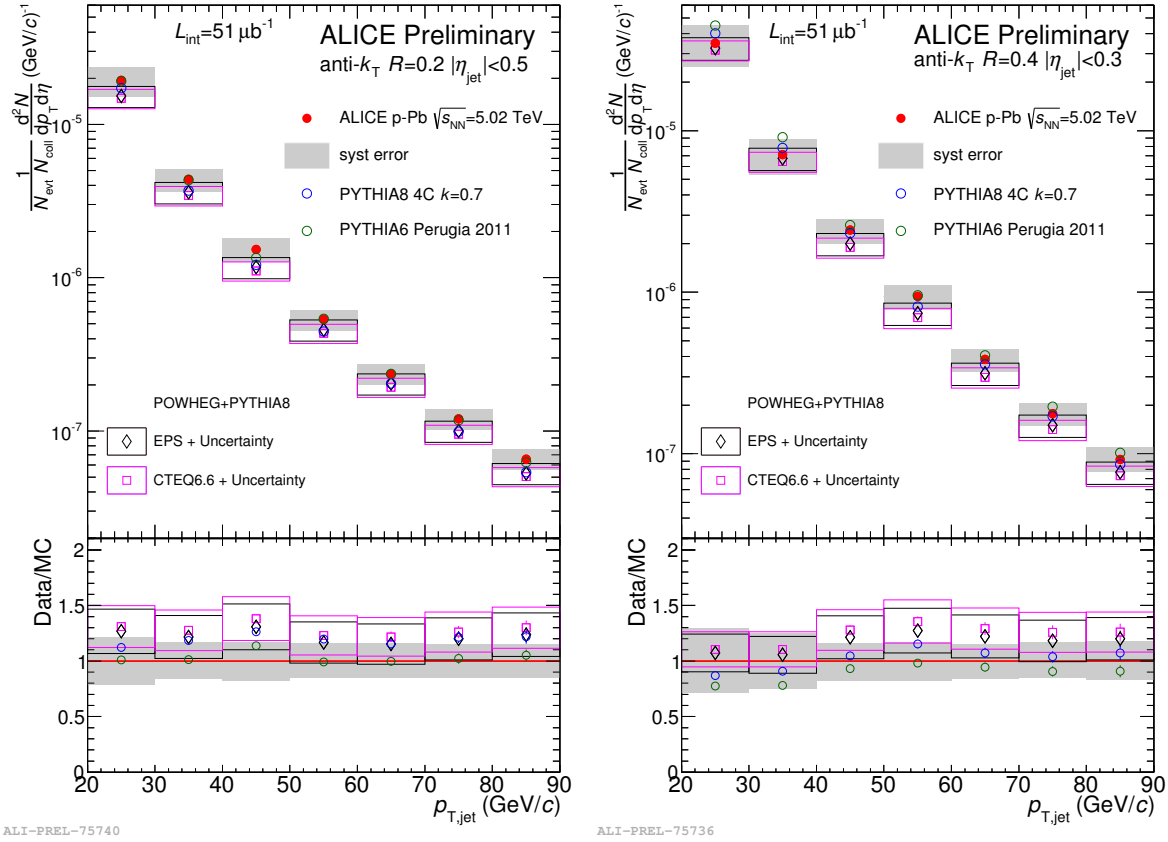


Figure 8.20: Spectra of fully reconstructed jets in p -Pb collisions measured by ALICE for $R = 0.2$ (left) and $R = 0.4$ (right) compared to several Monte Carlo simulations (bottom panels).

Preliminary results on full jets measured by ALICE are depicted for $R = 0.2$ and $R = 0.4$ in Fig. 8.20 [Con14]. The upper panels show the spectra while the lower panels represent ratios of the measured data to several Monte Carlo references.

Within the uncertainties, also the full jet results are compatible with small or no nu-

clear matter effects. The ratio plots indicate a strong dependence on the Monte Carlo reference though.

A direct comparison of the measured spectra is possible. Their relation, given by the spectra ratio charged/full jets, should be similar to the ratio obtained from Monte Carlo simulations. Roughly speaking, the larger transverse momentum of full jets corresponds to a shift of the full jet spectrum towards larger momenta. This translates into a larger jet yield and the charged/full jet spectra ratio should be smaller than one.

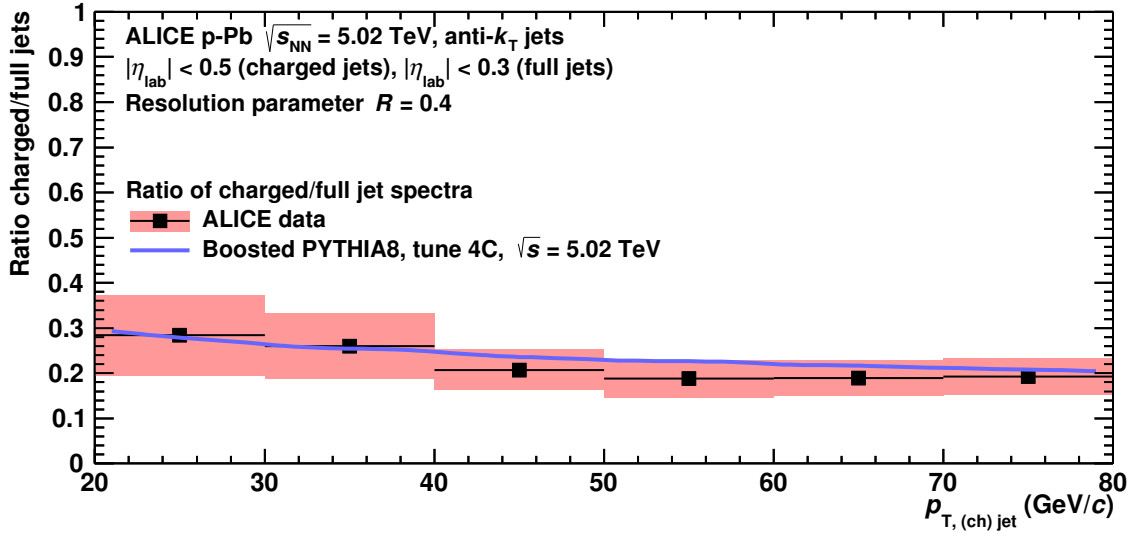


Figure 8.21: Ratio of charged and fully reconstructed jets in p-Pb collisions compared to MC prediction. Systematical uncertainties are depicted as red boxes. The statistical uncertainties are smaller than the data markers.

In Fig. 8.21, the charged jet spectra of this thesis and the preliminary full jet results are compared (for $R = 0.4$). In addition, the charged/full jet ratio is shown for Monte Carlo generated spectra. The ratios are in good agreement within the uncertainties. The results for $R = 0.2$ look very similar and are therefore not shown here.

Note that the uncertainties are probably overestimated. This is because many of the analysis parameters for the full and charged jet analyses are similar. For example, the uncertainty in the tracking efficiency is partly correlated in both analyses and should cancel to a certain fraction. However, the degree of correlation is not known and, therefore, no correlation has been assumed as a conservative estimate. For a very similar reason, the uncertainties of the Monte Carlo simulation are not shown: Most of the systematic uncertainties probably cancel in the ratio charged/full jets. But in principle, a very small uncertainty should remain for the ratio. Since this remaining uncertainty is not known, it is considered as negligible and omitted here.

9. Systematic uncertainties

Systematic uncertainties can be determined by the deviations of the observables when changing analysis parameters within reason. Analysis parameters are to be understood as numerical values as well as analysis methods or techniques. The more complex an analysis is the more important these uncertainties become. Jet analysis is relatively complex and especially the unfolding procedure is a source of uncertainties. Therefore, the evaluation of the systematic uncertainties is an integral part of the analysis. In Sec. 5.5.2, the basic idea of how to calculate the systematic uncertainties has already been described.

Unfortunately, there is no unambiguous way for the evaluation of uncertainties. A lot of effort was put into identifying possible uncertainty sources and their impact on jet analysis in this thesis and in preceding analyses.

A typical problem in the evaluation of the uncertainties is that it is not always clear how to decide whether a certain analysis parameter belongs to the definition of the measured objects or if it can be considered as a freely choosable parameter.

As an example, consider the jet finding algorithm. In this thesis, signal jets are solely reconstructed using the anti- k_T algorithm.² On the one hand, one could argue that this algorithm should be compared to other jet finding algorithms in order to estimate the uncertainty on the jets from the choice of the algorithm itself. But on the other hand, the jet algorithm could be considered as part of the definition of the observable. Here, the latter consideration is done and there is by construction no uncertainty on the chosen jet algorithm.

Another difficulty in the uncertainty calculation is that it is a priori not clear what a reasonable variation is, which is used for varying the parameter within reason.

For example, consider the regularization strength of the SVD unfolding technique. A certain integer value k is chosen as the nominal value. A reasonable variation could now be an upward or downward variation or both, e.g. $k \pm 1$, but at least in principle also $k \pm 2$.

Another complication is given by the fact that it is also unclear how to treat the deviations of the observables produced by parameter variations. Should they be treated as maximum errors or as Gaussian-distributed errors?

²The k_T algorithm is used for background evaluation only.

The whole procedure leaves some room for interpretation of the systematic uncertainty. In principle, the uncertainties in the individual parameters represent the ranges in which the analysis results is expected to vary when changing those parameters. In the following, the chosen parameters and the impact on the observables is presented in detail. The uncertainties are subdivided into four distinct categories: unfolding, background estimate, single-particle tracking efficiency, and normalization.

In order to estimate the uncertainty on the nuclear modification factor R_{pPb} , the uncertainties in the p–Pb numerator and pp denominator are taken as uncorrelated uncertainties and are propagated, except for the tracking efficiency uncertainty (see below).

The jet production cross section ratio uncertainty is evaluated in the same way as it is done for the spectra: The observable is calculated for different parameter configurations and the deviations are used for the estimation of the uncertainties. In principle, the uncertainty could also be calculated by propagating the $R = 0.2$ and the $R = 0.4$ spectra uncertainties into the ratio. This would overestimate the uncertainties since both spectra are partly correlated. Additionally, using the same analysis parameters for numerator and denominator is most sensible for the calculation of the jet production cross section ratio.

This chapter provides detailed information on the example of the $R = 0.4$ jets in minimum bias p–Pb collisions. In the summary section, the uncertainties are also given for the $R = 0.2$ jet observables. Detailed plots for $R = 0.2$ can be found in Appendix A.2.1.

9.1. Unfolding

Unfolding is an important component of the jet analyses in this thesis. Much effort was put on the evaluation of the optimum unfolding parameters and the analysis of the behavior of the different methods (cf. Sec. 6.2). To estimate the uncertainty of the whole unfolding procedure, several parameters have been varied.

9.1.1. Unfolding method

The baseline measurement uses SVD unfolding. Additionally, also χ^2 -unfolding, Bayesian unfolding, and a manual unfolding approach were tested. The manual unfolding was only tested for sanity checks and is not considered for systematic uncertainties, because it does not include an explicit regularization.

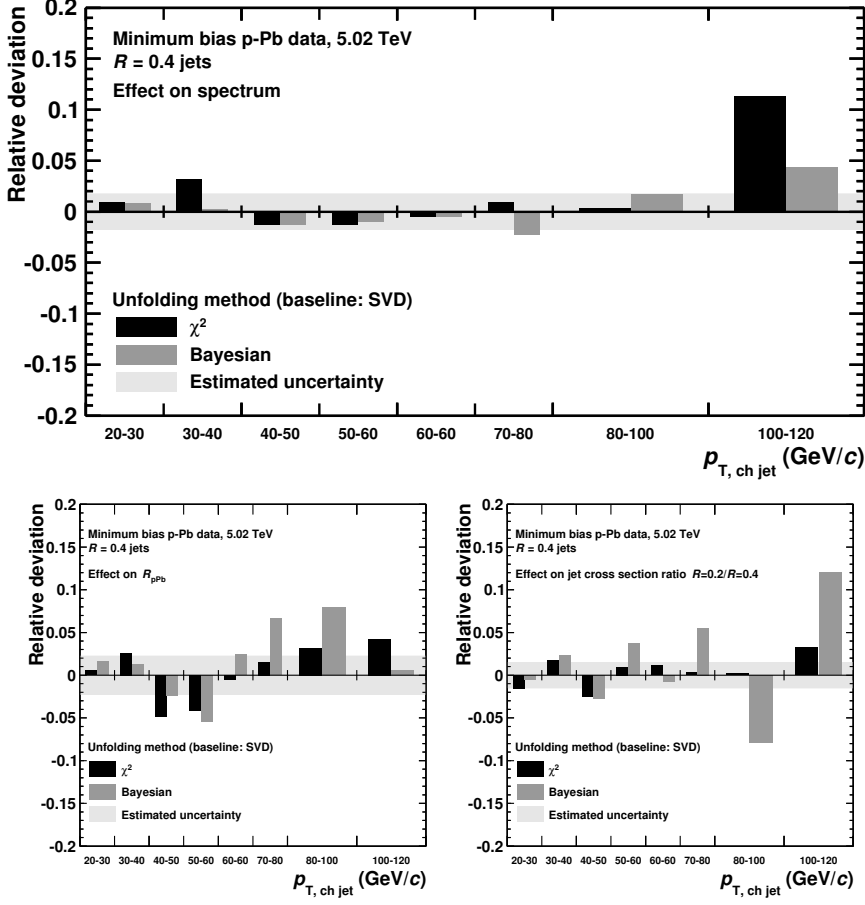


Figure 9.1: Relative deviations of varied spectrum (upper plot), R_{pPb} (left), and jet production cross section ratio (right) from the corresponding baselines when changing unfolding method.

Just using the bin-by-bin differences of the spectra to calculate the uncertainty would overestimate it as there are different strengths of statistical fluctuations. Therefore, a mean uncertainty value is calculated using the deviations of the baseline and the χ^2 -unfolded and Bayesian-unfolded spectra.

The relative deviation when using a different unfolding method is shown in Fig. 9.1. While the deviations of the single unfolding methods are depicted as bars, the final uncertainty is shown as a gray band around zero for the considered bins. Additionally to the uncertainty of the spectrum, also the uncertainties on R_{pPb} and the jet cross section ratio are shown in Fig. 9.1. This figure template is also used for the other uncertainties.

Note that the final uncertainties for R_{pPb} are calculated by propagating the uncertainties in numerator and denominator, as described above. Therefore, the deviations of R_{pPb} do not necessarily have to represent exactly the systematic uncertainty.

9.1.2. Regularization strength

The variation of the regularization strength in an SVD unfolding procedure is possible only in integer steps. The baseline strength $k = 5$ was chosen based on test results (see Sec. 6.2.3) and the variation was done by varying $k \pm 1$. In Fig. 9.2, the relative deviations are shown.

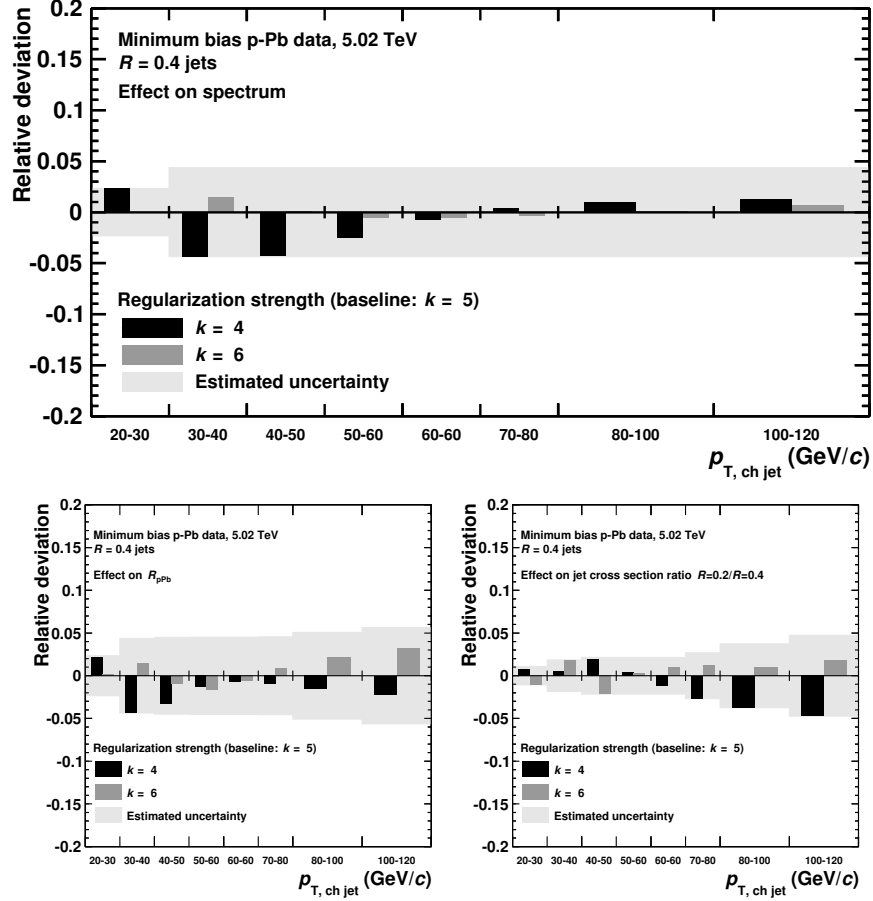


Figure 9.2: Relative deviations of varied spectrum (upper plot), R_{pPb} (left), and jet production cross section ratio (right) from the corresponding baselines when changing regularization strength.

The uncertainty estimated from the variation (the gray band in Fig. 9.2) is not allowed to fall in p_T . Note that this probably leads to a slightly overestimated uncertainty. This specific constraint is applied, because the regularization smooths the whole spectrum and especially the highest p_T bins, for which the statistics are low. This smoothing reduces the statistical fluctuations but also increases the systematic uncertainty. The regularization strength uncertainty takes this into account.

9.1.3. Prior

All unfolding methods need a prior distribution. This distribution has to be similar to the expected true distribution. For the analyses in this thesis, a modified power-law fit of the data was used as prior distribution.

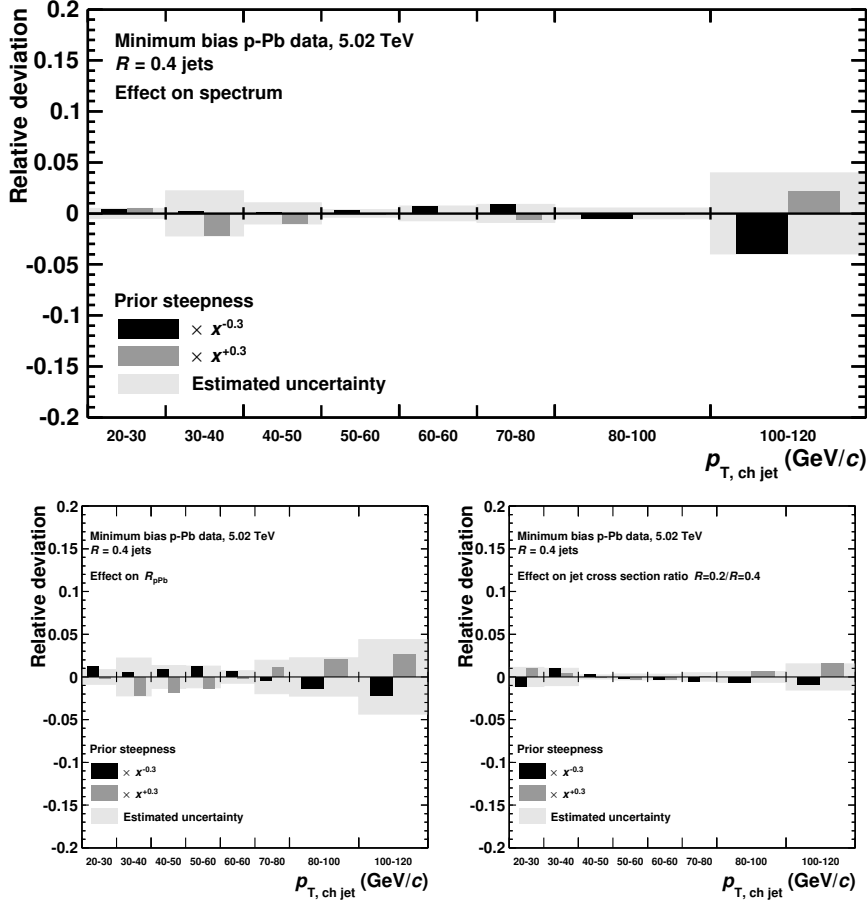


Figure 9.3: Relative deviations of varied spectrum (upper plot), R_{pPb} (left), and jet production cross section ratio (right) from the corresponding baselines when changing the steepness of the prior.

Many other choices were tested for sanity checks and it turned out that the results do not very strongly depend on the shape of the prior. However, a fluctuating prior proved to produce fluctuating unfolded results. In Fig. 9.4, this behavior is illustrated for an unfolding toy model: While the result is essentially the same using a prior fitted to $R = 0.2$ or $R = 0.4$ jets (slightly different shapes of the distributions), fluctuations are plainly visible when using the data-based prior. Note that the given example is chosen for illustration purposes. Usually, the effect is less strong, but principally the same.

Therefore, a fit is used as prior distribution to avoid the implementation of statistical uncertainties in the prior.

In order to estimate the sensitivity to the prior, the steepness of the prior distribution is changed by multiplication with a power law

$$f_{\text{prior}}^{\text{new}} = f_{\text{prior}} \times p_{\text{T}}^{\pm 0.3}. \quad (9.1)$$

The corresponding uncertainty plots can be found in Fig. 9.3.

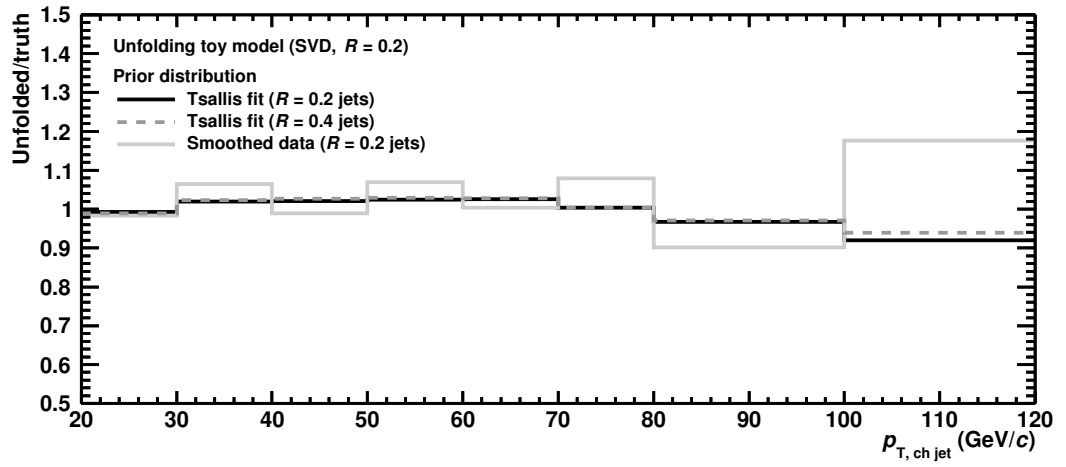


Figure 9.4: Ratio toy model unfolded/truth for $R = 0.2$ jets for different priors.

9.1.4. Minimum p_T threshold

The full unfolding procedure is carried out for a specific binning. Of course, the analysis should not be too sensitive to changes in this binning. To estimate the uncertainty arising from the arbitrarily chosen binning, the minimum measured jet p_T and the minimum unfolded jet p_T are varied. By default, it is $p_{T, \text{ch jet}}^{\text{measured}} > 10 \text{ GeV}/c$ and $p_{T, \text{ch jet}}^{\text{unfolded}} > 0 \text{ GeV}/c$.

The impact is evaluated for the tighter cuts $p_{T, \text{ch jet}}^{\text{measured}} > 15 \text{ GeV}/c$ and $p_{T, \text{ch jet}}^{\text{unfolded}} > 5 \text{ GeV}/c$. Note that this uncertainty was also evaluated in several other jet analyses, e.g. in [Ver13].

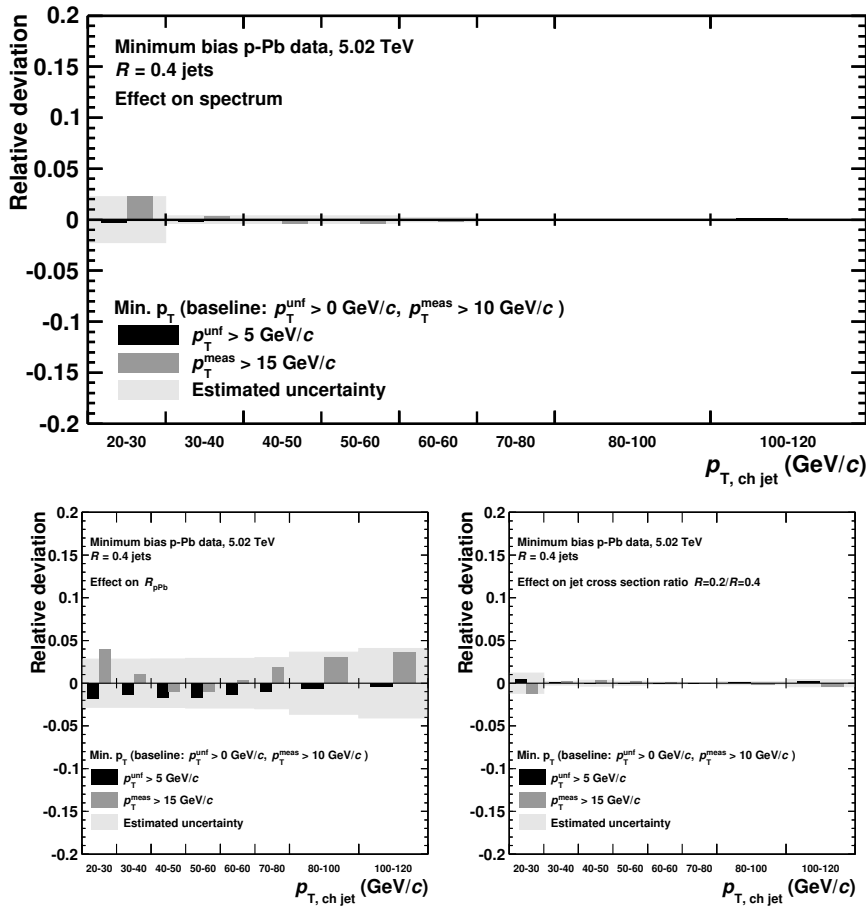


Figure 9.5: Relative deviations of varied spectrum (upper plot), R_{pPb} (left), and jet production cross section ratio (right) from the corresponding baselines when changing the minimum p_T in the analysis.

9.2. Background

As described in Sec. 6.1, the optimum background evaluation technique is not known. Although there are strong reasons to believe that the default p–Pb approach is a reasonable choice, it is not clear how precise the background is subtracted from the jets. Therefore, different approaches were tested and considered for systematic uncertainties.

For the sake of completeness, also the impact of using or not using a signal exclusion for δp_T is shown.

9.2.1. Signal exclusion in δp_T

As described in detail in Sec. 6.1.3, the random cone that probes the event has a slightly higher probability to overlap a jet than a jet which is produced in a hard scattering. However, simply excluding a certain percentage of random cones overlapping with jets is an ambiguous task. In short, the ambiguity is introduced by the definition of what a jet is.

Hence, by default no signal exclusion is used. In fact, it turns out that the effect on the final jet spectra is completely negligible, see Fig. 9.6.

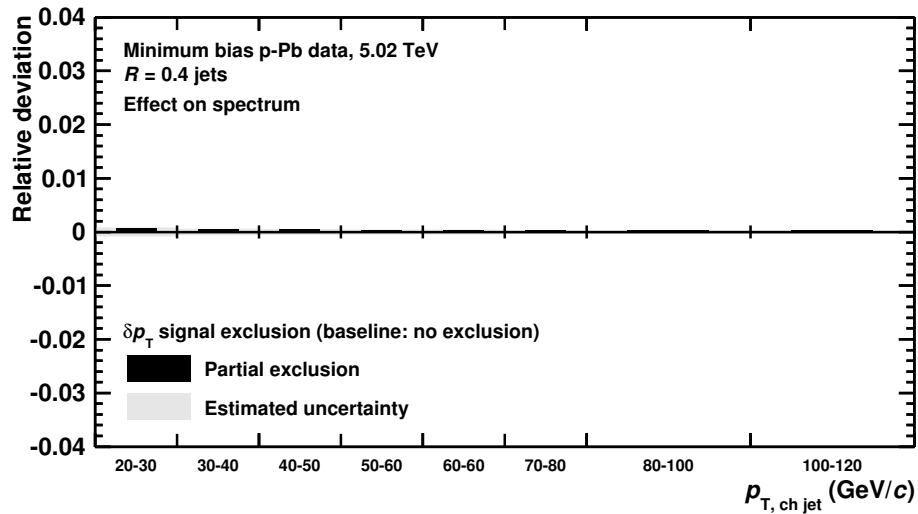


Figure 9.6: Relative deviations of varied spectrum from the baseline when using a signal exclusion in the evaluation of δp_T in the analysis.

9.2.2. Background estimate

Comparing the results of the different background evaluation techniques, it turns out that they produce very similar results. Tests show that for the final result it is not so

much important which background technique is used as the fact *that* the background is subtracted.

For the evaluation of the background estimate uncertainty, the two mean-based methods were considered. Other methods described in Sec. 6.1 are regarded as unrealistic choices and are therefore not compared to the default baseline approach.

In Fig. 9.7, the results of the track-based approach are shown as well. The track-based approach is conceptually the simplest and does not rely on the k_T algorithm. It is expected to overestimate the background because of signal contamination by hard scatterings though. But even for this simple and biased method, the eventual effect on the jet spectra turns out to be relatively small.

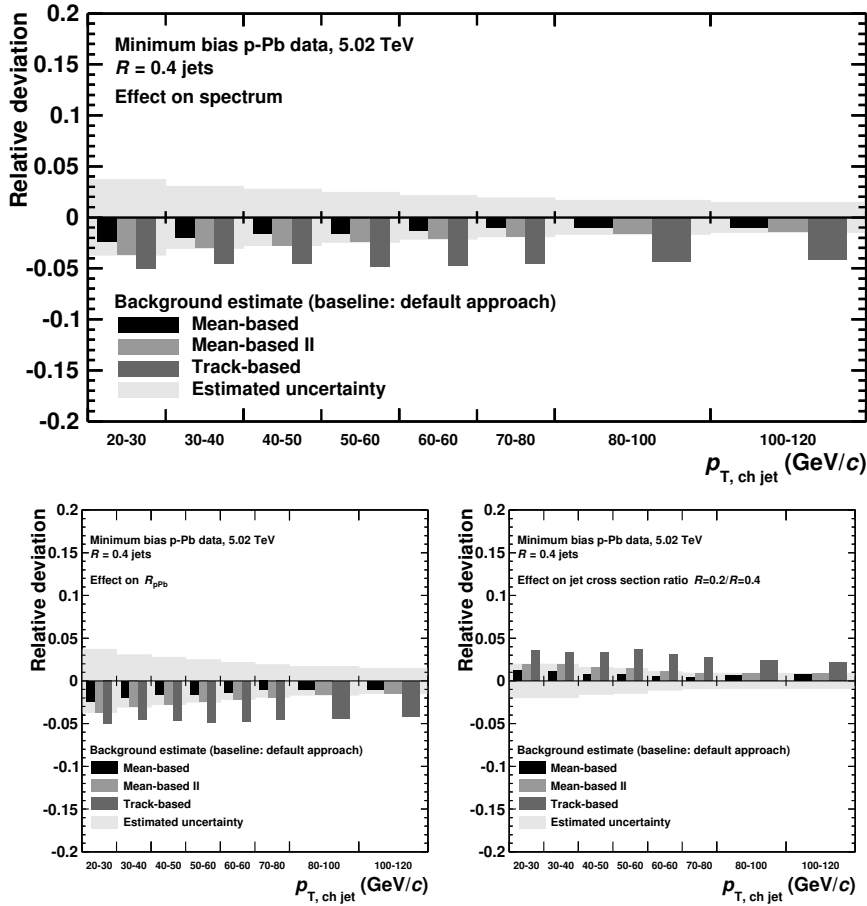


Figure 9.7: Relative deviations of varied spectrum (upper plot), R_{pPb} (left), and jet production cross section ratio (right) from the corresponding baselines when varying the background estimate in the analysis.

9.3. Tracking efficiency

The single-particle tracking efficiency is corrected for implicitly in the unfolding procedure using a response matrix created with a full detector simulation. The predominant contribution to the overall uncertainty of the jet analyses, especially for the bare spectra, originates from this uncertainty. This is mainly because an uncertainty on the jet momentum – introduced by the tracking efficiency – translates into a much larger uncertainty on the jet yields/cross sections. This is a consequence of the steepness of the spectrum: A small change in jet momentum means a much larger change in the jet yield. For instance, when comparing 20 and 24 GeV/ c jets with $R = 0.4$ (5% more transverse momentum), 60% less jets are constructed for the larger transverse momentum.

9.3.1. Evaluation of tracking efficiency uncertainty

There are currently efforts to calculate a collaboration-wide value for the tracking efficiency. Up to date, there is no such uncertainty value for the tracking efficiency uncertainty in p–Pb collisions recorded with ALICE. Therefore, and also to estimate the degree of correlation of the uncertainties in p–Pb and 7 TeV pp collisions, the evaluation had to be done for this analysis.

In this thesis, a commonly known approach used before in ALICE was applied to estimate the uncertainty on the tracking efficiency: For different track cut parameters, the tracking efficiency was measured in data and Monte Carlo simulations. The differences in the efficiencies are interpreted to come from an imperfect detector description in the Monte Carlo model and are hence a measure for the tracking efficiency uncertainty.

Apart from the uncertainty originating from the track cuts, also the uncertainty in the TPC-ITS/ITS-TPC track matching efficiency is taken into account in the same way as it was done for the track cuts. Technically, the TPC-ITS matching is switched off by applying no cuts on the χ^2 of the TPC-constrained track and the ITS clusters. The impact of the ITS-TPC matching is tested by explicitly matching or not matching.

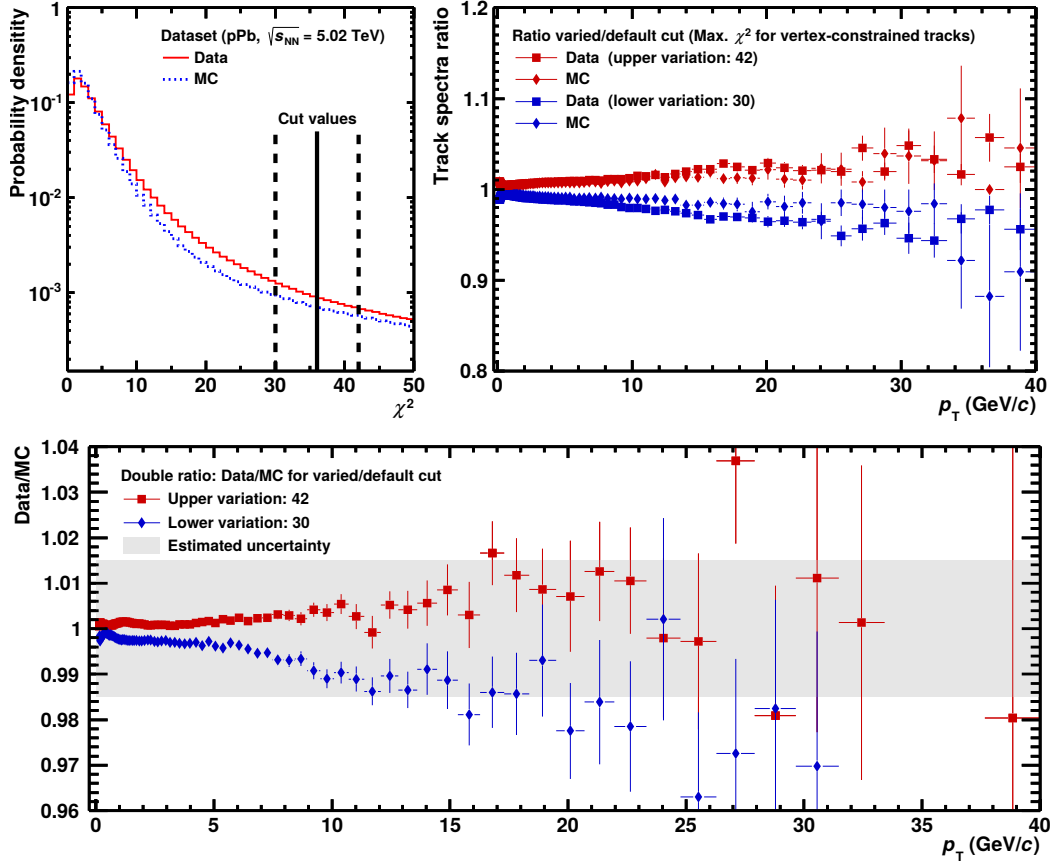


Figure 9.8: Illustration of the analysis to extract the systematic uncertainty on the tracking efficiency for the χ^2 cut on vertex-constrained tracks. The cut variation values, here the value of max. χ^2 for vertex-constrained tracks, are given in the legends: 30 is the lower variation, 42 the upper variation.

The following procedure is performed to extract the tracking efficiency uncertainty. A depiction of the necessary steps is exemplary shown for the χ^2 cut for vertex-constrained tracks in Fig. 9.8:

1. Change all free track cut parameters within reason,
2. evaluate the impact of the variation in data and Monte Carlo,
3. calculate the double ratio that compares the impacts of variations in data and Monte Carlo,

$$\frac{\text{Data}}{\text{MC}} = \frac{\frac{\text{Data with varied cut}}{\text{Data with default cut}}}{\frac{\text{MC with varied cut}}{\text{MC with default cut}}}, \quad (9.2)$$

4. extract one uncertainty value for each cut parameter from the strongest (reliable) deviation from unity,

5. calculate the full uncertainty by summing up all single uncertainties, assuming they are uncorrelated.

The question what reasonable variations are, is often hard to decide. To exclude unrealistic variations, the distributions of the cut values are examined in data and Monte Carlo. It is expected that the detector description is best in the parameter region of the nominal cut values. A detailed description of the parameters that are varied is given in Sec. 7.3.1.

In the following, the cut variation effects are shown for all varied cut parameters together with the extracted uncertainty value. The above mentioned double ratios are shown for pp and p-Pb. Additionally, for those cuts shared by the pp and p-Pb analyses, also the difference between both double ratios is shown. This difference can serve as a visual hint on how strong the uncertainties are correlated for both datasets.

Initially, the extraction of the degree of correlation of the tracking efficiency uncertainty in pp and p-Pb has been the main motivation for the whole track cut analysis: The uncorrelated uncertainty can be directly used as uncertainty for R_{pPb} , reducing massively the overall systematic uncertainty. Without this analysis, the tracking efficiency uncertainty should actually be assumed as fully uncorrelated in pp and p-Pb.

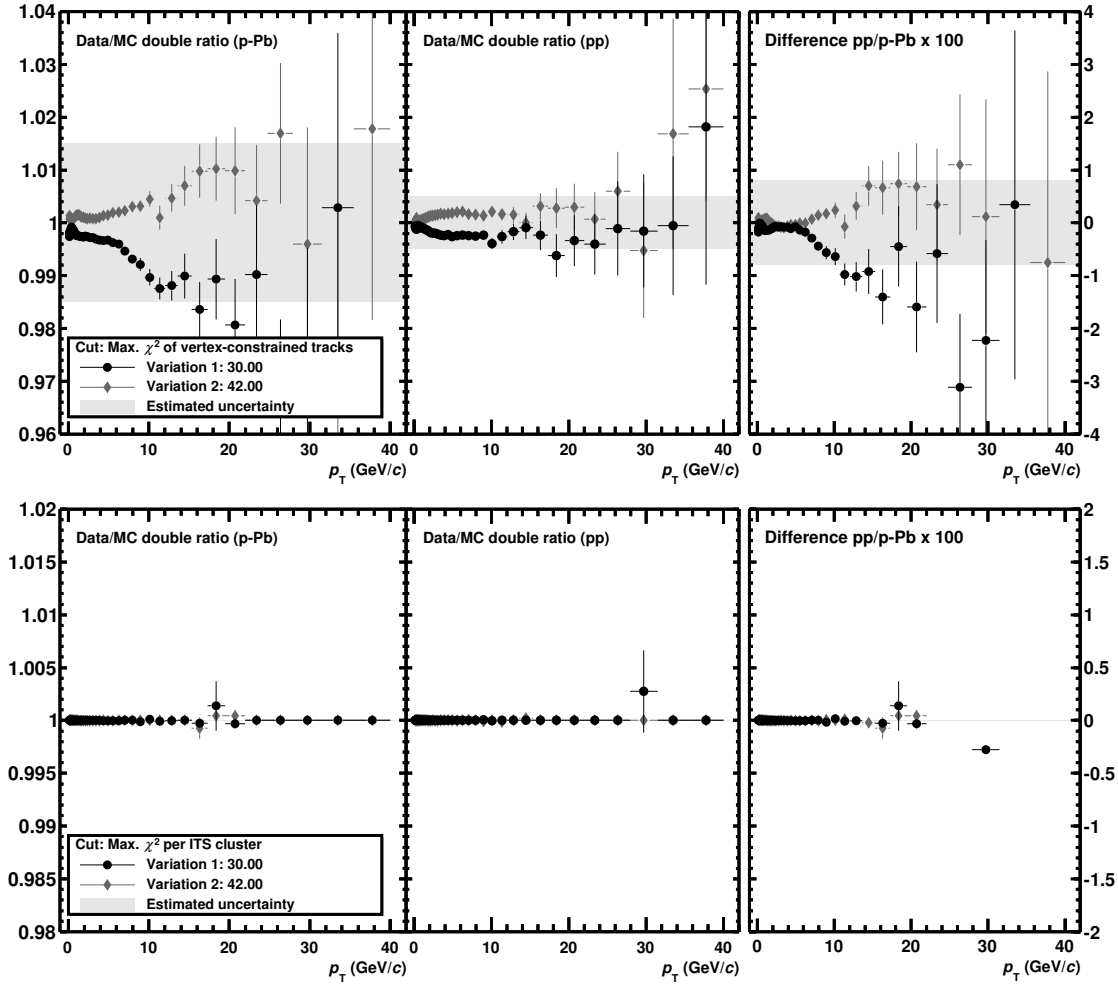


Figure 9.9: Data over MC double ratios in p-Pb and pp. The difference of both, pp-p-Pb, is shown on the right-hand side.

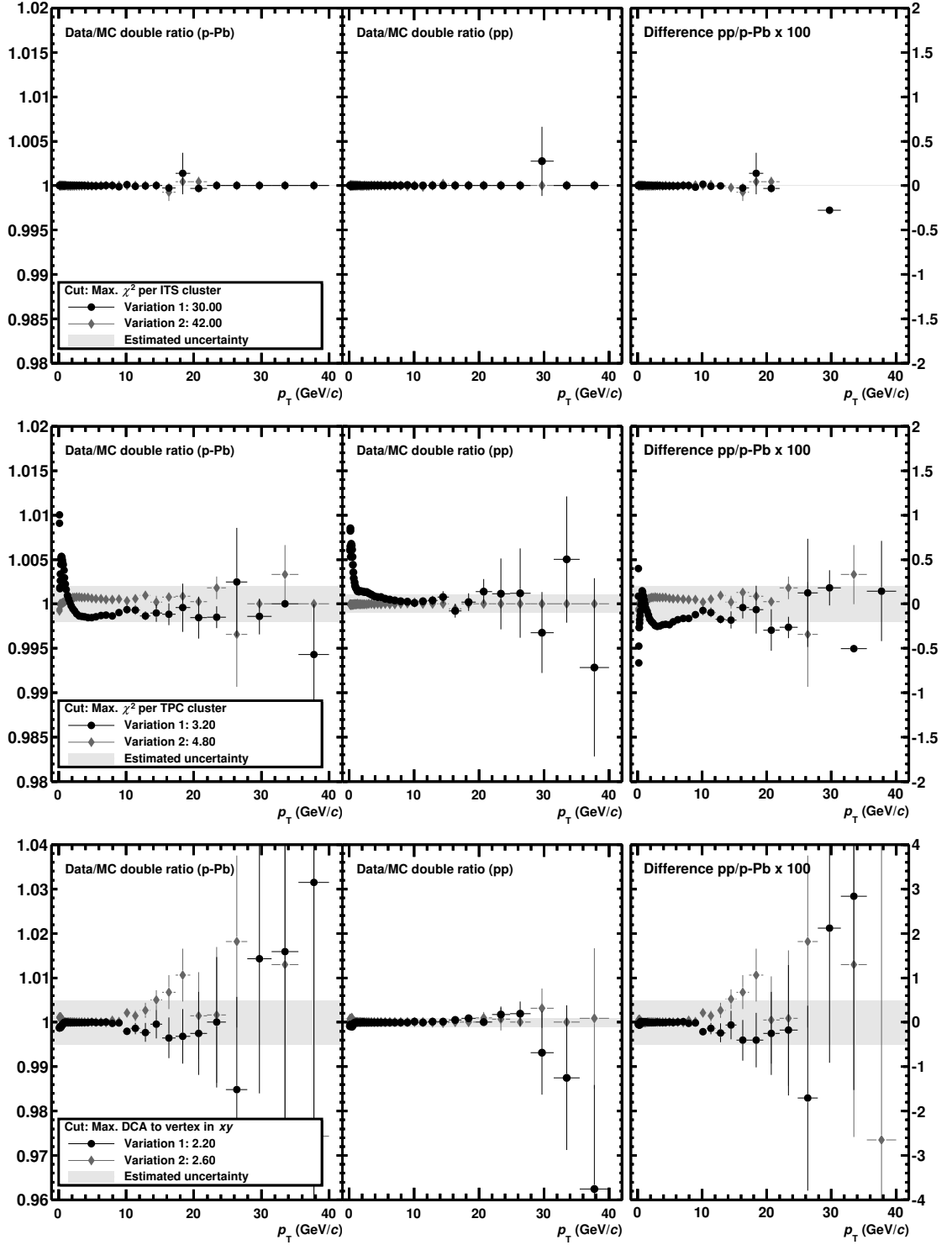


Figure 9.10: Data over MC double ratios in p-Pb and pp. The difference of both, pp-p-Pb, is shown on the right-hand side.

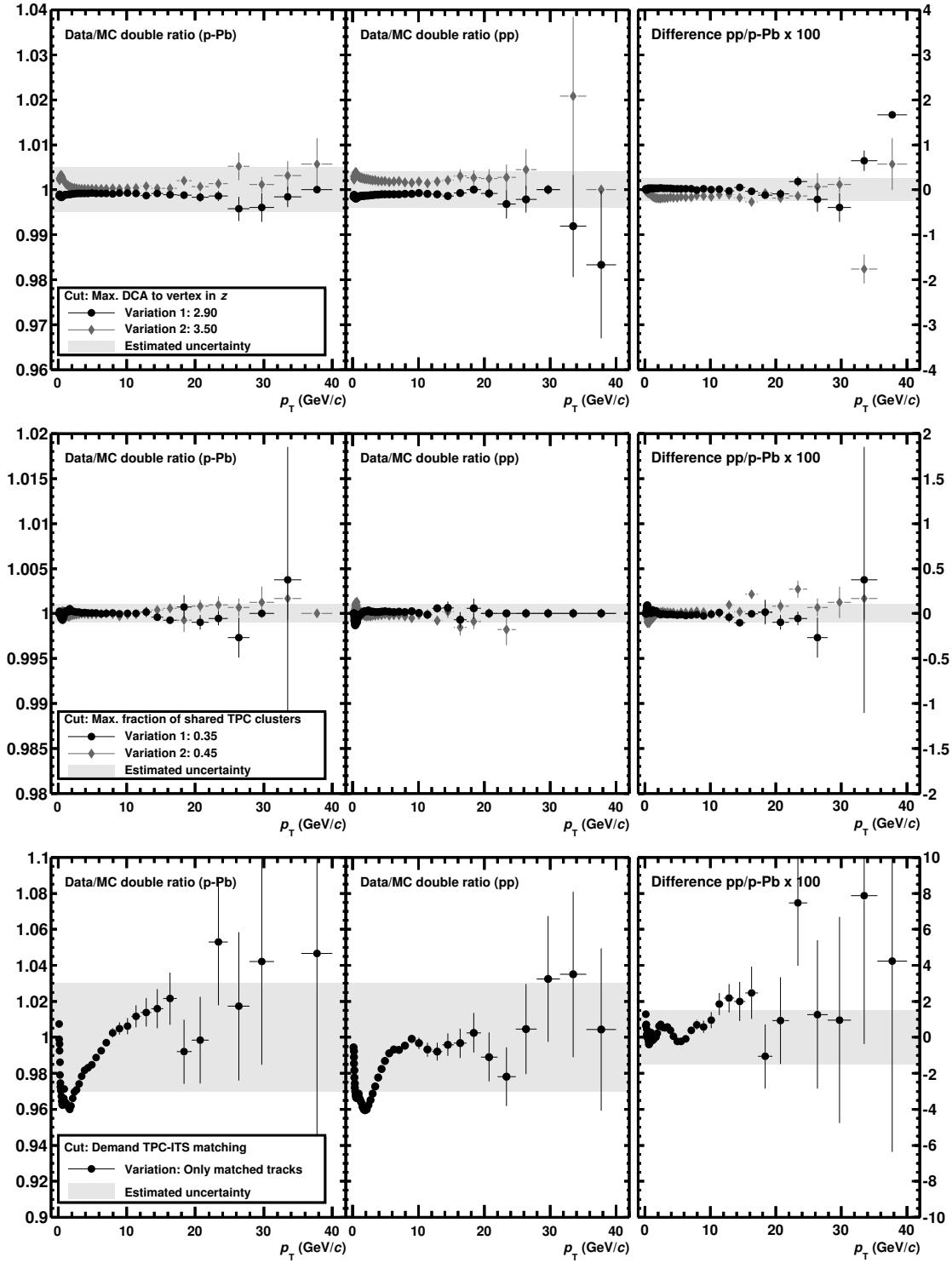


Figure 9.11: Data over MC double ratios in p-Pb and pp. The difference of both, pp-p-Pb, is shown on the right-hand side.

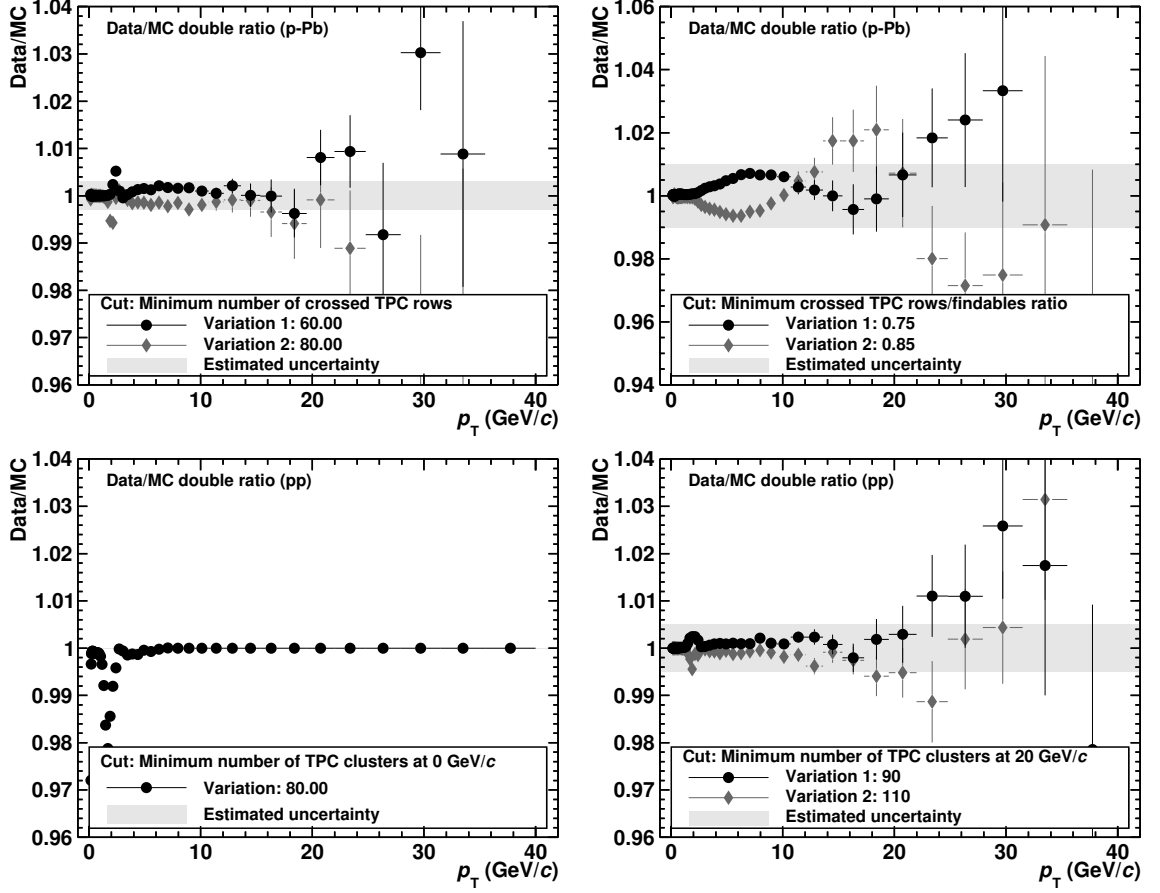


Figure 9.12: Data over MC double ratios for p–Pb-specific cuts (upper plots) and pp-specific cuts (lower plots).

For the track cut analysis, the p–Pb and pp data samples described in Sec. 7.1 were analyzed. In addition, Monte Carlo productions are needed to test the detector description. For p–Pb, the production LHC13b2_efix was used. This is a DPMJET dataset with $\sqrt{s_{NN}} = 5.02$ TeV using the detector configurations of the p–Pb run. For pp, the 7 TeV PYTHIA dataset LHC10f6a was used. It is anchored in the LHC10d runs, which were used for the pp analysis.

From this analysis, the relative uncertainty of the tracking efficiency for p–Pb is determined to be 4% in total (see Tab. 9.1). Taking into account the correlation of the uncertainties of the utilized pp and p–Pb datasets, the uncertainty for the nuclear modification factor R_{pPb} is estimated to be 2%. R_{pPb} is a ratio of p–Pb and pp data and, therefore, the uncertainty partly cancels out.

Note that these uncertainties are justified estimates. Further analyses, probably also making use of different Monte Carlo simulations and perhaps more adequate cut value variations, are necessary to extract more precise values.

Table 9.1: Uncertainties on the tracking efficiency for the different tracking parameters.

Uncertainty type	Uncertainty values (in %)		
	p-Pb	pp	R_{pPb}
χ^2 for vertex-constrained tracks	1.5	0.5	0.8
χ^2 per ITS cluster	0.0	0.0	0.0
χ^2 per TPC cluster	0.2	0.1	0.2
DCA to vertex cut in xy	0.5	0.1	0.5
DCA to vertex cut in z	0.5	0.4	0.25
Fraction of shared TPC clusters	0.1	0.1	0.1
ITS-TPC and TPC-ITS matching	3.0	3.0	1.5
Crossed rows	0.3	–	0.3
Min. ratio crossed rows/findables	1.0	–	1.0
Number of clusters	–	0.0	0.0
Slope of cluster cut p_{T} dependence	–	0.5	0.5
Total	$3.6\% \approx 4\%$	$3.1\% \approx 3\%$	$2.1\% \approx 2\%$

9.3.2. Effect on jet observables

The evaluation of the impact of the tracking efficiency uncertainty on the jet spectrum can be done in several ways. For example, tracks can be discarded with a given probability simulating the effect of a reduced tracking efficiency before the jet finding takes place. A clear drawback of this method is that statistics is lost.

Another approach is to introduce a varied tracking efficiency in the detector response. This approach was chosen in this thesis. Here, tracks are discarded with a given probability in the creation of the response. Of course, statistics is also lost in this case but the simulated datasets do not suffer from poor statistics even at high p_{T} .

The response matrices in p-Pb, which have been created that way, describe the detector with a reduced tracking efficiency (4% in p-Pb, 3% in pp, see Sec. 9.3.1). This means that the jet spectra unfolded with such a response are enhanced compared to those unfolded with the nominal tracking efficiency.

The uncertainties of the spectra are simply extracted from the differently unfolded spectra, using nominal and 4% reduced tracking efficiency. To estimate the uncertainty on the nuclear modification factor, the spectra with 4% reduced and 6% reduced efficiency are compared. Principally, this is equivalent to comparing nominal and 2% reduced efficiency.

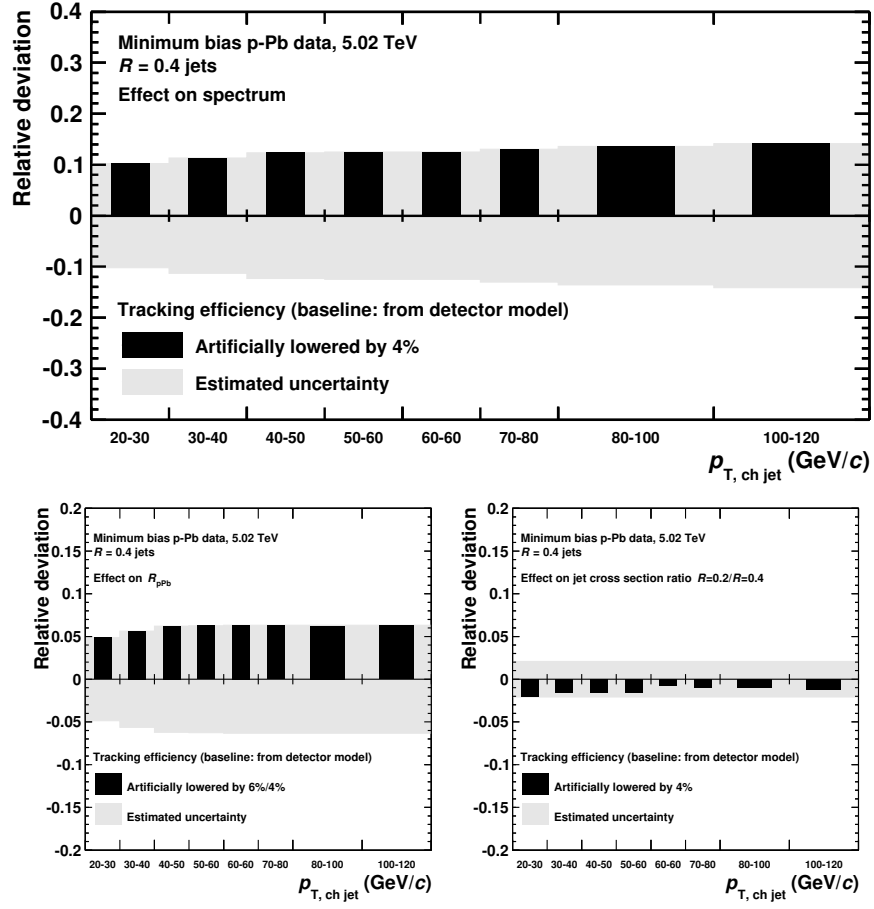


Figure 9.13: Relative deviations of varied spectrum (upper plot), R_{pPb} (left), and jet production cross section ratio (right) from the corresponding baselines for reduced tracking efficiency.

Note that the jet yield uncertainty is obtained by *reducing* the tracking efficiency by a certain percentage. It is assumed that this uncertainty is also the same if the tracking efficiency was artificially *enlarged* by the same amount.

9.4. Normalization

The normalization of the different observables is performed using several parameters. Depending on the observable, the normalization is different. A graphical summary of the normalization uncertainties can be found in Fig. 9.14.

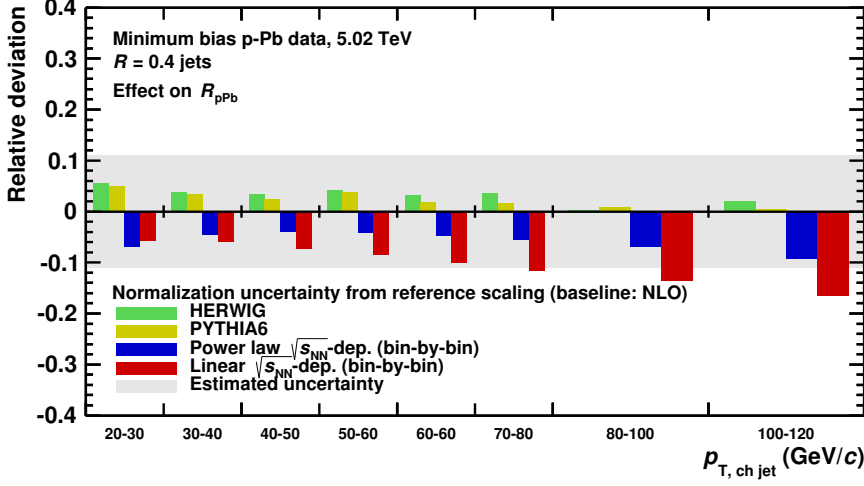


Figure 9.14: Relative deviations of varied R_{pPb} from the corresponding baselines for different reference scaling techniques. Note that the depicted total uncertainty (gray band) also includes all normalization uncertainties for the nuclear modification factor and not only those of the energy scaling.

Since the spectra are shown as cross sections, they are normalized to the total (visible) cross section in p-Pb. This cross section was measured by a van-der-Meer scan to $\sigma_{V0} = 2.09 \pm 0.07$ b. According to the corresponding publication [Abe14c], the exact systematic uncertainty is 3.5%.

In order to create the nuclear modification factor R_{pPb} , several uncertainties enter the calculation. First, the p-Pb jet spectra are scaled with the nuclear overlap function T_{pPb} , given by $T_{pPb} = 0.0983 \text{ mb}^{-1} \pm 3.4\%$ [Ada14]. This introduces a relative uncertainty of 3.4%.

The NSD efficiency correction, which has also been performed for the p-Pb spectra, is only poorly known, leading to an uncertainty of 3.1%.

Additional normalization uncertainties for R_{pPb} can be found in the pp reference. The measured jet yields have to be scaled with the total (visible) cross section in pp. It is measured to be 62.2 ± 2.2 mb [Abe13c], which introduces an uncertainty of 3.5%. In addition, the jet spectra have been measured at 7 TeV and have to be scaled down to 5 TeV. In Sec. 8.2, this procedure is described in detail. The uncertainty on this scaling

is estimated using several different scaling factors. The NLO baseline is compared to PYTHIA6- and HERWIG-generated scaling factors. These scaling factors differ mainly in normalization and, therefore, a mean uncertainty value is calculated and used as normalization uncertainty. This yields an uncertainty of 3.3%.

In order to additionally compare the nominal scaling to a non-MC-based energy scaling, the scaling factors have also been calculated using a bin-by-bin power-law interpolation between fitted measured ALICE spectra at 2.76 TeV and 7 TeV. The deviations to the nominal scaled spectra yields an uncertainty of about 5.8%.

At last, also the slight difference between the official 7 TeV charged jet measurement [Abe14a] and the measurement done for this thesis is taken into account. A small deviation is expected, since the utilized analysis frameworks were completely different and some analysis details like binning, background method, or regularization strength were chosen in a slightly different way. Therefore, the mean difference of the analysis carried out for this thesis and the final official result, amounting to roughly 6%, is taken as an additional normalization uncertainty.

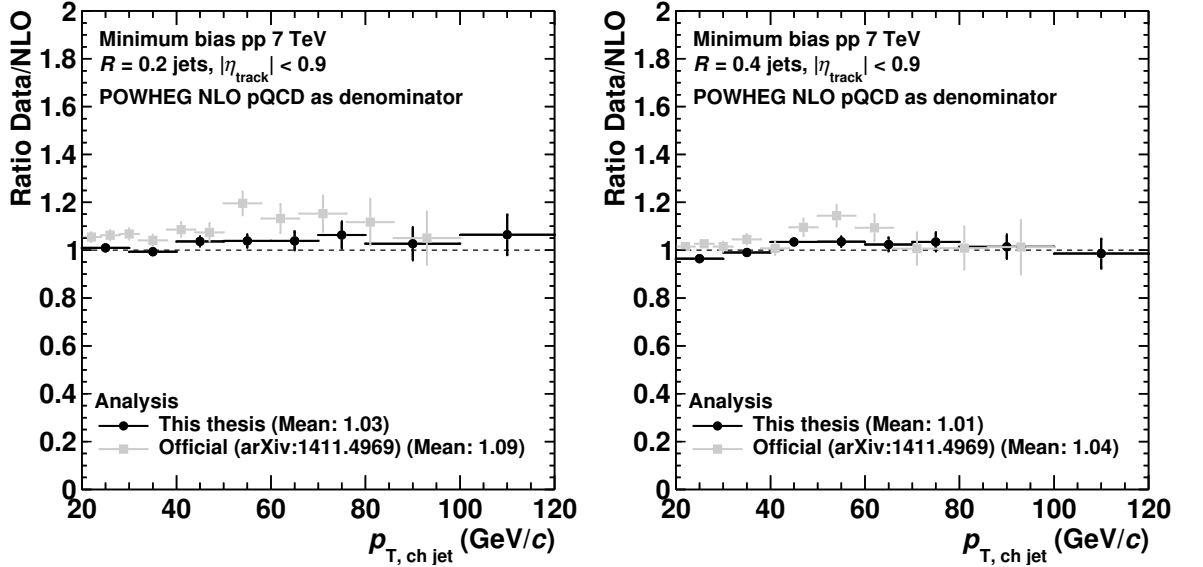


Figure 9.15: Ratios of pp charged jet spectra at 7 TeV and the corresponding NLO calculation. Note that the statistical uncertainties are highly correlated and that it is $|\eta_{\text{jet}}| < 0.9 - R$ for the official result and $|\eta_{\text{jet}}| < 0.5$ for this thesis' analysis.

Both spectra are shown as ratios compared to NLO calculations in Fig. 9.15. A direct ratio is not possible because of the different binning of both analyses. Rebinning is also no option, because binning is an integral part of the analysis. Both analyses show a

good agreement with each other and they are fully compatible within the systematic uncertainties.

Eventually, the global normalization uncertainties are assumed to be uncorrelated and added in quadrature. To conclude, the final normalization uncertainty for the nuclear modification factor consists of

- 3.4% from T_{pPb} ,
- 3.1% from NSD inefficiency,
- 3.5% from pp visible cross section uncertainty,
- 3.3% from different MC-based scaling factors,
- 5.8% from interpolation-based scaling factors,
- and 6% from the difference between the present and the final pp analysis.

In total, this results in a 10.7% normalization uncertainty for R_{pPb} . For the centrality-dependent Q_{pPb} (see subsequent chapter), the NSD inefficiency uncertainty is not taken into account, since the correction is not applied in this case.

The actual deviations of different scaling factors can be found in Fig. 9.14. In this plot, also a linear bin-by-bin interpolation is shown for illustration purposes, but not considered for systematic uncertainties since the scaling factors do not scale linearly with $\sqrt{s_{\text{NN}}}$.

For the jet production cross section ratio, the considered normalization uncertainties cancel by construction.

9.5. Summary of uncertainties in minimum bias events

Apart from the normalization uncertainties, main uncertainty sources have been identified to originate from the tracking efficiency uncertainty and from the unfolding procedure, for which especially the regularization strength and the choice of the minimum p_T cut-off are the predominant uncertainties. Detailed plots on the deviations from parameter variations were shown for $R = 0.4$.

It was also shown that the partial correlation of the tracking efficiency uncertainty in p-Pb and pp can be used to massively reduce the uncertainty for the nuclear modification factor R_{pPb} . In Tab. 9.2, the uncertainties are summarized for the $R = 0.2$ and $R = 0.4$ spectra, for the nuclear modification factor R_{pPb} , and for the jet production cross section ratio.

Table 9.2: Summary of systematic uncertainties (in %) on the fully corrected jet spectrum, the nuclear modification factor R_{pPb} , and the jet production cross section ratio for the resolution parameters $R = 0.2$ and $R = 0.4$. The percentages are given for the whole shown transverse momentum range 20-120 GeV/ c .

Observable Resolution parameter Uncertainty source	Jet cross section		R_{pPb}		Ratio
	$R = 0.2$	$R = 0.4$	$R = 0.2$	$R = 0.4$	$R = 0.2/0.4$
Single-particle efficiency	7.9 – 12.8	10.2 – 14.2	4.1 – 5.9	4.9 – 6.3	2.1 – 2.1
Unfolding	2.2	1.7	2.8	2.2	1.5
Prior steepness	1.4 – 4.8	0.5 – 4.0	2.9 – 8.0	0.9 – 4.4	1.1 – 1.5
Regularization strength	3.1 – 3.9	2.3 – 4.4	3.6 – 5.8	2.3 – 5.6	1.1 – 4.7
Minimum p_T cut-off	1.1 – 0.3	2.3 – 0.1	1.3 – 1.4	2.8 – 4.1	1.2 – 0.4
Background estimate	1.8 – 0.6	3.7 – 1.5	1.8 – 0.6	3.7 – 1.5	2.0 – 0.9
δp_T^{ch} estimate	0.0 – 0.0	0.1 – 0.0	0.0 – 0.0	0.1 – 0.0	0.1 – 0.0
Combined uncertainty	9.2 – 14.4	11.5 – 15.5	7.1 – 11.9	7.5 – 10.7	3.8 – 5.7
$\langle T_{pPb} \rangle$ & pp cross section	-	-	4.9	4.9	-
NSD efficiency p-Pb	-	-	3.1	3.1	-
pp reference	-	-	9.0	9.0	-
Combined scaling uncertainty	-	-	10.7	10.7	-

To conclude this chapter, the bin-by-bin contributions of all uncertainty sources and the final uncertainty are shown for the spectra, R_{pPb} , and the jet production cross section ratio. In Figs. 9.16, 9.17, and 9.18 the relative contributions of all uncertainty sources are shown stacked on a linear scale to show how they relate. Note that the stacked sum of the single contributions does not represent the full uncertainty. The full uncertainty is calculated by summing up those contributions quadratically assuming uncorrelated errors. It is shown in the bottom panels of the figures.

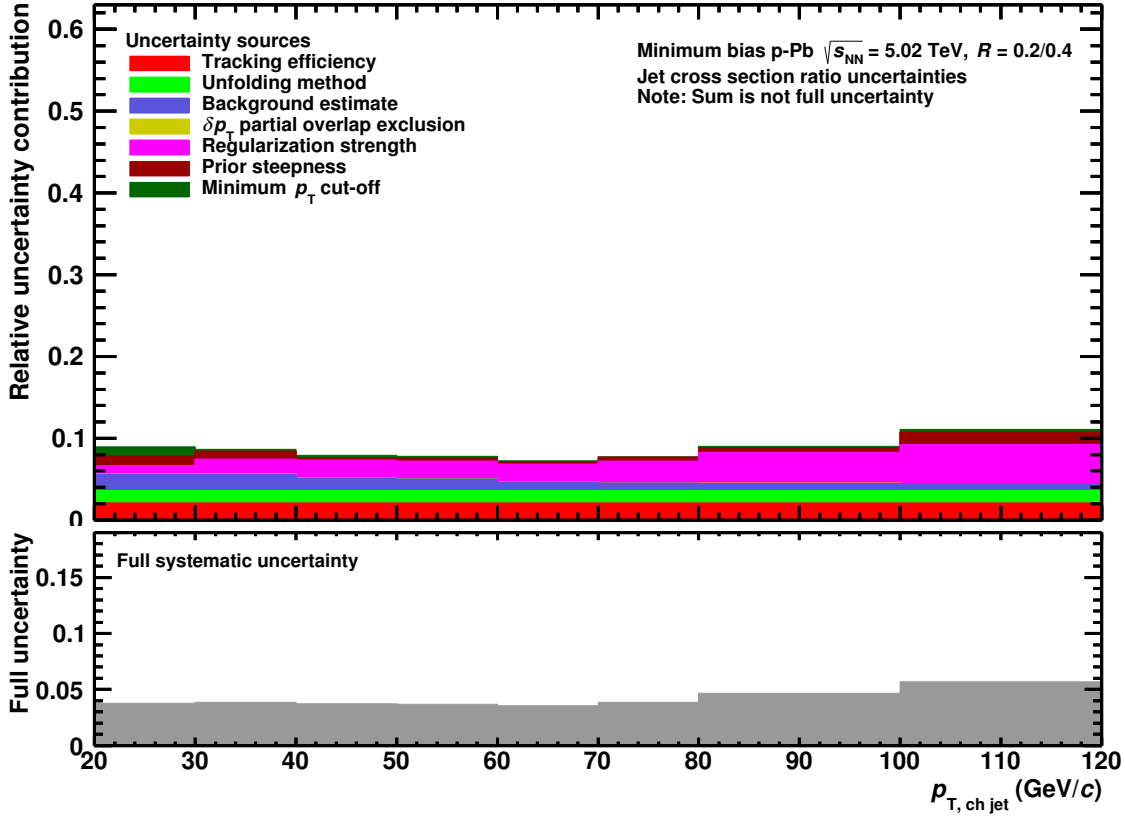


Figure 9.16: Stacked uncertainty contributions to illustrate how they relate (top panel) and total systematic uncertainty for the jet production cross section ratio $R = 0.2/R = 0.4$.

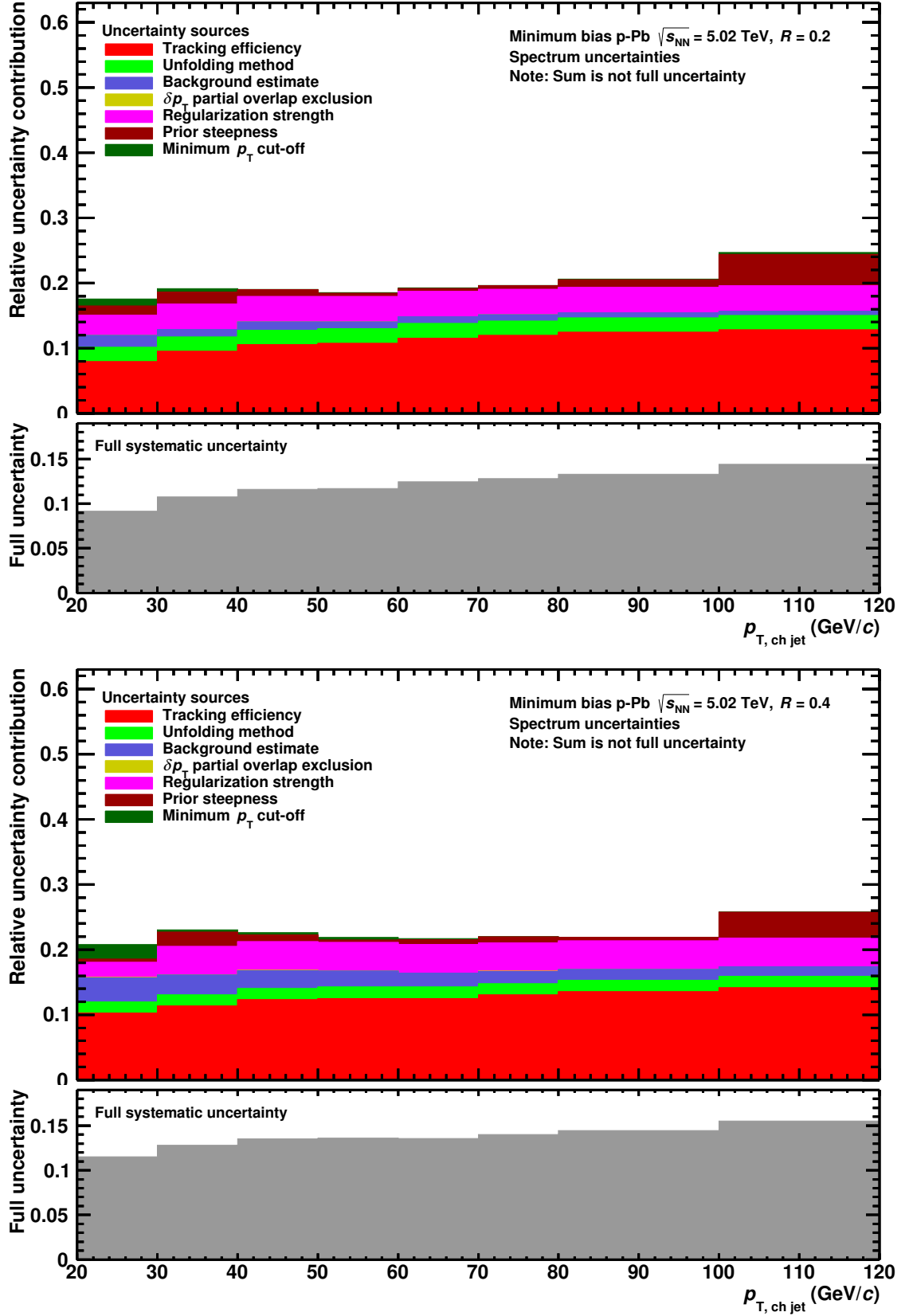


Figure 9.17: Stacked uncertainty contributions to illustrate how they relate (top panels) and total systematic uncertainty for the spectra.

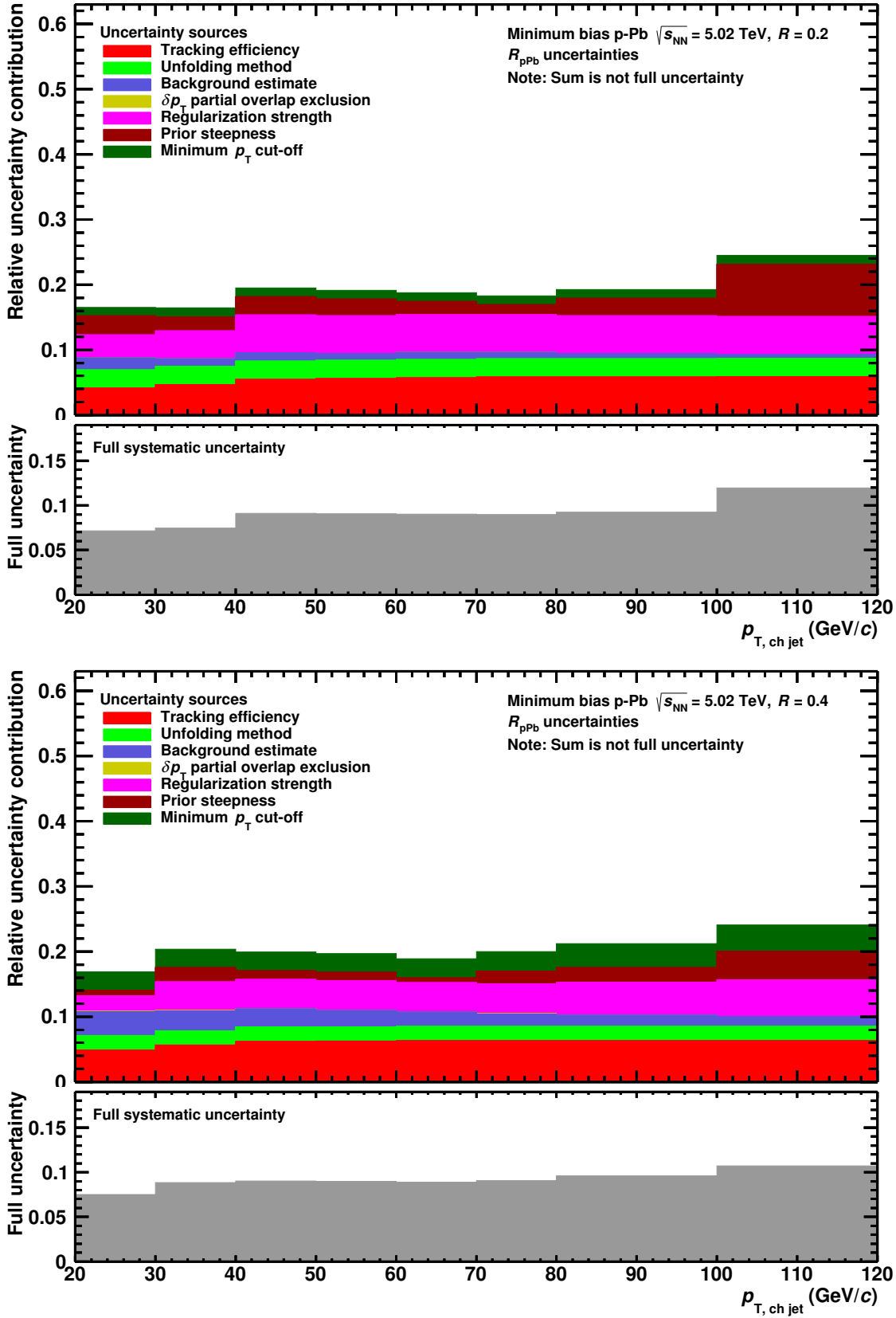


Figure 9.18: Stacked uncertainty contributions to illustrate how they relate (top panels) and total systematic uncertainty for the R_{pPb} .

10. Jets in pp collisions

In this chapter, the results obtained from the proton–proton analysis performed on 7 TeV data are presented. Initially, the data were measured only for the creation of the pp reference. A full analysis including the calculation of systematic uncertainties is necessary for this purpose.

The selected data, i.e. the runs, were chosen according to the ALICE measurement of 7 TeV charged jets in pp collisions, published in [Abe14a]. A completely different analysis framework was used and binning, regularization strength, background estimation differ though.

10.1. Charged jet production cross sections

Like for p–Pb, the background-corrected and SVD-unfolded charged jet spectra are shown as cross sections for $R = 0.2$ and $R = 0.4$ in Figs. 10.1 and 10.2. Also the observable definition is similar:

$$\frac{d\sigma}{dp_T} = \frac{c_{\text{vtx}}}{N_{\text{ev}}} \frac{dN}{dp_T} \cdot \sigma_{V0}. \quad (10.1)$$

The total number of events seen by the trigger after all cuts, N_{ev} , is described in Sec. 7.2. To transform the yield into a cross section, it is multiplied by the total cross section seen by the trigger, which is $\sigma_{V0} = 62.2 \pm 2.2$ mb [Abe13c] for pp collisions.

Compared to p–Pb, the vertex reconstruction efficiency is much worse in pp because of the lower mean multiplicity. c_{vtx} is given by

$$c_{\text{vtx}} = \frac{N_{\text{events}}^{\text{w/ vertex}}}{N_{\text{events}}^{\text{all}}} = 0.819. \quad (10.2)$$

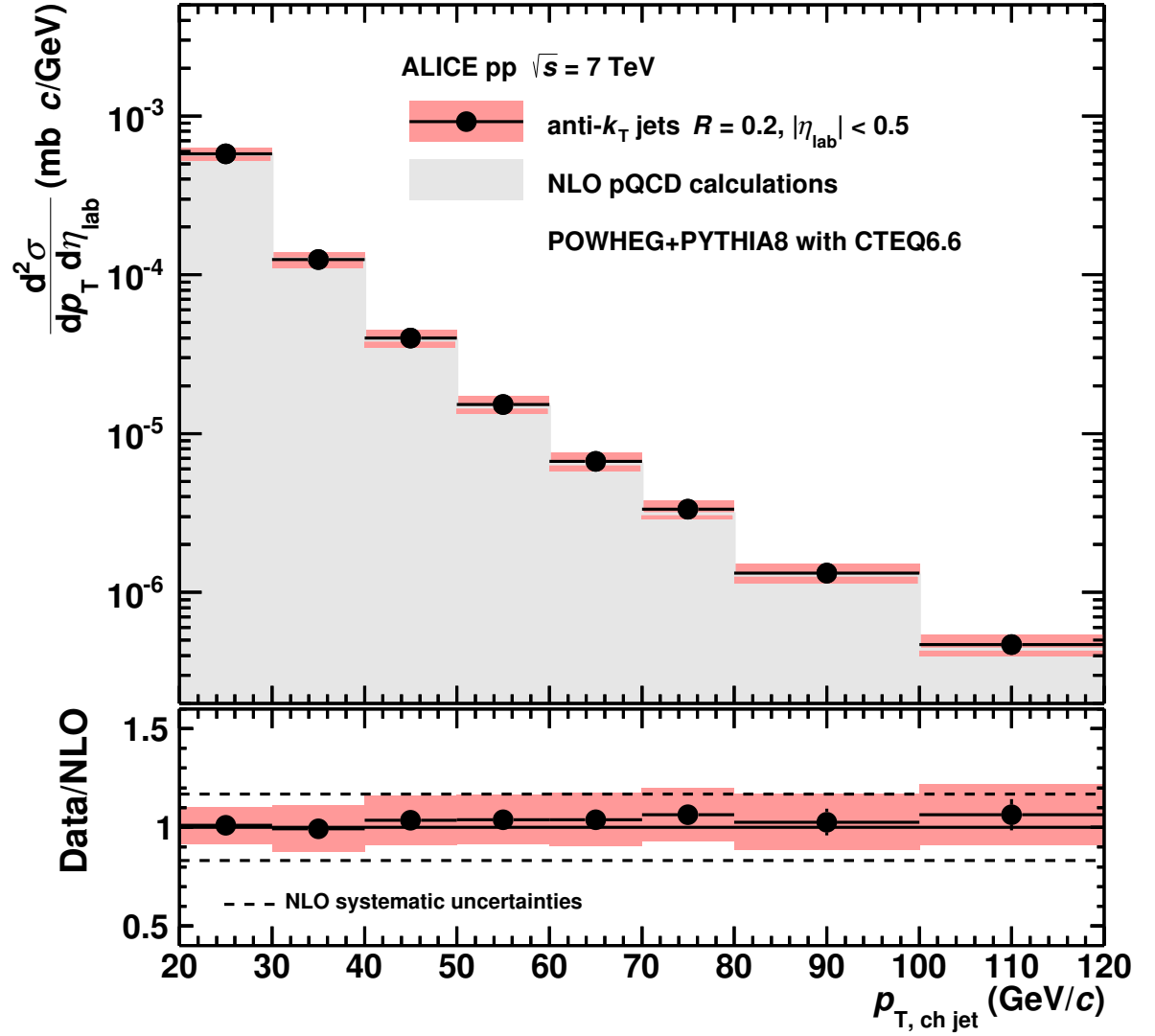


Figure 10.1: Top panel: Cross section of charged jet production for $R = 0.2$ in pp. Bottom panel: Ratio of data and NLO pQCD calculations. The global uncertainty of the measurement of the visible cross section is 3.5% and not shown. The uncertainties on the pQCD calculation are only shown in the ratio plot as dashed lines.

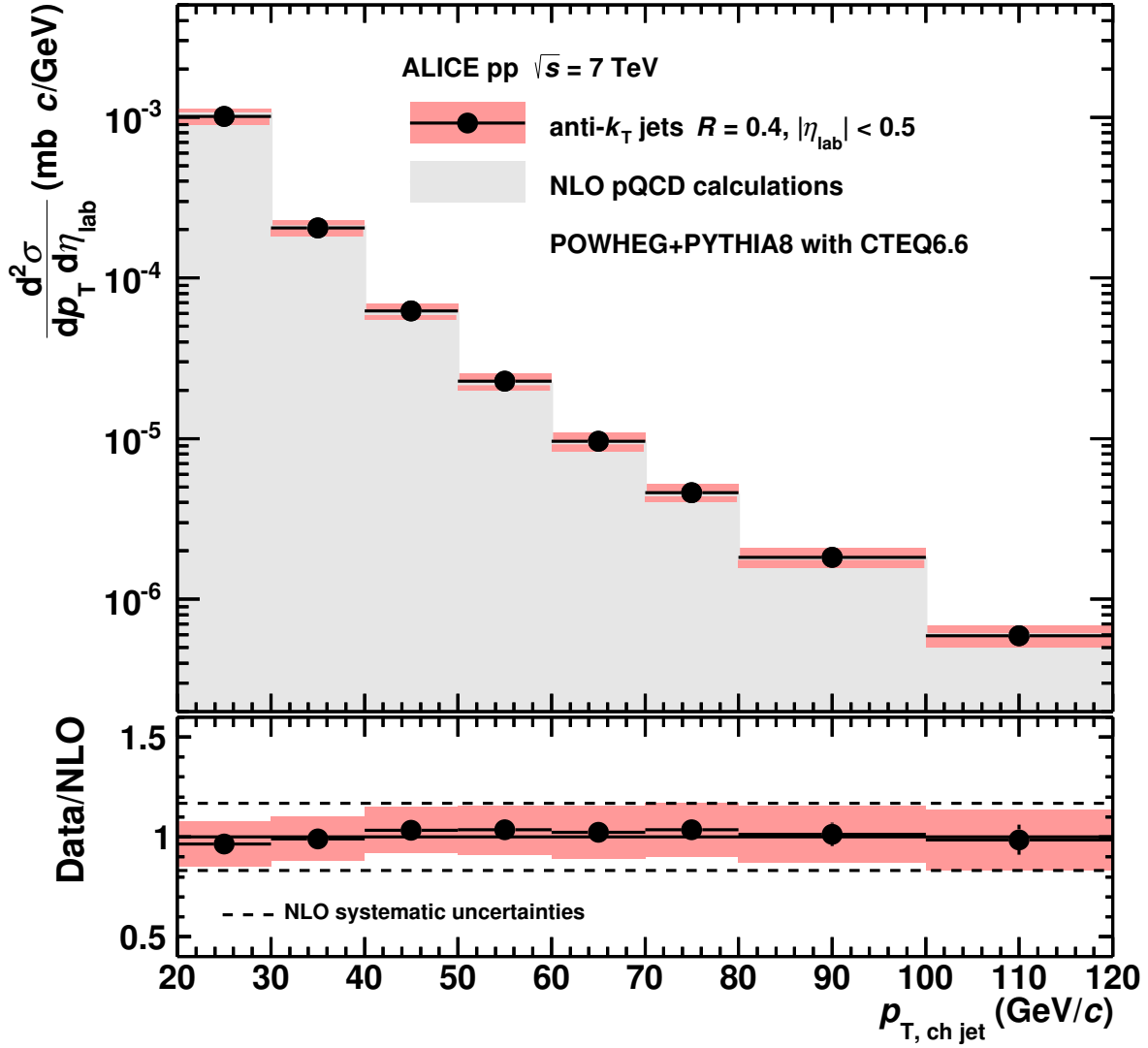


Figure 10.2: Top panel: Cross section of charged jet production for $R = 0.4$ in pp. Bottom panel: Ratio of data and NLO pQCD calculations. The global uncertainty of the measurement of the visible cross section is 3.5% and not shown. The uncertainties on the pQCD calculation are only shown in the ratio plot as dashed lines.

The systematic uncertainties are represented as red bars. Like for p–Pb, a comparison to NLO pQCD calculations with POWHEG at the same energy is shown in the bottom panels of Figs. 10.1 and 10.2.

The presented charged jet spectra for both resolution parameters show an excellent agreement with the NLO calculation. Within the uncertainty, measurement and calculations are compatible. The comparison to the final ALICE measurement results has already been shown in Sec. 9.4 as Fig. 9.15: Within the uncertainties, both analyses agree.

10.2. Jet production cross section ratio

The jet production cross section ratio as a simple estimate for the radial jet structure was also measured in pp. Since $R = 0.2$ and $R = 0.4$ pp spectra had to be measured for the creation of the R_{pPb} reference, the cross section ratio $R = 0.2/R = 0.4$ can easily be calculated.

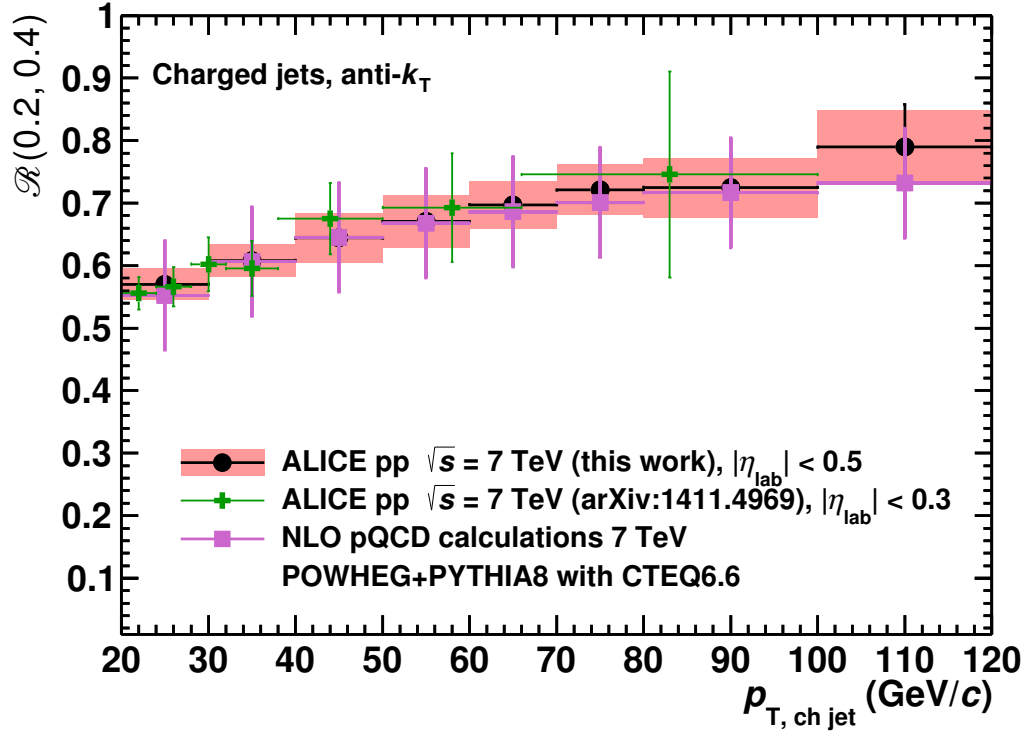


Figure 10.3: Charged jet production cross section ratio for different resolution parameters. The data in pp collisions at $\sqrt{s} = 7$ TeV is compared to POWHEG+PYTHIA8 (stat. uncertainties shown as error bars) at the same energy and to final ALICE measurement pp collisions at 7 TeV.

In Fig. 10.3, the jet production cross section ratio for charged jets in pp collisions is presented. For comparison, also results from NLO pQCD calculations with POWHEG and the final measurement result from ALICE [Abe14a] are shown.

Within uncertainties, the measured jet production cross section ratio in pp is in good agreement with POWHEG calculations and also with the final ALICE result. Compared to the jet production cross section ratio in p -Pb in Fig. 8.6, a slightly stronger statistical fluctuation is observed in the last p_T bin. This means the regularization is not as effective in pp as in p -Pb, which is expected because there are less jets in pp than in p -Pb for high p_T .³

As for the p -Pb cross section ratio, the statistical correlation of numerator and denominator is taken into account.

10.3. Summary of systematic uncertainties

In this section, the contributions of the systematic uncertainties for the pp cross sections and the cross section ratio are shown for the sake of completeness. Table 10.1 summarizes the numerical values of the systematic uncertainties. Single bin-by-bin uncertainty values can be found in Figs. 10.4 and 10.5.

Table 10.1: Summary of systematic uncertainties (in %) on the fully corrected jet spectra in pp and on the jet production cross section ratio for the resolution parameters $R = 0.2$ and $R = 0.4$. The percentages are given for the whole shown transverse momentum range 20-120 GeV/ c .

Observable Resolution parameter Uncertainty source	Jet cross section		Ratio
	$R = 0.2$	$R = 0.4$	$R = 0.2/0.4$
Single-particle efficiency	8.5 – 13.2	10.9 – 14.2	2.1 – 2.1
Unfolding	1.7	1.4	2.9
Unfolding prior steepness	2.5 – 6.4	0.7 – 1.8	1.8 – 4.7
Regularization strength	1.8 – 4.3	0.2 – 3.6	1.6 – 3.2
Minimum p_T cut-off	0.8 – 0.8	1.7 – 3.4	1.1 – 3.3
Combined uncertainty	9.3 – 15.4	11.1 – 15.2	4.5 – 7.5

³For the $p_T = 100$ -120 GeV/ c bin, there are 32 jets in p -Pb and 19 jets in pp for $R = 0.4$.

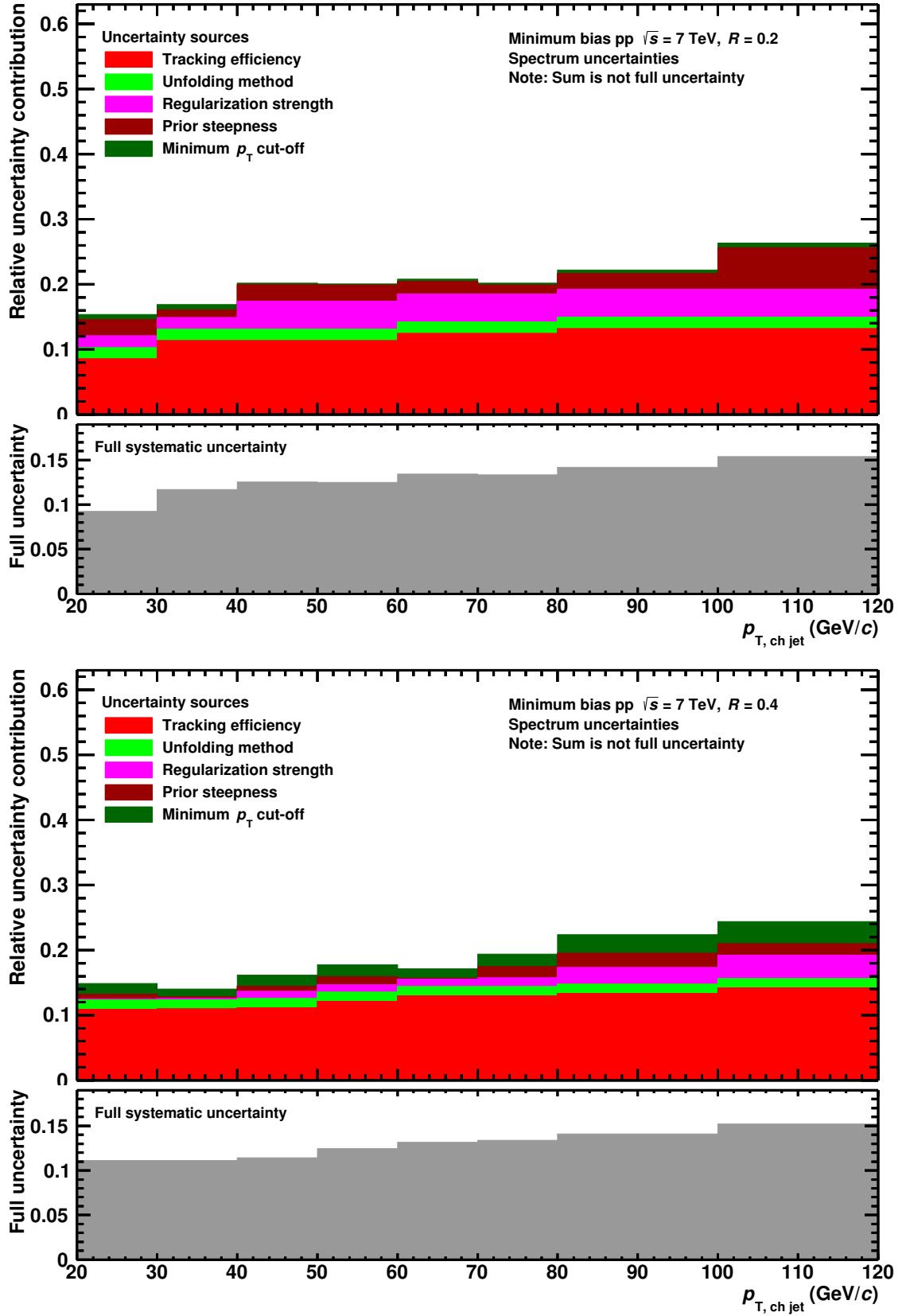


Figure 10.4: Stacked uncertainty contributions to illustrate how they relate (top panels) and total systematic uncertainty for the spectra.

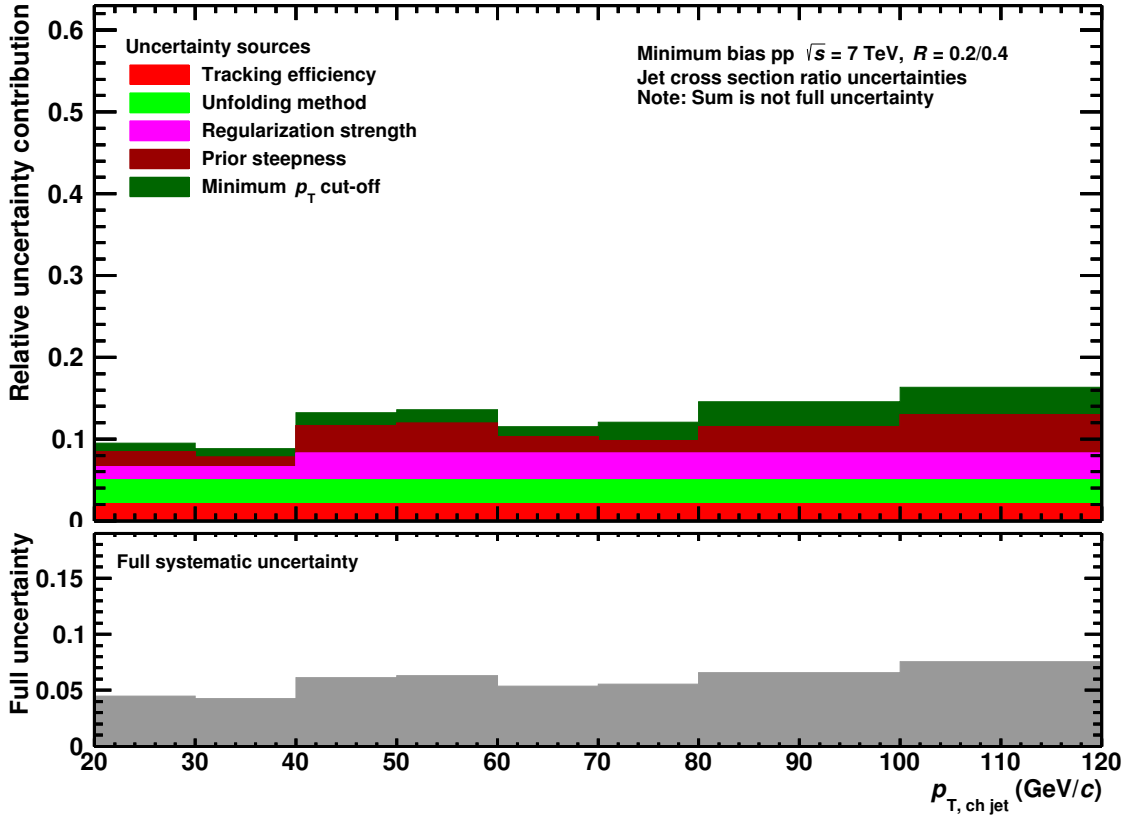


Figure 10.5: Stacked uncertainty contributions to illustrate how they relate (top panel) and total systematic uncertainty for the jet production cross section ratio $R = 0.2/R = 0.4$ in pp.

11. Centrality dependence of jets in p -Pb collisions

From the technical perspective, the analysis of centrality-dependent jets closely resembles the analysis of minimum bias jets. Both analyses differ in a dissimilar normalization – centrality-dependent jets are scaled with a different nuclear overlap function T_{pPb} – and the event selection. Of course, accurate centrality-dependent event selection and calculation of T_{pPb} is anything but trivial. This work was done by the ALICE centrality task force [Ada14], as described in Sec. 5.3.

The main results of this section have already been published as preliminary results in [Haa15]. A publication of final centrality-dependent results is in preparation.

11.1. Charged jet production cross sections

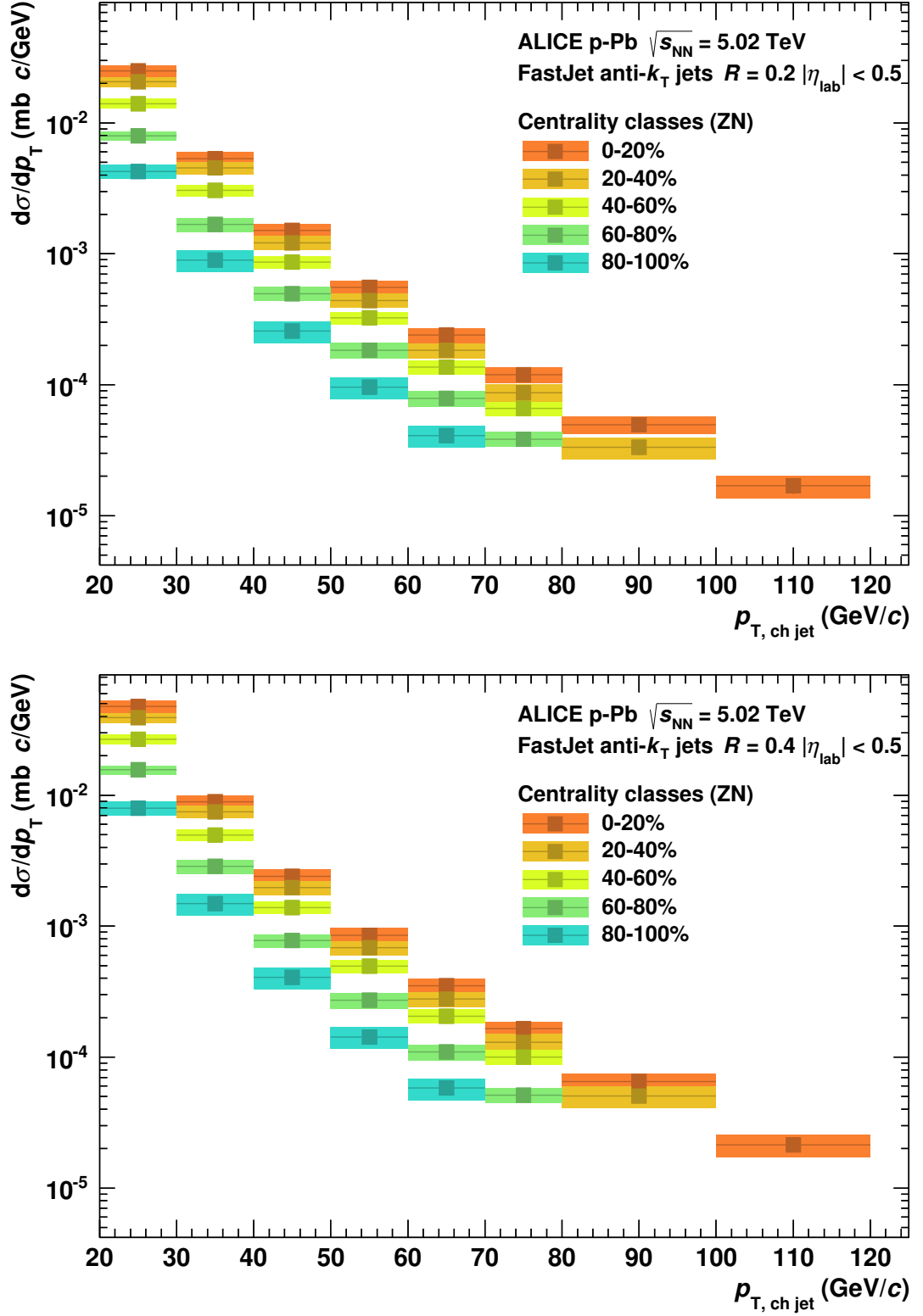
In this section, the fully corrected cross sections are shown for the resolution parameters $R = 0.2$ and $R = 0.4$. Like the minimum bias spectra, they are defined as

$$\frac{d\sigma}{dp_T} = \frac{c_{\text{vtx}}}{N_{\text{ev}}^{\text{cent}}} \frac{dN}{dp_T} \cdot \sigma_{\text{V0}} \cdot \frac{N_{\text{ev}}^{\text{cent}}}{N_{\text{ev}}^{\text{MB}}} = \frac{c_{\text{vtx}}}{N_{\text{ev}}^{\text{MB}}} \frac{dN}{dp_T} \cdot \sigma_{\text{V0}} \quad (11.1)$$

for each centrality subsample. σ_{V0} represents the visible cross section of the full data sample and is therefore multiplied with a weighting factor according to the centrality classes. The values of the vertex efficiency in the selected centrality bins are listed in Tab. 11.1. For further details on Eq. 11.1 see Sec. 8.1.

Table 11.1: Vertex finding efficiency for different centrality classes.

Centrality class	c_{vtx}
0-20	0.999
20-40	0.998
40-60	0.993
60-80	0.978
80-100	0.954
Minimum bias	0.983

Figure 11.1: Charged jet spectra for all centrality intervals for $R = 0.2$ and $R = 0.4$.

The plots in Fig. 11.1 depict the fully corrected cross sections. The colored boxes represent the systematic uncertainties. Note that several high- p_T bins have been rejected for the reason of too low statistics, i.e. too few jets for stable unfolding. An overall normalization uncertainty of 3.5% originating from the visible cross section measurement is not shown.

11.2. Nuclear modification factor Q_{pPb}

The general concept of the nuclear modification factor has already been introduced in Sec. 8.3: It is a very descriptive measure for the nuclear modification, indicating a modification for any deviation from unity for spectra which directly scale with the number of binary collisions N_{coll} . For centrality-dependent results, it is called Q_{pPb} by ALICE to emphasize that it is potentially biased by the centrality selection.

Technically, the centrality-dependent nuclear modification factor Q_{pPb} is defined by

$$Q_{pPb} = \frac{dN^{pPb}/dp_T \cdot c_{\text{vtx}}}{d\sigma^{pp}/dp_T} \cdot \frac{1}{T_{pPb}}, \quad (11.2)$$

in which T_{pPb} is the centrality-dependent nuclear overlap function, calculated using the hybrid centrality approach [Ada14], which has already been introduced in Sec. 5.3. In Tab. 11.2, the relevant values are listed. Their systematic uncertainties are assumed to be the same as for the minimum bias result: 3.4%.

The pp reference is the same as for minimum bias, introduced in Sec. 8.2.

Please note that in contrast to the minimum bias R_{pPb} , no correction for the NSD efficiency is done. This is in concordance with the ALICE p -Pb centrality paper, in which the charged particle Q_{pPb} is also not corrected for this inefficiency.

Anyhow, even if the centrality classes were defined as fractions of the *total* cross section, the NSD inefficiency would only affect events from the most peripheral 80-100% bin, for the other bins it is expected to be negligible. For the most peripheral 80-100% bin, the NSD inefficiency is assumed to be 11% with an absolute uncertainty of 15%.

Roughly speaking, if ignoring the NSD efficiency, the nuclear modification factor Q_{pPb} is valid for the *visible* cross section.

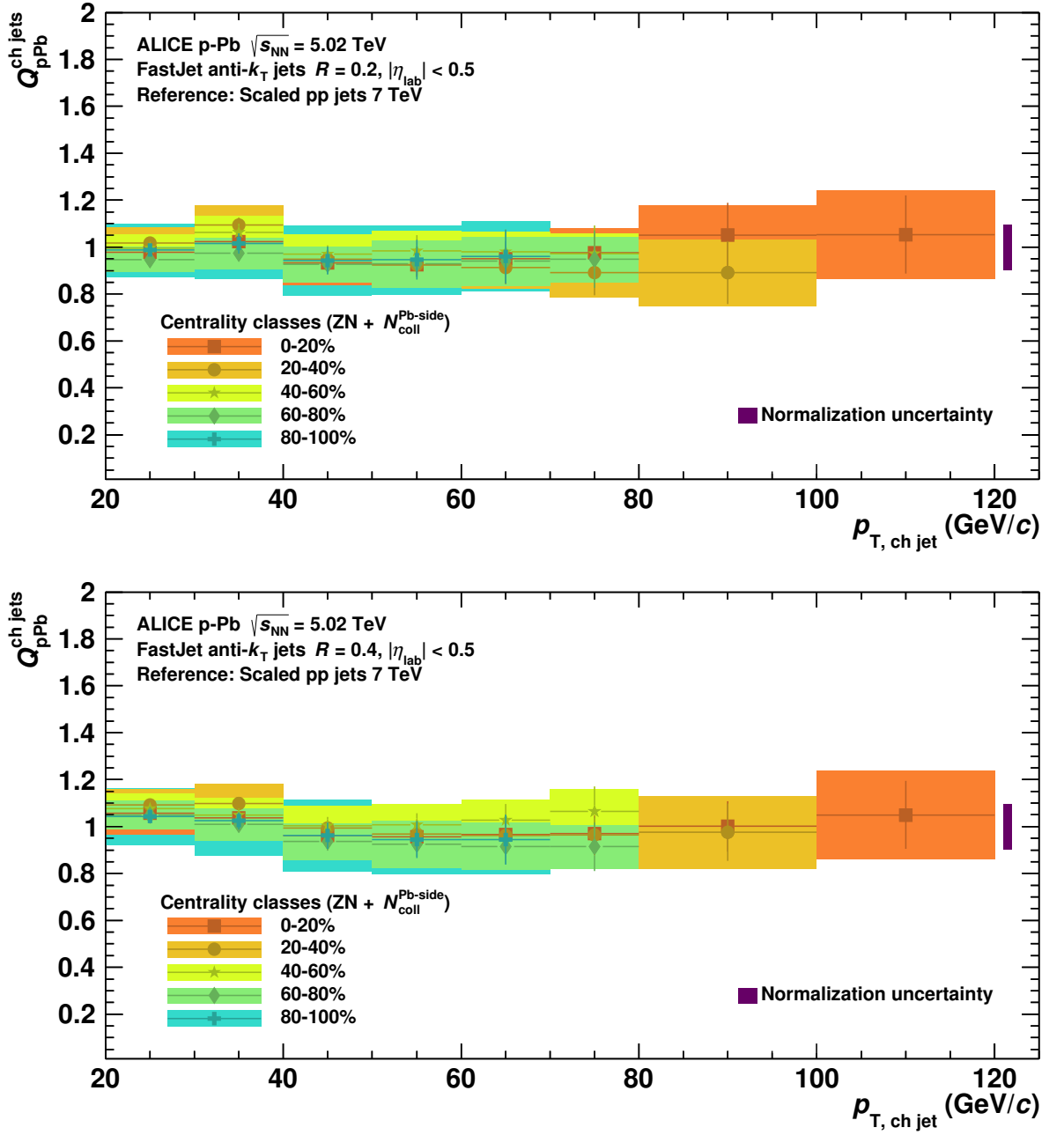


Figure 11.2: Charged jet nuclear modification factor Q_{pPb} for selected centrality intervals for $R = 0.2$ and $R = 0.4$ ($N_{\text{coll}}^{\text{Pb-side}}$ estimator).

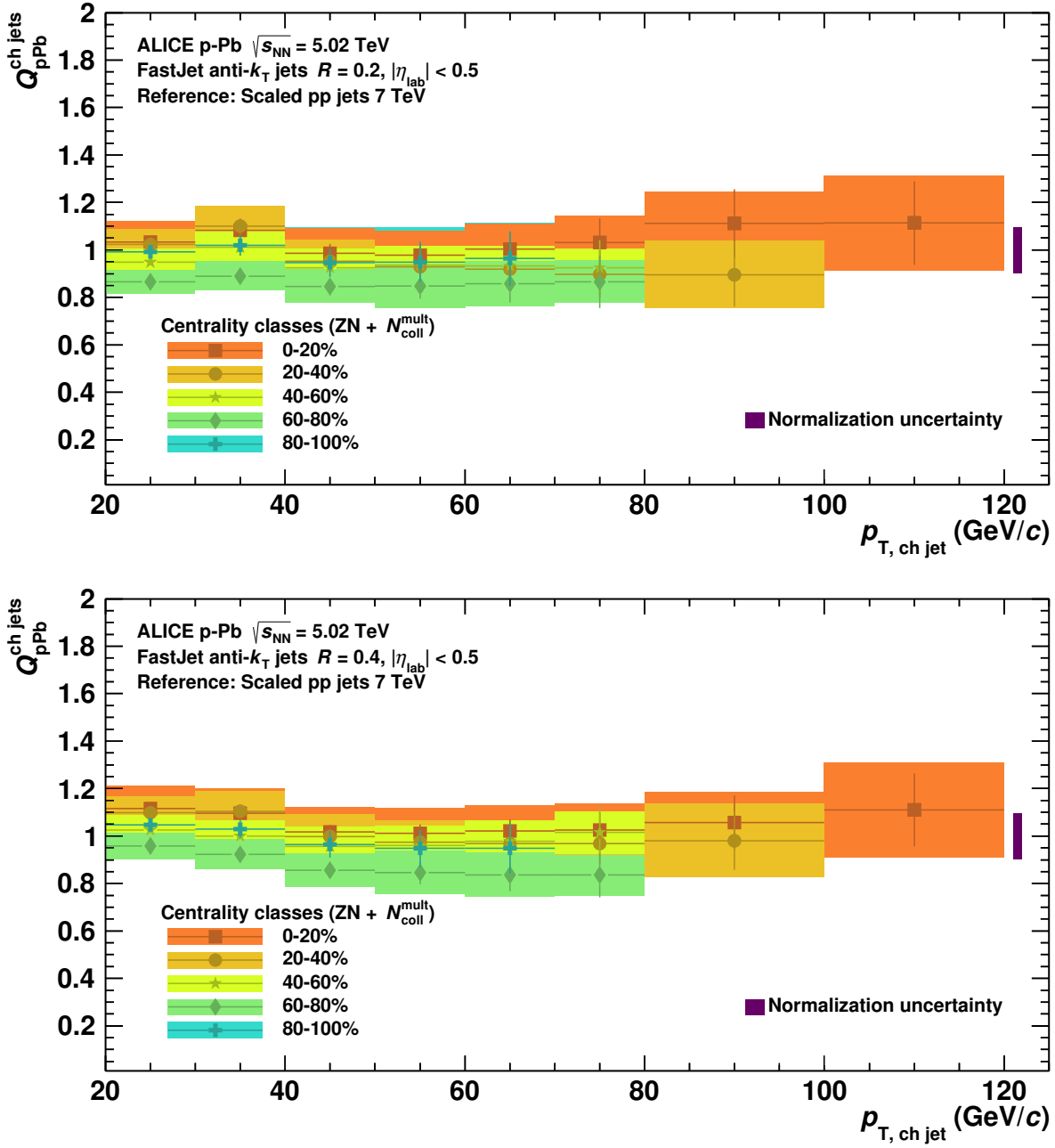


Figure 11.3: Charged jet nuclear modification factor Q_{pPb} for selected centrality intervals for $R = 0.2$ and $R = 0.4$ ($N_{\text{coll}}^{\text{mult}}$ estimator).

In Figs. 11.2 and 11.3, the centrality-dependent nuclear modification factor Q_{pPb} is shown for different assumptions for the N_{coll} calculations, using $N_{\text{coll}}^{\text{Pb-side}}$ and $N_{\text{coll}}^{\text{mult}}$, respectively. Each figure shows the Q_{pPb} for $R = 0.2$ (upper plot) and $R = 0.4$ (lower plot).

Table 11.2: Nuclear overlap functions for different centrality classes calculated with differing assumptions. The minimum bias value is calculated using Glauber calculations only.

Centrality class	$T_{\text{pPb}}^{\text{mult}}$	$T_{\text{pPb}}^{\text{Pb-side}}$	$T_{\text{pPb}}^{\text{V0A}}$
0-20	0.163	0.173	0.180
20-40	0.136	0.137	0.134
40-60	0.101	0.0963	0.0917
60-80	0.0626	0.0571	0.0544
80-100	0.0293	0.0294	0.0277
Minimum bias	0.0983		

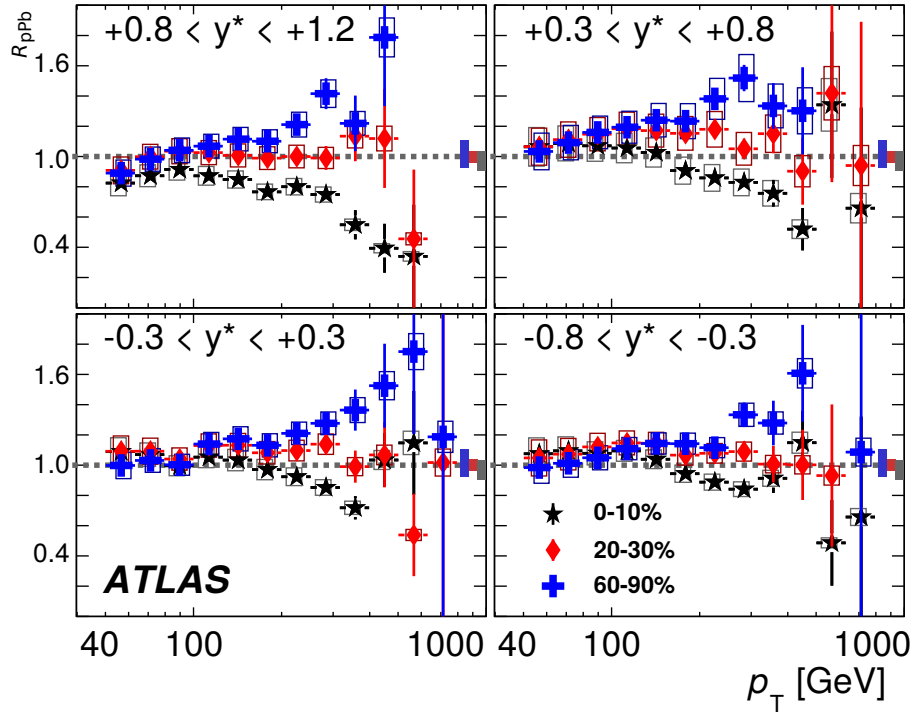


Figure 11.4: Centrality-dependent nuclear modification factors R_{pPb} measured by the ATLAS collaboration for $R = 0.4$ jets for selected rapidity intervals. y^* represents the jet rapidity. The results from this thesis can best be compared to $0.3 < y^* < 0.8$. Plot extracted from [Aad14].

Within the uncertainties, the nuclear modification factor is not significantly modified for both N_{coll} estimates and the different centrality classes. Like for the charged jet spectra, several high- p_T bins were omitted in case of too low statistics. For the $N_{\text{coll}}^{\text{mult}}$, a slightly stronger spread of the different distributions can be observed.

To some extent, the difference between the two nuclear modification factors Q_{pPb} can be seen as a measure for the systematic uncertainty of the hybrid centrality approach: According to the p -Pb centrality paper, both N_{coll} values are valid choices of the centrality for the jet measurement scenario.⁴

For comparison, the ATLAS measurement is shown in Fig. 11.4 for selected rapidity intervals and for different centralities. Like for the minimum bias results, ALICE and ATLAS also agree for centrality-dependent jets within the uncertainties and in comparable transverse momentum ranges.

11.3. Central over minimum bias ratios R_{CM}

A well-known quantity in heavy-ion physics is the ratio R_{CP} , which compares central to peripheral collisions. In Pb-Pb collisions, for example, it is used as a measure for jet quenching. Broadly speaking, the ratio can be interpreted as “spectra strongly affected by medium” over “pp-like spectra”. Compared to R_{AA} , R_{CP} is a simpler estimate for nuclear effects since it does not require a reference measured in a different collision system. On the other hand, a robust centrality estimate is necessary, which is the case for Pb-Pb collisions.

In p -Pb collisions, the ratio R_{CM} , comparing central to minimum bias collisions, is more adequate but essentially the same observable as R_{CP} . Here, it is already known that the minimum bias result shows no significant modification and the peripheral result is potentially biased.

Another advantage of R_{CM} , as a measure for nuclear effects, is that the systematic uncertainties are smaller than for Q_{pPb} . Many uncertainties cancel in the ratio. The uncertainties were calculated by varying this observable and not by varying the numerator and denominator separately. This was also performed that way for the jet production cross section ratio.

The central over minimum bias ratio can be defined by

$$R_{\text{CM}} = \frac{N_{\text{coll}}^{\text{MB}}}{N_{\text{coll}}^{0-20}} \frac{d\sigma^{0-20}/dp_T}{d\sigma^{\text{MB}}/dp_T} \cdot \frac{N_{\text{ev}}^{\text{MB}}}{N_{\text{ev}}^{0-20}}, \quad (11.3)$$

⁴In principle, also $N_{\text{coll}}^{\text{high } p_T}$ provides a valid centrality estimator, but it is not used in this thesis because its main assumption is that the high- p_T particle yield is proportional to N_{coll} , i.e. the nuclear modification factor for high- p_T particles is flat by construction.

in which the cross sections are fully corrected and given by Eqs. 8.1 and 11.1. The factor $N_{\text{ev}}^{\text{MB}}/N_{\text{ev}}^{0-20}$ corrects for the event fraction of the subsample of central collisions. Note that the centrality-dependent numerator is not corrected for an NSD inefficiency, since the centrality classes are defined as fractions of the visible cross section.

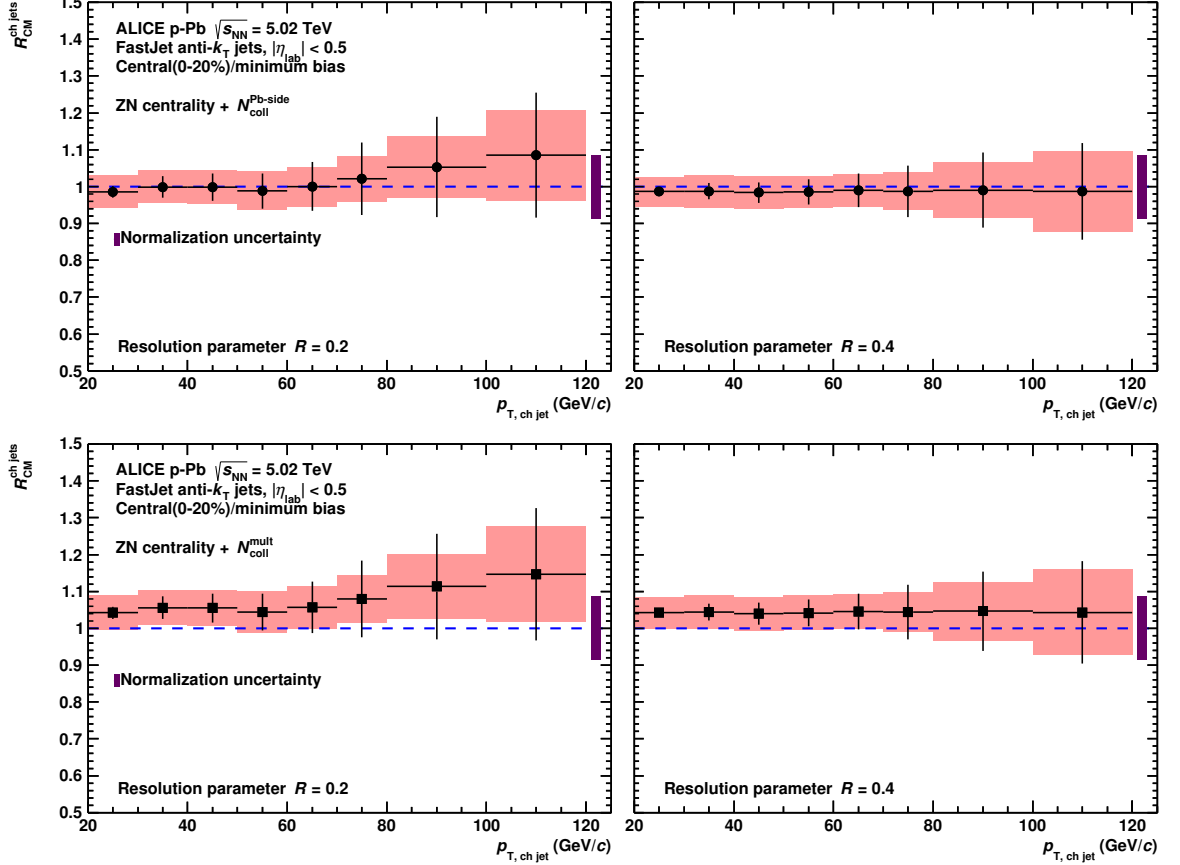


Figure 11.5: Ratio 0-20% central over minimum bias jets for $N_{\text{coll}}^{\text{Pb-side}}$ (upper plots) and $N_{\text{coll}}^{\text{mult}}$ (lower plots). Upper and lower plots differ only in normalization.

The correlation of numerator and denominator has been taken into account for the calculation of the statistical uncertainties as in Sec. 8.4.1. The global uncertainty comprises a 3.1% uncertainty on the NSD correction applied on the minimum bias spectrum and an 8% uncertainty on N_{coll} , resulting in 8.6%. Note that the 8% uncertainty on N_{coll} is most probably overestimated: It is the uncertainty given in the p-Pb centrality paper on N_{coll} . Since the correlation of the uncertainty on the N_{coll} values for most central and minimum bias collisions is not known, the given value of 8% was assumed.

In Fig. 11.5, the central over minimum bias ratio is shown for the two N_{coll} methods and for $R = 0.2$ and $R = 0.4$. Note that the range is different than for Q_{pPb} for better visibility.

Even without the – probably overestimated – global normalization uncertainty, the ratios do not indicate any significant centrality dependence within uncertainties, neither for $N_{\text{coll}}^{\text{Pb-side}}$ nor $N_{\text{coll}}^{\text{mult}}$. Especially the R_{CM} for $R = 0.4$ differs only about 4% ($N_{\text{coll}}^{\text{mult}}$) or even 2% ($N_{\text{coll}}^{\text{Pb-side}}$) from unity.

For $R = 0.2$, there is a small, non-significant upward trend visible. It should be noted that this can easily be caused e.g. by a statistical fluctuation. The regularization of the unfolding can “smooth” this fluctuation in such a way that it looks like a trend.

11.4. Jet production cross section ratios

As a very simple measure for the radial jet structure, the jet production cross section ratios allow to check whether the jet shape is modified for different centralities.

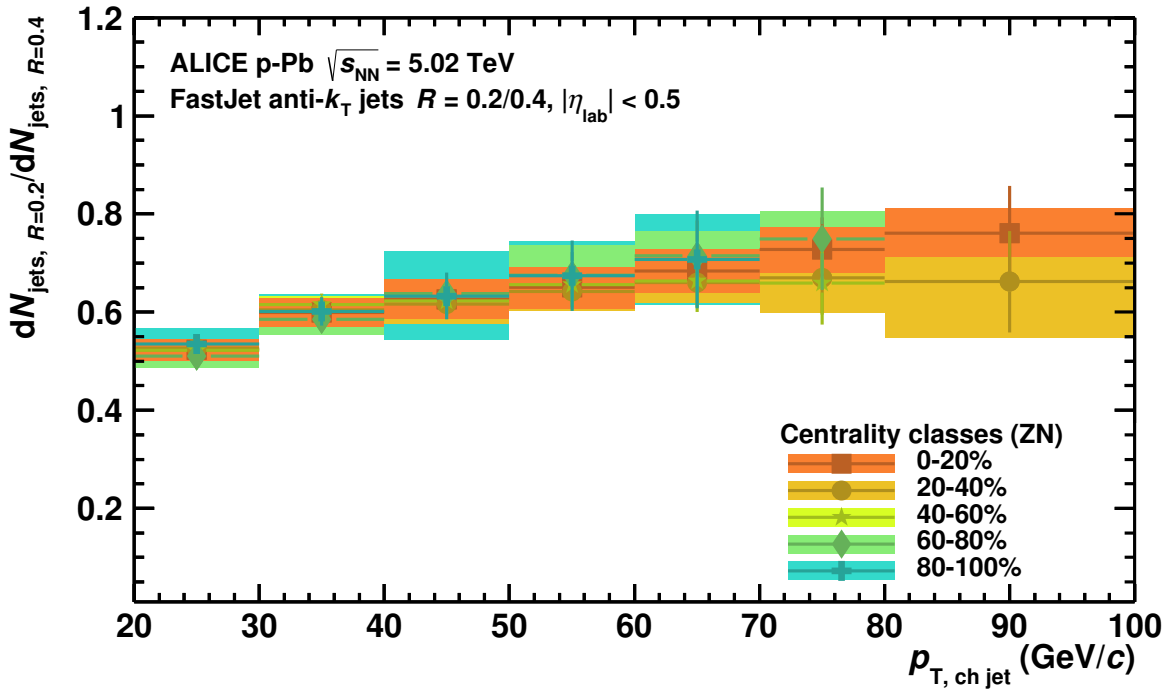


Figure 11.6: Jet production cross section ratio for selected centrality classes.

Centrality-dependent jet production cross section ratios are defined like their pendant in minimum bias collisions,

$$\mathcal{R}(0.2, 0.4) = \frac{d\sigma_{\text{pPb}, R=0.2}/dp_T}{d\sigma_{\text{pPb}, R=0.4}/dp_T}. \quad (11.4)$$

The utilized cross sections are, of course, calculated using events from selected centrality classes. Figure 11.6 shows the ratio for selected cross section intervals.

Within the uncertainties, no centrality dependence of the jet production cross section ratio is measured.

This result is fully compatible with the expectations: Even in Pb–Pb collisions measured by ALICE, no significant structure modification could be observed for jets [Abe14b].

For this observable, the low jet count in the most peripheral events becomes apparent by fluctuating systematic uncertainties of the 80-100% jet shape above 40 GeV/ c , especially for the 40-50 GeV/ c bin. Spectra with low statistics are potentially more affected by a certain systematic variation than spectra with high statistics. In particular, the regularization parameter which is connected to the *smoothing* of the spectrum has a stronger influence on spectra with low statistics.

Since it is hard to decide to which extent the uncertainties are of statistical or systematic nature, the systematic uncertainty of spectra with low statistics is extracted in the same way as of spectra with high statistics. Therefore, the uncertainty potentially contains a “statistical part” and is probably slightly overestimated.

11.5. Nuclear modification using NBD-Glauber fit centrality

As described in the centrality section (Sec. 5.3), the hybrid centrality estimation approach is preferred over the biased NBD-Glauber fit approach known from Pb-Pb. However, the p-Pb centrality task force in ALICE also implemented the event classification using the V0A detector and the number of binary collisions N_{coll} was also calculated using the NBD-Glauber fit.

Analyzing jets in this different centrality binning is therefore technically realized by changing a parameter in the event characterization and the normalization with different values for the nuclear overlap function $T_{\text{Pb}}^{\text{V0A}}$. Those values are listed in Tab. 11.2.

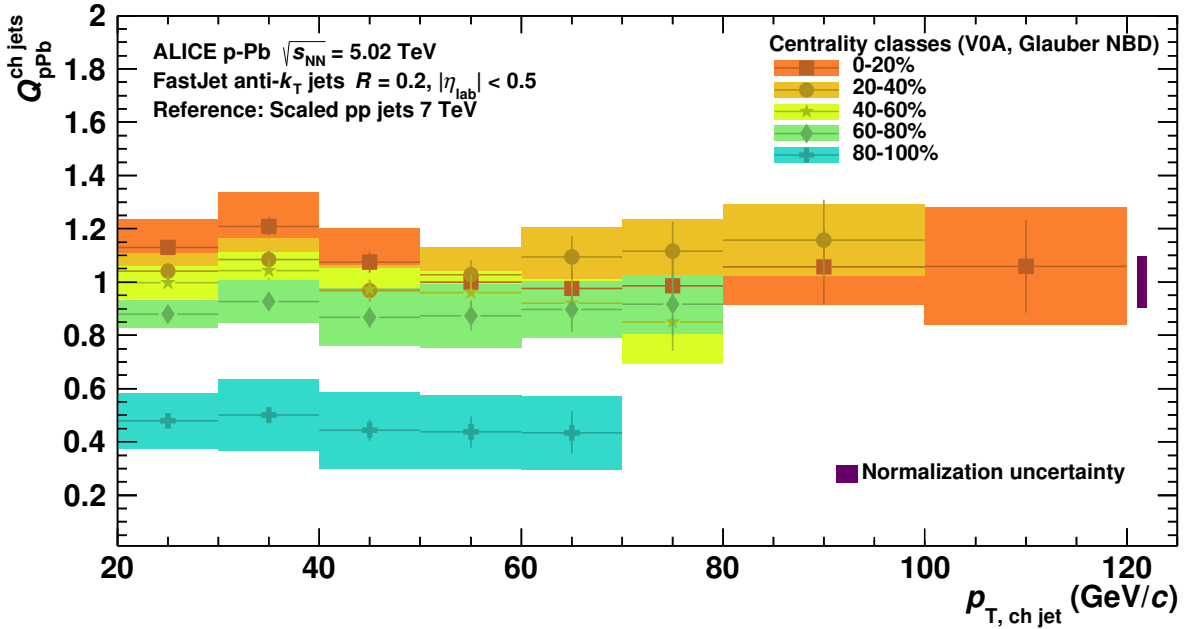


Figure 11.7: Charged jet nuclear modification factor Q_{pPb} for selected centrality intervals for $R = 0.2$ using the bias NBD-Glauber fit centrality estimate.

In Figs. 11.7 and 11.8, the nuclear modification factor Q_{pPb} is shown for the biased centrality determination. The method and its biases have already been described in Sec. 5.3.2. Except for the most peripheral 80-100% jets, the factors do not deviate more than 25% from one. A direct comparison of the two centrality approaches is shown as a ratio plot in Fig. 11.9 for the $N_{\text{coll}}^{\text{Pb-side}}$ estimator.

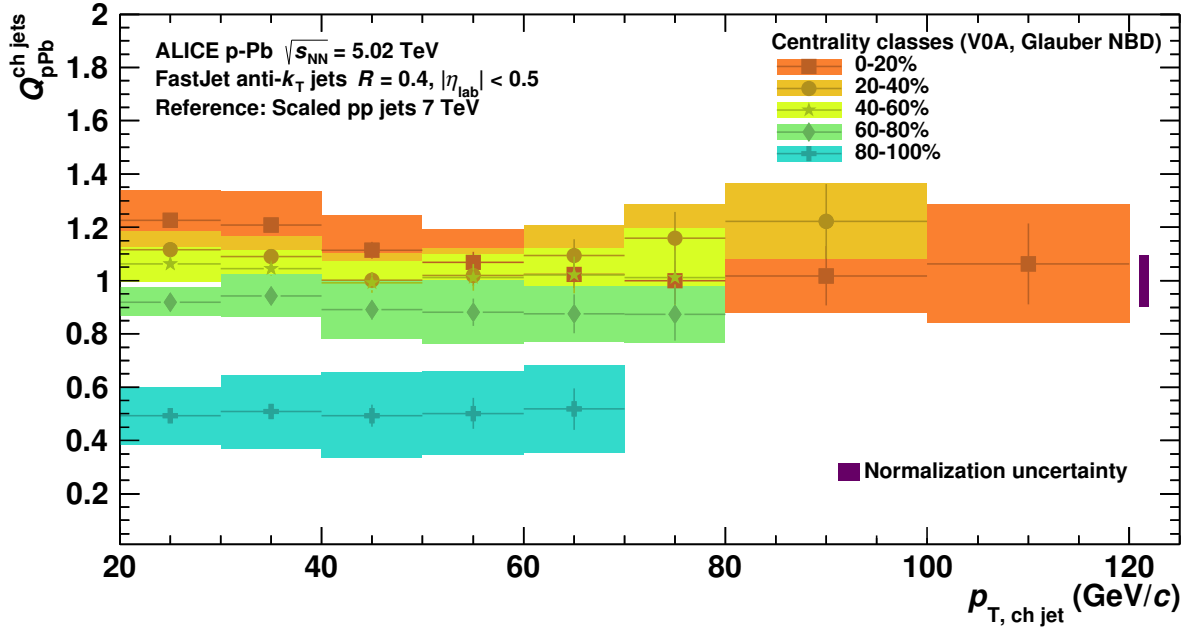


Figure 11.8: Charged jet nuclear modification factor Q_{pPb} for selected centrality intervals for $R = 0.4$ using the bias NBD-Glauber fit centrality estimate.

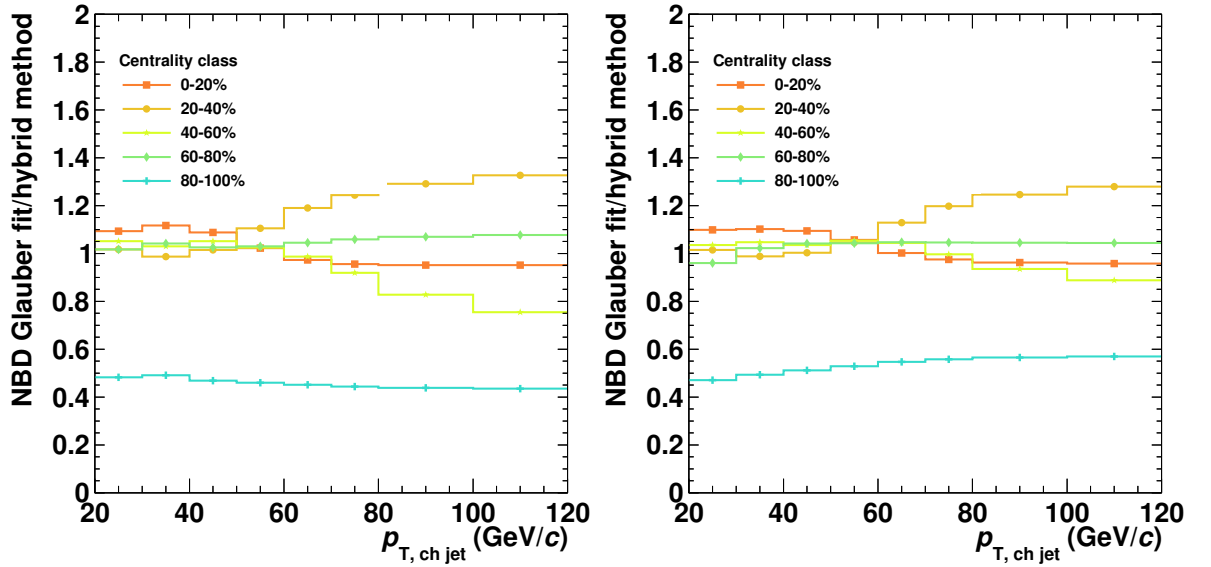


Figure 11.9: Ratios of centrality-dependent nuclear modification factors using V0A NBD-Glauber fit centrality over hybrid method centrality for $R = 0.2$ (left) and $R = 0.4$ (right).

For the biased NBD-Glauber estimator, also the shape of the jet spectra differs compared to the hybrid method. The nuclear modification factor shows a stronger spread for different centrality classes.

Individually, the single nuclear modification factors for the NBD-Glauber centrality – except for the most peripheral jets – do not significantly deviate from one, taking the global uncertainty into account. However, since the global uncertainty is nearly completely correlated for all curves, there is at least some tension between the curves within their systematic uncertainties. But to remind, the curves are actually expected to be different since the centrality method is expected to be biased.

In the end, this is clearly visible only for the 80-100% jets: The spectrum shows a strong deviation from one and no compatibility with the other curves. This can possibly be explained by the jet-veto bias: The selection of the most peripheral collisions with a multiplicity-driven centrality favors events without a jet.

Note that here intentionally no full comparison of the different centrality approaches is performed. The present analysis is supposed to demonstrate that the biased centrality determination using the NBD-Glauber fit produces compatible results for charged jets using the considered centrality classes up to 80% centrality. In [Ada14], the analysis and detailed presentation of the different centrality methods was published.

11.6. Summary of systematic uncertainties in bins of centrality

In Chapter 9, the systematic uncertainties were analyzed in great detail. In principle, the observations are also roughly valid for centrality-dependent results and, therefore, the analysis will not be documented in same details.

However, since the systematic uncertainties are evaluated separately for each observable, they slightly differ. Especially and as already mentioned, it can be observed that lower statistics lead to larger systematic uncertainties. Both uncertainties cannot be fully separated and it can therefore happen that a systematic variation has a larger effect on a data sample with lower statistics. This leads to an uncertainty on the systematic uncertainties.

Besides, the systematic uncertainties can of course also vary because the considered systematic variation is indeed different for the considered centrality intervals.

In the following, the systematic uncertainties of the centrality-dependent charged jet observables are presented for the example of $R = 0.4$ jets in Figs. 11.10, 11.11, and 11.12 to illustrate the impact of the different systematic uncertainties. In Appendix A.2.2, the uncertainty stack histograms for $R = 0.2$ are shown in Figs. A.10 and A.11.

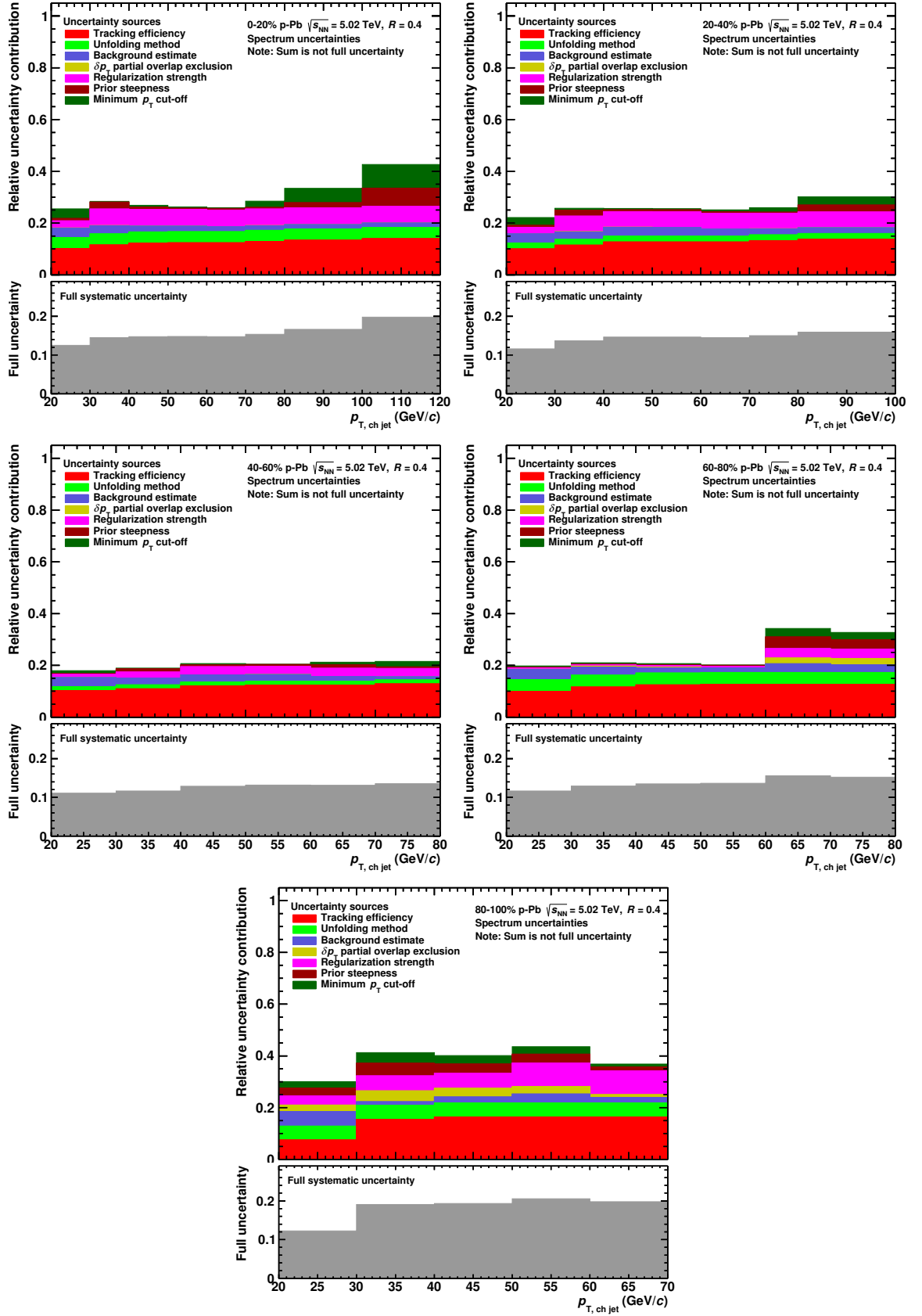


Figure 11.10: Stacked uncertainty contributions to illustrate how they relate (top panels) and total systematic uncertainty for the $R = 0.4$ spectrum.

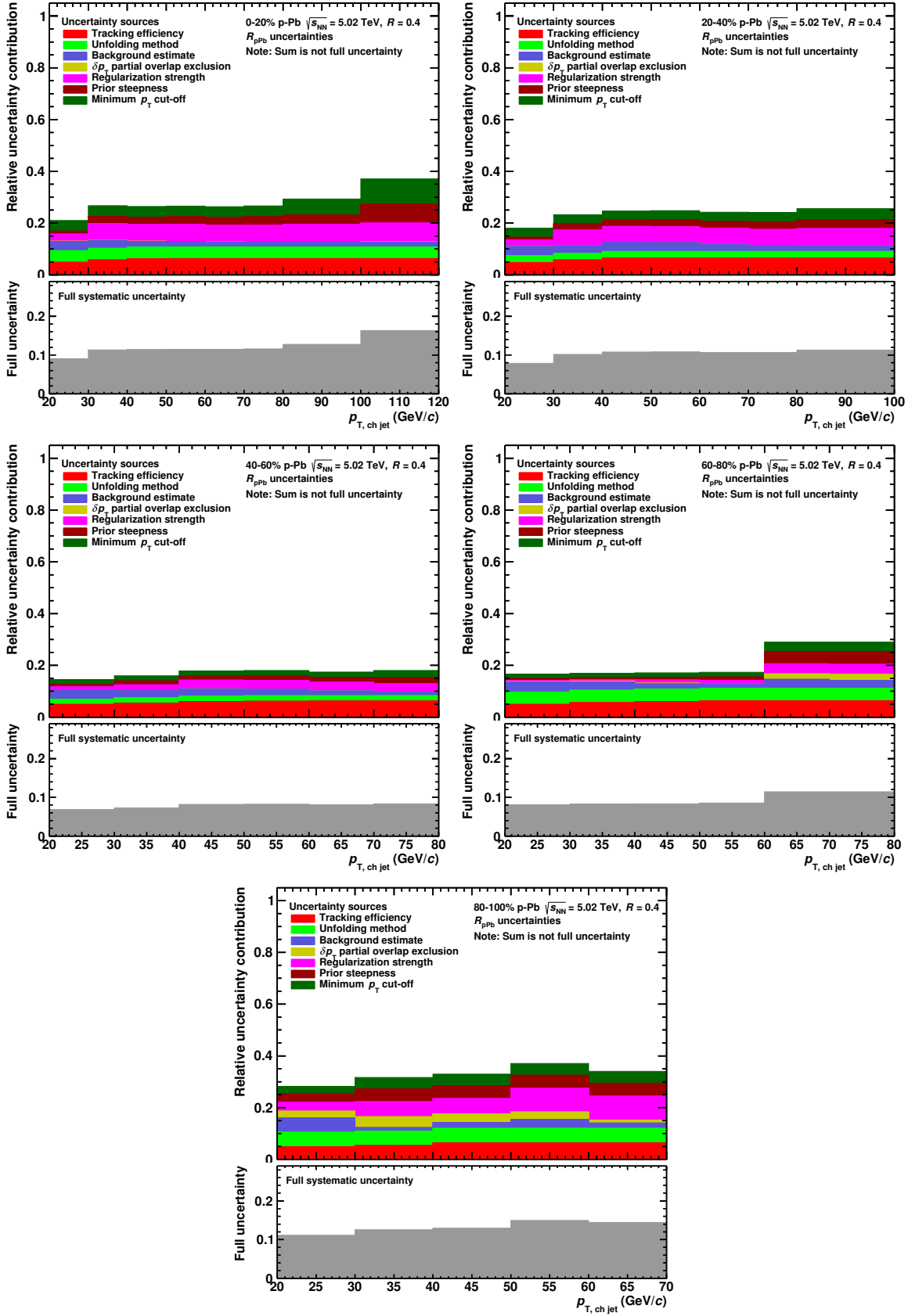


Figure 11.11: Stacked uncertainty contributions to illustrate how they relate (top panels) and total systematic uncertainty for the $R = 0.4$ nuclear modification factor.

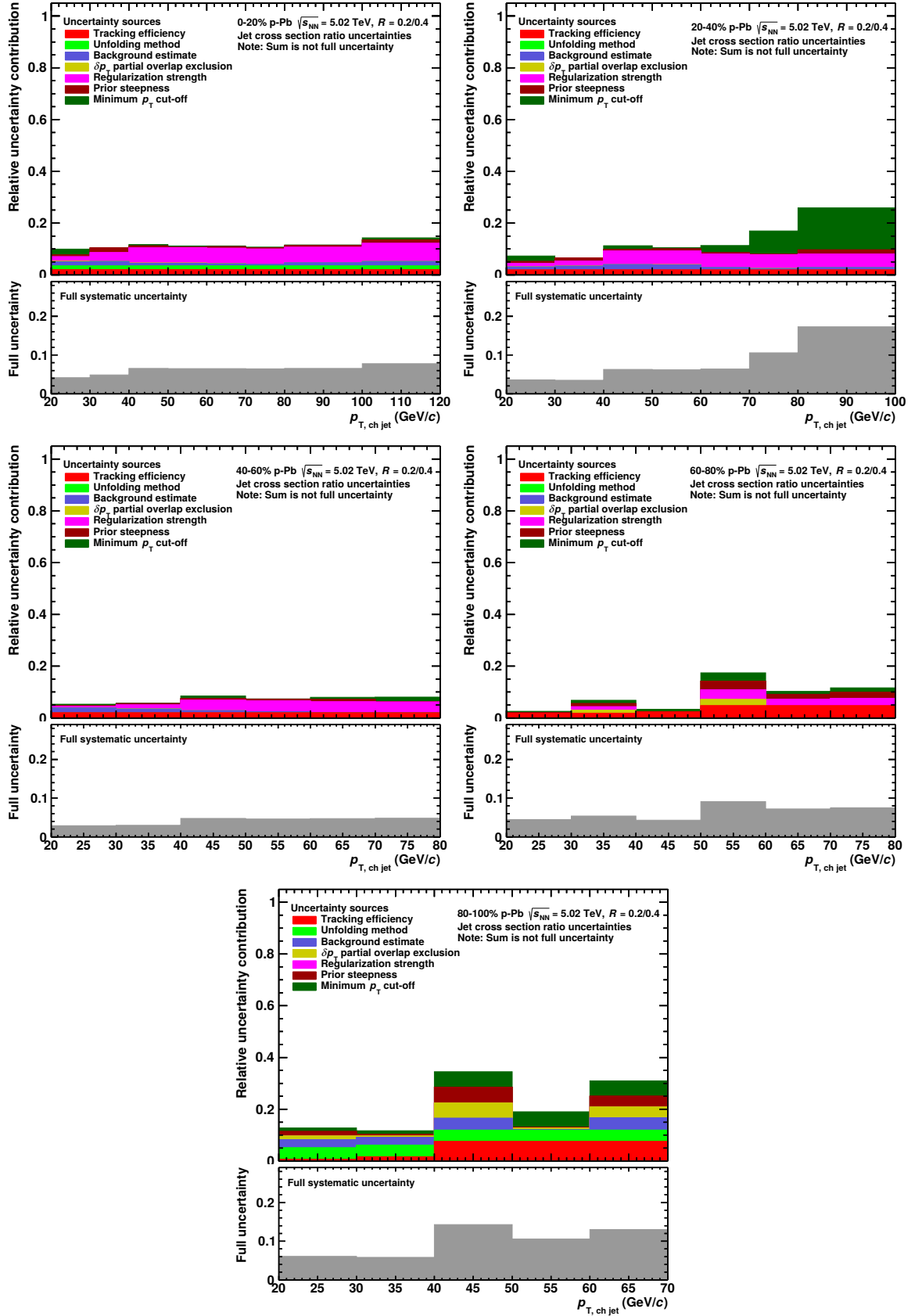


Figure 11.12: Stacked uncertainty contributions to illustrate how they relate (top panels) and total systematic uncertainty for the jet production cross section ratio.

Summary

In this thesis, several analyses on charged jets measured with the ALICE detector at the Large Hadron Collider (LHC) were presented. While the focus was on the careful evaluation of charged jet production in proton–lead (p–Pb) collisions at a center-of-mass energy of $\sqrt{s_{\text{NN}}} = 5.02$ TeV, also proton–proton (pp) collision data, measured with ALICE at 7 TeV, have been analyzed to connect p–Pb and pp collisions and to estimate nuclear effects in the p–Pb collision system.

Jets are the final state remnants of fragmented and hadronized partons that scattered off in a collision with relatively high momentum transfer. They typically allow access to the earliest stage in the collision.

The measurement and analysis of p–Pb collisions serve multiple purposes. First, this measurement is crucial for the interpretation of the corresponding observables in lead–lead (Pb–Pb) collisions. For instance, the observed jet quenching in Pb–Pb collisions is explained as a consequence of the interaction with a hot and dense medium created in Pb–Pb, the quark-gluon plasma (QGP). This interpretation strongly relies on the assumption that cold nuclear matter effects, which arise from the properties of the colliding nuclei like parton distributions, are small compared to hot nuclear matter effects from the QGP medium. At least in principle, this question can be addressed by analyzing p–Pb collisions.

Apart from serving as a baseline, the jet measurement of p–Pb collisions is of course interesting on its own to investigate the interplay between jets and the nuclear environment.

The jet analysis was performed using the currently most prevalent jet algorithm at the LHC: the anti- k_T algorithm, which is implemented in the FastJet package. These jets are very regular in shape. Jets were measured using the resolution parameters $R = 0.2$ and $R = 0.4$.

The correction techniques to obtain fully corrected theory-comparable jets are mainly the background correction and the unfolding of detector effects. For the background correction, several approaches were tested. The correction is applied by first subtracting an eventwise background density jet-by-jet, taking into account the jet’s area. Since the background fluctuates within one event from one region to another, background fluctuations have been considered on an ensemble basis in an SVD unfolding procedure. The same procedure was also used for detector effects like finite momentum resolution

and efficiency. A detailed simulation of the ALICE detector was deployed to transport PYTHIA-generated jets through the detector using GEANT3. A toy model allowed the validation of the unfolding mechanism.

Using these fully corrected jets, several observables were evaluated with detailed systematic checks. The most basic measured observable is the jet production cross section. Fully corrected jet production cross sections were measured and compared to NLO pQCD calculations with POWHEG. Within the uncertainties, an excellent agreement was measured in the transverse momentum (p_T) range $20 \leq p_T \leq 120$ GeV/ c between NLO pQCD calculations and p-Pb cross sections for both considered resolution parameters $R = 0.2$ and $R = 0.4$. This already indicates the absence of strong nuclear effects and that the binary N_{coll} scaling is not violated.

In order to extract an estimate for nuclear effects that does not strongly rely on a Monte Carlo simulation, the nuclear modification factor R_{pPb} was created using a (mostly) data-based pp reference.

As already indicated by the comparison of the jet spectra to NLO pQCD calculations, the nuclear modification factor shows no significant deviation from one for $R = 0.2$ and $R = 0.4$ in the full considered momentum range of $20 \leq p_T \leq 120$ GeV/ c . Additionally, the nuclear modification is compatible with the predictions obtained with the EPS09 nuclear parton distribution functions (nPDFs). However, it has to be noted that the performed measurement is not sensitive enough to give detailed conclusions on the validity of the nPDFs.

The charged jet spectra have also been compared to fully reconstructed jet spectra measured by the ALICE and ATLAS collaborations. Both full jet nuclear modification factors are compatible within uncertainties with the charged jet factor. In addition, the ratio of charged and full jet spectra of ALICE results agrees well with PYTHIA calculations within uncertainties.

A more detailed analysis was performed on the radial jet structure utilizing the jet production cross section ratio $R = 0.2/R = 0.4$ as the simplest estimate for a change of the jet shape and jet constituent profiles for more differential investigations. Within systematic uncertainties, no modification of the cross section ratio was observed for p-Pb collisions compared to pp collisions.

By means of jet constituent profiles, the basic observation of the jet production cross section ratio, i.e. that the jet collimation rises for larger jet transverse momenta, was confirmed in a directer way. It was also shown that the harder components in a jet are more collimated than the softer components. Note that this is not necessarily a physics effects but it could also be a trivial consequence of the jet finding algorithm or background. More differential analyses, e.g. with randomized events, could be performed in the future to explore the origin of this different shapes.

Regardless of the origin of the different spatial distributions for hard and soft jet con-

stituents, this different behavior is probably mostly responsible for the different jet collimation depending on jet momentum. This is because low- p_T jets are dominated rather by the soft constituents profile (weak collimation) than by the hard constituents (strong collimation).

An explicit comparison of jet constituent profiles in pp and p-Pb suggests that jets are probably broader in p-Pb than in pp for the lower momenta.

It should be noted that no systematic uncertainties were obtained for jet constituent profiles, because those profiles are distributions of rather technical nature for non-unfolded jet spectra. However, only qualitative conclusions were derived from those distributions.

To create the pp reference for the nuclear modification factor, a full pp analysis was performed. A good agreement with the NLO pQCD calculations is observed for the fully corrected pp spectra as well as for the jet production cross section ratio. Since this analysis has already been carried out by ALICE, the results of this work were compared to the “official” result: They are fully compatible within the systematic uncertainties.

For the spectra, nuclear modification factors, and jet production cross section ratios, the systematic uncertainties were evaluated carefully in a systematic way. The evaluation also included the extraction of the tracking efficiency uncertainty for the measured p-Pb data and the evaluation of how strong it is correlated to the uncertainty in the utilized pp data sample. This analysis was done this way in this thesis for the first time in ALICE.

Apart from minimum bias results, also the centrality dependence was examined in p-Pb collisions with the hybrid centrality approach that makes use of the deposited energy in the Zero Degree Calorimeter. Centrality-dependent spectra, nuclear modification factors Q_{pPb} , and jet production cross section ratios were calculated using essentially the same framework applied to minimum bias collisions for selected centrality classes. Additionally, the central over minimum bias ratio R_{CM} was measured.

In summary, no significant centrality dependence was observed for the hybrid centrality approach. Using the (biased) NBD-Glauber fit centrality approach, the spread of the centrality-dependent nuclear modification factors is larger, but except for the most peripheral 80-100% bin, the tension between the spectra assuming no centrality dependence is relatively small.

To conclude, the charged jet production is found to be compatible with scaled pQCD calculations at the same energy with or without nuclear PDFs. The nuclear modification factor R_{pPb} does not show strong nuclear effects on jet production and is consistent with unity in the measured p_T range between 20 and 120 GeV/ c . The jet cross section ratio does not indicate a strong nuclear modification of the jet radial profile. All these conclusions also hold for centrality-dependent results and, therefore, no strong centrality dependence is measured.

Zusammenfassung

In dieser Doktorarbeit wurden Analysen geladener Teilchenjets präsentiert, die mit dem ALICE-Detektor am Large Hadron Collider (LHC) gemessen wurden. Der Schwerpunkt lag in der Untersuchung der Jetproduktion in Kollisionen von Protonen und Bleikernen (p-Pb) bei einer Schwerpunktsenergie von $\sqrt{s_{\text{NN}}} = 5.02$ TeV. Allerdings wurden ebenfalls Kollisionen von Protonen (pp) bei einer Energie von 7 TeV analysiert, um beide Kollisionssysteme zu verknüpfen und um etwaige Kerneffekte abschätzen zu können.

Teilchenjets sind die Endprodukte fragmentierter und hadronisierter Partonen, die in einer Hochenergiekollision mit hohem Impulsübertrag aneinander streuen. Sie erlauben einen Einblick in die früheste Phase der Kollision.

Die Untersuchung von p-Pb-Kollisionen ist auf der einen Seite wichtig für die Interpretation von Pb-Pb-Kollisionen. Dort wird z.B. die beobachtete Unterdrückung von Jetspektren verglichen mit pp-Kollisionen ("jet quenching") als Konsequenz der Wechselwirkung der gestreuten Partonen mit einem heißen und dichten Medium, dem Quark-Gluon-Plasma, beschrieben. Diese Interpretation setzt allerdings voraus, dass die Effekte der kalten Kernmaterie wie z.B. durch Partonverteilungen relativ klein sind. Diese Frage kann zumindest prinzipiell durch die Analyse von p-Pb-Kollisionen beantwortet werden. Neben ihrer Wichtigkeit als Baseline ist die Messung von Jets in p-Pb-Kollisionen durchaus auch für sich interessant, um die Wechselwirkung von Jets und Kernumgebung genauer zu beleuchten.

Das Suchen von Jets wurde von dem bewährten und am LHC sehr häufig verwendeten anti- k_T -Algorithmus durchgeführt. Dieser ist im FastJet-Paket enthalten und erzeugt Jets mit sehr regulären (runden) Formen. Es wurden die Auflösungsparameter $R = 0.2$ und $R = 0.4$ verwendet.

Die wichtigsten Korrekturtechniken, um die Jetspektren mit der Theorie vergleichen zu können, sind die Untergrundkorrektur und die Entfaltung der Detektoreffekte. Für den Untergrund, der ereignisweise berechnet wird und von den Jets in Abhängigkeit ihrer Fläche abgezogen wird, wurden mehrere Methoden verglichen. Weil der Untergrund innerhalb eines Ereignisses fluktuieren kann, wurden auch die Untergrundfluktuationen in einer SVD-Entfaltungsprozedur berücksichtigt. Die gleiche Prozedur wurde auch für die Entfaltung der Detektoreffekte verwendet. Letztere verlangt eine detaillierte Simulation des ALICE-Detektors, durch welche PYTHIA-erzeugte Jets mittels GEANT3 transportiert werden. Ein toy model wurde zur Validierung der Entfaltungsprozedur verwendet.

Verschiedene Observablen wurden unter Berücksichtigung ausführlicher systematischer Tests berechnet. Die grundlegende Observable ist hierbei der Wirkungsquerschnitt der Jetproduktion. Ein Vergleich der korrigierten Spektren mit NLO pQCD Simulationen von POWHEG zeigt innerhalb der Unsicherheiten eine exzellente Übereinstimmung im gesamten betrachteten Transversalimpulsbereich für $R = 0.2$ und $R = 0.4$. Dies ist bereits ein klarer Hinweis auf die Abwesenheit starker Kerneffekte und dass die Spektren mit N_{coll} skalieren.

Zur Bestimmung der Kerneffekte ohne eine all zu starke Abhängigkeit von Monte Carlo Simulation einzuführen, wurde der Kernmodifikationsfaktor R_{pPb} mithilfe eines hauptsächlich datenbasierten pp-Referenzspektrums erzeugt.

Wie der Vergleich zu den NLO-Spektren zeigt auch R_{pPb} keine signifikante Abweichung von Eins und ist ebenfalls kompatibel mit den Vorhersagen der Kernpartonverteilungsfunktionen (nPDFs). Die von den nPDFs vorhergesagten Effekte sind allerdings auch sehr klein.

Die gemessenen Spektren der geladenen Jets wurden auch mit Spektren vollständig rekonstruierter Jets der ALICE- und ATLAS-Kollaborationen verglichen. Innerhalb der Unsicherheiten sind die Messungen kompatibel. Gleichzeitig wurde das Spektren-Verhältnis geladener Jets und vollständig rekonstruierter Jets von ALICE berechnet, welches mit PYTHIA-Berechnungen innerhalb der Unsicherheit übereinstimmt.

Detaillierte Untersuchungen wurden auch zur radialen Struktur von Jets durchgeführt. Das einfachste Maß, das Wirkungsquerschnittsverhältnis $R = 0.2/R = 0.4$ zeigt innerhalb der Unsicherheiten in p-Pb-Kollisionen keine Modifikation verglichen zu pp-Kollisionen. Eine Untersuchung der radialen Jetprofile bestätigt die Beobachtung verstärkter Jetkollimation bei steigendem Transversalimpuls (p_T). Ebenso konnte gezeigt werden, dass die Konstituenten mit hohem p_T eine stärkere Kollimation zeigen als solche mit niedrigem p_T . Dies muss nicht unbedingt ein physikalischer Effekt sein, sondern kann auch durch triviale Effekte durch den Jetalgorithmus oder den Untergrund erzeugt werden. Weitere Untersuchungen, z.B. mit randomisierten Ereignissen, könnten über die Ursache der unterschiedlichen Kollimation Aufschluss geben.

Unabhängig von der Ursache ist diese unterschiedliche Kollimation vermutlich für die stärkere Kollimation bei hohem Jet- p_T verantwortlich, weil die radialen Profile von Jets mit niedrigem p_T eher von Teilchen mit niedrigem p_T und die von Jets mit hohem p_T eher von Teilchen mit hohem p_T dominiert sind.

Der Vergleich der Profile in pp und p-Pb deutet auf etwas breitere Jetprofile in p-Pb bei niedrigem Transversalimpuls hin. Es muss allerdings betont werden, dass die gemessenen Jetprofile unkorrigierte Größen sind.

Die Erzeugung des pp-Referenzspektrums erforderte eine vollständige Analyse der pp-Daten. Hier wurde eine gute Übereinstimmung mit NLO-Simulationen für Spektren und Spektrenverhältnis bei gleicher Energie festgestellt. Auch mit der "offiziellen" pp-Analyse stimmen die in der Arbeit berechneten Größen überein.

Systematische Unsicherheiten wurden für die Spektren, Spektrenverhältnisse und für die Kernmodifikationsfaktoren auf methodische Art und Weise berechnet. Dies beinhaltet ebenfalls eine Analyse der Trackingeffizienz und ihrer Korrelation in pp- und p-Pb-Kollisionen. Die Bestimmung der Korrelation wurde in dieser Arbeit das erste Mal in dieser Form in ALICE durchgeführt.

Neben Ergebnissen für Minimum-Bias-Kollisionen wurden mithilfe der *Hybridmethode* zur Zentralitätsbestimmung auch zentralitätsabhängige Spektren, Spektrenverhältnisse und Kernmodifikationsfaktoren berechnet. Zusätzlich wurde das Verhältnis aus zentralen und Minimum-Bias-Kollisionen R_{CM} berechnet.

Insgesamt wurde keine signifikante Zentralitätsabhängigkeit beobachtet. Selbst bei Nutzung der nicht zuverlässigen NBD-Glauber Zentralitätsbestimmung zeigt sich mit Ausnahme der periphersten Kollisionen (80-100%) nur ein geringer Unterschied der einzelnen Größen.

Zusammenfassend kann gesagt werden, dass die Messungen der Produktion geladener Teilchenjets kompatibel sind mit skalierten pQCD-Simulationen bei gleicher Energie mit oder ohne nPDFs. Der Kernmodifikationsfaktor R_{pPb} zeigt keine starken Kerneffekte und ist innerhalb des gesamten Transversalimpulsbereichs kompatibel mit Eins. Das Spektrenverhältnis $R = 0.2/R = 0.4$ deutet ebenfalls nicht auf eine starke Modifikation durch Kerneffekte hin. Diese Schlussfolgerungen gelten auch für die zentralitätsabhängigen Ergebnisse. Somit wurde auch keine starke Zentralitätsabhängigkeit gemessen.

A. Appendix

A.1. Basic kinematics

The kinematic description of high energy collisions follows a certain terminology. Since the corresponding terms and observables are used multiple times throughout this thesis, they are briefly introduced in this section.

A.1.1. Center-of-mass energy

A basic property of every collision is the center-of-mass energy. It represents the whole energy that is available in the collision from rest and kinetic energy of the colliding particles. In the following, natural units with $c = 1$ are used. To calculate the total energy of a collision of two particles A and B in the center-of-mass system, consider the squared four-momentum of the system,

$$p^2 = (E_A + E_B)^2 - (\vec{p}_A + \vec{p}_B)^2, \quad (\text{A.1})$$

where E_i and \vec{p}_i represent the energy and the (three-)momentum, respectively. Per definition, in the center-of-mass system it is $\vec{p}_A + \vec{p}_B = 0$ and thus

$$p^2 = (E_A + E_B)^2 = E_{\text{tot}}^2 \equiv s. \quad (\text{A.2})$$

This formula is equal to one of the Mandelstam variables $s = (p_A + p_B)^2$. The energy available in a collision is commonly expressed by \sqrt{s} :

$$\sqrt{s} = \sqrt{(p_A + p_B)^2} = E_{\text{tot}}. \quad (\text{A.3})$$

Note that p_A and p_B are four-momenta. In heavy-ion collisions, energy and momenta are typically normalized per colliding nucleon and the quantity is called $\sqrt{s_{\text{NN}}}$.

In a symmetric collision, the total energy is easily calculable using Eq. A.2 since $E_A = E_B$ and, thus, it is

$$\sqrt{s} = 2E, \quad (\text{A.4})$$

where E is the energy of the colliding particles or nucleons in the rest frame of the collision.

In a collision, in which the projectiles have different energies in the rest frame, the total energy can be calculated based on Eq. A.1 [Per87]. It is

$$\sqrt{s} = \sqrt{p^2} = \sqrt{E_A^2 + E_B^2 + 2E_A E_B - \vec{p}_A \cdot \vec{p}_A - \vec{p}_B \cdot \vec{p}_B + 2(\vec{p}_A \cdot \vec{p}_B)}. \quad (\text{A.5})$$

With $E^2 = \vec{p}^2 + m^2$, it follows

$$\sqrt{s} = \sqrt{2(E_A E_B + \vec{p}_A \cdot \vec{p}_B) + m_A^2 + m_B^2}. \quad (\text{A.6})$$

For fixed-target experiments, i.e. $E_B = m_B$ and $\vec{p}_B = 0$, this simplifies to

$$\sqrt{s} = \sqrt{2E_A m_B + m_A^2 + m_B^2}. \quad (\text{A.7})$$

In the general case of two particle beams, but using the approximation that the collision energy is much larger than the projectile masses, $E_{\text{tot}} \gg m_A, m_B$, Eq. A.6 can be written as

$$\sqrt{s} \approx 2\sqrt{E_A E_B}. \quad (\text{A.8})$$

In the per-nucleon representation, the energies E_i have to be normalized by the corresponding mass number A_i . Additionally, in the case of collisions taking place at the LHC, the particle momenta are directly related by $p_i = Q_i p_{\text{proton}}$ depending on their charge Q_i . This is due to the two-in-one magnet design of the LHC [Sal12].

Therefore, with $E_i \approx p_i = Q_i p_{\text{proton}}$, it follows

$$\sqrt{s_{\text{NN}}} \approx 2p_{\text{proton}} \sqrt{\frac{Q_A Q_B}{A_A A_B}} \approx 2E_{\text{proton}} \sqrt{\frac{Q_A Q_B}{A_A A_B}}. \quad (\text{A.9})$$

Comparing Eqs. A.6 and A.7, the advantages of colliding two beams instead of performing a fixed-target experiment becomes obvious. In contrast to the collision of two beams where the center-of-mass energy rises linearly with the beam energies, the available cms energy in a fixed-target experiment does only grow with the square root of the projectile beam energy [Dem04].

A.1.2. Rapidity and pseudorapidity

The basic properties to describe the position of objects originating from a collision, e.g. tracks, are given by pseudorapidity and azimuthal angle. The naive ansatz to use the polar angle θ is disfavored, mainly because the particle production is roughly constant as a function of pseudorapidity. Pseudorapidity is defined by

$$\eta = \frac{1}{2} \ln \frac{|\vec{p}| + p_L}{|\vec{p}| - p_L} = -\ln(\tan \theta/2). \quad (\text{A.10})$$

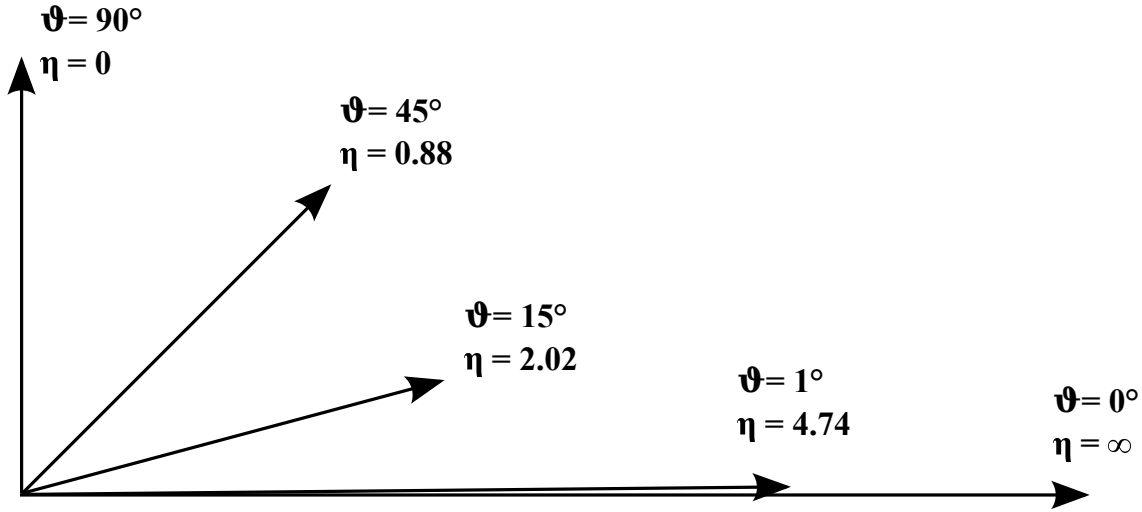


Figure A.1: Examples for various pseudorapidities.

Here, p_L is the longitudinal component of the particle's momentum $p = p_T + p_L$, $p_L = |\vec{p}| \cos(\theta)$. The relation of pseudorapidity and polar angle is depicted in Fig. A.1. In the limit of vanishing masses, pseudorapidity turns into rapidity, which is given by

$$y = \frac{1}{2} \ln \frac{E + p_L}{E - p_L}. \quad (\text{A.11})$$

In contrast to pseudorapidity, rapidity is not only defined by the polar angle but it also depends on the mass. Therefore, energy and momentum must be measured simultaneously and this in general requires particle identification and is much more complex.

In asymmetric collisions, in which the laboratory frame and the center-of-mass do not coincide, the particles are shifted in rapidity [Sal12]:

$$\Delta y \approx \frac{1}{2} \ln \sqrt{\frac{Q_1 A_2}{Q_2 A_1}}. \quad (\text{A.12})$$

In the special case of proton–lead collisions, which are of interest for this thesis, the rapidity shift for a colliding nucleon–nucleon pair is given by $\Delta y \approx 0.465$.

A.2. Systematic uncertainties

In this appendix, several detailed plots on systematic deviations/uncertainties are shown.

A.2.1. Uncertainties for minimum bias $R = 0.2$ jets

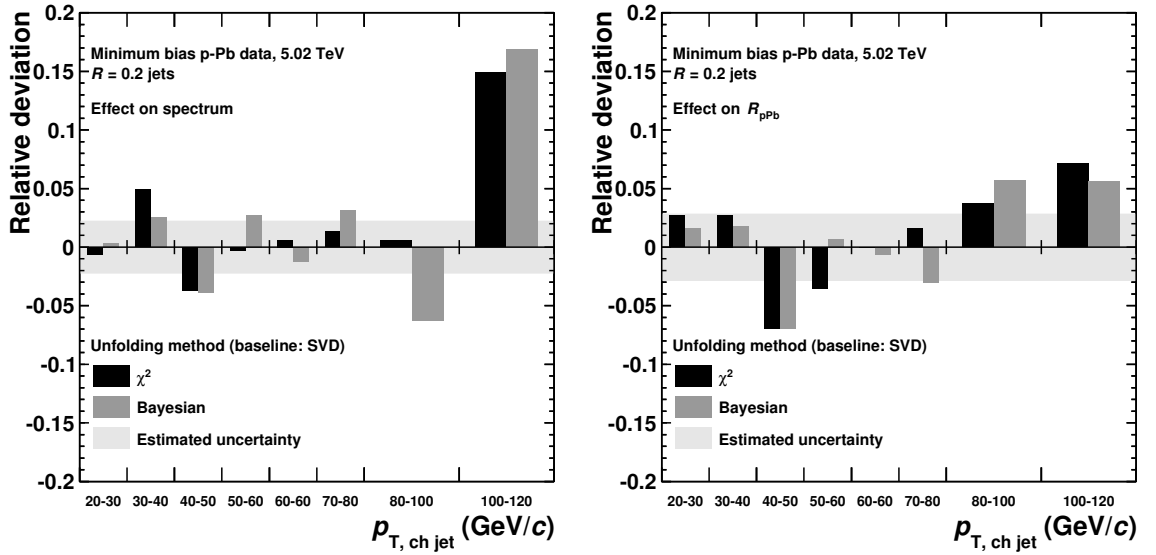


Figure A.2: Relative deviations of varied R_{pPb} (left), and jet production cross section ratio (right) from the corresponding baselines when changing unfolding method.

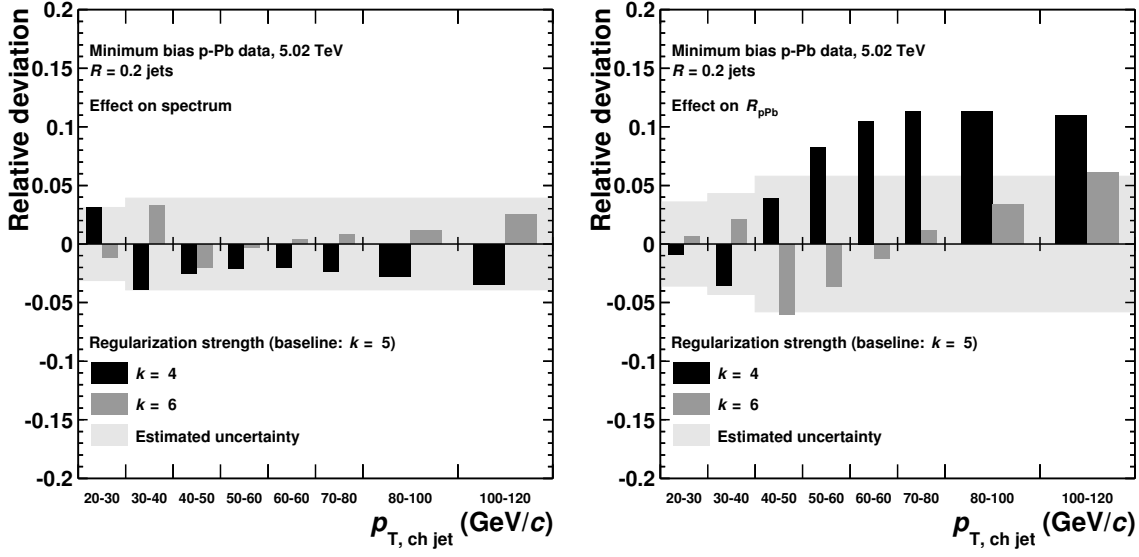


Figure A.3: Relative deviations of varied R_{pPb} (left), and jet production cross section ratio (right) from the corresponding baselines when changing regularization strength. Note that for the parameter $k = 4$ the pp spectrum is strongly overregularized. Therefore, this parameter setting is not considered as a reasonable variation and is discarded.

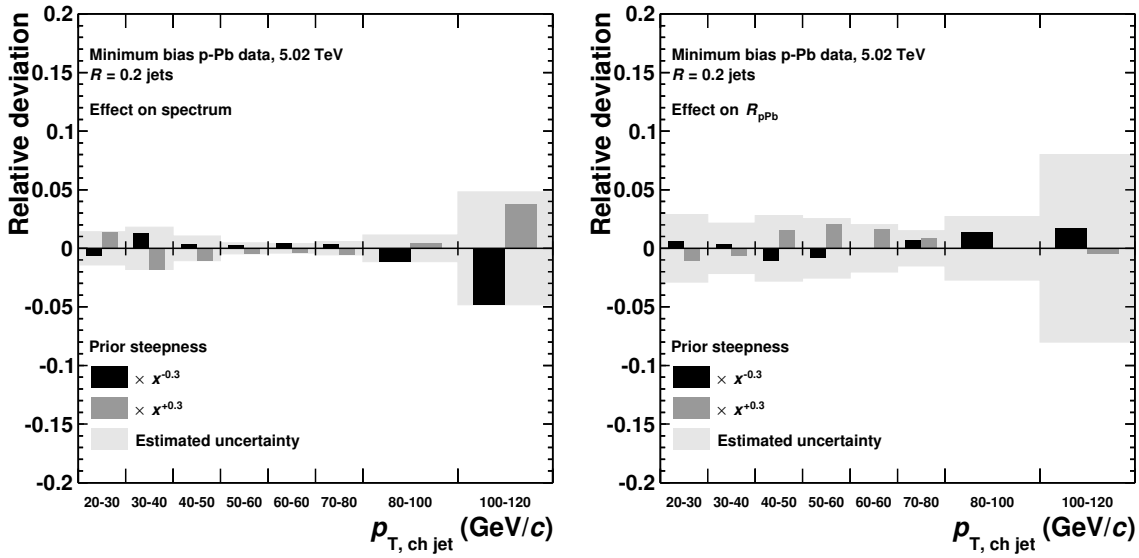


Figure A.4: Relative deviations of varied R_{pPb} (left), and jet production cross section ratio (right) from the corresponding baselines when changing the steepness of the prior.

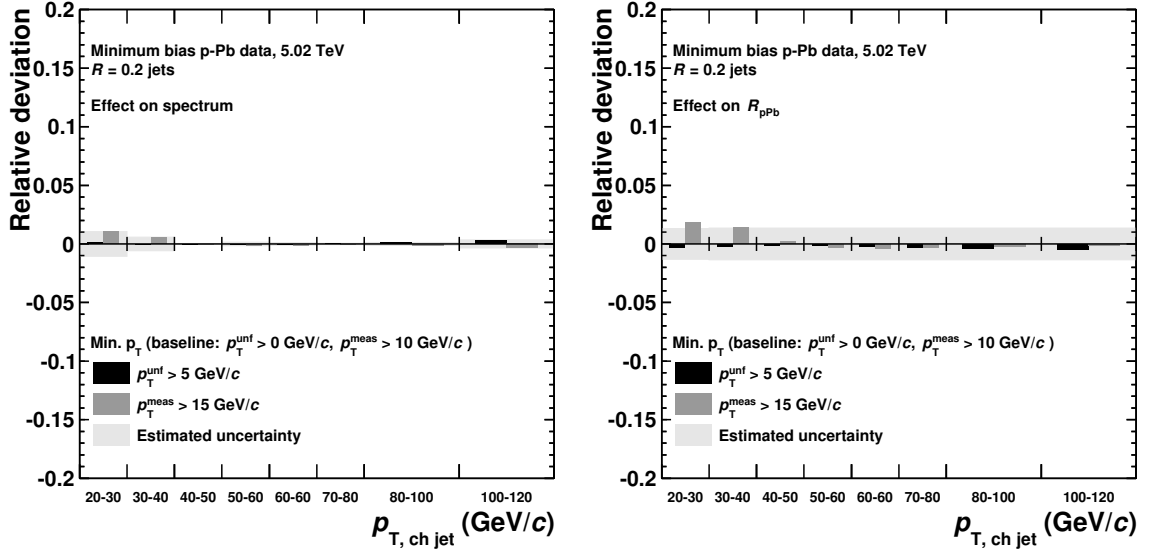


Figure A.5: Relative deviations of varied R_{pPb} (left), and jet production cross section ratio (right) from the corresponding baselines when changing the minimum p_T in the analysis.

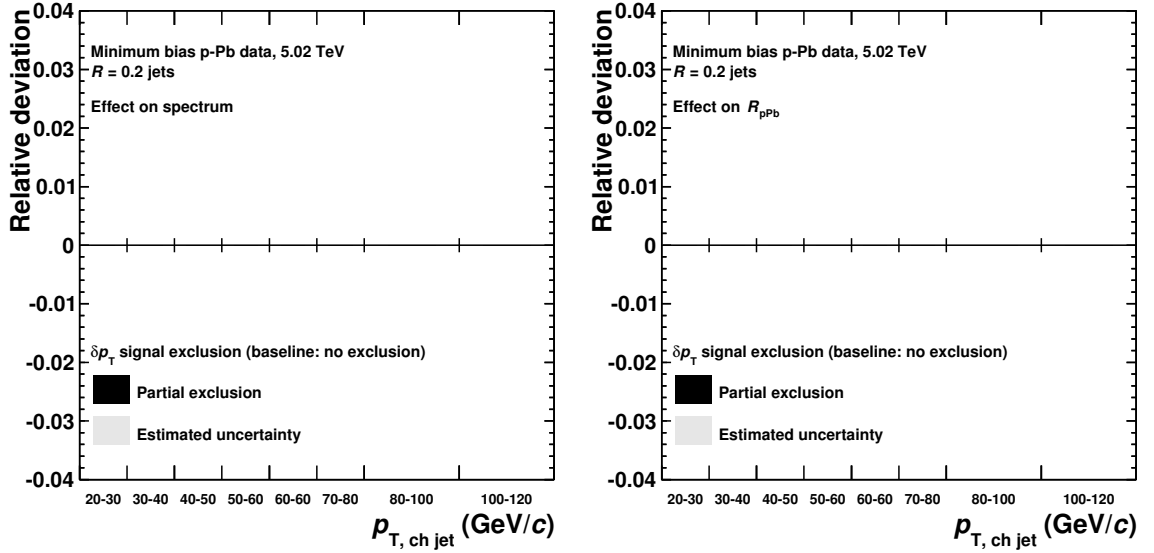


Figure A.6: Relative deviations of varied R_{pPb} (left), and jet production cross section ratio (right) from the corresponding baselines when using a δp_T signal exclusion in the analysis.

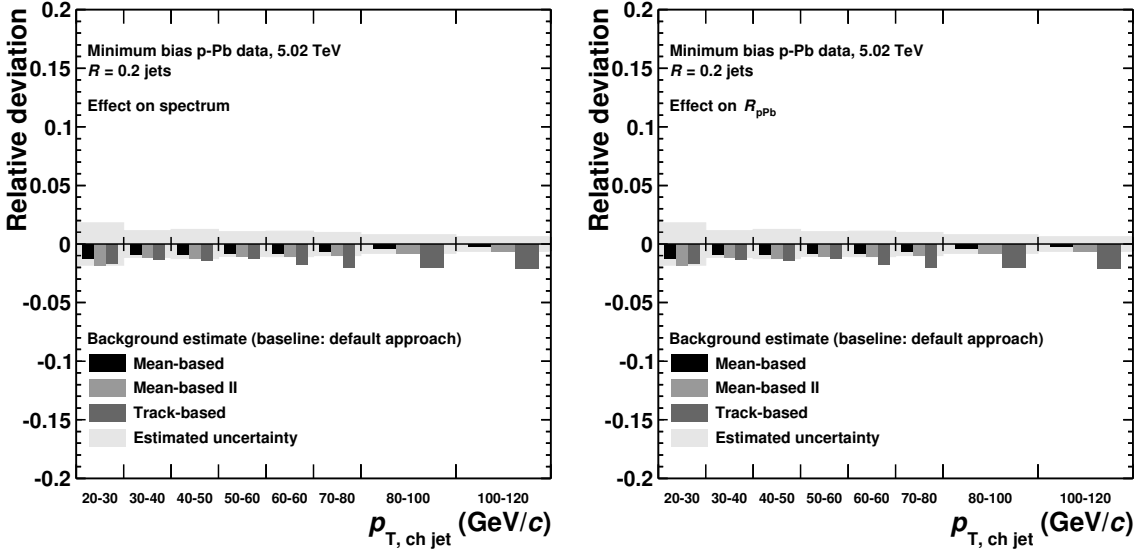


Figure A.7: Relative deviations of varied R_{pPb} (left), and jet production cross section ratio (right) from the corresponding baselines when varying the background estimate in the analysis.

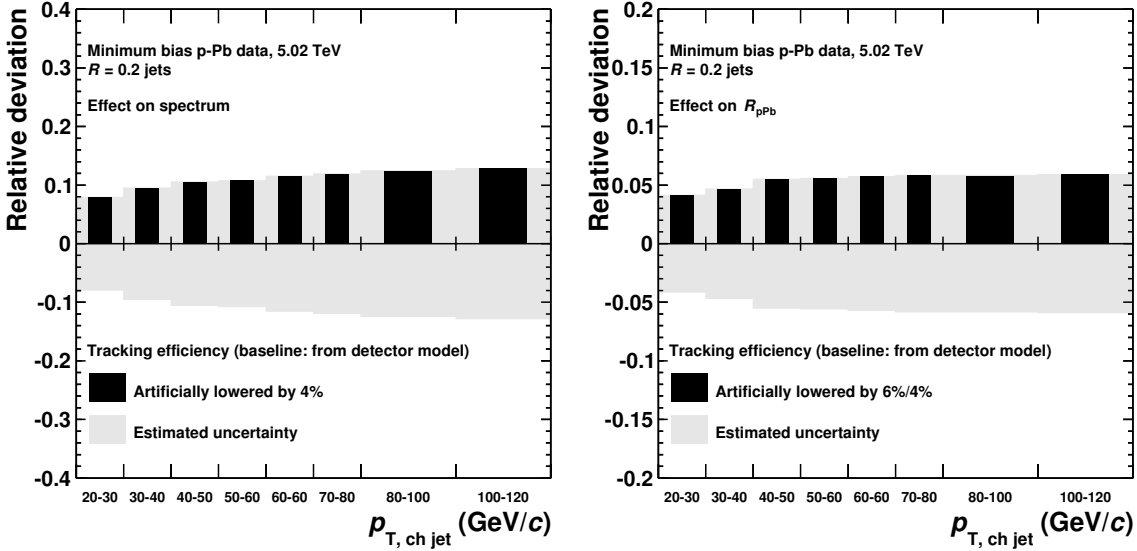


Figure A.8: Relative deviations of varied R_{pPb} (left), and jet production cross section ratio (right) from the corresponding baselines for reduced tracking efficiency.

A.2.2. Uncertainty summary for centrality-dependent $R = 0.2$ jets

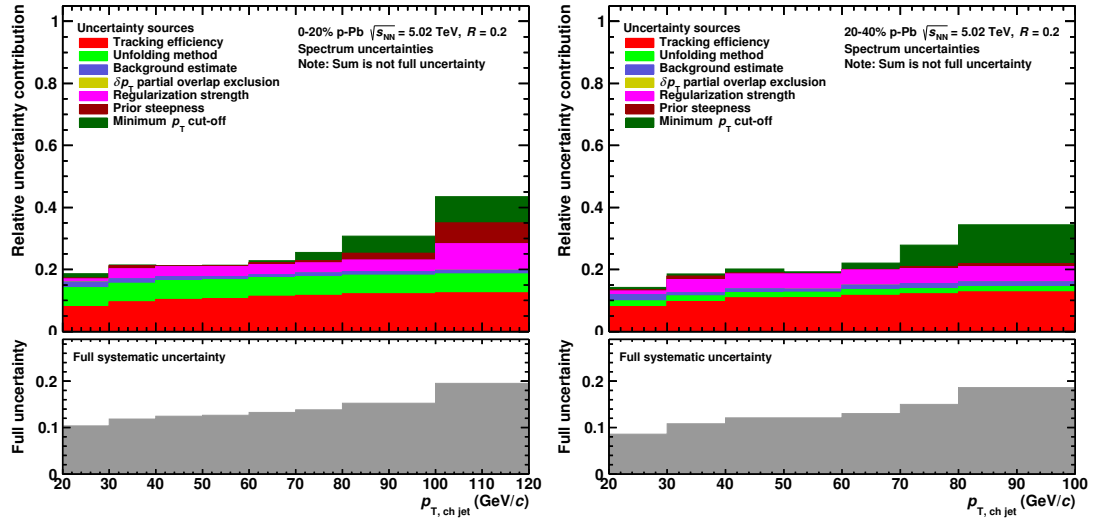


Figure A.9: Stacked uncertainty contributions to illustrate how they relate (top panels) and total systematic uncertainty for the $R = 0.2$ spectrum.

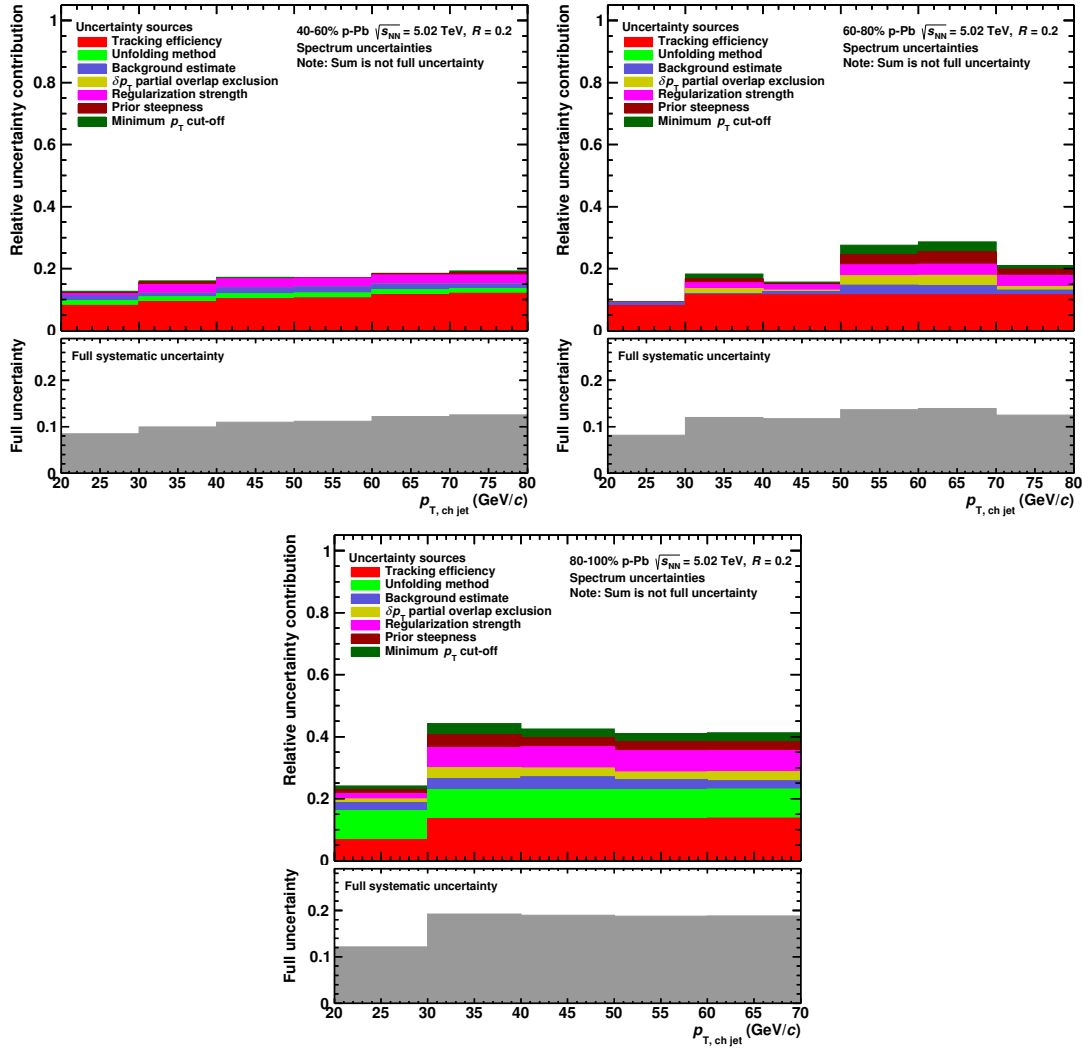


Figure A.10: Stacked uncertainty contributions to illustrate how they relate (top panels) and total systematic uncertainty for the $R = 0.2$ spectrum.

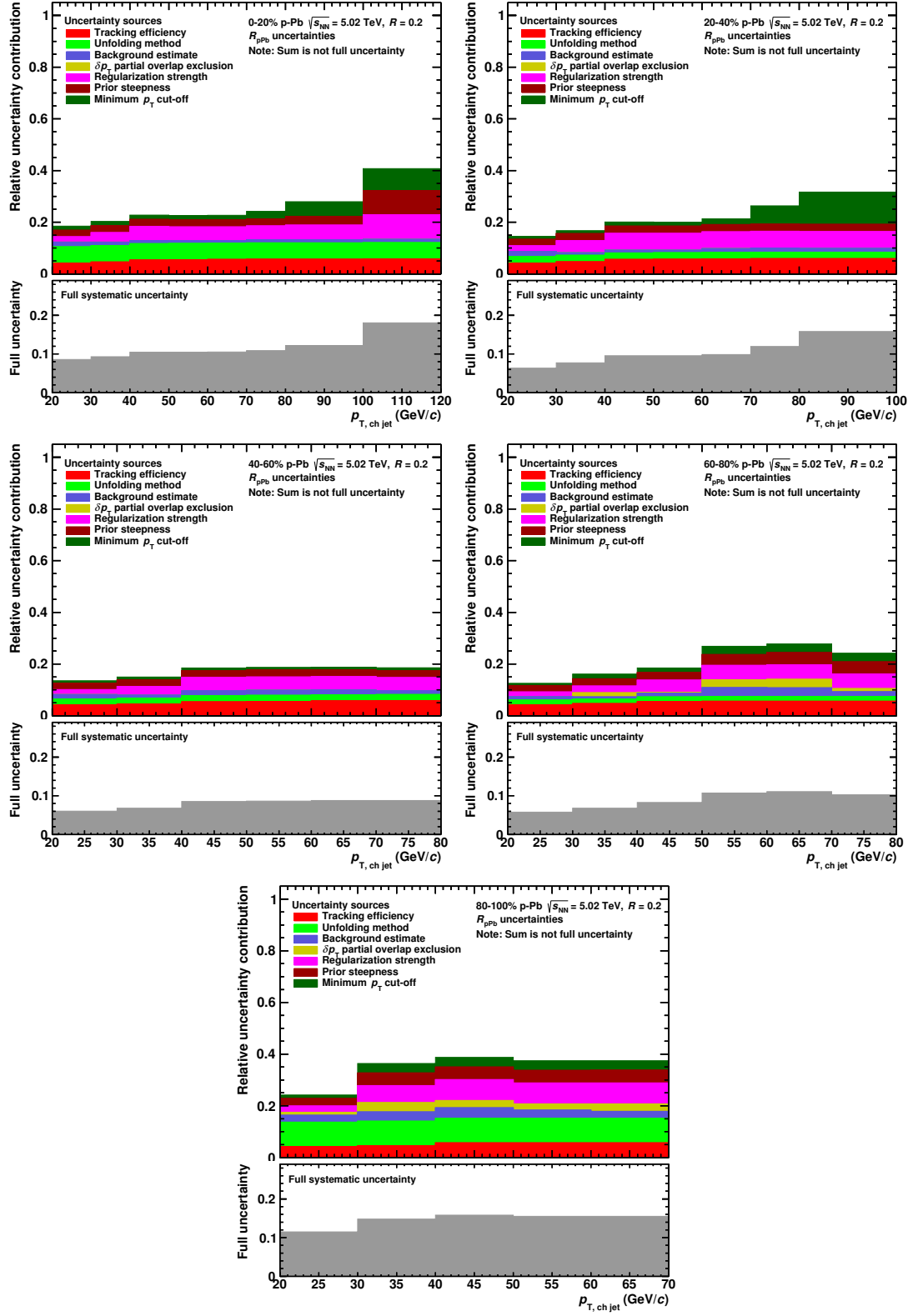


Figure A.11: Stacked uncertainty contributions to illustrate how they relate (top panels) and total systematic uncertainty for the $R = 0.2$ nuclear modification factor.

List of tables

2.1. Elementary particles and their masses	6
5.1. N_{coll} for different centrality classes	50
6.1. Values of background density and fluctuations for different methods . . .	69
6.2. Characteristic values for residuals of response matrix	83
7.1. Number of events with and without vertex cut	95
7.2. Track cut definitions in pp and p-Pb	98
8.1. Mean constituent distances in pp and p-Pb	122
9.1. Uncertainties on the tracking efficiency	151
9.2. Summary of systematic uncertainties in minimum bias p-Pb collisions . .	156
10.1. Summary of systematic uncertainties in pp collisions	165
11.1. Centrality-dependent vertex finding efficiency	169
11.2. Centrality-dependent nuclear overlap functions	174

List of figures

2.1. Illustration of the factorized hard scattering process	10
2.2. Possible phases of nuclear media (illustration)	11
2.3. Charged track invariant yield for pp collisions (example)	13
2.4. Illustration of semi-central nucleus–nucleus collision	14
3.1. Parton distribution functions (CJ12mid)	18
3.2. Nuclear modification for lead nuclei predicted by EPS09NLO	19
3.3. Explanation of nuclear modification	19
3.4. Gluon saturation in protons (example)	21

3.5.	Jet quenching for particles/full jets	24
3.6.	Illustration of elliptic flow in heavy-ion collisions	25
3.7.	Double-ridge observation in p–Pb collisions with ALICE	26
3.8.	Comparison of p–Pb data to hydrodynamic models	27
3.9.	Fourier coefficients measured in p–Pb by ALICE	27
4.1.	Illustration of the LHC accelerator chain	29
4.2.	General layout of ALICE	31
4.3.	General layout of the ITS	32
4.4.	General layout of the TPC	33
4.5.	General layout of the ZDC	35
5.1.	Illustration of collinear and infrared safety	40
5.2.	Comparison of anti- k_T and k_T jets	41
5.3.	Illustration of ghost distribution	43
5.4.	Illustration of a Glauber Monte Carlo simulation	45
5.5.	NBD-Glauber fit	47
5.6.	Correlation of multiplicity, N_{part} , and N_{part} in p–Pb	48
6.1.	Event display in p–Pb	58
6.2.	Background density for original Pb–Pb approach	60
6.3.	Background density and fluctuations in p–Pb (default approach)	61
6.4.	Impact of taking the signal jet overlap probability into account on δp_T	64
6.5.	Jet p_T dependence of δp_T	65
6.6.	Background centrality interval dependence	65
6.7.	Background centrality estimator dependence	66
6.8.	Jet p_T dependence of background	67
6.9.	η dependence of background	68
6.10.	Comparison of background density for different estimates	70
6.11.	Comparison of δp_T for different estimates	71
6.12.	Response matrix for background fluctuations (illustration)	78
6.13.	Response and unfolding matrices (illustration)	80
6.14.	Kinematic and jet rec. efficiency for p–Pb	81
6.15.	Slices of response matrices	82
6.16.	Toy model: Regularization parameter analysis for SVD unfolding	84
6.17.	Toy model: Comparison of true and SVD-unfolded jets	85
6.18.	Pearson coefficients for Bayesian and χ^2 -unfolding	86
6.19.	Toy model: Comparison of unfolded and truth results	87
6.20.	Unfolding method comparison in p–Pb	88
6.21.	Unfolding method comparison in pp	88
6.22.	Measured, unfolded, and refolded spectrum for p–Pb and pp	89
7.1.	Distribution of vertex z for p–Pb collisions	95

7.2.	η distribution of raw hybrid tracks in p-Pb collisions	96
7.3.	Azimuthal distribution of track samples in p-Pb collisions	97
7.4.	Jet η distributions in p-Pb	101
7.5.	Jet area distribution	102
8.1.	Charged jet production cross section in p-Pb for $R = 0.2$	107
8.2.	Charged jet production cross section in p-Pb for $R = 0.4$	108
8.3.	pp reference energy scaling factors, effect of Lorentz Boost	110
8.4.	Nuclear modification factor R_{pPb} of charged jets	112
8.5.	Nuclear modification factor R_{pPb} measured by ATLAS for $R = 0.4$. . .	113
8.6.	Charged jet production cross section ratio $R = 0.2/R = 0.4$ in p-Pb . .	115
8.7.	Correlation matrix in p-Pb for $R = 0.2$ and $R = 0.4$	117
8.8.	Corrections for and impact of correlation matrix (illustration)	117
8.9.	Jet constituent profiles in p-Pb	120
8.10.	Jet constituent profiles in p-Pb (lowest p_{T})	121
8.11.	Jet constituent profiles in pp and p-Pb	123
8.12.	Comparison of mean distance distributions in pp and p-Pb	123
8.13.	Nuclear modification factor including one bin below 20 GeV/ c	125
8.14.	Jet constituent count distributions in pp and p-Pb	126
8.15.	Difference of jet profiles in pp and p-Pb	126
8.16.	Azimuthal distributions of track subsamples for good and all runs	128
8.17.	Impact of using only good runs on jets	129
8.18.	CMS charged particle R_{pPb} ; track-jet spectra scaling	130
8.19.	Comparison of nuclear modification factors R_{pPb} for jets and particles .	131
8.20.	Full jets in p-Pb measured by ALICE	133
8.21.	Ratio of charged and full jets in p-Pb compared to MC prediction . . .	134
9.1.	Jet systematics in p-Pb for $R = 0.4$ jets (unfolding)	137
9.2.	Jet systematics in p-Pb for $R = 0.4$ jets (regularization)	138
9.3.	Jet systematics in p-Pb for $R = 0.4$ jets (Prior)	139
9.4.	Toy model: Influence of difference prior on unfolded result	140
9.5.	Jet systematics in p-Pb for $R = 0.4$ jets (minimum p_{T})	141
9.6.	Jet systematics in p-Pb for $R = 0.4$ jets (δp_{T})	142
9.7.	Jet systematics in p-Pb for $R = 0.4$ jets (background)	143
9.8.	Calculation of tracking efficiency uncertainty (illustration)	145
9.9.	Tracking efficiency uncertainty evaluation I	147
9.10.	Tracking efficiency uncertainty evaluation II	148
9.11.	Tracking efficiency uncertainty evaluation III	149
9.12.	Tracking efficiency uncertainty evaluation IV	150
9.13.	Jet systematics in p-Pb for $R = 0.4$ jets (tracking efficiency)	152
9.14.	Jet systematics in p-Pb for $R = 0.4$ jets (normalization)	153
9.15.	Comparison of 7 TeV charged jet analysis results	154

9.16.	Stacked uncertainty contributions for jet cross section ratio in p-Pb . . .	157
9.17.	Stacked uncertainty contributions for jet cross sections in p-Pb	158
9.18.	Stacked uncertainty contributions for jet nuclear modification factor . . .	159
10.1.	Charged jet production cross section in pp for $R = 0.2$	162
10.2.	Charged jet production cross section in pp for $R = 0.4$	163
10.3.	Charged jet production cross section ratio $R = 0.2/R = 0.4$ in pp	164
10.4.	Stacked uncertainty contributions for jet cross sections in pp	166
10.5.	Stacked uncertainty contributions for jet cross section ratio in pp	167
11.1.	Centrality-dependent jet spectra in p-Pb for $R = 0.2$ and $R = 0.4$. . .	170
11.2.	Centrality-dependent jet Q_{pPb} for $R = 0.2$ and $R = 0.4$ ($N_{\text{coll}}^{\text{Pb-side}}$)	172
11.3.	Centrality-dependent jet Q_{pPb} for $R = 0.2$ and $R = 0.4$ ($N_{\text{coll}}^{\text{mult}}$)	173
11.4.	Centrality-dependent jet nuclear modification factors (ATLAS)	174
11.5.	Ratio of central over MB jet spectra	176
11.6.	Centrality-dependent jet cross section ratio	177
11.7.	Centrality-dependent jet Q_{pPb} for $R = 0.2$ (NBD-Glauber centrality) . .	179
11.8.	Centrality-dependent jet Q_{pPb} for $R = 0.4$ (NBD-Glauber centrality) . .	180
11.9.	Comparison of NBD-Glauber fit and hybrid method centrality	180
11.10.	Stacked uncertainties for centrality-dependent jet cross sections	182
11.11.	Stacked uncertainties for centrality-dependent jet R_{pPb}	183
11.12.	Stacked uncertainties for centrality-dependent jet cross section ratios . .	184
A.1.	Pseudorapidity (illustration)	193
A.2.	Jet systematics in p-Pb for $R = 0.2$ jets (unfolding)	194
A.3.	Jet systematics in p-Pb for $R = 0.2$ jets (regularization)	195
A.4.	Jet systematics in p-Pb for $R = 0.2$ jets (prior)	195
A.5.	Jet systematics in p-Pb for $R = 0.2$ jets (minimum p_T)	196
A.6.	Jet systematics in p-Pb for $R = 0.2$ jets (δp_T)	196
A.7.	Jet systematics in p-Pb for $R = 0.2$ jets (background)	197
A.8.	Jet systematics in p-Pb for $R = 0.2$ jets (tracking efficiency)	197
A.9.	Stacked uncertainties for centrality-dependent jet in p-Pb for $R = 0.2$.	198
A.10.	Stacked uncertainties for centrality-dependent jet in p-Pb for $R = 0.2$.	199
A.11.	Stacked uncertainties for centrality-dependent R_{pPb} for $R = 0.2$	200

Bibliography

- [Aad11] G. Aad *et al.*, Study of jet shapes in inclusive jet production in pp collisions at $\sqrt{s} = 7$ TeV using the ATLAS detector, *Phys. Rev. D* **83** (2011), DOI link, arXiv:1101.0070.
- [Aad12] G. Aad *et al.*, Observation of a new particle in the search for the Standard Model Higgs boson with the ATLAS detector at the LHC, *Phys. Lett. B* **716** (2012), 1–29, DOI link, arXiv:1207.7214.
- [Aad14] G. Aad, Centrality and rapidity dependence of inclusive jet production in $\sqrt{s_{\text{NN}}} = 5.02$ TeV proton–lead collisions with the ATLAS detector, *to be published in Phys. Lett. B* (2014), arXiv:1412.4092.
- [Aam08] K. Aamodt *et al.*, The ALICE experiment at the CERN LHC, *JINST* **3** (2008), 8002, DOI link.
- [Aam10a] K. Aamodt *et al.*, Alignment of the ALICE Inner Tracking System with cosmic-ray tracks, *JINST* **5** (2010), 3003, DOI link, arXiv:1001.0502.
- [Aam10b] K. Aamodt *et al.*, Charged-Particle Multiplicity Density at Midrapidity in Central Pb–Pb Collisions at $\sqrt{s_{\text{NN}}} = 2.76$ TeV, *Phys. Rev. Lett.* **105** (2010), 252301, DOI link, arXiv:1011.3916.
- [Aam11] K. Aamodt *et al.*, Suppression of charged particle production at large transverse momentum in central Pb–Pb collisions at $\sqrt{s_{\text{NN}}} = 2.76$ TeV, *Phys. Lett. B* **696** (2011), 30–39, DOI link, arXiv:1012.1004.
- [Abe93] F. Abe *et al.*, Measurement of jet shapes in $\bar{p}p$ collisions at $\sqrt{s} = 1.8$ TeV, *Phys. Rev. Lett.* **70** (1993), 713–717, DOI link.
- [Abe12a] B. Abelev *et al.*, Measurement of event background fluctuations for charged particle jet reconstruction in Pb–Pb collisions at $\sqrt{s_{\text{NN}}} = 2.76$ TeV, *JHEP* **03** (2012), 053, DOI link, arXiv:1201.2423.
- [Abe12b] B. Abelev *et al.*, Underlying Event measurements in pp collisions at $\sqrt{s} = 0.9$ and 7 TeV with the ALICE experiment at the LHC, *JHEP* **2012** (2012), DOI link, arXiv:1112.2082.

- [Abe13a] B. Abelev *et al.*, Centrality determination of Pb–Pb collisions at $\sqrt{s_{\text{NN}}} = 2.76$ TeV with ALICE, *Phys. Rev. C* **88** (2013), 44909, DOI link, arXiv:1301.4361.
- [Abe13b] B. Abelev *et al.*, Long-range angular correlations on the near and away side in p-Pb collisions at $\sqrt{s_{\text{NN}}} = 5.02$ TeV, *Phys. Lett. B* **719** (2013), 29–41, DOI link, arXiv:1212.2001.
- [Abe13c] B. Abelev *et al.*, Measurement of inelastic, single- and double-diffraction cross sections in proton–proton collisions at the LHC with ALICE, *Eur. Phys. J. C* **73** (2013), 2456, DOI link, arXiv:1208.4968.
- [Abe13d] B. Abelev *et al.*, Measurement of the inclusive differential jet cross section in pp collisions at $\sqrt{s} = 2.76$ TeV, *Phys. Lett. B* **722** (2013), 262–272, DOI link, arXiv:1301.3475.
- [Abe13e] B. Abelev *et al.*, Pseudorapidity Density of Charged Particles in p–Pb Collisions at $\sqrt{s_{\text{NN}}} = 5.02$ TeV, *Phys. Rev. Lett.* **110** (2013), DOI link, arXiv:1210.3615.
- [Abe14a] B. Abelev *et al.*, Charged jet cross sections and properties in proton–proton collisions at $\sqrt{s} = 7$ TeV, *to be published in Phys. Rev. D* (2014), arXiv:1411.4969.
- [Abe14b] B. Abelev *et al.*, Measurement of charged jet suppression in Pb–Pb collisions at $\sqrt{s_{\text{NN}}} = 2.76$ TeV, *JHEP* **03** (2014), 013, DOI link, arXiv:1311.0633.
- [Abe14c] B. Abelev *et al.*, Measurement of visible cross sections in proton–lead collisions at $\sqrt{s_{\text{NN}}} = 5.02$ TeV in van der Meer scans with the ALICE detector, *JINST* **9** (2014), P11003–P11003, DOI link, arXiv:1405.1849.
- [Abe14d] B. Abelev *et al.*, Multi-particle azimuthal correlations in p-Pb and Pb-Pb collisions at the LHC, *Phys. Rev. C* **90** (2014), 054901, DOI link, arXiv:1406.2474.
- [Abe14e] B. Abelev *et al.*, Transverse momentum dependence of inclusive primary charged-particle production in p–Pb collisions at $\sqrt{s_{\text{NN}}} = 5.02$ TeV, *Eur. Phys. J. C* **74** (2014), DOI link, arXiv:1405.2737.
- [Abe15] B. Abelev *et al.*, Measurement of charged jet production cross sections and nuclear modification in p–Pb collisions at $\sqrt{s_{\text{NN}}} = 5.02$ TeV, *to be published in Phys. Lett. B* (2015), arXiv:1503.0068.
- [Acc02] A. Accardi, Cronin Effect in Proton Nucleus Collisions: A Survey of Theoretical Models, *contribution to the CERN Yellow report on Hard Probes* (2002), hep-ph/0212148.

-
- [Ada07] A. Adare *et al.*, Scaling Properties of Azimuthal Anisotropy in Au+Au and Cu+Cu Collisions at $\sqrt{s_{\text{NN}}} = 200$ GeV, *Phys. Rev. Lett.* **98** (2007), DOI link, nucl-ex/0608033.
- [Ada14] J. Adam *et al.*, Centrality dependence of particle production in p-Pb collisions at $\sqrt{s_{\text{NN}}} = 5.02$ TeV, *to be published in Phys. Rev. C* (2014), arXiv:1412.6828.
- [Adc01] K. Adcox *et al.*, Suppression of Hadrons with Large Transverse Momentum in Central Au+Au Collisions at $\sqrt{s_{\text{NN}}} = 130$ GeV, *Phys. Rev. Lett.* **88** (2001), DOI link.
- [Ade14] P. Ade *et al.*, Planck 2013 results. XVI. Cosmological parameters, *Astron. Astrophys.* (2014), DOI link, arXiv:1303.5076.
- [Adl01] C. Adloff *et al.*, On the rise of the proton structure function F_2 towards low x , *Phys. Lett. B* **520** (2001), 183–190, DOI link, hep-ex/0108035.
- [Ady11] T. Adye, Unfolding algorithms and tests using RooUnfold, *Proceedings of the PHYSTAT 2011 Workshop* (2011), physics.data-an/1105.1160.
- [Aio14] S. Aiola, Measurement of jet p_{T} spectra and R_{AA} in pp and Pb–Pb collisions at $\sqrt{s_{\text{NN}}} = 2.76$ TeV with the ALICE detector, *Nucl. Phys. A* **931** (2014), 382, DOI link, arXiv:1408.0479.
- [Ale06] B. Alessandro *et al.*, ALICE: Physics Performance Report, Volume II, *J. Phys. G* **32** (2006), 1295–2040, DOI link.
- [Alf01] M. Alford, Color-Superconducting Quark Matter, *Ann. Rev. Nucl. Part. Sci.* **51** (2001), 131–160, DOI link, hep-ph/0102047.
- [Alm10] J. Alme *et al.*, The ALICE TPC, a large 3-dimensional tracking device with fast readout for ultra-high multiplicity events, *Nucl. Instrum. Meth. A* **622** (2010), 316–367, DOI link, arXiv:1001.1950.
- [And83] B. Andersson, G. Gustafson, G. Ingelman, and T. Sjöstrand, Parton fragmentation and string dynamics, *Phys. Rep.* **97** (1983), 31–145, DOI link.
- [Arn94] M. Arneodo, Nuclear effects in structure functions, *Phys. Rept.* **240** (1994), 301–393, DOI link.
- [Arn07] R. Arnaldi *et al.*, The zero degree calorimeters for the ALICE experiment, *Nucl. Instrum. Meth.* **581** (2007), 397–401, DOI link.
- [Aub83] J. J. Aubert *et al.*, The ratio of the nucleon structure functions F_2^{N} for iron and deuterium, *Phys. Lett. B* **123** (1983), 275–278, DOI link.

- [Bal14] P. Balek, Measurements of charged particle spectra and nuclear modification factor in p+Pb collisions with the ATLAS detector, *Nucl. Phys. A* **931** (2014), 399–403, DOI link.
- [Ber06] C. Berger, *Elementarteilchenphysik*, Springer-Lehrbuch (2006).
- [Bjo73] J. Bjorken, Can We Measure Parton-Parton Cross Sections?, *Phys. Rev. D* **8** (1973), 4098–4106, DOI link.
- [Bjo82] J. Bjorken, Energy Loss of Energetic Partons in Quark – Gluon Plasma: Possible Extinction of High p_T Jets in Hadron – Hadron Collisions, *FERMILAB-PUB 82-059-THY* (1982).
- [Bla00] G. C. Blazey *et al.*, Run II Jet Physics: Proceedings of the Run II QCD and Weak Boson Physics Workshop, *conference proceedings* (2000), hep-ex/0005012.
- [Blo69] E. D. Bloom *et al.*, High-Energy Inelastic e-p Scattering at 6° and 10°, *Phys. Rev. Lett.* **23** (1969), 930–934, DOI link.
- [Bor13] S. Borsanyi, Thermodynamics of the QCD transition from lattice, *Nucl. Phys. A* **904** (2013), 270–277, DOI link, arXiv:1210.6901.
- [Boz14] P. Bozek and W. Broniowski, Hydrodynamic approach to p–Pb, *Nucl. Phys. A* **926** (2014), 16–23, DOI link, arXiv:1401.2367.
- [Bre69] M. Breidenbach *et al.*, Observed Behavior of Highly Inelastic Electron-Proton Scattering, *Phys. Rev. Lett.* **23** (1969), 935–939, DOI link.
- [Bru94] R. Brun, F. Carminati, and S. Giani, GEANT Detector Description and Simulation Tool, *CERN Program Library Long Writeup CERN-W-5013* (1994).
- [Bru97] R. Brun and F. Rademakers, ROOT - An object oriented data analysis framework, *Nucl. Instr. Meth. Phys. Res. A* **389** (1997), 81–86, DOI link.
- [Cac06] M. Cacciari and G. P. Salam, Dispelling the N^3 myth for the k_T jet-finder, *Phys. Lett. B* **641** (2006), 57–61, DOI link, hep-ph/0512210.
- [Cac08a] M. Cacciari and G. P. Salam, Pileup subtraction using jet areas, *Phys. Lett. B* **659** (2008), 119–126, DOI link, arXiv:0707.1378.
- [Cac08b] M. Cacciari, G. P. Salam, and G. Soyez, The anti- k_t jet clustering algorithm, *JHEP* **04** (2008), 063, DOI link, arXiv:0802.1189.
- [Cac08c] M. Cacciari, G. P. Salam, and G. Soyez, The catchment area of jets, *JHEP* **2008** (2008), 005–005, DOI link, arXiv:0802.1188.

-
- [Cac12] M. Cacciari, G. P. Salam, and G. Soyez, FastJet user manual, *Eur. Phys. Jour. C* **72** (2012), 1896, DOI link, arXiv:1111.6097.
- [Car04] F. Carminati *et al.*, ALICE: Physics Performance Report, Volume I, *J. Phys. G* **30** (2004), 1517–1763, DOI link.
- [Cha12a] S. Chatrchyan *et al.*, Measurement of the underlying event activity in pp collisions at $\sqrt{s} = 0.9$ and 7 TeV with the novel jet-area/median approach, *JHEP* **2012** (2012), DOI link, arXiv:1207.2392.
- [Cha12b] S. Chatrchyan *et al.*, Observation of a new boson at a mass of 125 GeV with the CMS experiment at the LHC, *Phys. Lett. B* **716** (2012), 30–61, DOI link.
- [Cha13] S. Chatrchyan *et al.*, Charged particle nuclear modification factor and pseudorapidity asymmetry in pPb collisions at $\sqrt{s_{\text{NN}}} = 5.02$ TeV, *CMS-PAS-HIN-12-017* (2013).
- [Cha14] S. Chatrchyan *et al.*, Measurement of inclusive jet nuclear modification factor in pPb collisions at $\sqrt{s_{\text{NN}}} = 5.02$ TeV with CMS, *CMS-PAS-HIN-14-001* (2014).
- [Che03] S. Chekanov *et al.*, ZEUS next-to-leading-order QCD analysis of data on deep inelastic scattering, *Phys. Rev. D* **67** (2003), 12007, DOI link, hep-ex/0208023v2.
- [Col85] J. C. Collins, D. E. Soper, and G. Sterman, Factorization for short distance hadron-hadron scattering, *Nucl. Phys. B* **261** (1985), 104–142, DOI link.
- [Col88] J. Collins, D. Soper, and G. Sterman, Factorization of Hard Processes in QCD, *Adv. Ser. Direct. High Energy Phys.* **5** (1988), 1–91, hep-ph/0409313.
- [Con14] M. Connors, Inclusive jet spectra in p–Pb collisions at ALICE, *Nucl. Phys. A* **931** (2014), 1174–1178, DOI link, arXiv:1409.3468.
- [Cor08] P. Cortese *et al.*, ALICE Electromagnetic Calorimeter Technical Design Report, *CERN-LHCC-2008-014* (2008).
- [Cro75] J. W. Cronin *et al.*, Production of hadrons at large transverse momentum at 200, 300, and 400 GeV, *Phys. Rev. D* **11** (1975), 3105–3123, DOI link.
- [D’A03] G. D’Agostini, Bayesian inference in processing experimental data: principles and basic applications, *Rept. Prog. Phys.* **66** (2003), 1383–1419, DOI link, physics/0304102.
- [Das95] A. Das and T. Ferbel, *Kern- und Teilchenphysik*, Spektrum Akademischer Verlag (1995).

- [Dem04] W. Demtröder, *Experimentalphysik 4*, Springer (2004).
- [DF12] D. De Florian, R. Sassot, M. Stratmann, and P. Zurita, Global Analysis of Nuclear PDFs, *DIS2012 proceedings* (2012), DOI link, arXiv:1204.3797.
- [Dok97] Y. Dokshitzer, G. Leder, S. Moretti, and B. Webber, Better jet clustering algorithms, *JHEP* **1997** (1997), 001–001, DOI link, hep-ph/9707323.
- [Dok01] Y. Dokshitzer and D. Kharzeev, Heavy-quark colorimetry of QCD matter, *Phys. Lett. B* **519** (2001), 199–206, DOI link, hep-ph/0106202.
- [Esk09] K. J. Eskola, H. Paukkunen, and C. A. Salgado, EPS09 - A new generation of NLO and LO nuclear parton distribution functions, *JHEP* **04** (2009), 065, DOI link, arXiv:0902.4154.
- [Fro61] M. Froissart, Asymptotic Behavior and Subtractions in the Mandelstam Representation, *Phys. Rev.* **123** (1961), 1053–1057, DOI link.
- [Fru87] R. Fruehwirth, Application of Kalman filtering to track and vertex fitting, *Nucl. Instr. Meth. Phys. Res. A* **262** (1987), 444–450, DOI link.
- [Gan95] O. Ganel and R. Wigmans, Quartz fiber calorimetry for LHC experiments, *Nucl. Instr. Meth. Phys. Res. A* **365** (1995), 104–116, DOI link.
- [Gat10] C. Gattringer and C. B. Lang, *Quantum Chromodynamics on the Lattice. An Introductory Presentation*, Springer (2010).
- [GM64] M. Gell-Mann, A schematic model of baryons and mesons, *Phys. Lett.* **8** (1964), 214–215, DOI link.
- [GO09] J. F. Große-Oetringhaus, Measurement of the Charged-Particle Multiplicity in Proton–Proton Collisions with the ALICE Detector, Ph.D. thesis, Westfälische Wilhelms-Universität (2009).
- [Haa13] R. Haake, Charged Jets in Minimum Bias p–Pb Collisions at $\sqrt{s_{\text{NN}}} = 5.02$ TeV with ALICE, *PoS EPS-HEP2013* (2013), 176, arXiv:1310.3612.
- [Haa15] R. Haake, Centrality dependence of charged jets in p–Pb collisions at $\sqrt{s_{\text{NN}}} = 5.02$ TeV measured with the ALICE detector, *to be published in PoS* (2015), arXiv:1503.0644.
- [Hir04] M. Hirai, S. Kumano, and T.-H. Nagai, Nuclear parton distribution functions and their uncertainties, *Phys. Rev. C* **70** (2004), 44905, DOI link, hep-ph/0404093.
- [Hut90] J. E. Huth *et al.*, Toward a standardization of jet definitions, *Snowmass 1990, conference proceedings, FERMILAB-Conf-90-249* (1990).

-
- [Hö96] A. Höcker and V. Kartvelishvili, SVD approach to data unfolding, *Nucl. Instr. Meth. Phys. Res. A* **372** (1996), 469–481, DOI link, hep-ph/9509307.
- [Ian08] E. Iancu and R. Venugopalan, The Color Glass Condensate and High Energy Scattering in QCD, *Review for QGP3* (2008), hep-ph/0303204.
- [Jam75] F. James and M. Roos, Minuit - a system for function minimization and analysis of the parameter errors and correlations, *Comput. Phys. Commun.* **10** (1975), 343–367, DOI link.
- [KB04] C. Klein-Bösing, Production of Neutral Pions and Direct Photons in Ultra-Relativistic Au+Au Collisions, Ph.D. thesis, Westfälische Wilhelms-Universität (2004).
- [KB13] C. Klein-Bösing, Study of the Quark-Gluon Plasma with Hard and Electromagnetic Probes, Ph.D. thesis, Westfälische Wilhelms-Universität (2013).
- [Kha10] V. Khachatryan *et al.*, Observation of long-range, near-side angular correlations in proton-proton collisions at the LHC, *JHEP* **09** (2010), 091, DOI link, arXiv:1009.4122.
- [Kni01] B. Kniehl, G. Kramer, and B. Pötter, Testing the universality of fragmentation functions, *Nucl. Phys. B* **597** (2001), 337–369, DOI link, hep-th/0011155.
- [Lef08] C. Lefevre, The CERN accelerator complex, *CERN Document Server*, *CERN-DI-0812015* (2008).
- [Loh05] E. Lohrmann, *Hochenergiephysik*, Teubner (2005).
- [Mil07] M. L. Miller, K. Reygers, S. J. Sanders, and P. Steinberg, Glauber Modeling in High-Energy Nuclear Collisions, *Ann. Rev. Nucl. Part. Sci.* **57** (2007), 205–243, DOI link, nucl-ex/0701025.
- [Nas04] P. Nason, A New Method for Combining NLO QCD with Shower Monte Carlo Algorithms, *JHEP* **2004** (2004), 040–040, DOI link, hep-ph/0409146.
- [Oli14] K. Olive, Review of particle physics, *Chin. Phys. C* **38** (2014), 090001, DOI link.
- [Owe13] J. F. Owens, A. Accardi, and W. Melnitchouk, Global parton distributions with nuclear and finite- Q^2 corrections, *Phys. Rev. D* **87** (2013), 94012, DOI link, arXiv:1212.1702.
- [Per87] D. H. Perkins, *Introduction to High Energy Physics*, Cambridge University Press (1987).

- [Per13] D. V. Perepelitsa, Inclusive jet production in ultrarelativistic proton-nucleus collisions, Ph.D. thesis, Columbia University (2013).
- [Rit14] K. Rith, Present Status of the EMC effect, *conference proceedings* (2014), arXiv:1402.5000.
- [Sai85] K. Saito and T. Uchiyama, Effect of the Fermi motion on nuclear structure functions and the EMC effect, *Z. Phys. A* **322** (1985), 299–307, DOI link.
- [Sal10] G. P. Salam, Towards jetography, *Eur. Phys. J. C* **67** (2010), 637–686, DOI link, arXiv:0906.1833.
- [Sal12] C. A. Salgado *et al.*, Proton-nucleus collisions at the LHC: Scientific opportunities and requirements, *J. Phys. G* **39** (2012), 5010, DOI link, arXiv:1105.3919.
- [Sar10] S. Sarkar, H. Satz, and B. Sinha, *The Physics of the Quark-Gluon Plasma*, Springer (2010).
- [Sjo06] T. Sjostrand, S. Mrenna, and P. Skands, PYTHIA 6.4 Physics and Manual, *JHEP* **05** (2006), 026, DOI link, hep-ph/0603175.
- [Ska10] P. Z. Skands, Tuning Monte Carlo Generators: The Perugia Tunes, *Phys. Rev. D* **82** (2010), DOI link, arXiv:1005.3457.
- [Sne11] R. Snellings, Elliptic flow: a brief review, *New J. Phys.* **13** (2011), 055008, DOI link, arXiv:1102.3010.
- [Ste06] M. Stephanov, QCD phase diagram: An overview, *PoS LAT2006* (2006), 024, hep-lat/0701002.
- [Tay97] J. R. Taylor, *An Introduction to Error Analysis*, University Science Books (1997).
- [Ver13] M. Verweij, Modelling and measurement of jet quenching in relativistic heavy-ion collisions at the LHC, Ph.D. thesis, Utrecht University (2013).
- [Wil74] K. G. Wilson, Confinement of quarks, *Phys. Rev. D* **10** (1974), 2445–2459, DOI link.
- [Zwe64] G. Zweig, An SU(3) model for strong interaction symmetry and its breaking, *CERN-TH-412, NP-14146, PRINT-64-170* (1964).

Acknowledgements

During the creation of this thesis, I received support from many people who I wish to thank.

Der größte Dank gebührt meiner Frau Elisabeth, die mich immer unterstützt hat und auch meine anderthalb Jahre am CERN mitgetragen hat. Auch profitierte diese Arbeit ganz massiv von ihrer sprachlichen Korrektur.

At CERN, I wish to thank the whole 587 crew for fruitful discussions. Especially I would like to thank Constantin Loizides for pushing me in exactly the right way to allow me to find my maximum performance. His valuable support during my whole PhD was an important contribution in the process of creation of this thesis.

In Münster, I especially want to thank Johannes Wessels and Christian Klein-Bösing for always having a friendly ear and for allowing me to attend so many conferences. Thanks for all your trust and support with my thesis and beyond. And, of course, thank you for allowing me to spend the first half of my PhD at CERN.

Last but not least, I also wish to thank Jana Bielcikova for supporting my work in PWGJE.

CURRICULUM VITAE

Education

- May 2012 – April 2015: PhD student at the University of Münster
- October 2006 – April 2012: Studies of physics at the University of Münster
Diploma thesis in lattice gauge theory
Title: *Methoden zur Bestimmung des Sommer-Parameters auf dem Gitter*
- 1997 – 2006: School education, Bertha-von-Suttner-Gymnasium Oberhausen, Germany

Publications and proceedings

- ALICE COLLABORATION, “Measurement of charged jet production cross sections and nuclear modification in p–Pb collisions at $\sqrt{s_{\text{NN}}} = 5.02$ TeV”, cf. arXiv:1503.00681 (to be published in Phys. Lett. B).
- R. HAAKE, “Charged Jets in Minimum Bias p–Pb Collisions at $\sqrt{s_{\text{NN}}} = 5.02$ TeV with ALICE”, conference proceedings, in: PoS EPS-HEP2013 (2013) 176; cf. arXiv:1310.3612
- R. HAAKE, “Measurement of inclusive jet spectra in pp, p–Pb, and Pb–Pb collisions with the ALICE detector”, conference proceedings, cf. arXiv:1410.4437 (to be published in JPCS).
- R. HAAKE, “Centrality dependence of charged jets in p–Pb collisions at $\sqrt{s_{\text{NN}}} = 5.02$ TeV measured with the ALICE detector”, conference proceedings, cf. arXiv:1503.06441 (to be published in PoS).

Summary of research and employment history

- January 2014 – June 2015: Research associate at the Institute for Nuclear Physics, University of Münster
- May 2012 – December 2013: Research stay at CERN (ALICE Collaboration) as associated member of the personnel
- April 2010 – April 2012: Student research assistant at the Institute for Theoretical Physics, University of Münster
- June 2008 – January 2010: Student research assistant at the Institute for Biomagnetism and Biosignalanalysis, University of Münster

